Tackling viscoelastic turbulence

by

Ismail Hameduddin

A dissertation submitted to The Johns Hopkins University in conformity with the requirements for the degree of Doctor of Philosophy.

Baltimore, Maryland

May, 2018

Abstract

Turbulence in viscoelastic flows is a fascinating phenomenon with important technological implications, e.g. drag reduction at high Reynolds numbers and increased mixing efficiencies at low Reynolds numbers. The dynamics of these flows have been extensively studied experimentally over the last seventy years and more recently, in direct numerical simulations (DNS). However, theoretical progress in viscoelastic turbulence has been hindered by the fundamental challenges posed by the need to account for both the velocity as well as the elastic deformation history, encapsulated in the positive–definite conformation tensor. Due to the positivity constraint, the latter tensor is not a vector space quantity and thus classical approaches used to quantitatively analyze turbulence in Newtonian flows cannot be directly extended to viscoelastic flows. This fundamental issue is addressed in the present thesis in two parts. Firstly, we develop a decomposition of the conformation tensor about a given base–state that respects the mathematical and physical nature of this quantity. Scalar measures to quantify the resulting fluctuating conformation tensor are developed based on the non-Euclidean Riemannian geometry of the set of positive–definite

ABSTRACT

tensors. The three measures are (a) the logarithmic volume ratio of the conformation tensor with respect to the base–state conformation tensor (b) the squared geodesic distance of the conformation tensor from the base–state, (c) the geodesic distance of the fluctuating conformation tensor from the closest isotropic tensor. Secondly, we develop an approach to perturb the conformation tensor in a physically consistent manner. This approach is an alternative to the classical weakly nonlinear expansion of vector space quantities, and is thus termed the weakly nonlinear deformation. When specialized to linear perturbations, this approach reveals the correct Hilbert space structure for the linearized problem. Viscoelastic (FENE-P) channel flow DNS are developed and used to illustrate the theoretical framework: fully turbulent flow is used for the first part, and the nonlinear evolution of Tollmien–Schlichting waves are considered for the second part. Several important insights are gleaned from these simulations, demonstrating the efficacy of the proposed approach. The fundamental contributions in the present thesis pave the road for theoretical modelling and analysis of viscoelastic turbulence.

Primary Reader: Dennice F. Gayme

Secondary Readers: Tamer A. Zaki, Charles Meneveau

Acknowledgments

I would like to acknowledge my graduate advisor, Professor Dennice F. Gayme. This dissertation would not have been possible without her continuous support over the past five years. I would like to thank her for teaching me about non-normal operators, introducing me to the turbulence problem, serving as an examiner for my DQE and GBO, and for everything else.

I also owe a great debt of gratitude to my collaborators, Professors Tamer A. Zaki and Charles Meneveau. Their support, encouragement, and scientific insights were critical during the last few years. I would like to thank Professor Zaki for teaching me hydrodynamic stability, introducing me to viscoelastic turbulence, writing and running parallel codes on clusters, and for everything else. I would like to thank Professor Meneveau for teaching me turbulence theory, always asking the most thought provoking questions, serving as an examiner for my GBO, for showing me the tightrope that is the art of being balanced, and for everything else.

I would like to thank Professor Danielle Tarraf for teaching me robust control, for her jolly demeanour and very funny jokes, and for serving as an examiner for my

ACKNOWLEDGMENTS

GBO; Professor Robert Leheny for teaching me the Boltzmann equation, statistical mechanics, and for serving as an examiner for my GBO; Professor Tony Dalrymple for serving as an examiner for my GBO; Professor Andrea Prosperetti for being the greatest inspiration an aspiring first-year student could ask for, for burning the midnight oil to bring us the best possible graduate courses, and for serving as an examiner for my DQE; Professor Rajat Mittal for teaching me computational fluid dynamics and for serving as an examiner for my DQE; Professor Noah Cowan for examining me on linear systems theory for my DQE; Professor Joseph Katz for teaching me potential flow and serving as an examiner for my DQE.

The department back office are the unsung heroes of my PhD career. I cannot count how many times I was rescued by the able seaman/women that guide the departmental ship. I would like to thank Michael Bernard, Melissa, Kevin Adams, Shawna O'Brien, Deana Santoni, Cindy Larichiuta, Martin Devaney, and others in ME administrative support.

I would also like to thank Christine Kavanagh and the Whiting School of Engineering for their unwavering support of graduate students.

The assistance provided by my friends Jin Lee and Sang Jin Lee was crucial in setting up the simulations in this dissertation, and for that I am most grateful to them. I would also like to thank my friend, Carl R. Shapiro, for his invaluable comments on early drafts of this dissertation and for all the useful feedback that he gave me on my work over the years.

ACKNOWLEDGMENTS

I would like to thank those of my dear friends that I found at Johns Hopkins and who were not only great fun but also proved formidable debate opponents and valuable scientific interlocutors: Xiang Yang, Jasim Sadique, Parastou Islami, Vijay Vedula, Joel Bretheim, Theodore Grunberg, Vaughan Thomas, Qi Wang, Perry Johnson, Kourosh Shoele, Neda Yaghoobian, Luis Martinez, Eshwan Ramudu, Aaron Rips, Sri Kamal Kandala, Venkat Prava, Hani Bakhshaee, Leen Alawieh, and Anirban Gosh.

I would also like to thank my friends 'Doctor' Syed Ali Rahman and Nasir Ismail for all the great times, and for their continuous care. I would like to acknowledge my friend Abdullah Nabil for his support and his untiring exertions that helped me maintain a semblance of the spiritual life. Old friends don't always make good friends, but Afif Antabli is perhaps the greatest, and was always there when I needed help.

I would like to thank my parents, for I owe them everything. I would like to acknowledge all my siblings (Nasira, Bushra, Yasir, Saadia, Taha) and their families. Their emotional support and encouragement, coming in from all corners of the globe, sustained me through many years.

Finally, I would like to thank my wonderful and loving wife Atiya Ullah. At the end of the day, your presence by my side is what made all the difference.

وردوا على نهر الحياة و كلهم　　شربوا وكم فى الركب من متضلع

حاشا الكريم يردهم عطشى وقد　　وردوا وأصل الجود من ذا المنبع

Dedication

Dedicated to my parents, Nadira (née Qamruddin) and Mohamed Hameduddin.

Contents

List of Tables

List of Figures

Chapter 1

Introduction

The interplay of viscous and elastic effects in incompressible viscoelastic flows leads to a greatly enriched dynamics that produces intriguing phenomena not found in purely viscous, Newtonian flows. A classic example is the rod–climbing, or Weissenberg, effect first discovered by Garner and Nissan[2] and later by the eponymous Weissenberg.[3] When a vertical rotating rod is submerged in an open container of viscoelastic fluid, the fluid begins to ascend, or 'climb', upwards along the rod. In a purely viscous fluid, there is no climbing but rather the fluid is pushed outwards towards the walls of the container. Another related phenomenon occurs when a siphoning tube connected to a vacuum source is submerged in an open container of viscoelastic fluid and then is slowly extricated from it. As the tube is removed above the free surface, the siphoning action continues, unlike in a viscous fluid where air entrainment disrupts the siphon. This 'device' is called a tubeless siphon and appears

to be first used by Astarita and Nicodemo[4] to quantify the extensional behaviour of viscoelastic fluids.

This dissertation focuses on transition and turbulence in viscoelastic fluids. The term viscoelastic turbulence encompasses a wide range of phenomena, depending on the relative importance of inertial, viscous and elastic effects. Viscoelastic turbulence is a rich and growing area of research due to the diversity of the phenomena observed and their technological importance.

At high Reynolds numbers, drag reduction in dilute polymer solutions was discovered by Toms[5] and Mysels[6] well over half a century ago. In turbulent pipe and channel flow of a Newtonian solvent, adding minute amounts of flexible polymers can significantly reduce drag; experiments have demonstrated drag reduction up to 60% or more.[7,8] This dramatic drag reduction can lead to significant energy savings and arises due to the elasticity imparted by the polymers to the viscous solvent. Polymer additives have been used to great effect in the Trans-Alaska Pipeline System (TAPS)[9] and, more recently, surfaces that shed polymers (ablative surfaces) have been shown to reduce drag up to 30% in cargo ships.[10] The potential technological implications of such large drag reduction drove early research in viscoelastic turbulence; the reviews by Lumley[7] and by Berman[11] provide a good synopsis of these early efforts.

Mixing efficiency and heat transfer in microfluidic devices is challenging because turbulence does not exist in low Reynolds number flows of Newtonian fluids. However, in viscoelastic fluids there is a possibility of transitioning from a laminar state to a

turbulent one at such Reynolds numbers. The resulting turbulence is usually referred to as elastic turbulence due to the predominance of elastic effects, and has been observed in a variety of flows.[12–19] The technological importance of low Reynolds number turbulence has spurred research in elastic turbulence.[17,20]

A great variety of distinct viscoelastic turbulence regimes have been described in the literature and their number is still growing: Recently, direct numerical simulations demonstrated the existence of a regime of viscoelastic turbulence at significantly lower Reynolds numbers than possible in Newtonian flows but one that still depends on inertial effects.[21–24] This new regime has been termed elasto-inertial turbulence. Experimental evidence has also emerged that appears to support the existence of this new regime of turbulence.[25]

The description of viscoelastic turbulence above is a brief selection of a wide area of intensive study. Numerous reviews have been written on various aspects of the subject.[7,8,11,17,26–33] Despite the wide scholarship on the subject, recent discoveries of several distinct phenomena in experiments and simulations demonstrate that a conclusive description of all the regimes of viscoelastic turbulence is incomplete. Additionally, detailed quantitative descriptions of the known regimes of viscoelastic turbulence, analogous to that available for Newtonian turbulence, are lacking. A reason for the absence of such quantitative descriptions is that the velocity field by itself is insufficient to describe the flow, and one also needs a physically consistent description of the microstructure which provides the elastic properties of the fluid. As a

result, the highly refined methods developed for transition and turbulence in Newtonian flows are not sufficient for the viscoelastic case and appropriate alternatives need to be formulated. The latter is the goal of the present work. The approach adopted in the present dissertation is to develop theoretical tools for viscoelastic turbulence in a similar spirit as those already established for Newtonian turbulence, rather than directly extend the particular forms. Viscoelasticity is a descriptive term and can be achieved in a fluid by many different means. The developments in this dissertation are theoretical and therefore do not depend on a particular instantiation of a viscoelastic fluid. However, the fluids that are relevant to viscoelastic turbulence are invariably polymer solutions: flexible polymers dissolved in a Newtonian solvent.

The remainder of this introduction is organized as follows: in §1.1, we review the basic approach used to analyse turbulence and transition in Newtonian flows, in §1.2 we discuss the specific problems that arise with viscoelastic flows and whose remedy is the goal of the present dissertation, in §1.3.1 we present details of channel flow that will be used to illustrate the framework throughout the dissertation and in §1.3 we provide a chapter by chapter outline of the remainder of the dissertation.

1.1 Newtonian turbulence

Incompressible Newtonian flows, described by the Navier–Stokes equations, are purely dissipative: there is no capacity to store potential energy in the fluid. The

Cauchy stress tensor in such fluids is composed of the isotropic pressure and a deviatoric part that is proportional to the symmetric part of the velocity gradient tensor. The dynamics are thus completely determined by instantaneous rates and only the velocity field $\boldsymbol{u}$ is required for a complete description of Newtonian turbulence.

Turbulence in Newtonian flows is a mature field of research and a full review is beyond the scope of the present work. Rather, we briefly examine the earliest historical contributions that led to the development of the field of turbulence research as it is known today. The goal of such an exercise is to contexualize the challenges presently faced by researchers in viscoelastic turbulence and also to provide perspective on how to attack the problems at hand in viscoelastic turbulence.

The modern approach to Newtonian turbulence research can be traced back to two seminal papers by Reynolds, published in 1883[34] and 1895.[35] The 1883 paper was experimental and focused on the problem of laminar–turbulent transition in pipe flow. This paper introduced the Reynolds number as an expression of the relative importance of viscosity and inertia, and recognized its role in determining whether the flow transitions.

The 1895 paper was theoretical and its purpose was to understand the laminar–turbulent transition by examining fully turbulent flows and, in particular, the conditions under which turbulence may be sustained. To tackle the complex and apparently random flow fields in turbulence, Reynolds proposed an approach motivated by the kinetic theory of gases. Accordingly, he developed the following additive decomposition

of the flow field

$$\boldsymbol{u} = \overline{\boldsymbol{u}} + \boldsymbol{u}' \tag{1.1}$$

where $\overline{\boldsymbol{u}}$ is the time-averaged velocity field and $\boldsymbol{u}'$ is a fluctuation about this mean, and then derived the governing equations for both $\overline{\boldsymbol{u}}$ and $\boldsymbol{u}'$. He also evaluated the turbulent kinetic energy balance and identified the production–dissipation balance as the determining factor in whether turbulence is sustained for a given Reynolds number. With such considerations, Reynolds introduced the idea of studying turbulence statistically rather than by examining the complete flow all at once. Furthermore, he introduced the idea of separating fluctuations from the statistically persistent state and studying turbulence through the behaviour of the fluctuations.

The decomposition (1.1) is known as the Reynolds decomposition and is a cornerstone of turbulence research today.[36] It is difficult to overstate the importance of the decomposition to modern turbulence research and any list of important achievements that depend on the Reynolds decomposition is bound to be incomplete. It is sufficient to note that the decomposition has had a large impact on turbulence theory, modelling, simulations and also experiments. Nearly every modern textbook on turbulence is predominantly based on some form of it.[37–41]

It is now recognized that the particular averaging Reynolds used to define the mean flow is frequently inappropriate.[42,43] As a result, several variants have been

suggested.[42,44,45] Generally, the averaging can be represented as a filtering operation: a convolution with a prescribed kernel that satisfies certain properties.[44] The equations for the mean and the fluctuation in this case are not always the same as those derived by Reynolds. However, all such variants may be viewed as equivalent to the Reynolds decomposition because they are all based on an additive decomposition of the velocity field. Other extensions of the Reynolds decomposition have also been proposed, e.g. the triple decomposition in time-periodic flows further additively decomposes the fluctuations in Reynolds decomposition into a phase-averaged component and a fluctuation about it.[46]

Reynolds viewed his decomposition in geometric terms, as described in his paper[35]

> The geometrical basis of the method of analysis used in the kinetic theory of gases has hitherto consisted:
>
> (1) Of the geometrical principle that the motion of any point of a mechanical system may, at any instant, be abstracted into the mean motion of the whole system at that instant, and the motion of the point relative to the mean-motion ...

and thus the fluctuation was interpreted as a 'relative' component of velocity. Reynolds also mentions the geometrical interpretation at the beginning of his response to Lord Rayleigh, who was one of reviewers of the 1895 paper,[36]

> From the copy of the remarks on my paper on the criterion, which you sent me, it is clear that the referees have found great difficulty in understanding the drift of the main argument; namely that which relates to the geometrical separation of the components u, v, w at each point of a system into mean-components $\bar{u}$, $\bar{v}$, $\bar{w}$, and relative components u', v', w' and as to the conditions of distribution of $\bar{u}$, $\bar{v}$, $\bar{w}$ under which such separation is possible.

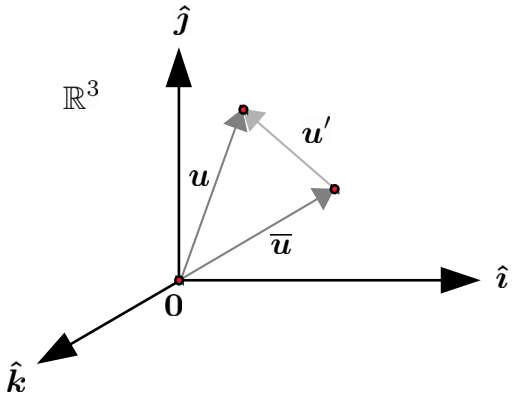

Figure 1.1: Geometric interpretation of Reynolds decomposition.

The geometrical interpretation is illustrated in figure 1.1; the velocities are viewed not component-wise but rather as vectors in $\mathbb{R}^3$ and the decomposition is a vectorial operation. The fluctuating turbulent kinetic energy is then the Euclidean norm of the vector $\boldsymbol{u}'$. The importance of geometry might not be evident in the present case because the underlying space is Euclidean. When the underlying space is not Euclidean, as with the variables that appear in viscoelastic flows, geometry becomes critical and component-wise decompositions are not necessarily meaningful.

The Reynolds decomposition is also intimately related to classical linear stability analysis. If we let $\overline{\boldsymbol{u}}$ be the laminar base-state, and let $\boldsymbol{u} \sim \mathcal{O}(\epsilon)$ where $\epsilon \to 0$, then the Navier–Stokes equations can be linearized by ignoring $\mathcal{O}(\epsilon^2)$ terms. The resulting equations, along with appropriate boundary conditions, can be used to determine stability of the base-flow to infinitesimal perturbations.

The stability equations in viscous flow were derived by Orr[47] in the case of two-dimensional channel flow and axisymmetric pipe flow (see also the work of Som-

merfeld[48]). The approach Reynolds adopted to study transition to turbulence was well-known to Orr who included a section discussing it in his paper. Tollmien[49] and Schlichting[50,51] studied the Orr–Sommerfeld equation and obtained the neutral curve in wavelength–Reynolds number space delineating the region of linear instability. Their results were confirmed in the highly controlled boundary layer experiments of Schubauer and Skramstad,[52] which substantially verified the theoretical developments of the decades prior. Accordingly, the mode with the largest growth in an unstable wall-bounded shear flow is now known as a Tollmien–Schlichting wave.

If the flow is linearly unstable, it is unstable to infinitesimally small perturbations. However, as already noted by Reynolds in his 1883 paper,[34] transition to turbulence can depend on the size of the initial perturbation indicating a bypass of the natural transition process (that which happens due to unstable modes). It was later found that bypass transition is enabled by the underlying linear operator representing the linearized dynamics. The operator is non-normal and thus even if the base-flow is stable, an initial perturbation can grow transiently before subsequently decaying.[53–58] Thus, if the basin of attraction of the laminar base-state is sufficiently small, and the transient growth of an initial perturbation is sufficiently large, the systems can leave the basin of attraction and become turbulent.[59,60]

In order to further understand the evolution of Tollmien–Schlichting waves, Benny and Lin[61] generalized (1.1) and expressed the velocity field as weakly nonlinear ex-

pansion in a small parameter ϵ as follows

$$\boldsymbol{u} = \overline{\boldsymbol{u}} + \boldsymbol{u}' = \overline{\boldsymbol{u}} + \sum_{k=1}^{N} \epsilon^k \boldsymbol{u}_{(k)}. \tag{1.2}$$

where $\boldsymbol{u}_{(k)}$ for $k > 0$ are the perturbation velocity vectors. The first–order truncation of (1.2) is the expansion used to obtain the stability equations. Other authors also considered similar nonlinear expansions in order to forward theories of the weakly nonlinear development of unstable modes.[62–66] Small perturbations to the base-flow as in (1.2) are useful beyond classical linear stability analysis. For instance, one may seek solutions for a flow that can be cast as a perturbation of another known flow (see Reference 67 for an example). The expansion (1.2) can also be interpreted geometrically, in the spirit of Reynolds. Such a geometric interpretation is shown in figure 1.2 when $\boldsymbol{u}_{(k)} = 0$ for $k > 2$. Here $\epsilon^k \boldsymbol{u}_{(k)}$ are vectors that connect the base-flow velocity $\overline{\boldsymbol{u}}$ to the instantaneous velocity $\boldsymbol{u}$.

A relatively novel application of small perturbation analysis has been to fully turbulent flows. Here the turbulent mean flow is used as the base-state instead of the laminar flow. An early proponent of this approach was Landahl, who used it to predict convective velocities[68] and to study sublayer streaks in turbulent parallel shear flows.[69] The linearized equations with such a base-state and augmented with an eddy viscosity can predict nontrivial features of fully turbulent flows, such as the spanwise spacing of observed structures.[70,71] Such equations have also been used to

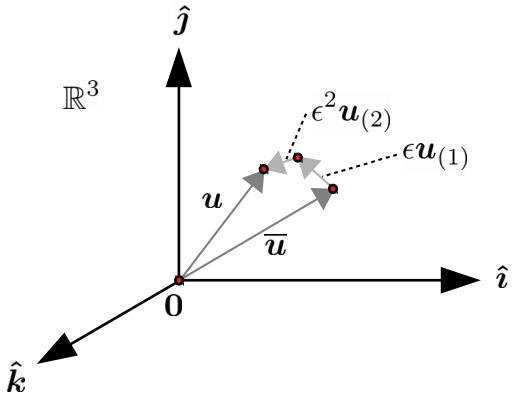

Figure 1.2: Geometric interpretation of a second–order weakly nonlinear expansion of the velocity.

study the mechanisms at play in fully turbulent flows.[55,58,72]

We would like to pursue a line of inquiry in viscoelastic transition and turbulence along a path similar to what has been described above for Newtonian turbulence. However, fundamental differences arise between Newtonian and viscoelastic fluids that do not allow an immediate extension. In the next section, we discuss these challenges and provide historical context.

1.2 The problem of viscoelastic turbulence

Viscoelastic fluids are not only dissipative but also have a capacity to store energy. As a result, instantaneous rates are insufficient to describe their dynamics and the material deformation history is also needed. It is for this reason that the problem of viscoelastic turbulence is inherently more complex than Newtonian turbulence. One may then identify two questions that must be addressed in order to develop theories

of viscoelastic turbulence: (a) what are the necessary variables needed to describe the flow? and (b) what is an appropriate way to separate the statistically persistent or laminar base-state from the fluctuations, and quantify the latter? In Newtonian flows, the velocity field is sufficient to describe the flow, and the Reynolds decomposition separates the mean flow from the fluctuations. The fluctuations can then be quantified using the norm of the fluctuating velocity vector, whose square is proportional to the kinetic energy. We briefly review the history of viscoelastic turbulence research up to the present time through the lens of the two questions posed above, and then discuss the contribution of the present dissertation.

Initial efforts in understanding viscoelastic turbulence were driven by the drag reduction phenomenon discovered by Toms[5] and Mysels.[6] These initial efforts were largely experimental because of the unavailability of reliable models and also due to the high computational costs associated with numerical simulations. Due to the experimental inaccessibility of the polymer microstructure, the experiments were primarily focused on the rheology of drag reducing solutions and also on measuring pressure drops and velocities. Numerous reviews written between 1960 and 1980 summarize the developments during that era.[7,11,26–29,73] Several competing theories were put forward in order to explain the phenomenon of drag reduction[7,27] but none provided a complete, quantitative description because they did not incorporate the dynamics of the microstructure. One of the important conclusions from these studies was that in solutions of flexible polymers, it is the time-scale of the polymers that

determines the nature of the viscoelastic turbulence, rather than the length-scale.[11]

At the same time as these developments were taking place, steps were taken towards formulating constitutive models to describe viscoelastic turbulence. A significant breakthrough was achieved by Oldroyd, who developed frame indifferent rates for second–order tensors.[74] Oldroyd's approach led to the celebrated Oldroyd-B model. This model was then derived from kinetic theory by assuming individual polymers in a flow behaved like two beads connected with a Hookean spring submersed in a solvent bath and experiencing random fluctuations. Generalizing the spring model led to other models, such as the FENE-P (Finite Extensibility Nonlinear Elastic – Peterlin) model.[75] These and other models were subsequently used to analyse viscoelastic laminar flows[76–80] but their applicability to complex turbulent flows was still an open question.

In a pioneering work, Sureshkumar *et al.*[81] performed the first three-dimensional direct numerical simulations of fully turbulent viscoelastic flow and demonstrated that the FENE-P model qualitatively captures the behaviour of real viscoelastic turbulence. Several other authors have subsequently studied viscoelastic turbulence using direct numerical simulations of the FENE-P and Oldroyd-B models,[8,82–87] and found reasonable qualitative agreement with experiments.

Another success of the models discussed above was the prediction of the curved streamline instability. Workers in the early 90s used the Oldroyd-B model to predict an instability in viscoelastic Taylor–Couette and Taylor–Dean flows that is not present

in the purely viscous case.[78,79] Pakdel and McKinley associated this instability with the curvature of the base-flow streamlines and suggested an instability onset criterion based on a new non-dimensional group, analogous to the Taylor and Görtler numbers in Newtonian flows.[88] The instability was also confirmed experimentally[79,89] and most notably by Groisman and Steinberg[13] in von Kármán flow at exceedingly low Reynolds numbers. The low Reynolds number elastic instability has since been observed in a variety of other flows with curved streamlines[17] and the resulting elastic turbulence is now considered a technologically important regime of viscoelastic turbulence.[17,20]

All the models mentioned above, and those that are used to simulate realistic viscoelastic turbulence have a common set of state variables: the velocity field, and the conformation tensor. The conformation tensor is a positive–definite tensor used to account for the material deformation. A large variety of viscoelastic flows can be expressed using these two quantities.[75,90] As a result, they together form a satisfactory answer to the first question (a) posed at the start of this section.

The second question (b) is the subject of this dissertation. While the velocity field can be analysed in the same way as is done in Newtonian turbulence, an appropriate approach to quantify the fluctuations in the conformation tensor has been elusive. In particular, for the conformation tensor, we seek analogs of the Reynolds decomposition (1.1), the weakly nonlinear expansion (1.2), and appropriate scalar measures that can be used to quantify the fluctuations.

Prior researchers have attempted to directly extend Newtonian approaches by

considering a Reynolds decomposition of the conformation tensor (see Reference 91 for an example). While such an approach can be used to formulate RANS (Reynolds-Averaged Navier–Stokes) type models for viscoelastic flows,[92–95] the application is limited by the fact that the Reynolds decomposition of the conformation tensor does not yield physically or mathematically sensible quantities. The underlying reason is that the set of positive–definite tensors is not a Euclidean space, unlike $\mathbb{R}^3$. Here it is useful to revert to the original geometric interpretation of the Reynolds decomposition: it is only tenable when the underlying space is Euclidean.

An alternative method that avoids the conformation tensor is one which only considers the polymer stress. The latter quantity is not restricted to be positive–definite and therefore resides in the larger space of symmetric tensors. This approach is problematic because, for many models including the Oldroyd-B and FENE-P models, the polymer stress can be made positive–definite by adding a constant symmetric tensor. The eigenvalues of this tensor are then still bounded from below, similar to the eigenvalues of positive–definite tensors. Thus, the approach only hides the positivity of the conformation tensor and does not address the fundamental problem. It can lead to a problem of realizability of stress fields because arbitrary symmetric tensors are then not admissible stress tensors. Beyond such considerations, using polymer stresses instead of the conformation tensor is undesirable because it is only indirectly related to the deformation of the underlying medium, which is the source of the elastic behaviour of the fluid.

An associated problem is that of scalar measures to quantify the fluctuations in the conformation tensor. Clearly, if a Reynolds decomposition is not meaningful then the norm of a Reynolds decomposed quantity is also not meaningful. In order to sidestep this difficulty, previous researchers have resorted to the elastic energy;[81,86,87,96] the analogy being with the kinetic energy interpretation of the norm of the velocity field. The drawback with this approach is that the elastic energy may be ill-defined in that the definition may depend on the approach taken to derive the equations. Furthermore, even when the elastic energy is well-defined, it normally is not a mathematically sensible way to quantify the fluctuations because it is not a metric on the set of positive–definite tensors. The kinetic energy, on the other hand, has no such difficulty because it is precisely half the squared Euclidean norm in $\mathbb{R}^3$. Finally, the constitutive equations themselves are not conservative and therefore the prescription of only the elastic energy is insufficient to describe the dynamics.

We outlined two interrelated difficulties with quantifying viscoelastic turbulence: the lack of an appropriate fluctuating conformation tensor, and a lack of scalar measures to quantify the magnitude of the fluctuations. In addition to these difficulties, another arises when studying small perturbations to a given base-state, e.g. in the context of linear stability analysis or when performing asymptotic analyses. For Newtonian flow, a general way to generate a perturbation to the base-flow velocity is through a weakly nonlinear expansion (1.2). This same approach does not appear to be appropriate to the conformation tensor because the latter is not a vector space

quantity.

In this dissertation, we address all the issues discussed above. We propose an alternative approach to the Reynolds decomposition that allows us to define a fluctuating conformation tensor. We develop scalar measures, based on the geometry of the set of positive–definite tensors to quantify the magnitude of turbulence fluctuations in the conformation tensor. Finally, we develop an alternative to the weakly nonlinear expansion, called the weakly nonlinear deformation, that can be used to generate small perturbations to the conformation tensor. The approach adopted in this dissertation is based both on admissible physical interpretations of the conformation tensor and the Riemannian geometric structure of the set of positive–definite tensors.

1.3 Outline and channel flow geometry

This dissertation consists of five chapters, including introduction and conclusions. We provide an outline of each chapter below to illuminate the thread that brings them together.

Chapter 2 concerns constitutive models. In this chapter, we provide a broad discussion of different constitutive models, describe the class of models to be used in the present dissertation, present two derivations of a model, and finally provide a discussion. In addition to outlining the constitutive models of interest, the goals

of this chapter include determining admissible interpretations of the conformation tensor and also to develop the kinematic tools that will be invoked in the remainder of the dissertation.

In chapter 3 we develop an alternative to the Reynolds decomposition (1.1) for the conformation tensor that can be used to analyse viscoelastic turbulence, and then formulate appropriate scalar measures to characterize the resulting fluctuating conformation tensor. We illustrate the approach using a direct numerical simulation of drag-reduced turbulent channel flow.

In chapter 4, we propose an alternative to the weakly nonlinear expansion (1.2) for the conformation tensor. We develop the necessary theoretical details of the linearized problem, including the formulation of appropriate scalar products based on the geometry of the manifold of positive–definite tensors, and finally illustrate the formulation using direct numerical simulations of the nonlinear evolution of Tollmien–Schlichting waves. Conclusions and open questions are presented in chapter 5.

1.3.1 Channel flow

As mentioned above, throughout the dissertation, we illustrate the proposed approach with direct numerical simulations. In chapter 3, these are of drag-reduced fully turbulent channel flow, and in chapter 4, these are of viscoelastic Tollmien–Schlichting waves in channel flow.[97] Details of the code developed for the direct numerical simulations are documented in appendix B. The channel flow geometry is described in

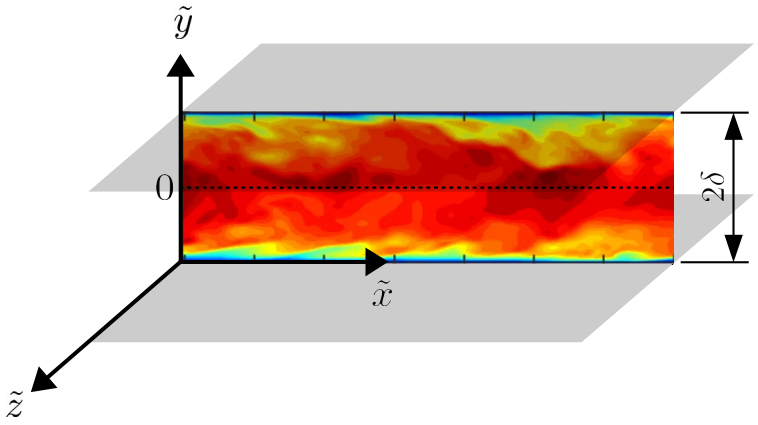

Figure 1.3: Geometry of channel flow.

the next section.

The channel flow geometry is shown in figure 1.3. The streamwise, wall-normal and spanwise directions are denoted $\tilde{x}$, $\tilde{y}$, and $\tilde{z}$, respectively. The associated velocities are denoted $\tilde{u}$, $\tilde{v}$, $\tilde{w}$. The channel half-height is denoted δ and U_b is the bulk velocity. The flow is taken to be periodic in the streamwise and spanwise directions with fixed walls at $y = \pm\delta$. The flow is driven by a streamwise pressure gradient that is adjusted to maintain a constant bulk velocity and hence mass flow-rate.

When presenting the results, we will choose to non-dimensionalize by the channel half-height and the bulk velocity, so that $\boldsymbol{x} = \tilde{\boldsymbol{x}}/\delta$ with $\tilde{\boldsymbol{x}} = (\tilde{x}, \tilde{y}, \tilde{z})$ and $\boldsymbol{u} = \tilde{\boldsymbol{u}}/U_b$ with $\boldsymbol{u} = (u, v, w)$. As indicated above, dimensional quantities are denoted by tildes.

Chapter 2

Constitutive Models

2.1 Introduction

In this chapter we discuss constitutive models used to study viscoelastic flows, and in particular those that have been useful in the study of viscoelastic turbulence. We will outline the general form of constitutive models used in the present dissertation, and also describe two derivations in order to arrive at useful interpretations of the state variables in the resulting evolution equations.

Our starting point is the the Cauchy momentum equation, which reads

$$\frac{\mathrm{D}\rho\tilde{\boldsymbol{u}}}{\mathrm{D}\tilde{t}} = \tilde{\boldsymbol{\nabla}} \cdot \tilde{\boldsymbol{\sigma}} + \tilde{\boldsymbol{d}} \tag{2.1}$$

where

$$\frac{\mathrm{D}\phi}{\mathrm{D}\tilde{t}} \equiv \frac{\partial\phi}{\partial\tilde{t}} + \tilde{\boldsymbol{u}} \cdot \tilde{\boldsymbol{\nabla}}\phi \tag{2.2}$$

denotes the material time derivative of a variable ϕ, ρ is the density, $\tilde{\boldsymbol{u}}$ is the velocity field, $\tilde{\boldsymbol{\sigma}}$ is the stress and $\tilde{\boldsymbol{d}}$ is an applied force. We use tildes to denote dimensional quantities and operators. The incompressibility condition yields the additional equation

$$\tilde{\boldsymbol{\nabla}} \cdot \tilde{\boldsymbol{u}} = 0. \tag{2.3}$$

The Cauchy momentum equation is not closed because the stress tensor $\tilde{\boldsymbol{\sigma}}$ has not yet been specified. This is the goal of constitutive modelling of incompressible fluids: to specify $\tilde{\boldsymbol{\sigma}}$ in such a way that the Cauchy momentum equation can be evolved in time using only continuum-scale variables and the incompressibility constraint.

For an incompressible, purely viscous Newtonian fluid, the only continuum-scale variable needed is the velocity. The stress tensor in this case is given by

$$\tilde{\boldsymbol{\sigma}} = -\tilde{p}\boldsymbol{I} + \eta\tilde{\boldsymbol{T}}_{\mathrm{N}} \tag{2.4}$$

where $\tilde{p}$ is the pressure and η is the viscosity. The deviatoric part tensor $\tilde{\boldsymbol{T}}_{\mathrm{N}} = 2\,\tilde{\boldsymbol{D}}$,

where $\tilde{\boldsymbol{D}}$ is the rate-of-strain tensor,

$$\tilde{\boldsymbol{D}} \equiv \text{sym}\left(\tilde{\boldsymbol{\nabla}}\tilde{\boldsymbol{u}}\right) \tag{2.5}$$

where $\text{sym}\,\boldsymbol{A} = \frac{1}{2}(\boldsymbol{A} + \boldsymbol{A}^{\mathsf{T}})$ is the symmetric part of the second–order tensor $\boldsymbol{A}$, and we retain the convention for $\tilde{\boldsymbol{\nabla}}\tilde{\boldsymbol{u}}$ commonly used in the fluid mechanics literature: the first index represents the spatial derivative index and thuscs literature: the first index represents the spatial derivative index. The pressure can be written in terms of the velocity since the flow is isochoric,

$$\text{tr}\,\tilde{\boldsymbol{D}} = 0. \tag{2.6}$$

The equations (2.1), (2.4), and (2.6) form a closed set of equations describing a fluid where the stress has no memory of past deformations and is fully determined by instantaneous rates and spatial gradients of the velocity.

For a flow that is both viscous and elastic, it is not sufficient to consider only the velocity field because one requires the deformation history in order specify an elastic response. Generalizing (2.4) by adding in an elastic stress $\eta_p\tilde{\boldsymbol{T}}$ yields

$$\tilde{\boldsymbol{\sigma}} = -\tilde{p}\boldsymbol{I} + \eta_s\tilde{\boldsymbol{T}}_{\text{N}} + \eta_p\tilde{\boldsymbol{T}} \tag{2.7}$$

where η_s and η_p are viscosities that determine the relative contribution of viscous

and elastic contributions to the total stress. The simplest model for the elastic contribution to the stress is to assume that it is proportional to a 'delayed' version of the viscous contribution to the stress. The corresponding first–order delay equation reads

$$\frac{\mathrm{D}\tilde{\boldsymbol{T}}}{\mathrm{D}\tilde{t}} = -\vartheta\left(\tilde{\boldsymbol{T}} - \tilde{\boldsymbol{T}}_{\mathrm{N}}\right) \tag{2.8}$$

where ϑ^{-1} is the characteristic delay. Implicitly assuming that $\eta_s = 0$, the one-dimensional version of the equation (2.8) was introduced by James C. Maxwell[98] in 1867 as a general model to study the behaviour of gases. In 1915, George B. Jeffery[99] considered the more general case when $\eta_s \neq 0$. These models are known today as the Maxwell and Jeffery models, respectively. The equations (2.1), (2.7), and (2.8) are linear in a material frame of reference and therefore describe *linear viscoelasticity*.

Models such as (2.8) are problematic because the constitutive equations do not satisfy material frame indifference. In particular, consider a time-dependent rotation $\boldsymbol{Q}(\tilde{t})$ of the observer, so that

$$\boldsymbol{x}_{\dagger} = \boldsymbol{Q}(\tilde{t}) \cdot \tilde{\boldsymbol{x}}. \tag{2.9}$$

A second–order tensor $\boldsymbol{A}$ is frame indifferent if it transforms under the rotation (2.9)

as follows

$$\boldsymbol{A}_{\dagger} = \boldsymbol{Q}^{\mathsf{T}} \cdot \boldsymbol{A} \cdot \boldsymbol{Q}. \tag{2.10}$$

Frame indifference (2.10) ensures that the tensor's basis vectors rotate in consonance with (2.9). It is easy to verify that the material time derivative of a frame indifferent second–order tensor is not frame indifferent. In particular, for a frame indifferent $\tilde{\boldsymbol{T}}$ we have

$$\frac{\mathrm{D}(\tilde{\boldsymbol{T}})_{\dagger}}{\mathrm{D}\tilde{t}} \neq \boldsymbol{Q}^{\mathsf{T}} \cdot \frac{\mathrm{D}\tilde{\boldsymbol{T}}}{\mathrm{D}\tilde{t}} \cdot \boldsymbol{Q} \tag{2.11}$$

and therefore the constitutive relation (2.8) defining the material behaviour depends on the rotation of the observer. This unphysical consequence makes (2.8) an inadequate model for most real materials.

In a seminal paper,[74] James G. Oldroyd set forth frame indifferent constitutive equations that can be seen as direct generalizations of (2.8). Oldroyd achieved this by developing the convected derivatives, which are operators that yield rates preserving frame indifference of second–order tensors. These rates are the partial time derivatives in a coordinate frame that deforms along with the material. The idea was most succinctly described by Oldroyd:

> Equations of state must be considered as equations defining the properties of an arbitrary material element, moving as part of a continuum. The quantities which may be involved in the equations are then quantities associated with that particular element over a period of time during which

> the element has moved and has been deformed continuously in an arbitrary manner. Since they necessarily represent physical concepts with a significance independent of any particular co-ordinate system, they may be regarded as three-dimensional tensors. *Moreover, only those tensor quantities need be considered which have a significance for the material element independent of its motion as a whole in space.* In order to specify these quantities in the general case, it is not at first convenient to use a frame of reference fixed in space, but a convected co-ordinate system of the type first envisaged by Hencky (1925). The co-ordinate surfaces $\xi^j =$ constant are chosen as surfaces drawn in the material and deforming continuously with it, and the ξ^j and the time t are taken as the independent variables.

The convected derivatives are special cases of the more general class of objective rates: operators that yield rates preserving frame indifference of second–order tensors. Several objective rates have been proposed since Oldroyd's work, e.g. those associated with Truesdell and Jaumann.[100,101] It can be shown that all the objective rates are special forms of the Lie derivative.[100]

One of the frame indifferent rates derived by Oldroyd, known as the upper-convected Maxwell derivative, has particular significance when modelling viscoelastic flows because it is the only objective rate that can be derived from a Poisson bracket and thus represents purely reversible processes.[90,102] Any other objective rate must arise due to irreversible (dissipative) thermodynamics.

The upper-convected Maxwell derivative can be easily justified by imposing a modification to the material time derivative that renders it frame indifferent. Consider a rotating reference frame as in (2.9). The material time derivative of a frame

indifferent tensor $\boldsymbol{A}$, satisfying (2.10), in the rotating reference frame is given by

$$\frac{\mathrm{D}\boldsymbol{A}_\dagger}{\mathrm{D}\tilde{t}} = \boldsymbol{Q}^\mathsf{T} \cdot \frac{\mathrm{D}\boldsymbol{A}}{\mathrm{D}\tilde{t}} \cdot \boldsymbol{Q} + \underbrace{\boldsymbol{Q}^\mathsf{T} \cdot \boldsymbol{A} \cdot \dot{\boldsymbol{Q}}}_{\text{(I)}} + \underbrace{\dot{\boldsymbol{Q}}^\mathsf{T} \cdot \boldsymbol{A} \cdot \boldsymbol{Q}}_{\text{(I)}^\mathsf{T}}. \tag{2.12}$$

The terms (I) and its transpose $(\mathrm{I})^\mathsf{T}$ prevent the frame indifference of the material time derivative. By adding appropriate terms to the material derivative, we seek to to eliminate these additional terms. These terms can be constructed using the velocity gradient tensor, since this tensor can be written in the rotating reference frame as follows

$$\tilde{\boldsymbol{\nabla}}_\dagger \tilde{\boldsymbol{u}}_\dagger = \boldsymbol{Q}^\mathsf{T} \cdot \tilde{\boldsymbol{\nabla}} \tilde{\boldsymbol{u}} \cdot \boldsymbol{Q} + \boldsymbol{Q}^\mathsf{T} \cdot \dot{\boldsymbol{Q}} \tag{2.13}$$

where we used the expression for the velocity in the rotating reference frame $\tilde{\boldsymbol{u}}_\dagger = \boldsymbol{Q} \cdot \tilde{\boldsymbol{u}} + \dot{\boldsymbol{Q}} \cdot \tilde{\boldsymbol{x}}$ and $\tilde{\boldsymbol{\nabla}}_\dagger$ is the gradient operator in the rotating reference frame. Contracting the velocity gradient tensor in (2.13) with $\boldsymbol{A}_\dagger$ and using (2.10) yields

$$\boldsymbol{A}_\dagger \cdot \tilde{\boldsymbol{\nabla}}_\dagger \tilde{\boldsymbol{u}}_\dagger = \boldsymbol{Q}^\mathsf{T} \cdot \boldsymbol{A} \cdot \tilde{\boldsymbol{\nabla}} \tilde{\boldsymbol{u}} \cdot \boldsymbol{Q} + \underbrace{\boldsymbol{Q}^\mathsf{T} \cdot \boldsymbol{A} \cdot \dot{\boldsymbol{Q}}}_{\text{(I)}}. \tag{2.14}$$

Subtracting (2.14) and its transpose from (2.12) gives

$$\frac{\mathrm{D}\boldsymbol{A}_\dagger}{\mathrm{D}\tilde{t}} - \boldsymbol{A}_\dagger \cdot \tilde{\boldsymbol{\nabla}}_\dagger \tilde{\boldsymbol{u}}_\dagger - \tilde{\boldsymbol{\nabla}}_\dagger^\mathsf{T} \tilde{\boldsymbol{u}}_\dagger \cdot \boldsymbol{A}_\dagger = \boldsymbol{Q}^\mathsf{T} \cdot \left(\frac{\mathrm{D}\boldsymbol{A}}{\mathrm{D}\tilde{t}} - \boldsymbol{A} \cdot \tilde{\boldsymbol{\nabla}} \tilde{\boldsymbol{u}} - \tilde{\boldsymbol{\nabla}}^\mathsf{T} \tilde{\boldsymbol{u}} \cdot \boldsymbol{A} \right) \cdot \boldsymbol{Q} \tag{2.15}$$

which proves the frame indifference of the upper-convected Maxwell derivative, $\overset{\tilde{\nabla}}{\boldsymbol{A}}$, defined as

$$\overset{\tilde{\nabla}}{\boldsymbol{A}} \equiv \frac{\mathrm{D}\boldsymbol{A}}{\mathrm{D}\tilde{t}} - \boldsymbol{A}\cdot\tilde{\boldsymbol{\nabla}}\tilde{\boldsymbol{u}} - \tilde{\boldsymbol{\nabla}}^{\mathsf{T}}\tilde{\boldsymbol{u}}\cdot\boldsymbol{A}. \tag{2.16}$$

Revising the Maxwell model (2.8) using the upper-convected Maxwell derivative yields the celebrated Oldroyd-B model

$$\overset{\tilde{\nabla}}{\tilde{\boldsymbol{T}}} = -\vartheta\left(\tilde{\boldsymbol{T}} - \tilde{\boldsymbol{T}}_{\mathrm{N}}\right), \tag{2.17}$$

which along with (2.1) and (2.7) completes the specification of frame indifferent evolution equations for a viscoelastic fluid.

The model in (2.17) is written in terms of the stress $\tilde{\boldsymbol{T}}$, which is not positive–definite. However, it can be written in terms of the positive–definite tensor $\boldsymbol{C}$ by substituting in the stress relation

$$\tilde{\boldsymbol{T}} = \vartheta(\boldsymbol{C} - \boldsymbol{I}). \tag{2.18}$$

At this point, such a substitution appears needless and artificial. However, we will see that it is more general to express models in terms of $\boldsymbol{C}$ rather than $\tilde{\boldsymbol{T}}$. The general models we consider in this dissertation, which are presented in §2.2, are also formulated in terms of $\boldsymbol{C}$.

The Oldroyd-B model (2.17) has proven to be very useful in studying the dynamics of viscoelastic flows.[80,103] A drawback of the model is that it does not exhibit shear-thinning or thickening[104] and is therefore not useful for modelling real fluids that exhibit these behaviours. However, there are specially designed fluids, known as Boger fluids, that exhibit elastic behaviour yet have a shear-independent viscosity.[103] The *raison d'être* for Boger fluids is to provide a fluid that shows elastic behaviour without a change in viscosity since the elasticity itself can contribute richly to the fluid dynamics.[76,77,89,103,105] The Oldroyd-B model, which is a relatively simple model and thus amenable to yielding elegant analytical results (see Reference 105 for an example), is an excellent representative for these fluids. Boger and Yeow[89] describe the importance of the Boger fluids in terms of their role as a bridge between theory and experiment in no uncertain terms:

> Research in non-Newtonian fluid mechanics has been characterized by the theoretical types (the left wing) who make predictions that cannot be observed and by the experimental types (the right wing), on the other hand, who make observations that no one can predict. In this paper, the authors demonstrate how the left wing and the right wing have been forced to interact as a result of the discovery and subsequent development of constant-viscosity elastic liquids, the so-called Boger fluids.

Despite the usefulness of the Oldroyd-B model, it has a glaring deficiency that

manifests when considering simple extensional flow. Here we have

$$\tilde{\boldsymbol{D}} = \begin{bmatrix} 1 & 0 & 0 \\ 0 & 1 & 0 \\ 0 & 0 & -2 \end{bmatrix} \dot{\varepsilon}_0 H_{\text{step}}(t) \tag{2.19}$$

where $\dot{\varepsilon}_0$ is a constant strain rate and $H_{\text{step}}(t)$ is the Heaviside step function. The extensional viscosity η_{ext} is defined as the ratio of (normal) stress to the strain, and is a useful tool for characterizing fluids under extension. In Newtonian flows, the ratio of the extensional viscosity to the shear viscosity is three. This result was first derived by Frederick T. Trouton,[106,107] and is referred to as Trouton's ratio. For the Oldroyd-B model, the steady-state ($t \to \infty$) extensional viscosity is given by (see equation 13.4–36 in 75)

$$\eta_{\text{ext}} = 3\eta_s + \frac{3\eta_p}{(1 - \dot{\varepsilon}_0 \vartheta^{-1})(1 + 2\dot{\varepsilon}_0 \vartheta^{-1})}. \tag{2.20}$$

When $\dot{\varepsilon}_0 = \vartheta$ or $\dot{\varepsilon}_0 = -\vartheta/2$, the extensional viscosity becomes unbounded. This result is clearly unphysical and reflects the ill-suitability of the Oldroyd-B model for extensional flows. As we will see later, this behaviour reflects the lack of finite-extensibility in the Oldroyd-B model.

Several models have been proposed that seek to model viscoelastic behaviour not captured by the Oldroyd-B model or to address the problem of divergent extensional

viscosity. These models generally involve modifications of the frame indifferent rate in the constitutive relation, the linear relaxation assumed in the Oldroyd-B model or the stress relation. Examples of such models are the Johnson-Segalman, FENE-P and Giesekus models.[104] In principle, further generalizations of the Oldroyd-B can be achieved by incorporating higher-order objective rates in the constitutive equations. As a whole, such models are known as rate type models because there is a relationship, possibly implicit, between the stress and its higher time derivatives.[108,109]

There is an alternative class of models, known as fluids of the differential type, which assume that the deviatoric stress is completely determined by the rate-of-strain tensor and its higher time derivatives.[108,110,111] We can define the n-th frame indifferent time derivative of the rate-of-strain tensor using the iterative scheme

$$\tilde{\boldsymbol{A}}_n = \frac{\mathrm{D}\tilde{\boldsymbol{A}}_{n-1}}{\mathrm{D}t} + \tilde{\boldsymbol{\nabla}}\tilde{\boldsymbol{u}} \cdot \tilde{\boldsymbol{A}}_{n-1} + \tilde{\boldsymbol{A}}_{n-1} \cdot \tilde{\boldsymbol{\nabla}}^{\mathsf{T}}\tilde{\boldsymbol{u}}, \tag{2.21}$$

where $\tilde{\boldsymbol{A}}_0 = \tilde{\boldsymbol{D}}$, and $\tilde{\boldsymbol{A}}_n$ for $n \geq 0$ are known as the Rivlin-Ericksen tensors.[101] It follows therefore that the deviatoric stress in fluids of the differential type is completely determined by the Rivlin-Ericksen tensors. The deviatoric stress in a differential type fluid of complexity n is completely determined by the Rivlin-Ericksen tensors of up to order $n-1$. Fluids of complexity one were first studied by Stokes[112] and are known as Stokesian fluids. Using the representation theorem, the stress in a Stokesian fluid

can be expressed as

$$\tilde{\boldsymbol{\sigma}} = \alpha_0 \boldsymbol{I} + \alpha_1 \tilde{\boldsymbol{A}}_0 + \alpha_2 \tilde{\boldsymbol{A}}_0^2 \tag{2.22}$$

where α_i are scalar functions of the invariants of $\tilde{\boldsymbol{A}}_0$. For the Navier–Stokes equations $\alpha_0 = -\tilde{p}$, $\alpha_1 = 2$ and $\alpha_2 = 0$. For power-law fluids, $\alpha_0 = -\tilde{p}$, $\alpha_2 = 0$ and α_1 is a proportional to a power of the second invariant of $\tilde{\boldsymbol{A}}_0$. The Reiner–Rivlin class of fluids are those where α_1 and α_2 can be expressed as polynomials of the invariants, and thus include both the Navier–Stokes equations and power-law fluids as special cases.[109, 113]

Lumley[114] theoretically examined the dissipation spectrum in homogenous isotropic turbulence of a generic Reiner–Rivlin fluid and found that it is similar in form to that in Newtonian fluids. Based on this consideration, Lumley forcefully contends that turbulence in Reiner–Rivlin fluids is essentially Newtonian:

> In the body of the paper arguments will be given supporting the proposition that the concept of an effective viscosity is valid for Reiner–Rivlin fluids (ones in which stress depends in the most general isotropic way only on current strain rate); we must therefore conclude that, in order to produce a turbulence which does not resemble a Newtonian one in the energy-containing range, it is necessary to have dependence on values other than current ones; in other words, a viscoelastic material is necessary.

On the other hand, numerical experiments by Kuo and Tanner[115] using a simplified modified Burgers equation mimicking a Reiner–Rivlin fluid found significant differences under some conditions, suggesting that subtle differences beyond the introduc-

tion of an 'effective viscosity' can be expected in turbulence of a Reiner–Rivlin fluid.

We will no longer consider fluids of the differential type because their dynamics are completely determined by the velocity, and thus their analysis does not require extensive or specialized theoretical machinery beyond what is already developed for Newtonian flows. Furthermore, the most well-developed subclass of fluids of the differential type, namely Reiner–Rivlin fluids, do not capture the memory effect that is characteristic of the viscoelastic flows of interest here.

In this dissertation, we will rather consider rate type models and specifically those that can be obtained from the Oldroyd-B model by generalizing the relaxational behaviour. Such models are appropriate for describing fluids like polymer solutions[75] and have been widely used to study viscoelastic turbulence.[8] The ad-hoc approach described above for specifying such constitutive models is not sufficient to ensure thermodynamic consistency and, more important to the purpose of the present dissertation, it does not offer a direct interpretation of the stress in terms of kinematic quantities such as deformations.

Several alternative approaches to deriving frame indifferent constitutive equations from thermodynamic first principles have been developed since Oldroyd. Of particular relevance to the viscoelastic flows considered here is the Beris-Edwards bracket formalism,[90,102] and the approaches developed by Rajagopal and Srinivasa.[116–118] In some cases, models can also be derived directly from kinetic theory by coarse-graining the microscopic dynamics.[75]

Our present interest in the derivation of constitutive equations is to aid us in assigning reasonable kinematic interpretations to the state variables. In addition to microscopic descriptions, we seek continuum-scale interpretations because our analysis of viscoelastic flows will be based on a continuum-scale description of the flow. A fundamental problem in modelling of viscoelastic fluids is that, in general, a model can only be derived using certain specific thermodynamic formulations and thus the interpretation of the state variables is dictated by the particular formulation used. The Oldroyd-B model and the Navier–Stokes equations are some of the few exceptions to this rule. These models can be derived from the frameworks mentioned above and also directly from kinetic theory.

The next section (2.2) introduces the general constitutive equations, in dimensionless form, that are used in this dissertation. Subsequently, in sections 2.3 and 2.4, we derive viscoelastic models using a continuum-scale thermodynamics framework[116] and from kinetic theory,[75] respectively. In both these approaches, the state variables are a velocity and a second–order positive definite tensor. In the continuum-scale thermodynamics framework developed in §2.3, the tensor is a left Cauchy–Green tensor representing the elastic deformation. On the other hand, in the kinetic theory approach shown in §2.4, the tensor represents the average polymer conformation: the coarse-grained dyad formed by the polymer molecule end-to-end vector. In addition to providing the correct context for interpreting the state variables, the derivations are also helpful in introducing fundamental quantities that will be referred to sub-

sequently. We close this chapter in §2.5, where we discuss the two derivations and supply the interpretation of the positive–definite tensor to be used in the present work.

2.2 General constitutive equations

We postulate that a general framework for the analysis of viscoelastic flows that respects the underlying interpretation of the state variables should not be entirely dependent on the particular details of a model. Instead, the framework should be valid for a class of models that have some well-defined commonalities. In this dissertation, we consider models that can be cast as variations on the standard Oldroyd-B model, and assume that the interpretations valid for this model can be extended to the variations. All the models we consider can be reduced to the Oldroyd-B model with an appropriate choice of parameters and have been previously used to study viscoelastic turbulence.[8,22,81,86,87,119–121]

Let L_0 and U_0 be characteristic length and velocity scales, respectively. The relevant dimensionless parameters in viscoelastic turbulence are

$$\begin{aligned} \beta &= \frac{\eta_s}{\eta_s + \eta_p} && \text{(viscosity ratio)} \\ Re &= \frac{\rho L_0 U_0}{\eta_s + \eta_p} && \text{(Reynolds number)} \\ Wi &= \frac{U_0}{L_0 \vartheta} && \text{(Weissenberg number)} \end{aligned} \tag{2.23}$$

where η_s and η_p are solvent and polymer viscosities, respectively, and ϑ^{-1} is the polymer relaxation time. The characteristic scales can be used to form the following dimensionless variables and operators,

$$\begin{aligned} &\boldsymbol{x} \equiv \frac{\tilde{\boldsymbol{x}}}{L_0}, \quad t \equiv \frac{\tilde{t} U_0}{L_0}, \quad \boldsymbol{u} \equiv \frac{\tilde{\boldsymbol{u}}}{U_0}, \quad p \equiv \frac{\tilde{p}}{\rho U_0^2}, \quad \boldsymbol{T} \equiv \tilde{\boldsymbol{T}} \frac{U_0}{L_0}, \quad \boldsymbol{d} \equiv \tilde{\boldsymbol{d}} \frac{L_0}{\rho U_0^2} \\ &\overset{\nabla}{(\cdot)} \equiv \overset{\tilde{\nabla}}{(\cdot)} \frac{L_0}{U_0}, \quad \boldsymbol{\nabla} \equiv L_0 \tilde{\boldsymbol{\nabla}}, \quad \boldsymbol{\Delta} \equiv L_0^2 \tilde{\boldsymbol{\Delta}}. \end{aligned} \tag{2.24}$$

Rather than use $\boldsymbol{u}$ and $\boldsymbol{T}$ as the state variables, it will be shown that it is more general to instead use $\boldsymbol{u}$ and a dimensionless second–order positive–definite tensor $\boldsymbol{C}$. The tensor $\boldsymbol{C}$ represents the material deformation, and its precise interpretation will be the subject of the next three sections. We then stipulate that $\boldsymbol{T}$ is an isotropic function of $\boldsymbol{C}$. Using the representation theorem,[101] we can then write

$$\boldsymbol{T} = \frac{1}{Wi} \left[\mu_0 \boldsymbol{I} + \mu_1 \boldsymbol{C} + \mu_2 \boldsymbol{C}^2 \right] \tag{2.25}$$

where μ_i, $i = 0, 1, 2$, are dimensionless scalar functions of the invariants of $\boldsymbol{C}$,

$$\mu_i = \mu_i \left(\mathrm{I}_{\boldsymbol{C}}, \mathrm{II}_{\boldsymbol{C}}, \mathrm{III}_{\boldsymbol{C}} \right). \qquad i = 0, 1, 2 \tag{2.26}$$

The invariants are defined as,

$$\mathrm{I}_{\boldsymbol{C}} \equiv \mathrm{tr}\ \boldsymbol{C}, \quad \mathrm{II}_{\boldsymbol{C}} \equiv \frac{1}{2} \left[(\mathrm{tr}\ \boldsymbol{C})^2 - \mathrm{tr}\ \boldsymbol{C}^2 \right], \quad \mathrm{III}_{\boldsymbol{C}} \equiv \det \boldsymbol{C}. \tag{2.27}$$

Model	μ_0	μ_1	μ_2
Oldroyd-B	-1	1	0
FENE-P	$-\left(1-(3/L_{\max}^2)\right)^{-1}$	$\left(1-(\mathrm{I}_{\boldsymbol{C}}/L_{\max}^2)\right)^{-1}$	0
FENE-CR	$-\left(1-(\mathrm{I}_{\boldsymbol{C}}/L_{\max}^2)\right)^{-1}$	$\left(1-(\mathrm{I}_{\boldsymbol{C}}/L_{\max}^2)\right)^{-1}$	0

Table 2.1: Coefficients μ_i for some common models of polymers. The FENE-CR model was proposed by Chilcott and Rallison.[1]

Table 2.1 lists coefficients μ_i for some common models of polymers that are within the ambit of those we consider in the present dissertation. Here $L_{\max}$ is the maximum polymer extensibility.

The evolution equations for all the models we consider shall be of the form

$$\boldsymbol{\nabla}\cdot\boldsymbol{u}=0 \tag{2.28}$$

$$\frac{\mathrm{D}\boldsymbol{u}}{\mathrm{D}t}=-\boldsymbol{\nabla}p+\frac{\beta}{Re}\boldsymbol{\Delta}\boldsymbol{u}+\frac{1-\beta}{Re}\boldsymbol{\nabla}\cdot\boldsymbol{T}+\boldsymbol{d} \tag{2.29}$$

$$\overset{\nabla}{\boldsymbol{C}}=-\boldsymbol{T} \tag{2.30}$$

where the dimensionless variables and operators are given in (2.24), the dimensionless parameters in (2.23), and $\boldsymbol{T}$ is as given in (2.25).

2.3 Rajagopal–Srinivasa formalism

2.3.1 Introduction

In this section, we derive the Oldroyd-B model using a thermodynamic framework introduced by Rajagopal and Srinivasa.[116] The framework was originally introduced for plasticity[122,123] and is in the spirit of the popular strain energy density approach introduced by Mooney[124] and later Rivlin[125,126] for deriving constitutive equations for isotropic elastic materials. In the latter framework, the assumption is made that all the work done on the material is stored as free energy (energy potential). Subsequently, it can be shown that the Cauchy stress is fully determined via the prescription of a scalar strain energy density function which itself is restricted to be a function of only the invariants of the left Cauchy–Green deformation tensor. Viscous materials are dissipative and therefore at least some of the work done on them is lost as heat. Therefore the prescription of a strain energy density function is insufficient and an additional scalar *rate of dissipation function* is needed to describe the irreversible part of the dynamics.

In addition to the rate of dissipation function, a key element in the Rajagopal–Srinivasa formalism is the notion of natural configurations.[122] This notion was originally introduced by other authors for modelling plasticity, where natural configurations are plastically deformed states that a material 'naturally' relaxes to.[127–129] Natural configurations are closely related to the dissipative nature of the material and

are also relevant to viscoelastic fluids. Below, we use an example to illustrate their application to such fluids. Consider the rotation-free deformation of a purely elastic body from a reference, stress-free configuration $\mathcal{R}$ to the configuration $\mathcal{P}_t$. Once the applied stress leading to the deformation ceases, the body returns elastically from $\mathcal{P}_t$ back to $\mathcal{R}$. A material element that was moved from point A in $\mathcal{R}$ to a point B in $\mathcal{P}_t$, is returned back to point A upon relaxation. Such behaviour is completely captured using the strain energy density. Now consider turbulent flow of a dilute solution of polymers that behave elastically. Again, assume that material deforms from a reference, stress-free configuration $\mathcal{R}$ to the configuration $\mathcal{P}_t$. A parcel of fluid containing polymers is stretched and rotated as it is moved along from point a point A in $\mathcal{R}$ to a point B in $\mathcal{P}_t$. If we suddenly stop the flow in the configuration $\mathcal{P}_t$, the parcel will not necessarily be moved back to A or rotated back anymore but, nevertheless, the elastic component of the parcel will relax to a stress-free state. The resulting configuration will be stress-free but will be distinct from $\mathcal{R}$. We refer to any such configuration as a natural configuration, $\mathcal{N}_t$. There are infinitely many natural configurations from which the response of the material is purely elastic, and the specification of the relevant natural configuration is part of the problem of constitutive modelling. In the absence of dissipation, the material will relax back to the reference configuration $\mathcal{R}$ and thus natural configurations are intimately related to the dissipative nature of the material.

Once the rate of dissipation function and strain energy density function are spec-

ified, a rule that fixes the evolution of the natural configuration is required. Following the thermodynamic principles suggested by Ziegler and co-authors,[130–132] the Rajagopal–Srinivasa formalism requires that the natural configuration be such that the rate of dissipation is maximized. This modelling prescription is reminiscent of approaches in analytical mechanics that involve extremizing a functional (the action).[133] Maximizing the rate of dissipation guarantees that the constitutive model satisfies the second-law of thermodynamics.[130] In fact, it can be interpreted as an extension of the second-law since it may be reformulated as a principle that requires maximization of the rate of entropy production.[130,132] Despite these appealing aspects, it is important to note that the principle is not fundamental and may possibly be replaced by another suitable prescription.[116]

In summary, the Rajagopal–Srinivasa formalism consists of three ingredients:

1. The strain energy density function and rate of dissipation function.

2. A natural configuration from which the material response is elastic.

3. Maximization of the rate of dissipation for a given elastic deformation.

Constitutive models can then be derived by mixing these three ingredients together with the standard kinematics of continua, the Clausius–Duhem inequality, and the method of Lagrange multipliers. In what follows, we set out the appropriate recipe by following the development in the original work by Rajagopal and Srinivasa.[116]

In the next subsection, we formulate the relevant kinematics. In §2.3.3 we con-

sider the power balance implied by the Clausius–Duhem inequality, and fix the general forms of the free energy and the rate of dissipation functions. We also use the kinematics and the general forms to arrive at generic formulas to use for generating constitutive models. Finally in §2.3.4, we derive constitutive equations through the use of the generic formulas and specific forms of the strain energy density function and the rate of dissipation function. In particular, we derive the Navier–Stokes equations, and a model which reduces to the Oldroyd-B model under a small deformation assumption.

2.3.2 Kinematics

As alluded to earlier, we consider three configurations: the reference configuration $\mathcal{R}$, the present configuration $\mathcal{P}_t$, and the natural configuration $\mathcal{N}_t$. While $\mathcal{R}$ is fixed, $\mathcal{P}_t$ and $\mathcal{N}_t$ are evolving in time. The relationship between the various configurations is illustrated in figure 2.1.

The push-forward map from the reference configuration $\mathcal{R}$ to the evolving present configuration $\mathcal{P}_t$ is given by

$$\boldsymbol{\chi}_{\mathcal{R}}(\tilde{\boldsymbol{X}}_{\mathcal{R}}, \tilde{t}) = \tilde{\boldsymbol{x}}(\tilde{\boldsymbol{X}}_{\mathcal{R}}, \tilde{t}) \tag{2.31}$$

where the coordinates in $\mathcal{R}$, denoted $\tilde{\boldsymbol{X}}_{\mathcal{R}}$, are referred to as the material or Lagrangian coordinates, and the coordinates in $\mathcal{P}_t$, denoted $\tilde{\boldsymbol{x}}$, are referred to as the spatial or

Eulerian coordinates. Similarly, the push-forward map from the evolving natural configuration $\mathcal{N}_t$ to $\mathcal{P}_t$ is given by

$$\boldsymbol{\chi}_{\mathcal{N}_t}(\tilde{\boldsymbol{X}}_{\mathcal{N}_t}, \tilde{t}) = \tilde{\boldsymbol{x}}(\tilde{\boldsymbol{X}}_{\mathcal{N}_t}, \tilde{t}) \tag{2.32}$$

where $\tilde{\boldsymbol{X}}_{\mathcal{N}_t}$ are the coordinates in the instantaneous relaxed configuration. Consequently, the push-forward map from $\mathcal{R}$ to $\mathcal{N}_t$ is given by

$$\boldsymbol{\chi}_{\mathcal{R}\to\mathcal{N}_t} = \boldsymbol{\chi}_{\mathcal{N}_t}^{-1}(\boldsymbol{\chi}_{\mathcal{R}}(\tilde{\boldsymbol{X}}_{\mathcal{R}}, \tilde{t}), \tilde{t}) \tag{2.33}$$

When $\mathcal{N}_t$ coincides with $\mathcal{P}_t$, then $\boldsymbol{\chi}_{\mathcal{N}_t}(\tilde{\boldsymbol{X}}_{\mathcal{N}_t}, \tilde{t}) = \tilde{\boldsymbol{X}}_{\mathcal{N}_t}$ and so $\boldsymbol{\chi}_{\mathcal{R}\to\mathcal{N}_t} = \boldsymbol{\chi}_{\mathcal{R}}(\tilde{\boldsymbol{X}}_{\mathcal{R}}, \tilde{t})$. This corresponds to the situation where the reference configuration is the one and only relaxed configuration available to the material.

A deformation gradient tensor is the Jacobian matrix associated with a push-forward map. The deformation gradient associated with $\boldsymbol{\chi}_{\mathcal{R}}(\tilde{\boldsymbol{X}}_{\mathcal{R}}, \tilde{t})$ is given by

$$\boldsymbol{F}_{\mathcal{R}} \equiv \frac{\partial \boldsymbol{\chi}_{\mathcal{R}}(\tilde{\boldsymbol{X}}_{\mathcal{R}}, \tilde{t})}{\partial \tilde{\boldsymbol{X}}_{\mathcal{R}}}, \tag{2.34}$$

The deformation gradient, $\boldsymbol{F}_{\mathcal{R}}$ is an invertible linear transformation with positive determinant that maps an infinitesimal line element $\mathrm{d}\boldsymbol{l}$ in $\mathcal{R}$ to a infinitesimal line

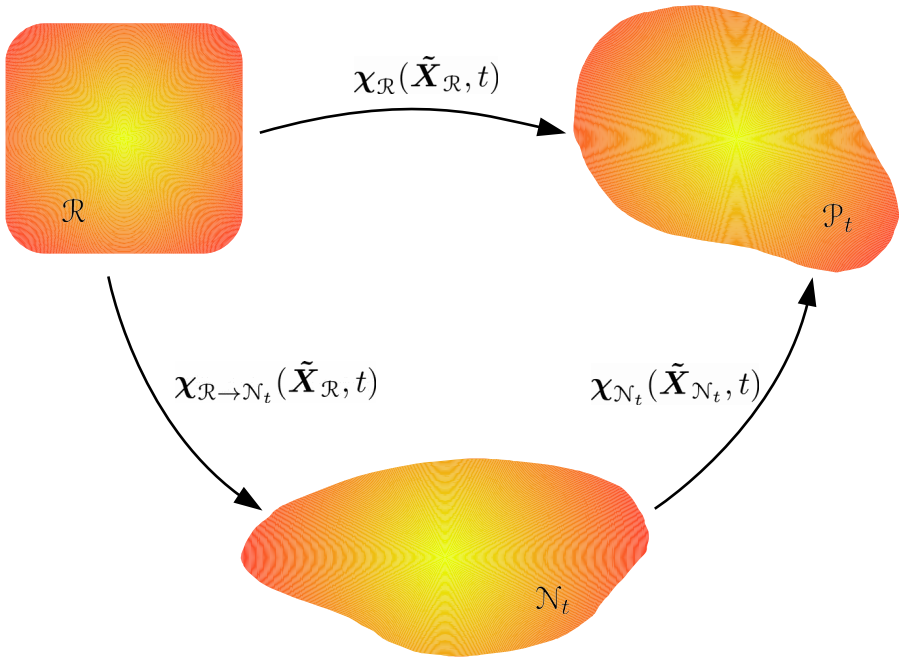

Figure 2.1: Schematic illustrating the various configurations and associated push-forward maps.

element $\mathrm{d}\boldsymbol{\ell}$ in $\mathcal{P}_t$, as follows

$$\mathrm{d}\boldsymbol{\ell} = \boldsymbol{F}_{\mathcal{R}} \cdot \mathrm{d}\boldsymbol{l}. \tag{2.35}$$

Similarly, we can define a deformation gradient associated with $\boldsymbol{\chi}_{\mathcal{N}_t}(\tilde{\boldsymbol{X}}_{\mathcal{N}_t}, \tilde{t})$ that maps line elements in $\mathcal{N}_t$ to line elements in $\mathcal{P}_t$, as follows

$$\boldsymbol{F}_{\mathcal{N}_t} \equiv \frac{\partial \boldsymbol{\chi}_{\mathcal{N}_t}(\tilde{\boldsymbol{X}}_{\mathcal{N}_t}, \tilde{t})}{\partial \tilde{\boldsymbol{X}}_{\mathcal{N}_t}}. \tag{2.36}$$

The deformation gradient tensor that maps line elements in $\mathcal{R}$ to those in $\mathcal{N}_t$ is given

by

$$\boldsymbol{F}_{\mathcal{R}\to\mathcal{N}_t} \equiv \frac{\partial \boldsymbol{\chi}_{\mathcal{R}\to\mathcal{N}_t}(\tilde{\boldsymbol{X}}_{\mathcal{R}}, \tilde{t})}{\partial \tilde{\boldsymbol{X}}_{\mathcal{R}}} = \boldsymbol{F}_{\mathcal{N}_t}^{-1} \cdot \boldsymbol{F}_{\mathcal{R}} \tag{2.37}$$

In deriving (2.37), we note the inverse of the deformation gradient is equal to the deformation gradient associated with the pull-back map (or inverse of the push-forward).

The deformation gradient is a two-point tensor: it maps line elements from one configuration to line elements in another configuration. This fact is relevant to how deformation gradients transform under rotations. Consider a rigid-body rotation $\boldsymbol{Q}(\tilde{t})$. When this rotation is applied to $\mathcal{P}_t$, each $\mathrm{d}\boldsymbol{\ell}$ transforms to $\boldsymbol{Q} \cdot \mathrm{d}\boldsymbol{\ell}$, and $\boldsymbol{F}_{\mathcal{R}}$ transforms to $\boldsymbol{Q}\cdot\boldsymbol{F}_{\mathcal{R}}$. Similarly, when applied to $\mathcal{R}$, then $\boldsymbol{F}_{\mathcal{R}}$ transforms to $(\boldsymbol{Q}\cdot\boldsymbol{F}_{\mathcal{R}}^{-1})^{-1} = \boldsymbol{F}_{\mathcal{R}} \cdot \boldsymbol{Q}^{\mathsf{T}}$.

The deformation gradients can be used to form single-point tensors that can be used to quantify the deformation. The lengths of line elements, in material ($\mathrm{d}\boldsymbol{l}$) and spatial ($\mathrm{d}\boldsymbol{\ell}$) coordinates, are given by

$$|\mathrm{d}\boldsymbol{l}|^2 = \mathrm{d}\boldsymbol{\ell} \cdot (\boldsymbol{F}_{\mathcal{R}} \cdot \boldsymbol{F}_{\mathcal{R}}^{\mathsf{T}})^{-1} \cdot \mathrm{d}\boldsymbol{\ell}, \tag{2.38}$$

$$|\mathrm{d}\boldsymbol{\ell}|^2 = \mathrm{d}\boldsymbol{l} \cdot (\boldsymbol{F}_{\mathcal{R}}^{\mathsf{T}} \cdot \boldsymbol{F}_{\mathcal{R}}) \cdot \mathrm{d}\boldsymbol{l} \tag{2.39}$$

The tensor $\boldsymbol{F}_{\mathcal{R}} \cdot \boldsymbol{F}_{\mathcal{R}}^{\mathsf{T}}$ is the left Cauchy–Green, or Finger, tensor and $\boldsymbol{F}_{\mathcal{R}}^{\mathsf{T}} \cdot \boldsymbol{F}_{\mathcal{R}}$ is the right Cauchy–Green tensor. Both Cauchy–Green tensors are single-point tensors, and their invariants also coincide. As such, both are useful single-point tensors to quantify the

deformation, but the left Cauchy–Green tensor only admits an interpretation in terms of its inverse. They are also both positive–definite tensors.

The left Cauchy–Green tensor is a spatial strain tensor because it describes the deformation of line elements in spatial (or Eulerian) coordinates (its basis vectors are in the deformed configuration, $\mathcal{P}_t$). The right Cauchy–Green tensor is a material (or Lagrangian) strain tensor because it describes the deformation of line elements in material coordinates (its basis vectors are in the reference configuration, $\mathcal{R}$). Consequently, the left Cauchy–Green tensor is invariant under rotations of the reference configuration while the right Cauchy–Green tensor is invariant under rotations of the deformed configuration. Using the definition in (2.10), it is easy to show that the left Cauchy–Green tensor is frame indifferent with respect to rigid-body rotations of the deformed configuration while the right Cauchy–Green tensor is not.

In the present work, we prefer spatial (or Eulerian) coordinates and thus we will quantify the deformation with the frame indifferent left Cauchy–Green tensors. Using the deformation gradients, we can define these as follows

$$\boldsymbol{B}_{\mathcal{R}} \equiv \boldsymbol{F}_{\mathcal{R}} \cdot \boldsymbol{F}_{\mathcal{R}}^{\mathsf{T}}, \qquad \boldsymbol{B}_{\mathcal{N}_t} \equiv \boldsymbol{F}_{\mathcal{N}_t} \cdot \boldsymbol{F}_{\mathcal{N}_t}^{\mathsf{T}} \tag{2.40}$$

Using (2.40) and $\boldsymbol{F}_{\mathcal{R}\to\mathcal{N}_t}$ as given in (2.37), it is easy to show that

$$\boldsymbol{B}_{\mathcal{N}_t} = \boldsymbol{F}_{\mathcal{R}} \cdot (\boldsymbol{B}^{\star}_{\mathcal{R}\to\mathcal{N}_t})^{-1} \cdot \boldsymbol{F}_{\mathcal{R}}^{\mathsf{T}} \tag{2.41}$$

where $\boldsymbol{B}^{\star}_{\mathcal{R}\to\mathcal{N}_t}$ is the right Cauchy–Green tensor associated with $\boldsymbol{F}_{\mathcal{R}\to\mathcal{N}_t}$,

$$\boldsymbol{B}^{\star}_{\mathcal{R}\to\mathcal{N}_t} \equiv \boldsymbol{F}^{\mathsf{T}}_{\mathcal{R}\to\mathcal{N}_t} \cdot \boldsymbol{F}_{\mathcal{R}\to\mathcal{N}_t}. \tag{2.42}$$

The tensor $\boldsymbol{B}_{\mathcal{N}_t}$ describes the deformation that leads to an elastic response in the material because the natural configuration is relaxed (stress-free).

The velocity, $\tilde{\boldsymbol{u}}$, is defined as the instantaneous time rate of change of the push-forward of a material point to $\mathcal{P}_t$, and thus

$$\tilde{\boldsymbol{u}}(\tilde{\boldsymbol{X}}_{\mathcal{R}}, \tilde{t}) \equiv \frac{\partial}{\partial \tilde{t}} \boldsymbol{\chi}_{\mathcal{R}}(\tilde{\boldsymbol{X}}_{\mathcal{R}}, \tilde{t}) \tag{2.43}$$

where the partial derivative and the function arguments imply that the material point is kept constant. The corresponding velocity (spatial) field is given by $\tilde{\boldsymbol{u}}(\boldsymbol{\chi}_{\mathcal{R}}^{-1}(\tilde{\boldsymbol{x}}, t), t) = \tilde{\boldsymbol{u}}(\tilde{\boldsymbol{x}}, t)$. Note that $\partial\tilde{\boldsymbol{u}}(\tilde{\boldsymbol{x}}, t)/\partial\tilde{t} \neq \partial\tilde{\boldsymbol{u}}(\tilde{\boldsymbol{X}}_{\mathcal{R}}, \tilde{t})/\partial\tilde{t}$. We can also define a velocity, $\tilde{\boldsymbol{u}}_{\mathcal{N}_t}$, that measures the instantaneous time rate of change of the push-forward of a material point to $\mathcal{N}_t$, as follows

$$\tilde{\boldsymbol{u}}_{\mathcal{N}_t}(\tilde{\boldsymbol{X}}_{\mathcal{R}}, \tilde{t}) \equiv \frac{\partial}{\partial \tilde{t}} \boldsymbol{\chi}_{\mathcal{R}\to\mathcal{N}_t}(\tilde{\boldsymbol{X}}_{\mathcal{R}}, \tilde{t}). \tag{2.44}$$

The velocity $\tilde{\boldsymbol{u}}_{\mathcal{N}_t}$ is the velocity in the natural configuration which is the instantaneous relaxed configuration, and is a theoretical construct rather than a directly physically observable velocity in the medium.

We next consider the velocity gradient tensor, $\tilde{\boldsymbol{\nabla}}\tilde{\boldsymbol{u}}$. While the deformation gradient tensor describes a gradient with respect to the material coordinates, the velocity gradient tensor, or velocity field gradient, is the gradient of the velocity field $\tilde{\boldsymbol{u}}(\tilde{\boldsymbol{x}}, t)$ with respect to the spatial coordinates and can be written in terms of the deformation gradient $\boldsymbol{F}_{\mathcal{R}}$ as follows

$$\tilde{\boldsymbol{\nabla}}^{\mathsf{T}}\tilde{\boldsymbol{u}} = \frac{\partial\tilde{\boldsymbol{u}}}{\partial\tilde{\boldsymbol{x}}} = \frac{\partial\tilde{\boldsymbol{u}}}{\partial\tilde{\boldsymbol{X}}_{\mathcal{R}}} \cdot \frac{\partial\tilde{\boldsymbol{X}}_{\mathcal{R}}}{\partial\tilde{\boldsymbol{x}}} \tag{2.45}$$

$$= \frac{\partial}{\partial\tilde{t}}\left(\frac{\partial\boldsymbol{\chi}_{\mathcal{R}}(\tilde{\boldsymbol{X}}_{\mathcal{R}}, \tilde{t})}{\partial\tilde{\boldsymbol{X}}_{\mathcal{R}}}\right) \cdot \frac{\partial\tilde{\boldsymbol{X}}_{\mathcal{R}}}{\partial\tilde{\boldsymbol{x}}} \tag{2.46}$$

$$= \frac{\mathrm{D}\boldsymbol{F}_{\mathcal{R}}}{\mathrm{D}\tilde{t}} \cdot \boldsymbol{F}_{\mathcal{R}}^{-1} \tag{2.47}$$

Similarly, we define the natural configuration velocity gradient, $\tilde{\boldsymbol{\nabla}}_{\tilde{\boldsymbol{X}}_{\mathcal{N}_t}}\tilde{\boldsymbol{u}}_{\mathcal{N}_t}$, as follows

$$\tilde{\boldsymbol{\nabla}}^{\mathsf{T}}_{\tilde{\boldsymbol{X}}_{\mathcal{N}_t}}\tilde{\boldsymbol{u}}_{\mathcal{N}_t} = \frac{\partial\tilde{\boldsymbol{u}}_{\mathcal{N}_t}}{\partial\tilde{\boldsymbol{X}}_{\mathcal{N}_t}} = \frac{\mathrm{D}\boldsymbol{F}_{\mathcal{R}\to\mathcal{N}_t}}{\mathrm{D}\tilde{t}} \cdot \boldsymbol{F}^{-1}_{\mathcal{R}\to\mathcal{N}_t} \tag{2.48}$$

The tensor $\tilde{\boldsymbol{\nabla}}_{\tilde{\boldsymbol{X}}_{\mathcal{N}_t}}\tilde{\boldsymbol{u}}_{\mathcal{N}_t}$ represents gradients of $\tilde{\boldsymbol{u}}_{\mathcal{N}_t}$ in the natural configuration. For convenience, we also define the strain rate tensor in the natural configuration,

$$\tilde{\boldsymbol{D}}_{\mathcal{N}_t} \equiv \mathrm{sym}\left(\tilde{\boldsymbol{\nabla}}_{\tilde{\boldsymbol{X}}_{\mathcal{N}_t}}\tilde{\boldsymbol{u}}_{\mathcal{N}_t}\right). \tag{2.49}$$

Since natural configuration does not involve any volumetric deformation, from (2.50)

we find that the natural configuration is also isochoric

$$\operatorname{tr} \tilde{\boldsymbol{D}}_{\mathcal{N}_t} = 0. \tag{2.50}$$

It can be shown that (2.6) and (2.50) imply that $\mathrm{III}_{\det \boldsymbol{B}_{\mathcal{N}_t}} = \det \boldsymbol{B}_{\mathcal{N}_t} = 1$. This, rather severe, restriction distinguishes the continuum models derived here from those obtained from molecular approaches, and will be discussed further later.

The material derivative of $\boldsymbol{B}_{\mathcal{N}_t}$ can be expressed using the equation for $\boldsymbol{B}_{\mathcal{N}_t}$ in (2.41) and the expression of $\tilde{\boldsymbol{\nabla}}\tilde{\boldsymbol{u}}$ in (2.47), as follows

$$\begin{aligned}
\frac{\mathrm{D}\boldsymbol{B}_{\mathcal{N}_t}}{\mathrm{D}\tilde{t}} &= \frac{\partial}{\partial \tilde{t}} \boldsymbol{B}_{\mathcal{N}_t}(\tilde{\boldsymbol{X}}_{\mathcal{R}}, \tilde{t}) \\
&= \frac{\mathrm{D}\boldsymbol{F}_{\mathcal{R}}}{\mathrm{D}\tilde{t}} \cdot (\boldsymbol{B}^{\star}_{\mathcal{R}\to\mathcal{N}_t})^{-1} \cdot \boldsymbol{F}^{\mathsf{T}}_{\mathcal{R}} + \boldsymbol{F}_{\mathcal{R}} \cdot (\boldsymbol{B}^{\star}_{\mathcal{R}\to\mathcal{N}_t})^{-1} \cdot \frac{\mathrm{D}\boldsymbol{F}^{\mathsf{T}}_{\mathcal{R}}}{\mathrm{D}\tilde{t}} + \boldsymbol{F}_{\mathcal{R}} \cdot \frac{\mathrm{D}(\boldsymbol{B}^{\star}_{\mathcal{R}\to\mathcal{N}_t})^{-1}}{\mathrm{D}\tilde{t}} \cdot \boldsymbol{F}^{\mathsf{T}}_{\mathcal{R}} \\
&= \tilde{\boldsymbol{\nabla}}^{\mathsf{T}} \tilde{\boldsymbol{u}} \cdot \boldsymbol{B}_{\mathcal{N}_t} + \boldsymbol{B}_{\mathcal{N}_t} \cdot \tilde{\boldsymbol{\nabla}}\tilde{\boldsymbol{u}} + \boldsymbol{F}_{\mathcal{R}} \cdot \frac{\mathrm{D}(\boldsymbol{B}^{\star}_{\mathcal{R}\to\mathcal{N}_t})^{-1}}{\mathrm{D}\tilde{t}} \cdot \boldsymbol{F}^{\mathsf{T}}_{\mathcal{R}}
\end{aligned} \tag{2.51}$$

where we introduced the notation for the material time derivative in lieu of retaining arguments. Then using definition of the upper-convected Maxwell derivative set forth in (2.17), we can re-write (2.51) as

$$\overset{\tilde{\nabla}}{\boldsymbol{B}}_{\mathcal{N}_t} = \boldsymbol{F}_{\mathcal{R}} \cdot \frac{\mathrm{D}(\boldsymbol{B}^{\star}_{\mathcal{R}\to\mathcal{N}_t})^{-1}}{\mathrm{D}\tilde{t}} \cdot \boldsymbol{F}^{\mathsf{T}}_{\mathcal{R}}. \tag{2.52}$$

Using the identity

$$\frac{\mathrm{D}\boldsymbol{F}^{-1}_{\mathcal{R}\to\mathcal{N}_t}}{\mathrm{D}\tilde{t}} = -\boldsymbol{F}^{-1}_{\mathcal{R}\to\mathcal{N}_t}\cdot\frac{\mathrm{D}\boldsymbol{F}^{-1}_{\mathcal{R}\to\mathcal{N}_t}}{\mathrm{D}\tilde{t}}\cdot\boldsymbol{F}^{-1}_{\mathcal{R}\to\mathcal{N}_t}, \tag{2.53}$$

the definition of $\boldsymbol{B}^{\star}_{\mathcal{R}\to\mathcal{N}_t}$ in (2.42), the expression for $\tilde{\boldsymbol{\nabla}}_{\tilde{\boldsymbol{X}}_{\mathcal{N}_t}}\tilde{\boldsymbol{u}}_{\mathcal{N}_t}$ in (2.48), and the expression $\boldsymbol{F}_{\mathcal{R}\to\mathcal{N}_t} = \boldsymbol{F}^{-1}_{\mathcal{N}_t}\cdot\boldsymbol{F}_{\mathcal{R}}$ in (2.37), we obtain

$$\begin{aligned}\frac{\mathrm{D}(\boldsymbol{B}^{\star}_{\mathcal{R}\to\mathcal{N}_t})^{-1}}{\mathrm{D}\tilde{t}} &= \boldsymbol{F}^{-1}_{\mathcal{R}\to\mathcal{N}_t}\cdot\frac{\mathrm{D}\boldsymbol{F}^{-\mathsf{T}}_{\mathcal{R}\to\mathcal{N}_t}}{\mathrm{D}\tilde{t}} + \frac{\mathrm{D}\boldsymbol{F}^{-1}_{\mathcal{R}\to\mathcal{N}_t}}{\mathrm{D}\tilde{t}}\cdot\boldsymbol{F}^{-\mathsf{T}}_{\mathcal{R}\to\mathcal{N}_t}\\ &= -2\boldsymbol{F}^{-1}_{\mathcal{R}\to\mathcal{N}_t}\cdot\tilde{\boldsymbol{D}}_{\mathcal{N}_t}\cdot\boldsymbol{F}^{-\mathsf{T}}_{\mathcal{R}\to\mathcal{N}_t}\\ &= -2\boldsymbol{F}^{-1}_{\mathcal{R}}\cdot\boldsymbol{F}_{\mathcal{N}_t}\cdot\tilde{\boldsymbol{D}}_{\mathcal{N}_t}\cdot\boldsymbol{F}^{\mathsf{T}}_{\mathcal{N}_t}\cdot\boldsymbol{F}^{-\mathsf{T}}_{\mathcal{R}}.\end{aligned} \tag{2.54}$$

Finally, using (2.54) in (2.52), we have

$$\overset{\tilde{\nabla}}{\boldsymbol{B}}_{\mathcal{N}_t} = -2\boldsymbol{F}_{\mathcal{N}_t}\cdot\tilde{\boldsymbol{D}}_{\mathcal{N}_t}\cdot\boldsymbol{F}^{\mathsf{T}}_{\mathcal{N}_t}. \tag{2.55}$$

We next develop the necessary thermodynamical constraints using the kinematic formulations.

2.3.3 Thermodynamics

The Clasius-Duhem inequality combines the Cauchy momentum equation and the first two laws of thermodynamics[101,123] and reads as follows

$$\mathrm{tr}\,(\tilde{\boldsymbol{\sigma}} \cdot \tilde{\boldsymbol{D}}) - \frac{\mathrm{D}W}{\mathrm{D}\tilde{t}} \geq 0 \tag{2.56}$$

where W is the stored energy density, in the sense of Helmholtz, and our assumption of incompressibility (2.6) eliminated pressure work from the inequality. The inequality (2.56) can be replaced with an equality by associating the left-hand side of (2.56) with a positive rate of dissipation density function ξ so that

$$\xi = \mathrm{tr}\,(\tilde{\boldsymbol{\sigma}} \cdot \tilde{\boldsymbol{D}}) - \frac{\mathrm{D}W}{\mathrm{D}\tilde{t}}. \tag{2.57}$$

In order to continue further, we require some assumptions that are outlined below.

1. The material is isotropic and therefore

$$W = W(\mathrm{I}_{\boldsymbol{B}_{\mathcal{N}_t}}, \mathrm{II}_{\boldsymbol{B}_{\mathcal{N}_t}}, \mathrm{III}_{\boldsymbol{B}_{\mathcal{N}_t}}) \tag{2.58}$$

where W only depends on the deformation from the natural configuration because the latter is the relevant stress free configuration. The invariants are

defined as

$$\mathrm{I}_{\boldsymbol{B}_{\mathcal{N}_t}} \equiv \mathrm{tr}\ \boldsymbol{B}_{\mathcal{N}_t}, \quad \mathrm{II}_{\boldsymbol{B}_{\mathcal{N}_t}} \equiv \frac{1}{2}\left[(\mathrm{tr}\ \boldsymbol{B}_{\mathcal{N}_t})^2 - \mathrm{tr}\ \boldsymbol{B}_{\mathcal{N}_t}^2\right], \quad \mathrm{III}_{\boldsymbol{B}_{\mathcal{N}_t}} \equiv \det \boldsymbol{B}_{\mathcal{N}_t}. \tag{2.59}$$

2. The dissipation function takes the form

$$\xi = \xi_e\left(\boldsymbol{B}_{\mathcal{N}_t}, \tilde{\boldsymbol{D}}_{\mathcal{N}_t}\right) + 2\,\eta_s \mathrm{tr}\,(\tilde{\boldsymbol{D}} \cdot \tilde{\boldsymbol{D}}) \tag{2.60}$$

where ξ_e represents the elastic dissipation and $2\,\eta_s \mathrm{tr}\,(\tilde{\boldsymbol{D}} \cdot \tilde{\boldsymbol{D}})$ is a contribution related to viscous dissipation. The latter is explicitly introduced to mimic mixed models like the Oldroyd-B model, as will be seen later.

3. Without loss of generality, let $\boldsymbol{F}_{\mathcal{N}_t}$ be symmetric, i.e. it involves no rotation. This is not a restrictive assumption because we are always free to define the natural configuration.

Now, using the identity for a scalar function ϕ of a second–order tensor $\boldsymbol{A}$

$$\frac{\mathrm{D}\phi(\boldsymbol{A})}{\mathrm{D}\tilde{t}} = \mathrm{tr}\left(\frac{\partial \phi}{\partial \boldsymbol{A}} \cdot \frac{\mathrm{D}\boldsymbol{A}}{\mathrm{D}\tilde{t}}\right), \tag{2.61}$$

it is easy to show that

$$\begin{aligned}
\frac{\mathrm{D}\mathrm{I}_{\boldsymbol{A}}}{\mathrm{D}\tilde{t}} &= \mathrm{tr}\,\frac{\mathrm{D}\boldsymbol{A}}{\mathrm{D}\tilde{t}}, \\
\frac{\mathrm{D}\mathrm{II}_{\boldsymbol{A}}}{\mathrm{D}\tilde{t}} &= \mathrm{tr}\,\left[(\mathrm{I}_{\boldsymbol{A}}\boldsymbol{I}-\boldsymbol{A})\cdot\frac{\mathrm{D}\boldsymbol{A}}{\mathrm{D}\tilde{t}}\right], \\
\frac{\mathrm{D}\mathrm{III}_{\boldsymbol{A}}}{\mathrm{D}\tilde{t}} &= \mathrm{tr}\,\left(\mathrm{III}_{\boldsymbol{A}}\boldsymbol{A}^{-1}\cdot\frac{\mathrm{D}\boldsymbol{A}}{\mathrm{D}\tilde{t}}\right).
\end{aligned} \tag{2.62}$$

Using the assumption (2.58) and the identities (2.62), the elastic power can be written in terms of the material time derivative of $\boldsymbol{B}_{\mathcal{N}_t}$ as follows

$$\frac{\mathrm{D}W}{\mathrm{D}\tilde{t}} = \mathrm{tr}\,\left\{\left[\frac{\partial W}{\partial \mathrm{III}_{\boldsymbol{B}_{\mathcal{N}_t}}}\mathrm{III}_{\boldsymbol{B}_{\mathcal{N}_t}}\boldsymbol{B}_{\mathcal{N}_t}^{-1}+\left(\frac{\partial W}{\partial \mathrm{I}_{\boldsymbol{B}_{\mathcal{N}_t}}}+\frac{\partial W}{\partial \mathrm{II}_{\boldsymbol{B}_{\mathcal{N}_t}}}\mathrm{I}_{\boldsymbol{B}_{\mathcal{N}_t}}\right)\boldsymbol{I}-\frac{\partial W}{\partial \mathrm{II}_{\boldsymbol{B}_{\mathcal{N}_t}}}\boldsymbol{B}_{\mathcal{N}_t}\right]\cdot\frac{\mathrm{D}\boldsymbol{B}_{\mathcal{N}_t}}{\mathrm{D}\tilde{t}}\right\}. \tag{2.63}$$

The material time derivative of $\boldsymbol{B}_{\mathcal{N}_t}$ was derived in (2.55) using kinematical approaches. Substituting (2.55) into the expression for the elastic power (2.63), and using the fact that $\boldsymbol{F}_{\mathcal{N}_t}$ is symmetric yields

$$\frac{\mathrm{D}W}{\mathrm{D}\tilde{t}} = 2\,\mathrm{tr}\,\left\{\left[\frac{\partial W}{\partial \mathrm{III}_{\boldsymbol{B}_{\mathcal{N}_t}}}\mathrm{III}_{\boldsymbol{B}_{\mathcal{N}_t}}\boldsymbol{I}+\left(\frac{\partial W}{\partial \mathrm{I}_{\boldsymbol{B}_{\mathcal{N}_t}}}+\frac{\partial W}{\partial \mathrm{II}_{\boldsymbol{B}_{\mathcal{N}_t}}}\mathrm{I}_{\boldsymbol{B}_{\mathcal{N}_t}}\right)\boldsymbol{B}_{\mathcal{N}_t}-\frac{\partial W}{\partial \mathrm{II}_{\boldsymbol{B}_{\mathcal{N}_t}}}\boldsymbol{B}_{\mathcal{N}_t}^2\right]\cdot\left(\tilde{\boldsymbol{D}}-\tilde{\boldsymbol{D}}_{\mathcal{N}_t}\right)\right\} \tag{2.64}$$

We now substitute the assumed form of ξ in (2.60) and also the elastic power

expression in (2.63) into Clausius–Duhem (2.57), so that

$$\begin{aligned}&\operatorname{tr}\left\{\left[\tilde{\boldsymbol{\sigma}}-2\left(\frac{\partial W}{\partial \mathrm{I}_{\boldsymbol{B}_{\mathcal{N}_t}}}+\frac{\partial W}{\partial \mathrm{II}_{\boldsymbol{B}_{\mathcal{N}_t}}}\mathrm{I}_{\boldsymbol{B}_{\mathcal{N}_t}}\right)\boldsymbol{B}_{\mathcal{N}_t}+2\,\frac{\partial W}{\partial \mathrm{II}_{\boldsymbol{B}_{\mathcal{N}_t}}}\boldsymbol{B}_{\mathcal{N}_t}^2-2\,\eta_s\tilde{\boldsymbol{D}}\right]\cdot\tilde{\boldsymbol{D}}\right\}\\&=\xi_e\left(\boldsymbol{B}_{\mathcal{N}_t},\tilde{\boldsymbol{D}}_{\mathcal{N}_t}\right)-\operatorname{tr}\left\{2\left[\left(\frac{\partial W}{\partial \mathrm{I}_{\boldsymbol{B}_{\mathcal{N}_t}}}+\frac{\partial W}{\partial \mathrm{II}_{\boldsymbol{B}_{\mathcal{N}_t}}}\mathrm{I}_{\boldsymbol{B}_{\mathcal{N}_t}}\right)\boldsymbol{B}_{\mathcal{N}_t}-\frac{\partial W}{\partial \mathrm{II}_{\boldsymbol{B}_{\mathcal{N}_t}}}\boldsymbol{B}_{\mathcal{N}_t}^2\right]\cdot\tilde{\boldsymbol{D}}_{\mathcal{N}_t}\right\}.\end{aligned}\tag{2.65}$$

The right-hand side of (2.65) is independent of $\tilde{\boldsymbol{D}}$, and therefore the presence of $\tilde{\boldsymbol{D}}$ on the left-hand side implies

$$\tilde{\boldsymbol{\sigma}}_*=-\tilde{p}\boldsymbol{I}+2\left[\left(\frac{\partial W}{\partial \mathrm{I}_{\boldsymbol{B}_{\mathcal{N}_t}}}+\frac{\partial W}{\partial \mathrm{II}_{\boldsymbol{B}_{\mathcal{N}_t}}}\mathrm{I}_{\boldsymbol{B}_{\mathcal{N}_t}}\right)\boldsymbol{B}_{\mathcal{N}_t}+\frac{\partial W}{\partial \mathrm{II}_{\boldsymbol{B}_{\mathcal{N}_t}}}\boldsymbol{B}_{\mathcal{N}_t}^2\right]\tag{2.66}$$

where $\tilde{p}$ is a constant and $\tilde{\boldsymbol{\sigma}}_*$ is the elastic part of the stress tensor,

$$\tilde{\boldsymbol{\sigma}}_*\equiv\tilde{\boldsymbol{\sigma}}-2\,\eta_s\tilde{\boldsymbol{D}}.\tag{2.67}$$

Substituting the expression for the elastic part of the stress in (2.66) into Clausius–Duhem (2.65) yields

$$\xi_e=\operatorname{tr}\left(\tilde{\boldsymbol{\sigma}}_*\cdot\tilde{\boldsymbol{D}}_{\mathcal{N}_t}\right),\tag{2.68}$$

which is a type of constraint on the choice of ξ_e.

We now require that for a fixed deformation $\boldsymbol{B}_{\mathcal{N}_t}$, the velocity gradient tensor $\tilde{\boldsymbol{D}}_{\mathcal{N}_t}$ is such that the elastic dissipation rate, ξ_e, is maximized.[116] In addition, the chosen

$\tilde{\boldsymbol{D}}_{\mathcal{N}_t}$ must satisfy the constraints (2.50) and (2.68). Using the method of Lagrange multipliers, we find that extremizing $\tilde{\boldsymbol{D}}_{\mathcal{N}_t}$ must satisfy

$$\tilde{\boldsymbol{\sigma}}_* - \varsigma_1 \frac{\partial \xi_e}{\partial \tilde{\boldsymbol{D}}_{\mathcal{N}_t}} - \varsigma_2 \boldsymbol{I} = \boldsymbol{0} \tag{2.69}$$

where ς_1 and ς_2 are constants that are formed from the Lagrange multipliers. In deriving 2.69, we used the expression (2.66) to determine that $\tilde{\boldsymbol{\sigma}}_*$ is independent of $\tilde{\boldsymbol{D}}_{\mathcal{N}_t}$ for fixed $\boldsymbol{B}_{\mathcal{N}_t}$. Multiplying (2.69) by $\tilde{\boldsymbol{D}}_{\mathcal{N}_t}$, taking the trace, invoking the isochoric condition (2.50), and using the expression for ξ_e in (2.68), we obtain

$$\varsigma_1 = \left[\mathrm{tr} \left(\frac{\partial \xi_e}{\partial \tilde{\boldsymbol{D}}_{\mathcal{N}_t}} \cdot \tilde{\boldsymbol{D}}_{\mathcal{N}_t} \right) \right]^{-1} \xi_e \tag{2.70}$$

and therefore (2.69) reduces to

$$\tilde{\boldsymbol{\sigma}}_* = \left[\mathrm{tr} \left(\frac{\partial \xi_e}{\partial \tilde{\boldsymbol{D}}_{\mathcal{N}_t}} \cdot \tilde{\boldsymbol{D}}_{\mathcal{N}_t} \right) \right]^{-1} \xi_e \frac{\partial \xi_e}{\partial \tilde{\boldsymbol{D}}_{\mathcal{N}_t}} + \varsigma_2 \boldsymbol{I}. \tag{2.71}$$

Finally, eliminating $\tilde{\boldsymbol{\sigma}}_*$ between (2.66) and (2.71) yields a master equation relating $\boldsymbol{B}_{\mathcal{N}_t}$ and the extremizing $\tilde{\boldsymbol{D}}_{\mathcal{N}_t}$ for a given choice of ξ_e and W

$$2 \left[\left(\frac{\partial W}{\partial \mathrm{I}_{\boldsymbol{B}_{\mathcal{N}_t}}} + \frac{\partial W}{\partial \mathrm{II}_{\boldsymbol{B}_{\mathcal{N}_t}}} \mathrm{I}_{\boldsymbol{B}_{\mathcal{N}_t}} \right) \boldsymbol{B}_{\mathcal{N}_t} + \frac{\partial W}{\partial \mathrm{II}_{\boldsymbol{B}_{\mathcal{N}_t}}} \boldsymbol{B}_{\mathcal{N}_t}^2 \right] - \left[\mathrm{tr} \left(\frac{\partial \xi_e}{\partial \tilde{\boldsymbol{D}}_{\mathcal{N}_t}} \cdot \tilde{\boldsymbol{D}}_{\mathcal{N}_t} \right) \right]^{-1} \xi_e \frac{\partial \xi_e}{\partial \tilde{\boldsymbol{D}}_{\mathcal{N}_t}} - (\varsigma_2 + \tilde{p}) \boldsymbol{I} = \boldsymbol{0}. \tag{2.72}$$

We now use the master equation (2.72) and specific assumptions regarding W and ξ to derive model fluids of interest.

2.3.4 Model fluids

For this subsection we assume that the elastic behaviour of the fluid is neo-Hookean. The strain energy density associated with neo-Hookean behaviour is

$$W = \frac{\eta_p \vartheta}{2}(\mathrm{I}_{\boldsymbol{B}_{\mathcal{N}_t}} - 3) \tag{2.73}$$

where $\eta_p\vartheta$ is a spring constant density, and η_p and ϑ are two free parameters. Here we choose η_p to have units of viscosity and ϑ to have units of strain rate. We use these two parameters to make $\dot{W}$ comparable with the viscous rate of dissipation per unit volume, i.e. $2\eta_s \mathrm{tr}\,(\tilde{\boldsymbol{D}} \cdot \tilde{\boldsymbol{D}})$. Substituting W into (2.66) and using the definition for $\tilde{\boldsymbol{\sigma}}_*$ in (2.67), we obtain an expression for the stress

$$\tilde{\boldsymbol{\sigma}} = -\tilde{p}\boldsymbol{I} + \eta_s(2\tilde{\boldsymbol{D}}) + \eta_p(\vartheta \boldsymbol{B}_{\mathcal{N}_t}), \tag{2.74}$$

It now remains to specify a dynamical equation for $\boldsymbol{B}_{\mathcal{N}_t}$.

Assume now that the elastic part of the rate of dissipation function is given by

$$\xi_e = 2\,\eta_p\,\mathrm{tr}\,\left(\tilde{\boldsymbol{D}}_{\mathcal{N}_t} \cdot \boldsymbol{B}_{\mathcal{N}_t} \cdot \tilde{\boldsymbol{D}}_{\mathcal{N}_t}\right). \tag{2.75}$$

Such ξ_e is similar to a viscous dissipation but with an additional tensorial factor that depends on the elastic deformation. With this choice of ξ_e, we have

$$\frac{\partial \xi_e}{\partial \tilde{\boldsymbol{D}}_{\mathcal{N}_t}} = 4\,\eta_p \boldsymbol{B}_{\mathcal{N}_t} \cdot \tilde{\boldsymbol{D}}_{\mathcal{N}_t} \tag{2.76}$$

and note that it can be shown that eigenvectors of $\boldsymbol{B}_{\mathcal{N}_t}$ and $\boldsymbol{D}_{\mathcal{N}_t}$ coincide[116] so that $\boldsymbol{B}_{\mathcal{N}_t} \cdot \tilde{\boldsymbol{D}}_{\mathcal{N}_t} = \tilde{\boldsymbol{D}}_{\mathcal{N}_t} \cdot \boldsymbol{B}_{\mathcal{N}_t}$.

Substituting the expression for $\partial \xi_e / \partial \tilde{\boldsymbol{D}}_{\mathcal{N}_t}$ in (2.76) into the master equation in (2.72) yields

$$\eta_p \vartheta \boldsymbol{B}_{\mathcal{N}_t} - (\varsigma_2 + p)\boldsymbol{I} = 2\,\eta_p \boldsymbol{B}_{\mathcal{N}_t} \cdot \tilde{\boldsymbol{D}}_{\mathcal{N}_t} \tag{2.77}$$

$$= 2\,\eta_p \boldsymbol{F}_{\mathcal{N}_t} \cdot \tilde{\boldsymbol{D}}_{\mathcal{N}_t} \cdot \boldsymbol{F}_{\mathcal{N}_t} \tag{2.78}$$

where we premultiplied the equation by $\boldsymbol{F}_{\mathcal{N}_t}^{-1}$ and postmultiplied by $\boldsymbol{F}_{\mathcal{N}_t}$ to obtain the last equality. Premultiplying (2.77) by $\boldsymbol{B}_{\mathcal{N}_t}^{-1}$ and taking the trace yields

$$\varsigma_2 + \tilde{p} = 3\eta_p \vartheta \left(\operatorname{tr} \boldsymbol{B}_{\mathcal{N}_t}^{-1}\right)^{-1} \tag{2.79}$$

Substituting (2.55) and (2.79) into (2.78) we obtain the constitutive relation

$$\overset{\tilde{\nabla}}{\boldsymbol{B}}_{\mathcal{N}_t} = -\vartheta \left(\boldsymbol{B}_{\mathcal{N}_t} - 3\left(\operatorname{tr} \boldsymbol{B}_{\mathcal{N}_t}^{-1}\right)^{-1} \boldsymbol{I}\right) \tag{2.80}$$

The Cauchy momentum equation (2.1), the stress in (2.74) and the evolution equation in (2.80) together complete the dynamical description of a model fluid. We now consider different limits of this equation and derive well-known models.

2.3.4.1 Navier–Stokes fluid

The limit of a purely viscous liquid may be readily obtained by setting $\eta_p = 0$ in (2.74). However, the equations obtained this way are imposed via the assumption on the rate of dissipation function. This assumption does not factor into the extremization that leads to the final constitutive relation. We instead wish to obtain the equations for viscous flow by invoking the thermodynamic formalism involving maximizing the rate of dissipation.

Instead of setting $\eta_p = 0$, let $\eta_s = 0$ and define the purely viscous case as the situation when the natural configuration $\mathcal{N}_t$ coincides with the current configuration $\mathcal{P}_t$. With such an assumption, it is easy to show that $\boldsymbol{B}_{\mathcal{N}_t} = \boldsymbol{I}$ and $\tilde{\boldsymbol{D}}_{\mathcal{N}_t} = \tilde{\boldsymbol{D}}$.

The dissipation balance (2.65) along with the choice of ξ_e in (2.75) then yields

$$\operatorname{tr}\left(\tilde{\boldsymbol{\sigma}} \cdot \tilde{\boldsymbol{D}}\right) = 2\,\eta_p \operatorname{tr}\left(\tilde{\boldsymbol{D}} \cdot \tilde{\boldsymbol{D}}\right) \tag{2.81}$$

and the extremizing condition (2.69) yields

$$\tilde{\boldsymbol{\sigma}} - \frac{\operatorname{tr}\tilde{\boldsymbol{\sigma}}}{3}\boldsymbol{I} = 2\,\eta_p \tilde{\boldsymbol{D}} \tag{2.82}$$

where we used the isochoric condition (2.6) and (2.81) to calculate the Lagrange multipliers in (2.69). The expression (2.82) states that the deviatoric part of the stress tensor is proportional to $2\,\eta_p \tilde{\boldsymbol{D}}$. Identifying $-\mathrm{tr}\,\tilde{\boldsymbol{\sigma}}/3$ with the pressure and substituting (2.82) into the momentum equation (2.1) then yields

$$\frac{\mathrm{D}\rho\tilde{\boldsymbol{u}}}{\mathrm{D}\tilde{t}} = -\tilde{\boldsymbol{\nabla}} p + \eta\tilde{\boldsymbol{\Delta}}\tilde{\boldsymbol{u}} + \tilde{\boldsymbol{d}} \tag{2.83}$$

where $\eta = \eta_p$, and p here is distinct from that used in (2.66) and subsequently in (2.74). Following (2.82), p is the isotropic part of the stress in (2.83). On the other hand, p in (2.74) is only one part of the total isotropic stress. The equation (2.83) and the isochoric condition (2.6),

$$\tilde{\boldsymbol{\nabla}} \cdot \tilde{\boldsymbol{u}} = 0, \tag{2.84}$$

are together the Navier–Stokes equations.

2.3.4.2 Oldroyd-B fluid

Consider small strains so that $\boldsymbol{B}_{\mathcal{N}_t}^{-1} = \boldsymbol{I} + \epsilon\boldsymbol{X}$ for $\epsilon \ll 1$ and symmetric tensor $\boldsymbol{X}$. We then have

$$\det(\boldsymbol{I} + \epsilon\boldsymbol{X}) = 1 + \epsilon\mathrm{tr}\,\boldsymbol{X} + \mathcal{O}(\epsilon^2) \tag{2.85}$$

By the incompressibility constraint, we always have $\det \boldsymbol{B}_{\mathcal{N}_t} = \det \boldsymbol{B}_{\mathcal{N}_t}^{-1} = 1$, and so $\operatorname{tr} \boldsymbol{X} \sim \mathcal{O}(\epsilon)$ and thus

$$\operatorname{tr} \boldsymbol{B}_{\mathcal{N}_t}^{-1} \sim 3 + \mathcal{O}(\epsilon^2). \tag{2.86}$$

The Cauchy momentum equation (2.1), the stress in (2.74) and the evolution equation in (2.80) taken together then read

$$\frac{\mathrm{D}\rho\tilde{\boldsymbol{u}}}{\mathrm{D}\tilde{t}} = -\tilde{\boldsymbol{\nabla}}\tilde{p} + \eta_s \tilde{\boldsymbol{\Delta}}\tilde{\boldsymbol{u}} + \eta_p \tilde{\boldsymbol{\nabla}} \cdot \tilde{\boldsymbol{T}} + \tilde{\boldsymbol{d}} \tag{2.87}$$

$$\tilde{\boldsymbol{T}} = \vartheta \left(\boldsymbol{B}_{\mathcal{N}_t} - \boldsymbol{I} \right) \tag{2.88}$$

$$\overset{\tilde{\nabla}}{\boldsymbol{B}}_{\mathcal{N}_t} = -\tilde{\boldsymbol{T}} \tag{2.89}$$

where we used the small-strain assumption (2.86) in (2.80). These equations are equivalent to the Oldroyd-B model that was derived previously, cf. (2.7) and (2.17). This can be demonstrated by eliminating $\tilde{\boldsymbol{T}}$ from (2.88)–(2.89) and using the fact that $\overset{\tilde{\nabla}}{\boldsymbol{I}} = 2\,\tilde{\boldsymbol{D}}$.

The present derivation has shown that the elastic contribution to the stress, modulo a constant isotropic tensor, is proportional to the left Cauchy–Green tensor associated with the elastic deformation of the material from a natural configuration. Rather than the (elastic) stress, the left Cauchy–Green tensor appears to be the more fundamental quantity and thus is more appropriate as a state variable.

In the next section. we derive the Oldroyd-B equations from kinetic theory by considering the motion of polymer molecules. This derivation will supply us with a different kinematic intepretation of the state variables.

2.4 Kinetic theory

2.4.1 Introduction

Kinetic theory has proven immensely successful in modelling ideal gases. In the classical theory, one assumes a system of N particles, each representing a gas molecule. One then derives an evolution equation equation for the probability distribution function that fixes the positions and velocities of any $0 < s < N$ particles, but the evolution equation depends on the $(s + 1)$ particle distribution. The resulting set of equations are exact and are known as the Bogoliubov–Born–Green–Kirkwood–Yvon (BBGKY) hierarchy.[134,135] In order to obtain useful relations and quantities from the hierarchy, such as closed evolution equations at the continuum-scale, it is necessary to make significant simplifications. The most relevant of these simplifications arises in the Boltzmann gas limit (BGL). The BGL is described by $N \to \infty$ with m, $\sigma \to 0$ such that Nm and $N\sigma^2$ are non-zero finite constants,[134] and where m is the mass of a molecule and σ is the characteristic range of interparticle forces. With appropriate approximations in this limit and additional assumptions regarding particle collisions, one can derive the celebrated Boltzmann equation, a closed evolution equa-

tion for the single particle distribution function.[134,135] A solution to the Boltzmann equation is then sought in terms of a perturbation expansion in the normalized collision time-scale. The first–order truncation of the solution leads to the Navier-Stokes equations.[135]

A kinetic theory for viscoelastic fluids, specifically polymer solutions, can also be constructed.[75] As with the Newtonian case, significant assumptions are generally required to arrive at closed equations at the continuum-scale. We will outline the general assumptions required to derive the Oldroyd-B and similar equations first before proceeding to the mathematical details, which is based on the development in standard sources.[75,104,136] The presentation below will necessarily be adumbrated.

Polymer solutions consist of polymers dissolved in a good solvent. Individual polymer molecules are generally much larger than the solvent molecules; a polymer molecule consists of a linear sequence of individual monomers, each of which is comparable in size to a solvent molecule, or larger. The number of monomers varies widely but is not uncommonly $\sim 10^5$ or more.[137] Therefore, the large-scale variations in the solvent can be approximated as a continuum at length scales relevant to the polymer. The effect of the solvent on the polymer can then be attributed to two components: the random bombardment of the large polymer molecule by solvent molecules, and a drag force that arises because of a non-zero velocity of the polymer molecule.[75] The kinetic theory problem reduces to studying the coordinated behaviour of a large number of polymer molecules experiencing random fluctuations in a solvent bath.

Polymer solutions may be characterized by their number density in a solution as dilute, semidilute or concentrated. In dilute polymer solutions, the polymer-polymer interaction is weak enough that any physical property can be expressed as a virial expansion, an expansion in the polymer density. As the polymer density is increased, the intermolecular interactions increase, molecular fluctuations decrease and the polymer volume fraction increases. In semidilute solutions, the intermolecular interactions become significant but the molecular fluctuations cannot be ignored and polymer volume fraction remains small.[136] As the density is increased further, we obtain concentrated polymer solutions: solutions that can be described using mean field theory because the molecular fluctuations become negligible.[136] In what follows, we assume the polymers are dilute in the solution. The dilute solution assumption becomes invalid when the polymers begin to overlap, i.e when $n(4\pi R_g^3/3) \approx 1$ where n is the average number of molecules in a unit volume and R_g is the radius of gyration of the polymer molecule. This relation can be used to show that the polymer density where the dilute solution assumption fails is proportional to $M^{-4/5}$, where M is the molecular weight.[136] Dilute polymer solutions popular in drag reduction applications have polymer concentrations that are typically in the range from 10 to 100 parts per million by weight.[138]

An individual polymer molecule in a dilute solution bath is shown in figure 2.2. The very large number of monomers in a polymer chain makes the direct modelling of such molecules a difficult exercise. Kramer[75,139] approached this problem by dividing

the polymer molecule into submolecules, each of which contained a fixed number of monomers. The length of each submolecule is obtained by dividing the polymer contour length by the number of submolecules in the chain. Each submolecule is replaced with a rod of equivalent length, and the rods are connect using beads that are freely rotating joints. The behaviour of the polymer in solution is then described by the dynamics of this bead-rod chain experiencing Stokes' drag due to the ambient solution. The equilibrium distribution of the end-to-end vector $\boldsymbol{r}$, a vector connecting the first and last bead in the chain, can then be shown to be Gaussian.[75,136] Using this distribution and statistical mechanics, it is straightforward to show that the force experienced by the polymer molecule is then proportional to the end-to-end vector, which is simply Hooke's spring law. With a different statistical mechanics approach, one may also derive a nonlinear finite-extensibility force law: Hookean for small extensions and divergent at large extensions.[102] This result, that the polymer behaves like a spring, suggests that it may be more appropriate to replace the rods with springs. This was the approach followed by Rouse,[140] and later by Zimm,[141] both of whom used Hookean springs.

As a further approximation to make a continuum level model feasible, we replace the entire polymer chain with a dumbbell: two beads connected by a spring, as illustrated in figure 2.2. The dumbbell is in a solvent bath and is thus subjected to random fluctuations. The probability distribution function describing the system is time-dependent and is a function of the positions and velocities of the two beads. We

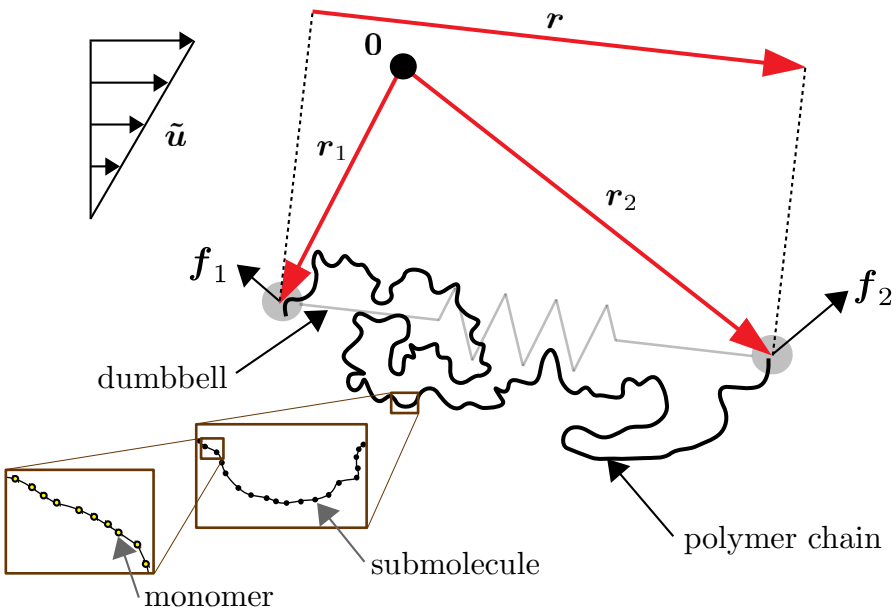

Figure 2.2: The polymer molecule, and dumbell model.

consider partially smoothed positions and velocities of the two beads, such that the resulting probability distribution function is only a function of time and positions of the two beads.

2.4.2 The distribution function

As shown in figure 2.2, the (smoothed) position and force on the k-th bead are denoted $\boldsymbol{r}_k$ and $\boldsymbol{f}_k$, respectively. Newton's second law for each bead then reads

$$\tilde{\boldsymbol{f}}_k = m_k \frac{\mathrm{d}^2 \tilde{\boldsymbol{r}}_k}{\mathrm{d}\tilde{t}^2}, \qquad k = 1, 2 \tag{2.90}$$

where m_k is the mass of the k-th bead. Repeated indices in (2.90) are not to be summed over. We now make the additional assumption that the inertia of the beads is negligible so that the right hand-side of (2.90) can be set to $\mathbf{0}$. We can then write the force balance on each bead as follows

$$\underbrace{\tilde{\boldsymbol{f}}_k}_{\substack{\text{force on}\\ k\text{-th bead}}} = \underbrace{\zeta_D\left(\tilde{\boldsymbol{u}}(\tilde{\boldsymbol{r}}_k) - \frac{\mathrm{d}\tilde{\boldsymbol{r}}_k}{\mathrm{d}\tilde{t}}\right)}_{\substack{\text{drag based on relative}\\ \text{velocity of bead}}} + \underbrace{(-1)^{k+1}\tilde{\boldsymbol{f}}_s}_{\text{spring force}} + \underbrace{\tilde{\boldsymbol{f}}_b(\tilde{\boldsymbol{r}}_k)}_{\substack{\text{molecular}\\ \text{fluctuations}}} = \mathbf{0}, \qquad k = 1, 2 \tag{2.91}$$

where ζ_D is the Stokes' drag coefficient, $\tilde{\boldsymbol{u}}(\tilde{\boldsymbol{r}}_k)$ is the solvent velocity at the k-th bead, the spring force $\tilde{\boldsymbol{f}}_s$ is not specified yet but it is not necessarily Hookean, and finally the force due to molecular fluctuations $\tilde{\boldsymbol{f}}_b(\tilde{\boldsymbol{r}}_k)$ is partially smoothed Brownian motion, in the sense described previously. In particular, if we assume that the distribution of velocities is Maxwellien,[75] then the force due to molecular fluctuations is given by

$$\tilde{\boldsymbol{f}}_b(\boldsymbol{s}) = -k_B T \tilde{\boldsymbol{\nabla}}_{\boldsymbol{s}} \log \Psi \tag{2.92}$$

where $\Psi = \Psi(\tilde{\boldsymbol{r}}_1, \tilde{\boldsymbol{r}}_2, t)$ is a type of reduced probability distribution function, since it does not depend on the velocities. We now further assume that the probability distribution does not depend on the absolute positions but only the relative positions of the beads. We thus have $\Psi(\tilde{\boldsymbol{r}}_1, \tilde{\boldsymbol{r}}_2, t) = \Psi(\tilde{\boldsymbol{r}}, t)$, where $\tilde{\boldsymbol{r}} \equiv \tilde{\boldsymbol{r}}_2 - \tilde{\boldsymbol{r}}_1$ is the end-to-end

vector. The smoothed Brownian motion force then reduces to

$$\tilde{\boldsymbol{f}}_b(\tilde{\boldsymbol{r}}_k) = (-1)^{k+1} k_B T \tilde{\boldsymbol{\nabla}}_{\tilde{\boldsymbol{r}}} \log \Psi, \qquad k = 1, 2 \tag{2.93}$$

Subtracting the equation for $k = 1$ in (2.91) from the equation for $k = 2$ and substituting (2.93) yields

$$\frac{\mathrm{d}\tilde{\boldsymbol{r}}}{\mathrm{d}\tilde{t}} = \tilde{\boldsymbol{\nabla}}^{\mathsf{T}} \tilde{\boldsymbol{u}} \cdot \tilde{\boldsymbol{r}} - \frac{2}{\zeta_D} \left[k_B T \tilde{\boldsymbol{\nabla}}_{\tilde{\boldsymbol{r}}} \log \Psi + \tilde{\boldsymbol{f}}_s \right]. \tag{2.94}$$

where we used the assumption that the velocity field is locally smooth and therefore can be represented by a linear approximation

$$\tilde{\boldsymbol{u}}(\tilde{\boldsymbol{r}}_2) = \tilde{\boldsymbol{u}}(\tilde{\boldsymbol{r}}_1) + \tilde{\boldsymbol{\nabla}}^{\mathsf{T}} \tilde{\boldsymbol{u}} \cdot \tilde{\boldsymbol{r}}. \tag{2.95}$$

The probability distribution function Ψ is conserved and therefore it satisfies the continuity equation

$$\left(\frac{\partial \Psi}{\partial \tilde{t}} \right)_{\tilde{\boldsymbol{r}}} + \tilde{\boldsymbol{\nabla}}_{\tilde{\boldsymbol{r}}} \cdot \left(\frac{\mathrm{d}\tilde{\boldsymbol{r}}}{\mathrm{d}\tilde{t}} \Psi \right) = 0. \tag{2.96}$$

Substituting the expression for the bead velocity (2.94) in the conservation law (2.96)

yields an evolution equation for Ψ

$$\left(\frac{\partial \Psi}{\partial \tilde{t}}\right)_{\tilde{\boldsymbol{r}}} + \tilde{\boldsymbol{\nabla}}_{\tilde{\boldsymbol{r}}} \cdot \left[\left(\tilde{\boldsymbol{r}} \cdot \tilde{\boldsymbol{\nabla}} \tilde{\boldsymbol{u}} - \frac{2}{\zeta_D} \tilde{\boldsymbol{f}}_s - \frac{2k_B T}{\zeta_D} \tilde{\boldsymbol{\nabla}}_{\tilde{\boldsymbol{r}}} \log \Psi\right) \Psi\right] = 0. \tag{2.97}$$

2.4.3 Stress and polymer conformation

Kramers[75,139] and others[142] have shown that the stress tensor for the dumbbell model can be written as

$$\tilde{\boldsymbol{\sigma}} = -\tilde{p}\boldsymbol{I} + \eta_s(2\tilde{\boldsymbol{D}}) + n\langle \tilde{\boldsymbol{r}} \tilde{\boldsymbol{f}}_s \rangle_\Psi - n k_B T \boldsymbol{I} \tag{2.98}$$

where n is the polymer number density, and $\langle \cdot \rangle_\Psi$ denotes the expectation obtained using the probability distribution function Ψ. The expression (2.98) can be easily obtained by evaluating the contribution of the spring force to the stress on the fluid. For a Hookean spring, $\tilde{\boldsymbol{f}}_s \sim \tilde{\boldsymbol{r}}$ and therefore we are interesting in the quantity $\langle \tilde{\boldsymbol{r}} \tilde{\boldsymbol{r}} \rangle_\Psi$. The latter is the polymer conformation.

Multiplying (2.97) by $\tilde{\boldsymbol{r}} \tilde{\boldsymbol{r}}$ and integrating over the probability event space $\Omega_{\tilde{\boldsymbol{r}}}$ gives

$$\int_{\Omega_{\tilde{\boldsymbol{r}}}} \tilde{\boldsymbol{r}} \tilde{\boldsymbol{r}} \left(\frac{\partial \Psi}{\partial \tilde{t}}\right)_{\tilde{\boldsymbol{r}}} + \tilde{\boldsymbol{r}} \tilde{\boldsymbol{r}} \tilde{\boldsymbol{\nabla}}_{\tilde{\boldsymbol{r}}} \cdot \left[\left(\tilde{\boldsymbol{r}} \cdot \tilde{\boldsymbol{\nabla}} \tilde{\boldsymbol{u}} - \frac{2}{\zeta_D} \tilde{\boldsymbol{f}}_s - \frac{2k_B T}{\zeta_D} \tilde{\boldsymbol{\nabla}}_{\tilde{\boldsymbol{r}}} \log \Psi\right) \Psi\right] \mathrm{d}V_{\tilde{\boldsymbol{r}}} = \boldsymbol{0} \tag{2.99}$$

For a second–order tensor $\boldsymbol{A}$ and a vector $\boldsymbol{q}$, we have

$$\begin{aligned}
[\tilde{\boldsymbol{r}}\tilde{\boldsymbol{r}}\tilde{\boldsymbol{\nabla}}_{\tilde{\boldsymbol{r}}} \cdot (\boldsymbol{q} \cdot \boldsymbol{A}\Psi)]_{ij} &= [\tilde{\boldsymbol{\nabla}}_{\tilde{\boldsymbol{r}}} \cdot (\tilde{\boldsymbol{r}}\tilde{\boldsymbol{r}}\boldsymbol{q} \cdot \boldsymbol{A}\Psi)]_{ij} - \frac{\partial}{\partial r_k}(r_i r_j) q_l A_{lk}\Psi \\
&= [\tilde{\boldsymbol{\nabla}}_{\tilde{\boldsymbol{r}}} \cdot (\tilde{\boldsymbol{r}}\tilde{\boldsymbol{r}}\boldsymbol{q} \cdot \boldsymbol{A}\Psi)]_{ij} - (\delta_{ik} r_j + r_i \delta_{jk}) q_l A_{lk}\Psi \\
&= [\tilde{\boldsymbol{\nabla}}_{\tilde{\boldsymbol{r}}} \cdot (\tilde{\boldsymbol{r}}\tilde{\boldsymbol{r}}\boldsymbol{q} \cdot \boldsymbol{A}\Psi)]_{ij} - (A^{\mathsf{T}}_{il} q_l r_j + r_i q_l A_{lj})\Psi
\end{aligned} \tag{2.100}$$

We also have

$$\begin{aligned}
(\tilde{\boldsymbol{r}}\tilde{\boldsymbol{r}}\tilde{\boldsymbol{\nabla}}_{\tilde{\boldsymbol{r}}} \cdot \tilde{\boldsymbol{\nabla}}_{\tilde{\boldsymbol{r}}}(\log\Psi)\Psi)_{ij} &= r_i r_j \frac{\partial}{\partial r_k}\left(\frac{\partial \log\Psi}{\partial r_k}\Psi\right) = r_i r_j \frac{\partial^2 \Psi}{\partial r_k \partial r_k} \\
&= \frac{\partial^2 (r_i r_j \Psi)}{\partial r_k \partial r_k} - 2\left[\frac{\partial (r_i \Psi)}{\partial r_j} + \frac{\partial (r_j \Psi)}{\partial r_i}\right] + 2\delta_{ij}\Psi
\end{aligned} \tag{2.101}$$

Using (2.100) and (2.101) in (2.99), and using the divergence theorem, yields an evolution equation for $\langle \tilde{\boldsymbol{r}}\tilde{\boldsymbol{r}} \rangle_{\Psi}$

$$\frac{1}{k_B T} \overset{\tilde{\boldsymbol{\nabla}}}{\langle \tilde{\boldsymbol{r}}\tilde{\boldsymbol{r}} \rangle_{\Psi}} = -\frac{4}{\zeta_D}\left(\frac{1}{2k_B T}\left(\langle \tilde{\boldsymbol{f}}_s \tilde{\boldsymbol{r}} \rangle_{\Psi} + \langle \tilde{\boldsymbol{r}} \tilde{\boldsymbol{f}}_s \rangle_{\Psi}\right) - \boldsymbol{I}\right) \tag{2.102}$$

where we assumed $\Psi = 0$ at the boundaries.

2.4.4 Model fluids

2.4.4.1 Oldroyd-B fluids

Now assume the spring force is Hookean,

$$\tilde{\boldsymbol{f}}_s = \tilde{\boldsymbol{f}}_s^{\text{Hooke}} = H\tilde{\boldsymbol{r}} \tag{2.103}$$

where H is a spring constant. Then the Cauchy momentum equation (2.1), Kramers stress relation (2.98), and (2.102) can be combined to yield the equations

$$\frac{\mathrm{D}\rho\tilde{\boldsymbol{u}}}{\mathrm{D}\tilde{t}} = -\tilde{\boldsymbol{\nabla}}\tilde{p} + \eta_s\tilde{\boldsymbol{\Delta}}\tilde{\boldsymbol{u}} + \eta_p\tilde{\boldsymbol{\nabla}}\cdot\tilde{\boldsymbol{T}} + \tilde{\boldsymbol{d}} \tag{2.104}$$

$$\tilde{\boldsymbol{T}} = \vartheta\left(\boldsymbol{C} - \boldsymbol{I}\right) \tag{2.105}$$

$$\overset{\tilde{\nabla}}{\boldsymbol{C}} = -\tilde{\boldsymbol{T}} \tag{2.106}$$

where $\boldsymbol{C}$ is the conformation tensor defined as

$$\boldsymbol{C} \equiv \frac{H}{k_B T}\langle\tilde{\boldsymbol{r}}\tilde{\boldsymbol{r}}\rangle_\Psi \tag{2.107}$$

and

$$\vartheta \equiv \frac{4H}{\zeta_D}, \quad \eta_p \equiv \frac{nk_BT\zeta_D}{4H}. \tag{2.108}$$

The equations (2.104)–(2.106) are the Oldroyd-B equations first derived in (2.17), and also in (2.87)–(2.89). The Oldroyd-B model derived from kinetic theory proposes that the positive–definite tensor associated with polymer deformation is the normalized average of the dyad obtained from the end-to-end vector describing the polymer.

The problem with the Oldroyd-B model that manifests with the divergent extensional viscosity (2.20) under an extensional flow arises because the Hookean spring force (2.103) is linear in the extension. As a result, there is no limit on how much the polymer can be extended. In reality, the polymer has a finite extensibility which is determined by the molecular structure.

2.4.4.2 FENE-P fluids

A popular variant on the Hookean spring that prevents infinite extension of the polymer is the finite extensibility nonlinear elastic (FENE) spring. The FENE spring force is given by

$$\tilde{\boldsymbol{f}}_s^{\text{FENE}} = \frac{H}{1 - (\tilde{\boldsymbol{r}} \cdot \tilde{\boldsymbol{r}})/L_{\max}^2} \tilde{\boldsymbol{r}}. \tag{2.109}$$

The FENE spring force in (2.109) is an approximation of the exact finite extension force law, which involves the inverse Langevin function and can be derived using statistical mechanics.[75] The approximation was originally suggested by Warner[143] to avoid calculation of the inverse Langevin function. The force law well-approximates

the behaviour of finitely extensible polymer molecules;[75] the spring is Hookean for small extensions and diverges for larger extensions. We can derive continuum-scale equations for a polymer with such a spring force by setting $\tilde{\boldsymbol{f}}_s = \tilde{\boldsymbol{f}}_s^{\mathrm{FENE}}$ in (2.102). However, the nonlinearity of the spring law means that the continuum-scale evolution equations are not closed; they cannot be completely written only in terms of $\langle \tilde{\boldsymbol{r}}\tilde{\boldsymbol{r}} \rangle_\Psi$. A widely adopted approximation that leads to closure was introduced by Bird[144] who attributed the original idea to Peterlin[145]

$$\left\langle \tilde{\boldsymbol{f}}_s^{\mathrm{FENE}}\tilde{\boldsymbol{r}} + \tilde{\boldsymbol{r}}\tilde{\boldsymbol{f}}_s^{\mathrm{FENE}} \right\rangle_\Psi = \left\langle \frac{2H}{1-(\tilde{\boldsymbol{r}}\cdot\tilde{\boldsymbol{r}})/L_{\max}^2}\tilde{\boldsymbol{r}}\tilde{\boldsymbol{r}} \right\rangle_\Psi \tag{2.110}$$

$$\approx \frac{2H}{1-\langle \tilde{\boldsymbol{r}}\cdot\tilde{\boldsymbol{r}} \rangle/L_{\max}^2} \langle \tilde{\boldsymbol{r}}\tilde{\boldsymbol{r}} \rangle_\Psi . \qquad \text{(Peterlin approximation)} \tag{2.111}$$

Such a model is known as a FENE-Peterlin or FENE-P model. As before, using (2.111) in (2.1), (2.98), and (2.102), leads to (2.104) and (2.106), but $\tilde{\boldsymbol{T}}$ now reads:

$$\tilde{\boldsymbol{T}} = \vartheta \left[f(\mathrm{I}_{\boldsymbol{C}})\boldsymbol{C} - f(3)\boldsymbol{I} \right] \tag{2.112}$$

where

$$f(s) = \left(1 - \frac{s}{L_{\max}^2} \right)^{-1} . \tag{2.113}$$

The Peterlin approximation is not without controversy, since it can be shown to significantly alter the statistics of the polymer deformation.[146] In turbulent flows, large extensions are overestimated by the FENE-P model and the alignment of the polymers with the rate-of-strain tensor is weaker.[147] Direct numerical simulations of turbulent flows using the FENE-P model have also not quantitatively agreed with experiments.[82] However, the model qualitatively reproduces experiments and the full FENE model.[82,147] It has also been widely used to numerically study viscoelastic turbulence.[8,81,148,149] In this dissertation we will use direct numerical simulations (DNS) of the FENE-P model.

2.5 Discussion

In the previous two sections, we derived the Oldroyd-B model from a continuum thermomechanics framework, and also from kinetic theory. In both cases, the continuum-scale state variables are a velocity and a positive–definite tensor. However, the interpretation of the positive–definite tensor varies. The thermodynamics framework suggests that the positive–definite tensor is a left Cauchy–Green tensor $\boldsymbol{B}_{\mathcal{N}_t}$ representing the elastic deformation from a natural configuration, while the kinetic theory derivation suggests that the positive–definite tensor is the conformation tensor $\boldsymbol{C}$, the coarse-grained dyad formed from the end-to-end vector of the polymer molecule.

A key difference between the two approaches is that the continuum model constrains the determinant of the positive–definite tensor to be unity, which amounts to an incompressibility constraint on the elastic deformation. The version of the Oldroyd-B equations derived from the continuum approach are thus only valid in the small deformation limit. If they are used in flows where the elastic deformation is large, the volume will exceed unity. The model derived from kinetic theory, on the other hand, allows such deformations.

The difference between the two approaches arises because, in the kinetic theory, polymers are dumbbells and therefore have zero volume. Averaging over molecular realizations replaces the dumbbells with ellipsoids that have three independent stretches, and which thus have a volume. However, the ellipsoid itself does not consist of matter where the solvent cannot intrude but is rather a volume that encloses the characteristic molecular configurations. In this case, the volume of the ellipsoid represents the conformational probability associated with the molecular structure.[102] Thus, the solvent and polymer phases can overlap and the incompressibility of the fluid is unaffected by arbitrary polymer deformation. In the model derived using continuum thermomechanics, there is necessarily only a single phase with both viscous and elastic properties. The incompressibility condition on the velocity field is then intrinsically linked to the constraint on the determinant of the left Cauchy–Green tensor.

The kinetic theory approach provides us with a firm basis in the observed be-

haviour of molecules, and has been widely adopted in the study of viscoelastic turbulence. However, since molecular details are unavailable from the continuum-scale equations, physical interpretations of important quantities at this scale are frequently inaccessible. For example, for a nonlinear spring, the elastic energy is inaccessible at the continuum-scale because the averaging cannot be taken inside the nonlinear function representing the spring force. On the other hand, the continuum thermomechanics approach provides us with exact relations for elastic energy and also for elastic dissipation. The role played by these two quantities in the dynamics is manifestly clear from the derivation of the equations. Also, the interpretation of the positive–definite tensor as a left Cauchy–Green tensor relates a macroscopic state to an actual physical deformation, rather than a statistical object based on an ensemble of realizations. However, the models developed using the Rajagopal–Srinivasa formalism are speculative in that they require specification of the elastic energy and dissipation, and are also based on a 'principle' of maximizing rate-of-dissipation. Moreover, the models have not been validated against existing experiments in viscoelastic turbulence so their faithfulness to observed phenomena is not firmly established yet.

For the purposes of the present dissertation, we require an interpretation of the positive–definite tensor that provides us with the maximum latitude to analyse viscoelastic turbulence. We thus treat the conformation tensor $\boldsymbol{C}$ as a left Cauchy–Green tensor but one associated with the deformation of the polymer from the thermodynamic equilibrium state, and not with an elastic deformation from a natural con-

figuration in the sense of Rajagopal and Srinivasa.[116] Furthermore, we assume that the fluid is a two-component material rather than a two-phase material, where we distinguish phases and components as does Woods:[150] phases are spatially distinct parts of the material while components are spatially overlapping subsystems that are allowed to have their own distinct thermodynamic variables. With such an assumption, the determinant of the conformation tensor is not restricted to be unity, which is consistent with the zero volume dumbbell assumption in kinetic theory.

The view of the conformation tensor described above is thermodynamically tenable; in the Beris–Edwards bracket formalism, a generic second–order tensor representing the microstructure, called a 'structure tensor' and without a particular physical interpretation, can be used to generate thermodynamically consistent evolution equations.[102] The only restriction on the structure tensor is that it must admit an interpretation as a Cauchy–Green tensor (or its inverse) in the small deformation limit (A. N. Beris, personal communication, January 26, 2018). This formalism can be used to derive most viscoelastic models, including all the ones listed in Table 2.1. As such, Beris and Edwards have freely interpreted the second–order positive–definite tensor that arises in the modelling of viscoelastic flows as both a Cauchy–Green tensor as well as a conformation tensor.[102]

An additional point of departure from the kinetic theory occurs on the continuum-scale: the conformation tensor is continuous whereas the polymer molecules are dilute in the solvent. Therefore 'polymer molecules' in the kinetic theory do not have any

corresponding quantity at the continuum-scale. However, it often convenient to interpret the conformation tensor at a single point in space in terms of a deformation ellipsoid (or cuboid) whose eigenvalues and eigenvectors, respectively, represent the squared principle stretches and principles axes of the polymer. We may identify a continuum-scale polymer 'molecule' with this deformation ellipsoid.

Finally, we note that the present interpretation of the conformation tensor is not without precedent; it has been used to model suspensions and colloids,[151–154] although the determinant in these cases is restricted to be unity.

Chapter 3

The geometric decomposition

3.1 Introduction

In this chapter, we address the following questions that are relevant to viscoelastic turbulent flows: (a) given a turbulent flow whose dynamics are partially governed by state variables that are positive-definite tensors representing material deformation, what is an appropriate method to decompose the flow into a mean, or nominal, component and a deviation about that mean that preserves the physical character of the state variables? and (b) are there corresponding scalar measures of the turbulence associated with these positive-definite state variables? The conformation tensor is the relevant positive-definite state variable in viscoelastic turbulence. As mentioned in the introduction, a complete physical description of viscoelastic turbulence requires characterization of both the velocity, $\boldsymbol{u}$, and the conformation tensor, $\boldsymbol{C}$, which to-

gether form the state variables.

In chapter 2, we showed that the conformation tensor affects the velocity field through the polymer stress, $\boldsymbol{T} = \boldsymbol{T}(\boldsymbol{C})$, while gradients in the velocity field are responsible for polymer stretching. Characterizing the mean polymer stress, or stress deficit, was the focus of early work because it was found to be necessary for closing the mean momentum balance.[155] A non-vanishing stress deficit suggests the possibility of maintaining a turbulent velocity profile in the absence of Reynolds stresses, in which case the polymer dynamics would sustain turbulence. Experiments[156] showed that a turbulent mean profile can, indeed, be maintained in the near absence of Reynolds stresses in channel flow. However, the polymer deformation itself is not readily accessible experimentally. Therefore, much of the work in understanding the mechanisms that lead to the behaviour cited above has resorted to analytical treatments or direct numerical simulations (DNS), which we will briefly review below.

The main approach to analyse the polymer dynamics has been to utilize the statistics of the polymer forces and torques, or the normal stresses. The polymer force is the divergence of the polymer stress and the polymer torque is the curl of the polymer force. For example, de Angelis *et al.*[157] and Dubief *et al.*[149] showed that cross-stream polymer force in turbulent channel flow counteracts spanwise variations in the velocity while enhancing streamwise advection, consistent with drag-reducing behaviour. The polymer torque acts in lockstep with the polymer force and counteracts streamwise vortices. It also inhibits generation of the heads of hairpin vortices.[158,159] Recent

theoretical work proposed a vorticity–polymer torque formulation of the linearised governing equations and used it to reveal a reverse Orr mechanism for turbulence production in viscoelastic parallel shear flows.[105,160] Min and co-authors,[86,87] on the other hand, studied viscoelastic turbulent channel flow but used the elastic energy, defined there as proportional to the sum of the normal polymer stresses, to posit a theory of drag reduction that relied on an active exchange of elastic and kinetic energies in the flow.

A more appropriate quantity to probe the polymer deformation, and one that is also a state variable, is the conformation tensor $\boldsymbol{C}$ itself. The trace of $\boldsymbol{C}$, denoted here as tr $\boldsymbol{C}$, is commonly used in the literature to analyse $\boldsymbol{C}$ since it is equal to the sum of its principal stretches and is therefore a measure of the polymer deformation. For example, Sureshkumar *et al.*[81] considered first–order statistics of tr $\boldsymbol{C}$ in their pioneering paper on the DNS of viscoelastic turbulent channel flows. The quantity tr $\boldsymbol{C}$ is frequently used because it is proportional to the elastic energy in purely Hookean constitutive models of the polymers.[87,102] However, it is often not a sufficiently complete descriptor of the polymer deformation; even if tr $\boldsymbol{C}$ is held constant, the polymer may undergo a volumetric deformation.

Housiadas and Beris[161] evaluated tr $\boldsymbol{C}$ for a wide range of flow parameters in a viscoelastic turbulent channel flow and found a surprising result for certain parameter ranges: the mean of tr $\boldsymbol{C}$ can increase with increasing elasticity without a commensurate effect on the mean velocity profile. A similar trend was also reported by Xi and

Graham[162] in minimal flow unit simulations. This trend is not inconsistent with the mean momentum balance as the mean of tr $\boldsymbol{C}$ in turbulent channel flows can increase without effecting the mean velocity profile; the time-average of (2.29) yields

$$\frac{\mathrm{d}\overline{p}}{\mathrm{d}x} = \frac{\beta}{Re}\frac{\mathrm{d}^2\overline{u}}{\mathrm{d}y^2} + \frac{1-\beta}{Re}\frac{\mathrm{d}\overline{T}_{xy}}{\mathrm{d}y} - \frac{\mathrm{d}\overline{u'v'}}{\mathrm{d}y} \tag{3.1}$$

where we assumed the geometry described in §1.3.1 and overlines indicate time-averages. If we assume that finite-extensibility effects are only weakly dependent on elasticity, we see that the behaviour arises because the (mean) stress deficit is not a function of any of the normal components of $\boldsymbol{C}$. The normal components of $\boldsymbol{C}$ do affect the mean momentum balance through the dynamical coupling between the different components of $\boldsymbol{C}$, but this relationship cannot be captured by tr $\boldsymbol{C}$. The situation described above highlights the importance of simultaneously considering all of the components of $\boldsymbol{C}$ in order to arrive at a complete picture of the polymer deformation and its effect on the velocity field. Additionally, mean quantities are in themselves insufficient descriptors of the fluctuating polymer deformation; higher-order statistical quantities associated with $\boldsymbol{C}$ are required to describe the fluctuations and their deviation away from the mean.

The fluctuating conformation tensor, $\boldsymbol{C}'$, and its various moments provide one method to obtain pertinent higher-order statistical descriptions of the full conformation tensor, $\boldsymbol{C}$. The tensor $\boldsymbol{C}'$ is obtained by subtracting the mean conformation

tensor from $\boldsymbol{C}$, in analogy with the Reynolds decomposition of $\boldsymbol{u}$ in (1.1). However, this fluctuating tensor is not guaranteed to be physically realizable; at least one realization of $\boldsymbol{C}'$ implies negative material deformation since it is guaranteed to lose positive-definiteness ($\mathrm{tr}\,\boldsymbol{C}'$ must be ≤ 0 for at least one sample pulled from a statistical ensemble). Furthermore, it is not clear which scalar functions of $\boldsymbol{C}'$ provide mathematically consistent measures of the turbulence intensity associated with $\boldsymbol{C}$.

Although $\boldsymbol{C}'$ is not a physical conformation tensor, it can still be used for modelling Reynolds-averaged quantities in turbulence that do not necessarily require physically realizable fluctuating quantities. Indeed, it has been used with varying degrees of success in recent work to develop turbulence models[92–94,163] and to quantify subgrid stress contributions in Large-Eddy Simulations (LES).[95] However, characterizing the polymer fluctuations using physically meaningful quantities is advantageous in that physical interpretations aid in modelling and provide a greater understanding of mechanism.

A physically motivated description of the velocity and conformation tensor field can be obtained using Karhunen-Loève or proper orthogonal decomposition (POD), as recently shown by Wang *et al.*[96] A POD is a global decomposition of a field quantity that yields an orthonormal basis that is optimally ordered in the sense of the best representation of the Euclidean norm (details can be found in standard texts such as Reference 164). For the velocity field this norm is the square–root of the kinetic energy but in a straightforward POD of the conformation tensor field the norm is not

directly related to the elastic energy. Wang *et al.*showed that a POD of the square–root of $\boldsymbol{C}$ instead ensures best representation in terms of the elastic energy. Their approach crucially assumed that tr $\boldsymbol{C}$ is proportional to the elastic energy. When this assumption is satisfied, their approach provides a valuable tool to extract the spatial structure of the dominant energetic components of viscoelastic turbulence. One can also use the individual modes to construct positive-definite tensors that represent modal polymer deformation, since the POD basis is orthogonal with respect to a Frobenius inner product integrated over the spatial domain. However, these tensors cannot be used to construct a local decomposition of the conformation tensor into mean and fluctuating components because the sum of squares is not equal to the square of the sum — the cross contributions of the tensors only vanish when we take the trace and integrate over the spatial domain. Reynolds decomposing the square–root of the conformation tensor is a local approach in which the cross contribution similarly does not vanish instantaneously.

In order to motivative our proposed formalism, we consider the following analogue encountered in the study of the stretching of material lines in turbulence.[165] In this case, the normalized squared length of a material line, $\ell^2(t) > 0$, serves as the scalar analogue of $\boldsymbol{C}$. Since material lines cannot vanish, $\ell^2 \neq 0$. Let us assume that a statistically stationary state is possible and that $\langle \ell^2 \rangle$ is then the expected value of the squared length of a material line. A Reynolds decomposition of $\ell^2 = \langle \ell^2 \rangle + (\ell^2)'$ yields a fluctuation $(\ell^2)'(t)$ that is not always positive, which implies a negative nor-

malized squared length. One may, for the sake of argument, side-step the physical ambiguity implied by the negative squared length by considering only $|(\ell^2)'|$ but this does not solve the problem of asymmetry of $|(\ell^2)'|$ with respect the direction of the stretching; when $\ell^2/\langle\ell^2\rangle \in (1,\infty)$, the material line is expanded with respect to $\langle\ell^2\rangle$ and when $\ell^2/\langle\ell^2\rangle \in (0,1)$ it is compressed, which means that similarly probable states (expansion and contraction) would be described by fluctuations with very different magnitudes. A meaningful way to study the fluctuations in ℓ^2 is by instead considering $\log(\ell^2/\langle\ell^2\rangle)$. Our goal is to generalize this latter type of construction to the conformation tensor, where one must take into account the tensorial nature of $\boldsymbol{C}$ which encodes directional information not included in a scalar such as ℓ^2.

Following the scalar case described above, one approach to evaluate fluctuations in $\boldsymbol{C}$ is to use $\log \boldsymbol{C}$, in lieu of $\boldsymbol{C}$, where log here refers to the matrix logarithm. This approach is appealing because the logarithm of a positive-definite matrix is a symmetric matrix and the set of symmetric matrices form a vector space, which therefore allows for a Reynolds decomposition analogous to that of $\boldsymbol{u}$, i.e.

$$\log \boldsymbol{C} = \langle \log \boldsymbol{C} \rangle + (\log \boldsymbol{C})',$$

where $\langle \log \boldsymbol{C} \rangle$ is the expected value of $\log \boldsymbol{C}$. Such a decomposition has not been previously used to characterize fluctuations in $\boldsymbol{C}$. However, $\log \boldsymbol{C}$ itself has been an object of some interest in the viscoelastic literature. Fattal and Kupferman[166]

introduced an approach for simulating viscoelastic flows that relied on evolving log $\boldsymbol{C}$ instead of $\boldsymbol{C}$. Fattal and Kupferman and also Hulsen *et al.*[167] then provided closed-form evolution equations for log $\boldsymbol{C}$ which explicitly depended on both log $\boldsymbol{C}$ as well as its spectral decomposition. Recently, Knechtges and co-authors[168,169] were able to eliminate the explicit dependence on the spectral decomposition but at the expense of either imposing restrictions on the spectral radius of $\boldsymbol{C}$ or introducing Dunford–Taylor type integrals into the equations.

At least two additional difficulties arise in using log $\boldsymbol{C}$. The first is that the expected value of $\boldsymbol{C}$ is not equal to $\mathrm{e}^{\langle \log \boldsymbol{C} \rangle}$. This fact implies that evaluating the effect of the polymer stress on the mean momentum balance requires all statistical moments of log $\boldsymbol{C}$, even when the polymer stress is a linear function of $\boldsymbol{C}$. The second difficulty is that, in general, $\mathrm{e}^{\langle \log \boldsymbol{C} \rangle + (\log \boldsymbol{C})'} \neq \mathrm{e}^{\langle \log \boldsymbol{C} \rangle} \cdot \mathrm{e}^{(\log \boldsymbol{C})'}$ which means that there is no way to associate $(\log \boldsymbol{C})'$ with a conformation tensor or a physical polymer deformation. It also means that there is no clear way to separate the effect of $\langle \log \boldsymbol{C} \rangle$ in the fluctuating momentum balance.

In this chapter, we derive a new conformation tensor, $\boldsymbol{G}$, from a physical decomposition of the polymer deformation. Instead of the traditional additive decomposition

$$\boldsymbol{C} = \overline{\boldsymbol{C}} + \boldsymbol{C}', \tag{3.2}$$

the proposed geometric decomposition of $\boldsymbol{C}$ is given by

$$\boldsymbol{C} = \overline{\boldsymbol{F}} \cdot \boldsymbol{G} \cdot \overline{\boldsymbol{F}}^{\mathsf{T}}, \tag{3.3}$$

where $\overline{\boldsymbol{F}}$ is a deformation gradient tensor that can be calculated directly from a base-flow conformation tensor, $\overline{\boldsymbol{C}}$, such that $\overline{\boldsymbol{F}} \cdot \overline{\boldsymbol{F}}^{\mathsf{T}} = \overline{\boldsymbol{C}}$ (this choice will be justified in §3.2 below). This conformation tensor $\boldsymbol{G}$ is analogous to the scalar fluctuating quantity, $\ell^2/\langle \ell^2 \rangle$.

The tensor $\boldsymbol{G}$ represents turbulent deviations from the mean conformation tensor and can be analysed by resorting to the curved, Riemannian geometry of the manifold of positive-definite tensors. Interestingly, the first two moment invariants of the tensorial equivalent of $\log(\ell^2/\langle \ell^2 \rangle)$, i.e. $\log \boldsymbol{G}$, then appear as the relevant scalar measures for the fluctuations in $\boldsymbol{G}$. The first moment invariant is the logarithm of the ratio of the volume of $\boldsymbol{C}$ to the volume of $\overline{\boldsymbol{C}}$, where the volume of the conformation tensor refers to its determinant. The latter is proportional to the squared volume of the ellipsoid representing the coarse-grained polymer.[101] The determinant also corresponds to the sphericity or conformational probability of the molecular structure.[102] The second moment invariant is the metric distance of $\boldsymbol{G}$ away from $\boldsymbol{I}$ on the manifold of second–order positive-definite tensors. Finally, we also propose a measure of the anisotropy of $\boldsymbol{C}$ relative to the mean. This measure is equal to the metric distance of $\boldsymbol{G}$ to the closest isotropic tensor and was previously introduced to be used in magnetic

resonance imaging applications.[170]

We use the proposed framework and direct numerical simulations to gain insight into the dynamics of viscoelastic (FENE-P) turbulent channel flow. As outlined in the introduction of this dissertation, such flows are known to exhibit greatly reduced drag relative to an equivalent Newtonian flow, up to 60% or more reduction in some cases.[5,8] For such turbulent flows, separating the mean and fluctuating components of the conformation tensor in a physically consistent manner is an important step towards developing a quantitative understanding of the dynamics and isolating the relevant mechanisms at play.

The rest of this chapter is organised as follows: §3.2 presents the geometric decomposition of the conformation tensor, the associated evolution equations, and the relation between the decomposition and the elastic energy. A review of a geometry constructed specifically for the set of positive-definite tensors along with scalar measures of the polymer deformation based on this geometry and associated evolution equations are presented in §3.3. In §3.4, we present an example case study of viscoelastic turbulent channel flow to illustrate the concepts developed in this chapter.

In the rest of this chapter, as in the remainder of the dissertation, we assume constitutive equations of the form laid out in §2.2.

In the following (primarily in §3.2.1, 3.2.2, and 3.3.3), angled brackets, $\langle\cdot\rangle$, denote Reynolds spatio-temporal filtering (see appendix A in Reference 44 for more details),

i.e. for a variable $\phi(\boldsymbol{x}, t)$

$$\langle\phi\rangle(\boldsymbol{x}, t) = \int \phi(\boldsymbol{r}, \tau)\mathscr{G}(\boldsymbol{x} - \boldsymbol{r}, t - \tau)\mathrm{d}^3\boldsymbol{r}\,\mathrm{d}\tau \tag{3.4}$$

where $\mathscr{G}$ is a filtering kernel that is normalized so that $\langle 1\rangle = 1$, and is defined such that

$$\langle\langle f_1\rangle\rangle = \langle f_1\rangle, \qquad \langle\langle f_1\rangle f_2\rangle = \langle f_1\rangle\langle f_2\rangle \tag{3.5}$$

for any two integrable functions $f_1 = f_1(\boldsymbol{x}, t)$, $f_2 = f_2(\boldsymbol{x}, t)$. The mean of a quantity ϕ is then $\langle\phi\rangle$ and the n-th moment of ϕ is $\langle\phi^n\rangle$. The properties, (3.5), further imply that $\langle\mathscr{F}(\langle\phi\rangle)\rangle = \mathscr{F}(\langle\phi\rangle)$ for any analytic function, $\mathscr{F}$. While the example case study presented in §3.4 uses traditional Reynolds time-averaging, we present definitions using the filtering formulation since the approach is also expected to be valid more generally.

We use an overlined symbol within the present text to denote the nominal or base-flow quantity associated with the symbol, which may be distinct from the averaged or filtered quantity.

3.2 Decomposition of the conformation tensor

In the following, we will denote the general linear group of degree n, i.e. the set of $n \times n$ matrices with non-zero determinant, as $\mathbf{GL}_n$. We define the structure-preserving group action of $\mathbf{GL}_n$ on a set $\mathbf{W}_n \subseteq \mathbb{R}^{n \times n}$ as

$$[\boldsymbol{B}]_{\boldsymbol{A}} \equiv \boldsymbol{A} \cdot \boldsymbol{B} \cdot \boldsymbol{A}^{\mathsf{T}}. \tag{3.6}$$

where $\boldsymbol{A} \in \mathbf{GL}_n$ and $\boldsymbol{B} \in \mathbf{W}_n$ and by definition, we require $\mathbf{W}_n$ to be invariant under the action.

In chapter 2, we showed that the conformation tensor can be interpreted as a left Cauchy-Green tensor. We thus have

$$\boldsymbol{C} = \boldsymbol{F} \cdot \boldsymbol{F}^{\mathsf{T}} = [\boldsymbol{I}]_{\boldsymbol{F}}\,, \tag{3.7}$$

where $\boldsymbol{F}$ is the deformation gradient of the deformation with respect to the thermodynamic equilibrium, similar to that which was introduced in §2.3.2. If the spatial coordinates in the microstructure are given by $\boldsymbol{a} = \boldsymbol{a}(\boldsymbol{a}_0, t)$ where $\boldsymbol{a}_0$ are the material (or Lagrangian) coordinates, then $\boldsymbol{F} = \boldsymbol{\nabla}_{\boldsymbol{a}_0}\boldsymbol{a} = \partial\boldsymbol{a}/\partial\boldsymbol{a}_0$ so that a material line $\mathrm{d}\boldsymbol{a}_0$ deforms to $\mathrm{d}\boldsymbol{a} = \boldsymbol{F} \cdot \mathrm{d}\boldsymbol{a}_0$ under the deformation represented by $\boldsymbol{C}$. When $\boldsymbol{F}$ is restricted to be symmetric, (3.7) reduces to the factorization proposed by Balci *et*

al.[171] to improve numerical schemes for evolving the conformation tensor equations.

Let $\overline{\boldsymbol{C}}$ be a nominal conformation tensor such as the mean or laminar base-flow conformation tensor. The only requirement we impose on $\overline{\boldsymbol{C}}$ is that it must be defined according to a rule that ensures that $\boldsymbol{C}$ and $\overline{\boldsymbol{C}}$ cannot be arbitrarily rotated with respect to each other. In other words, if $\boldsymbol{C}$ transforms to $[\boldsymbol{C}]_{\boldsymbol{R}}$ then $\overline{\boldsymbol{C}}$ must transform to $\left[\overline{\boldsymbol{C}}\right]_{\boldsymbol{R}}$ for any $\boldsymbol{R} \in \mathbf{SO}_3$, where $\mathbf{SO}_n$ denotes the $n \times n$ special orthogonal group (or rotation matrices). Define $\overline{\boldsymbol{F}} \in \mathbf{GL}_3$ with $\det \overline{\boldsymbol{F}} > 0$ as the tensor that satisfies

$$\overline{\boldsymbol{C}} = \overline{\boldsymbol{F}} \cdot \overline{\boldsymbol{F}}^{\mathsf{T}}. \tag{3.8}$$

Such an $\overline{\boldsymbol{F}}$ is non-unique as it can be parameterized as

$$\overline{\boldsymbol{F}} = \overline{\boldsymbol{C}}^{\frac{1}{2}} \cdot \boldsymbol{R} \tag{3.9}$$

for any $\boldsymbol{R} \in \mathbf{SO}_3$ and where $\overline{\boldsymbol{C}}^{\frac{1}{2}}$ is the unique matrix square–root of $\overline{\boldsymbol{C}}$. Since the polar decomposition of $\overline{\boldsymbol{F}}$ and the square–root of $\overline{\boldsymbol{C}}$ (up to a $\pm$ sign change) are both unique, (3.9) is a parametrisation of all possible $\overline{\boldsymbol{F}}$. The tensor $\overline{\boldsymbol{F}}$ serves as the deformation gradient associated with the deformation from the thermodynamic equilibrium to the mean configuration.

The n-th power of a positive-definite tensor $\boldsymbol{A}$ is a tensor with the same eigenvectors as $\boldsymbol{A}$ and associated eigenvalues equal to the corresponding eigenvalues of $\boldsymbol{A}$ raised to the n-th power. In practice, since these n-th powers are isotropic functions

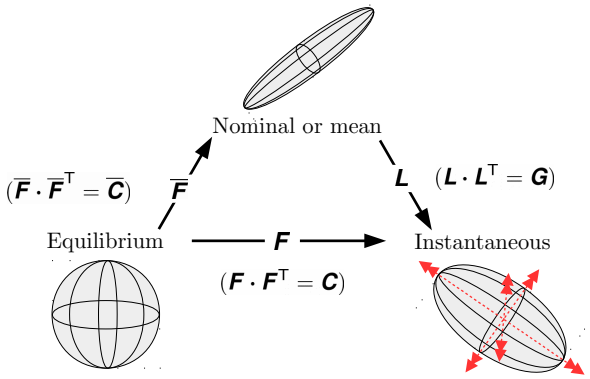

Figure 3.1: Schematic of the decomposition given in (3.10) and (3.12). The tensor $\boldsymbol{F}$ is a composition of $\overline{\boldsymbol{F}}$ and $\boldsymbol{L}$.

of $\boldsymbol{A}$, one need not explicitly perform a spectral decomposition to calculate them. For example, an application of the representation theorem can be used to express $\boldsymbol{A}^{\frac{1}{2}}$ and $\boldsymbol{A}^{-\frac{1}{2}}$ solely in terms of $\boldsymbol{A}$ and its invariants.[172,173]

Given a specific $\overline{\boldsymbol{F}}$ one satisfying (3.9), we then decompose the full deformation gradient tensor $\boldsymbol{F}$ about $\overline{\boldsymbol{F}}$ by considering successive transformations on the material line $\mathrm{d}\boldsymbol{a}_0$, i.e.

$$\mathrm{d}\boldsymbol{a} = \boldsymbol{F} \cdot \mathrm{d}\boldsymbol{a}_0 = \overline{\boldsymbol{F}} \cdot \boldsymbol{L} \cdot \mathrm{d}\boldsymbol{a}_0 \tag{3.10}$$

where $\boldsymbol{L} = \overline{\boldsymbol{F}}^{-1} \cdot \boldsymbol{F}$ is the fluctuating deformation gradient tensor. This decomposition is illustrated in figure 3.1. Thus, we have the following multiplicative decomposition of the deformation gradient

$$\boldsymbol{F} = \overline{\boldsymbol{F}} \cdot \boldsymbol{L}. \tag{3.11}$$

Substituting (3.11) in (3.7), we then arrive at a geometric decomposition of the conformation tensor

$$\boldsymbol{C} = [\boldsymbol{G}]_{\overline{\boldsymbol{F}}} = \overline{\boldsymbol{F}} \cdot \boldsymbol{G} \cdot \overline{\boldsymbol{F}}^{\mathsf{T}} \tag{3.12}$$

where $\boldsymbol{G} = \boldsymbol{L} \cdot \boldsymbol{L}^{\mathsf{T}}$ is a left Cauchy-Green tensor that is analogous to $\boldsymbol{C}$. Comparing (3.12) and (3.2), we can relate $\boldsymbol{C}'$ to $\boldsymbol{G}$ as follows

$$\boldsymbol{C}' = [\boldsymbol{G} - \boldsymbol{I}]_{\overline{\boldsymbol{F}}} \,. \tag{3.13}$$

From this point of view, the geometric decomposition provides a framework for interpreting the fluctuating tensor, $\boldsymbol{C}'$, obtained from the Reynolds decomposition.

Although a specific $\boldsymbol{G}$, and in particular only its set of principal axes, depends on $\boldsymbol{R} \in \mathbf{SO}_3$ chosen in (3.9), any function of only the invariants of $\boldsymbol{G}$ is independent of the choice of $\boldsymbol{R}$. This class of functions includes all objective scalar functions of $\boldsymbol{G}$; indeed, the scalar characterizations of the fluctuations that we develop later are also independent of $\boldsymbol{R}$. With respect to the full tensor, $\boldsymbol{G}$, we will later find that $\boldsymbol{R} = \boldsymbol{I}$ is a natural choice.

The decomposition of $\boldsymbol{F}$ into successive deformations, as in (3.10), is reminiscent of the multiplicative decomposition in large deformation theory that has found numerous applications over the last few decades.[174,175] For example, in elastoplasticity theory, the deformation gradient is decomposed into successive plastic and elastic

deformations with the objective of formulating constitutive laws for each of the deformations somewhat independently. Similar constructions are used in thermoelasticity and biomechanics.[176] Recently, Anand[177] used a multiplicative decomposition to derive equations for viscoelastic flows. A full review of that literature is beyond the scope of the present work but it suffices to note that the present case is greatly simplified because the constitutive laws are already specified and the focus is on the analysis of the polymer deformation due to turbulence.

We next present the equations for mean and fluctuating quantities in the geometric decomposition when the nominal conformation tensor is obtained by averaging or Reynolds-filtering.

3.2.1 Evolution equations: Reynolds-filtered case

In this section, we will consider the case when the nominal tensor is obtained using Reynolds-filtering. We choose to restrict our attention to Reynolds-filters but the development can be generalized to other filters, e.g. for applications in large-eddy simulations (LES). We thus have

$$\overline{\boldsymbol{C}} = \langle \boldsymbol{C} \rangle. \tag{3.14}$$

By the properties (3.5), the associated $\overline{\boldsymbol{F}}$ satisfies $\langle\overline{\boldsymbol{F}}\rangle = \overline{\boldsymbol{F}}$. Applying the averaging operation to (3.12) yields

$$\langle[\boldsymbol{G}]_{\boldsymbol{R}}\rangle = \boldsymbol{I} \tag{3.15}$$

where $\boldsymbol{R}(\boldsymbol{x}, t)$ is the rotation tensor field given in (3.9). Henceforth, we will restrict the rotation tensor field so that

$$\boldsymbol{R} = \langle\boldsymbol{R}\rangle. \tag{3.16}$$

By (3.5), we then have $\langle\boldsymbol{G}\rangle = \boldsymbol{I}$.

The Reynolds decomposition is applied to p and $\boldsymbol{u}$ while $\boldsymbol{C}$ is decomposed using (3.12) with $\overline{\boldsymbol{C}}$ defined according to (3.14). We thus have

$$p = \overline{p} + p', \quad \boldsymbol{u} = \overline{\boldsymbol{u}} + \boldsymbol{u}', \quad \boldsymbol{C} = [\boldsymbol{G}]_{\overline{\boldsymbol{F}}} \tag{3.17}$$

where $\overline{\boldsymbol{u}} = \langle\boldsymbol{u}\rangle$ and $\overline{p} = \langle p\rangle$ and the primes denote fluctuating quantities obtained via the Reynolds decomposition. In general, $\overline{p} = \overline{p}(\boldsymbol{x}, t)$, $\overline{\boldsymbol{u}} = \overline{\boldsymbol{u}}(\boldsymbol{x}, t)$, $\overline{\boldsymbol{C}} = \overline{\boldsymbol{C}}(\boldsymbol{x}, t)$. Note that $\overline{\boldsymbol{F}} \neq \langle\boldsymbol{F}\rangle$, in general.

Following the standard procedure, we can then decompose the momentum equa-

tion as follows

$$\partial_t \overline{\boldsymbol{u}} + \overline{\boldsymbol{u}} \cdot \boldsymbol{\nabla} \overline{\boldsymbol{u}} = -\boldsymbol{\nabla} \overline{p} + \frac{\beta}{Re} \Delta \overline{\boldsymbol{u}} + \frac{1-\beta}{Re} \boldsymbol{\nabla} \cdot \overline{\boldsymbol{T}} - \boldsymbol{\nabla} \cdot \overline{\boldsymbol{u}'\boldsymbol{u}'} \tag{3.18}$$

$$\partial_t \boldsymbol{u}' + \overline{\boldsymbol{u}} \cdot \boldsymbol{\nabla} \boldsymbol{u}' + \boldsymbol{u}' \cdot \boldsymbol{\nabla} \overline{\boldsymbol{u}} = -\boldsymbol{\nabla} p' + \frac{\beta}{Re} \Delta \boldsymbol{u}' + \frac{1-\beta}{Re} \boldsymbol{\nabla} \cdot \boldsymbol{T}' - \boldsymbol{\nabla} \cdot (\boldsymbol{u}'\boldsymbol{u}')' \tag{3.19}$$

where $\overline{\boldsymbol{T}} = \langle \boldsymbol{T} \rangle$, $\boldsymbol{T}' = \boldsymbol{T} - \overline{\boldsymbol{T}}$, $\overline{\boldsymbol{u}'\boldsymbol{u}'} = \langle \boldsymbol{u}'\boldsymbol{u}' \rangle$ and $(\boldsymbol{u}'\boldsymbol{u}')' = \boldsymbol{u}'\boldsymbol{u}' - \overline{\boldsymbol{u}'\boldsymbol{u}'}$.

The precise form of $\overline{\boldsymbol{T}}$, which appears in the mean momentum equation in (3.19), depends on the constitutive model used. In the Oldroyd-B model, $\overline{\boldsymbol{T}}$ only depends on $\overline{\boldsymbol{F}}$:

$$\overline{\boldsymbol{T}} = \frac{1}{Wi} \left(\overline{\boldsymbol{F}} \cdot \overline{\boldsymbol{F}}^{\mathsf{T}} - \boldsymbol{I} \right). \tag{3.20}$$

In models that are nonlinear in $\boldsymbol{C}$, the fluctuating tensor $\boldsymbol{G}$ cannot be eliminated or factored out of $\overline{\boldsymbol{T}}$. For example, in the FENE-P model, $\overline{\boldsymbol{T}}$ can be expressed as a series in which the dominant term is equal to (3.20) while the remaining terms depend on higher-order moments of $\boldsymbol{G}$. In general, we have

$$\overline{\boldsymbol{T}} = \frac{1}{Wi} \left[\langle \mu_0 \rangle \boldsymbol{I} + \overline{\boldsymbol{F}} \cdot \left\langle \mu_1 \boldsymbol{G} + \mu_2 \boldsymbol{G} \cdot \overline{\boldsymbol{F}}^{\mathsf{T}} \cdot \overline{\boldsymbol{F}} \cdot \boldsymbol{G} \right\rangle \cdot \overline{\boldsymbol{F}}^{\mathsf{T}} \right]. \tag{3.21}$$

Substituting (3.17) into (2.30) and applying the filtering operation $\langle \cdot \rangle$ defined in

(3.4) yields the following equations for $\overline{\boldsymbol{C}}$

$$\partial_t \overline{C}_{ij} + \overline{u}_k \partial_k \overline{C}_{ij} - \left(\overline{C}_{ik}\partial_k \overline{u}_j + \overline{C}_{jk}\partial_k \overline{u}_i\right) + \overline{T}_{ij} = -\partial_k \Big[\overline{F}_{ip}\overline{F}^{\mathsf{T}}_{qj} \underbrace{\langle G_{pq} u'_k \rangle}_{\text{(a)}}\Big] + \overline{F}_{ip}\overline{F}^{\mathsf{T}}_{qk} \underbrace{\langle G_{pq}\partial_k u'_j\rangle}_{\text{(b)}} + \overline{F}_{jp}\overline{F}^{\mathsf{T}}_{qk} \underbrace{\langle G_{pq}\partial_k u'_i\rangle}_{\text{(c)}}. \quad (3.22)$$

Term (a) is the averaged turbulent transport and terms (b), (c) describe the mean stretching and rotation of the polymer arising due to the gradients in the fluctuating velocity field. The right-hand side of the equation (3.22) is the cumulative effect of the turbulent fluctuations on the mean balance.

We can find the evolution equation for $\boldsymbol{G}$ by substituting (3.17) into (2.30):

$$\frac{\mathrm{D}\overline{\boldsymbol{F}}}{\mathrm{D}t} \cdot \boldsymbol{G} \cdot \overline{\boldsymbol{F}}^{\mathsf{T}} + \overline{\boldsymbol{F}} \cdot \frac{\mathrm{D}\boldsymbol{G}}{\mathrm{D}t} \cdot \overline{\boldsymbol{F}}^{\mathsf{T}} + \overline{\boldsymbol{F}} \cdot \boldsymbol{G} \cdot \frac{\mathrm{D}\overline{\boldsymbol{F}}^{\mathsf{T}}}{\mathrm{D}t} = 2\,\mathrm{sym}\left(\overline{\boldsymbol{F}} \cdot \boldsymbol{G} \cdot \overline{\boldsymbol{F}}^{\mathsf{T}} \cdot \boldsymbol{\nabla u}\right) - \boldsymbol{T}. \quad (3.23)$$

By multiplying on the left by $\overline{\boldsymbol{F}}^{-1}$ and on the right by $\overline{\boldsymbol{F}}^{-\mathsf{T}}$, the expression above can be re-written in a familiar form

$$\partial_t \boldsymbol{G} + \boldsymbol{u} \cdot \boldsymbol{\nabla G} = 2\,\mathrm{sym}\left(\boldsymbol{G} \cdot \boldsymbol{K}\right) - \boldsymbol{M} \quad (3.24)$$

where

$$\boldsymbol{E}(\boldsymbol{u}) \equiv \overline{\boldsymbol{F}}^{\mathsf{T}} \cdot \boldsymbol{\nabla u} \cdot \overline{\boldsymbol{F}}^{-\mathsf{T}} \tag{3.25}$$

$$\boldsymbol{M} \equiv \overline{\boldsymbol{F}}^{-1} \cdot \boldsymbol{T} \cdot \overline{\boldsymbol{F}}^{-\mathsf{T}}. \tag{3.26}$$

and where $\boldsymbol{K}$ is given by

$$\boldsymbol{K} \equiv \boldsymbol{E}(\boldsymbol{u}) - \left(\overline{\boldsymbol{F}}^{-1} \cdot \frac{\mathrm{D}\overline{\boldsymbol{F}}}{\mathrm{D}t} \right)^{\mathsf{T}}, \tag{3.27}$$

The quantity $\boldsymbol{K}$ represents the modified velocity gradient augmented with an additional stretching that arises due to the decomposition. Here, the tensors $\boldsymbol{E}$ and $\boldsymbol{M}$ serve as modified velocity gradient and polymer stress tensors. Note that the invariants of $\boldsymbol{\nabla u}$ and $\boldsymbol{E}$ coincide. The expression (3.24) is more general than considered here; an equivalent expression can be derived when the nominal tensor, $\overline{\boldsymbol{C}}$, is not equal to the mean conformation tensor.

Averaging (3.24), we obtain

$$\langle \boldsymbol{u}' \cdot \boldsymbol{\nabla G} \rangle = 2\,\mathrm{sym}\left(\overline{\boldsymbol{K}} + \langle \boldsymbol{G} \cdot \boldsymbol{K}' \rangle\right) - \overline{\boldsymbol{M}} \tag{3.28}$$

where we used the fact that $\langle \boldsymbol{G} \rangle = \boldsymbol{I}$ and we defined the mean and fluctuating parts

of $\boldsymbol{K}$ as follows

$$\overline{\boldsymbol{K}} \equiv \boldsymbol{E}(\overline{\boldsymbol{u}}) - \left[\overline{\boldsymbol{F}}^{-1} \cdot \left(\partial_t \overline{\boldsymbol{F}} + \overline{\boldsymbol{u}} \cdot \boldsymbol{\nabla} \overline{\boldsymbol{F}}\right)\right]^{\mathsf{T}}, \qquad \boldsymbol{K}' \equiv \boldsymbol{E}(\boldsymbol{u}') - \left(\overline{\boldsymbol{F}}^{-1} \cdot \boldsymbol{u}' \cdot \boldsymbol{\nabla} \overline{\boldsymbol{F}}\right)^{\mathsf{T}} \quad (3.29)$$

This expression is simply a different way of expressing the mean balance (3.22). Substituting in $\overline{\boldsymbol{K}}$ and $\boldsymbol{K}'$ we obtain

$$\overline{\boldsymbol{M}} = 2\,\mathrm{sym}\left\{\overline{\boldsymbol{E}} + \langle \boldsymbol{G} \cdot \boldsymbol{E}' \rangle - \left[\partial_t \overline{\boldsymbol{F}}^{\mathsf{T}} + (\overline{\boldsymbol{u}} + \langle \boldsymbol{G} \cdot \boldsymbol{u}' \rangle) \cdot \boldsymbol{\nabla} \overline{\boldsymbol{F}}^{\mathsf{T}}\right] \cdot \overline{\boldsymbol{F}}^{-\mathsf{T}}\right\} - \langle \boldsymbol{u}' \cdot \boldsymbol{\nabla} \boldsymbol{G} \rangle \quad (3.30)$$

where $\overline{\boldsymbol{E}} = \langle \boldsymbol{E} \rangle = \boldsymbol{E}(\overline{\boldsymbol{u}})$, $\boldsymbol{E}' = \boldsymbol{E} - \overline{\boldsymbol{E}} = \boldsymbol{E}(\boldsymbol{u}')$, $\overline{\boldsymbol{M}} = \langle \boldsymbol{M} \rangle$. The equation (3.30) shows that the mean modified stress, $\overline{\boldsymbol{M}}$, is a function of the mean velocity gradient, $\overline{\boldsymbol{E}}$, the mean stretching due to turbulent velocity gradients $\langle \boldsymbol{G} \cdot \boldsymbol{E}' \rangle$, and the turbulent advection of the fluctuating polymer deformation, $\langle \boldsymbol{u}' \cdot \boldsymbol{\nabla} \boldsymbol{G} \rangle$. Additionally, new terms appear due to the time-rate of change of $\overline{\boldsymbol{F}}$, and advection of $\overline{\boldsymbol{F}}$. There is a notational ambiguity in the expression (3.30) associated with the term representing advection of $\overline{\boldsymbol{F}}^{\mathsf{T}}$ because of the involvement of higher-order tensors. The ambiguity can be dispelled most clearly by using index notation

$$\left(\langle \boldsymbol{G} \cdot \boldsymbol{u}' \rangle \cdot \boldsymbol{\nabla} \overline{\boldsymbol{F}}^{\mathsf{T}} \cdot \overline{\boldsymbol{F}}^{-\mathsf{T}}\right)_{ij} = \left\langle G_{il} \left(u'_k \partial_k \overline{F}^{\mathsf{T}}_{lm}\right) \overline{F}^{\mathsf{T}}_{mj} \right\rangle \quad (3.31)$$

The higher-dimensional nature of $\boldsymbol{G}$ makes the quantification of the fluctuating

turbulent polymer deformation a more difficult task. We will examine the elastic potential energy as a method to evaluate this deformation in the next subsection and then introduce more general scalar characterizations of $\boldsymbol{G}$ in the next section.

3.2.2 Elastic energy and its relation to the fluctuating conformation tensor

The turbulent mean polymer configuration is not the thermodynamic equilibrium state, and thus $\boldsymbol{G}$ alone is not sufficient to fully determine thermodynamic quantities such as the elastic potential energy, $\varepsilon_\psi(\boldsymbol{C})$. For example, $\varepsilon_\psi(\boldsymbol{C})$ for an Oldroyd-B model is given by[102]

$$\varepsilon_\psi(\boldsymbol{C}) = \int_\Omega \psi \,\mathrm{tr}\,(\overline{\boldsymbol{C}} \cdot \boldsymbol{G})\,\mathrm{d}^3\boldsymbol{x}. \tag{3.32}$$

where we have rewritten the expression in terms of $\boldsymbol{G}$ and $\overline{\boldsymbol{C}}$ by setting $\overline{\boldsymbol{F}} = \overline{\boldsymbol{C}}^{\frac{1}{2}}$ and using the cyclic property of the trace to obtain $\mathrm{tr}\,\boldsymbol{C} = \mathrm{tr}\,(\overline{\boldsymbol{C}} \cdot \boldsymbol{G})$. Here, Ω is the spatial domain, and the scalar function $\psi(\boldsymbol{x})$ is proportional to the polymer elastic constant times the elasticity density.

The mean elastic potential, $\langle\varepsilon_\psi(\boldsymbol{C})\rangle$, for the Oldroyd-B model has the convenient property that it can be written solely in terms of the mean conformation tensor: $\langle\varepsilon_\psi(\boldsymbol{C})\rangle = \varepsilon_\psi(\overline{\boldsymbol{C}})$. However, the contribution of $\boldsymbol{G}$ in $\varepsilon_\psi(\boldsymbol{C})$ cannot be fully separated from that of $\overline{\boldsymbol{C}}$ because $\mathrm{tr}\,\boldsymbol{A}\cdot\boldsymbol{B} \neq \mathrm{tr}\,\boldsymbol{A}\,\mathrm{tr}\,\boldsymbol{B}$. Nonetheless, insight into the role of the

different contributions can be obtained by using trace inequalities. A particular one was mentioned by Wang *et al.*[178] and generalized by Mori.[179] For $\boldsymbol{A}, \boldsymbol{B} \in \mathbf{Pos}_3$, these authors showed that

$$\sigma_3(\boldsymbol{B})\mathrm{tr}\,\boldsymbol{A} \leq \mathrm{tr}\ (\boldsymbol{A}\cdot\boldsymbol{B}) \leq \sigma_1(\boldsymbol{B})\mathrm{tr}\,\boldsymbol{A} \tag{3.33}$$

where $\sigma_i(\boldsymbol{A})$ denotes the i-th largest eigenvalue of a tensor $\boldsymbol{A}$. Using the inequality (3.33) in the energy expression (3.32), we obtain

$$\varepsilon_{\psi_3}(\boldsymbol{G}) \leq \varepsilon_{\psi}(\boldsymbol{C}) \leq \varepsilon_{\psi_1}(\boldsymbol{G}), \qquad \psi_i \equiv \psi\sigma_i(\overline{\boldsymbol{C}}). \tag{3.34}$$

In terms of the bounds in (3.34), the contribution of $\overline{\boldsymbol{C}}$ to $\varepsilon_\psi(\boldsymbol{C})$ is equivalent to a modification of the local elasticity density or the elastic constant.

In other constitutive models, the contribution to the elastic potential energy from the mean polymer deformation is more difficult to separate. For example, the elastic potential energy for the FENE-P model[102] is

$$\varepsilon_\psi(\boldsymbol{C}; L_{\max}) = -\int_\Omega \psi L_{\max}^2 \log\left(1 - \frac{\mathrm{tr}\,(\overline{\boldsymbol{C}}\cdot\boldsymbol{G})}{L_{\max}^2}\right) \mathrm{d}^3\boldsymbol{x}, \tag{3.35}$$

where $L_{\max}$, Ω and ψ are as defined before. Here, the mean elastic potential energy, $\langle\varepsilon_\psi(\boldsymbol{C}; L_{\max})\rangle$, cannot be separated from $\boldsymbol{G}$ as in the Oldroyd-B model because, according to (3.35), $\langle\varepsilon_\psi(\boldsymbol{C})\rangle \neq \varepsilon_\psi(\overline{\boldsymbol{C}})$. However, we can again bound $\varepsilon_\psi(\boldsymbol{C}; L_{\max})$ using

the inequality (3.33) as follows

$$\varepsilon_\psi(\boldsymbol{G}; L_{\max,3}) \leq \varepsilon_\psi(\boldsymbol{C}; L_{\max}) \leq \varepsilon_\psi(\boldsymbol{G}; L_{\max,1}), \qquad L_{\max,i} \equiv L_{\max}/(\sigma_i(\overline{\boldsymbol{C}}))^{\frac{1}{2}}. \quad (3.36)$$

In terms of the bounds in (3.36), the contribution of $\overline{\boldsymbol{C}}$ in $\varepsilon_\psi(\boldsymbol{C}; L_{\max})$ is equivalent to a modification of the local polymer maximum extensibility.

Elastic energy may itself be insufficient to fully characterize the polymer deformation. For example, in both Oldroyd-B and FENE-P models, the elastic energy is equal for all conformation tensors that are given by

$$\boldsymbol{C} = [\mathrm{diag}(\alpha_1 + \delta, \alpha_2 - \delta, \alpha_3)]_{\boldsymbol{Q}}, \quad 0 \leq \delta < \alpha_2 \quad (3.37)$$

where $\mathrm{diag}(\phi_1, \phi_2, \phi_3)$ denotes a diagonal tensor with the i-th diagonal component given by ϕ_i, and $\alpha_1 \geq \alpha_2 \geq \alpha_3 > 0$ and $\boldsymbol{Q} \in \mathbf{SO}_3$ are fixed. Even though the trace is fixed, the volume of the deformation ellipsoid changes with δ, and is given by

$$\det \boldsymbol{C} = \alpha_1\alpha_2\alpha_3 + (\alpha_1 - \alpha_2)\alpha_3\delta + \delta^2\alpha_3. \quad (3.38)$$

In addition, since the governing equations are not Hamiltonian,[102] the elastic potential energy only provides a partial characterization of the dynamics underlying the polymer deformation. Due to the above limitations of the elastic energy, and its dependence on the choice of the particular constitutive model, we instead develop

an approach to characterizing the polymer deformation using the inherent geometric structure underyling $\boldsymbol{G}$. This approach, introduced in the next section, is mathematically rigorous and can be applied to any positive-definite tensor.

3.3 A Riemannian approach to fluctuations

Any scalar characterization of $\boldsymbol{G}$ obeying the principle of objectivity can be a function only of its invariants, $\mathrm{I}_{\boldsymbol{G}}$, $\mathrm{II}_{\boldsymbol{G}}$ and $\mathrm{III}_{\boldsymbol{G}}$. The invariants can be interpreted in terms of the fluctuating deformation ellipsoid, i.e. the ellipsoid associated with $\boldsymbol{G}$. The first invariant, $\mathrm{I}_{\boldsymbol{G}}$, is proportional to the average radius of the ellipsoid, the second invariant, $\mathrm{II}_{\boldsymbol{G}}$, is proportional to a lower bound for the surface area,[180] and the third invariant $\mathrm{III}_{\boldsymbol{G}}$ is the volume of the deformation ellipsoid. Note that the eigenvalues (or principal stretches) of a conformation tensor are equal to the squared polymer stretches.

In practice, multiple difficulties arise in naively using the invariants of $\boldsymbol{G}$ to characterize the conformation tensor. For example, consider the isotropic case with $\boldsymbol{C} = a\boldsymbol{I}$ and $\overline{\boldsymbol{C}} = b\boldsymbol{I}$. We then have $\boldsymbol{G} = (a/b)\boldsymbol{I}$ and the three invariants reduce to

$$\mathrm{I}_{\boldsymbol{G}} = 3a/b, \qquad \mathrm{II}_{\boldsymbol{G}} = 3(a/b)^2, \qquad \mathrm{III}_{\boldsymbol{G}} = (a/b)^3, \tag{3.39}$$

which implies that the invariants are bounded between 0 and 1 for compressions with respect to $\overline{\boldsymbol{C}}$ and between 1 and $+\infty$ for expansions with respect to $\overline{\boldsymbol{C}}$. This inherent asymmetry in the characterization is undesirable. The statistical moments of the invariants also vary over several orders of magnitude, rendering these moments uninformative predictors of the level of turbulent stretching in the polymers.

The problems discussed above arise because the set of $n \times n$ positive definite matrices, denoted $\mathbf{Pos}_n$, for $n > 0$, does not form a vector space and thus the Euclidean notions of translation and shortest distances between points are not valid. For example, let $\boldsymbol{A}, \boldsymbol{B} \in \mathbf{Pos}_3$, and define $\boldsymbol{X}$ as

$$\boldsymbol{X} \equiv r\boldsymbol{A} + (1-r)\boldsymbol{B}, \qquad r \in \mathbb{R}. \tag{3.40}$$

One may wish to use the parameter r to denote 'distance of $\boldsymbol{X}$ to $\boldsymbol{A}$' along the 'direction between $\boldsymbol{A}$ and $\boldsymbol{B}$'. However, $\boldsymbol{X}$ is then guaranteed to be positive-definite only if $r \in [0, 1]$. While $\mathbf{Pos}_3$ is not a vector space, it has a Riemannian geometric structure that can exploited to formulate alternative scalar measures of $\boldsymbol{G}$ that do not suffer from the problems mentioned above. We introduce this geometry in §3.3.1, including definitions of shortest paths and distances between tensors. Subsequently, in §3.3.2, we introduce scalar measures based on the development in §3.3.1 that can be used to quantify the turbulent fluctuations in the polymers. In §3.3.3, we derive the Reynolds-filtered evolution equations for the scalar measures.

3.3.1 Geodesic curves and distances between positive-definite tensors

The set $\mathbf{Pos}_3$ is a Cartan-Hadamard manifold: it is a simply-connected, geodesically complete Riemannian manifold with seminegative curvature.[181] We summarize this characterization in the present section in order to develop a notion of distances between positive-definite tensors that will be used to formulate appropriate scalar measures of the fluctuating conformation tensor $\boldsymbol{G}$. Details on the Riemannian structure of $\mathbf{Pos}_3$ and theorems leading to the results used in this section are presented in appendix A.

The set, $\mathbf{Pos}_3$, is an open subset of $\mathbb{R}^{3\times 3}$ and is therefore a manifold. By invoking the Fréchet derivative, it is easy to show that $\mathbf{Sym}_3$ is the tangent space at each point on the manifold. The Riemannian structure on $\mathbf{Pos}_3$ equips the tangent space at each $\boldsymbol{Z} \in \mathbf{Pos}_3$ with a scalar product

$$[\boldsymbol{\mathcal{X}}, \boldsymbol{\mathcal{Y}}]_{\boldsymbol{Z}} = \mathrm{tr}\,(\boldsymbol{Z}^{-1} \cdot \boldsymbol{\mathcal{X}} \cdot \boldsymbol{Z}^{-1} \cdot \boldsymbol{\mathcal{Y}}), \tag{3.41}$$

where $\boldsymbol{\mathcal{X}}, \boldsymbol{\mathcal{Y}} \in \mathbf{Sym}_3$. The collection of all the scalar products forms the Riemannian metric on $\mathbf{Pos}_3$. The Riemannian metric can be used to define a local distance metric at each $\boldsymbol{X} \in \mathbf{Pos}_3$. The length of a path on $\mathbf{Pos}_3$ can be calculated by patching together the local distance functions.

The manifold, $\mathbf{Pos}_3$, is geodesically complete: there is a unique, distance-minimizing

curve on $\mathbf{Pos}_3$ between every $\boldsymbol{X}, \boldsymbol{Y} \in \mathbf{Pos}_3$, called the geodesic, which can also be arbitrarily extended. The geodesic is given by

$$\boldsymbol{X}(r) = \boldsymbol{X} \#_r \boldsymbol{Y} = \boldsymbol{X}^{\frac{1}{2}} \cdot \left(\boldsymbol{X}^{-\frac{1}{2}} \cdot \boldsymbol{Y} \cdot \boldsymbol{X}^{-\frac{1}{2}} \right)^r \cdot \boldsymbol{X}^{\frac{1}{2}} = \left[\left([\boldsymbol{Y}]_{\boldsymbol{X}^{-\frac{1}{2}}} \right)^r \right]_{\boldsymbol{X}^{\frac{1}{2}}}, \quad r \in [0,1]. \tag{3.42}$$

The curve $\boldsymbol{X}(r)$ remains a geodesic on $\mathbf{Pos}_3$ for any $r \in [a,b] \subset \mathbb{R}$. Geodesically complete curves on a Riemannian manifold are analogous to straight lines in Euclidean space.

The minimizing distance between $\boldsymbol{X}, \boldsymbol{Y} \in \mathbf{Pos}_3$, the geodesic distance, is given by

$$d(\boldsymbol{X}, \boldsymbol{Y}) = \left[\sum_{i=1}^{3} (\log\, \sigma_i(\boldsymbol{X}^{-1} \cdot \boldsymbol{Y}))^2 \right]^{\frac{1}{2}} = \sqrt{\mathrm{tr}\, \log^2 \left(\boldsymbol{X}^{-\frac{1}{2}} \cdot \boldsymbol{Y} \cdot \boldsymbol{X}^{-\frac{1}{2}} \right)}. \tag{3.43}$$

where log here refers to the matrix logarithm. By the Hopf-Rinow theorem, $\mathbf{Pos}_3$ is a complete metric space under the distance function $d(\cdot,\cdot)$, and thus the geodesic distance is a natural analog to the standard 2–norm in a Euclidean space. The distance has other properties that accord well with our natural geometric intuitions. We outline some of these below.

1. The Euclidean norm in Euclidean space is invariant under translations (affine invariance). In an analogous manner, the distance metric is invariant under the

action of the general linear group, $\mathbf{GL}_3$,

$$d(\boldsymbol{X}, \boldsymbol{Y}) = d(\boldsymbol{Z} \cdot \boldsymbol{X} \cdot \boldsymbol{Z}^{\mathsf{T}}, \boldsymbol{Z} \cdot \boldsymbol{Y} \cdot \boldsymbol{Z}^{\mathsf{T}}), \tag{3.44}$$

for any $\boldsymbol{Z} \in \mathbf{GL}_3$.

2. The distance traversed along the Euclidean path (3.40) is given by $|r| \| \boldsymbol{Y} - \boldsymbol{X} \|_F$, where $\| \cdot \|_F$ is the Frobenius norm and we restrict $r \in [0, 1]$ in order to remain within $\mathbf{Pos}_3$. Similarly, the distance along the geodesic (3.42) is given by $|r|\, d(\boldsymbol{X}, \boldsymbol{Y})$, but the use of a consistent geometry means we can let $r \in \mathbb{R}$.

3. The Euclidean distance between $\boldsymbol{X}$ and $\boldsymbol{Y}$ is the same as the distance between $-\boldsymbol{X}$ and $-\boldsymbol{Y}$. Similarly, we have for the geodesic distance

$$d(\boldsymbol{X}, \boldsymbol{Y}) = d(\boldsymbol{X}^{-1}, \boldsymbol{Y}^{-1}). \tag{3.45}$$

This property is especially attractive from a physical point of view, since it means the distance metric treats expansions and compressions on an equal footing, unlike the Euclidean metric.

We now illustrate the geodesic distance derived above using two specific examples.

1. *Isotropic tensors*: Let $\boldsymbol{X} = a\boldsymbol{I}$ and $\boldsymbol{Y} = b\boldsymbol{I}$ be elements of the one-dimensional sub-manifold of $\mathbf{Pos}_3$ consisting of the isotropic tensors. The geodesic path

joining $\boldsymbol{X}$ and $\boldsymbol{Y}$ is given by

$$\boldsymbol{X} \#_r \boldsymbol{Y} = (a^{1-r} b^r) \boldsymbol{I} \tag{3.46}$$

and the geodesic distance is given by $d(\boldsymbol{X}, \boldsymbol{Y}) = \sqrt{3} \log (b/a)$.

Notice that $a^{1-r} b^r$, which appears in (3.46), is a generalized geometric mean of a and b with the classical definition realized at $r = 1/2$. It can be shown that a similar interpretation is admissible when $\boldsymbol{X}$ and $\boldsymbol{Y}$ are not isotropic.[182] This fact has formed the basis of efforts to formulate alternative definitions of statistical quantities such as means and covariances so that they conform to the geometric structure of $\mathbf{Pos}_3$.[183,184]

2. *Tensors differing by a rotation*: Consider $\boldsymbol{X}$ and $\boldsymbol{Y} = [\boldsymbol{X}]_{\boldsymbol{R}}$ for $\boldsymbol{R} \in \mathbf{SO}_3$. The geodesic joining $\boldsymbol{X}$ and $\boldsymbol{Y}$ is given by

$$\boldsymbol{X} \#_r \boldsymbol{Y} = \left[\left([\boldsymbol{X}]_{\boldsymbol{R} \cdot \boldsymbol{X}^{-\frac{1}{2}}} \right)^r \right]_{\boldsymbol{X}^{\frac{1}{2}}} . \tag{3.47}$$

By a well-known singular value inequality (see equation 9.6.2, p. 615 of Bernstein[185]), we obtain the two inequalities

$$\sigma_i(\boldsymbol{X}^{-1} \cdot \boldsymbol{Y}) \leq \frac{\sigma_i(\boldsymbol{Y})}{\sigma_3(\boldsymbol{X})}, \qquad \sigma_i(\boldsymbol{X}^{-1} \cdot \boldsymbol{Y}) \leq \frac{\sigma_1(\boldsymbol{Y})}{\sigma_i(\boldsymbol{X})}. \tag{3.48}$$

where we used the fact that $\sigma_i(\boldsymbol{X}^{-1}) = 1/\sigma_i(\boldsymbol{X})$. The expression (3.43) can be

used to yield the inequality

$$d(\boldsymbol{X}, \boldsymbol{Y}) \leq \left[3 \max_i \log^2 \sigma_i(\boldsymbol{X}^{-1} \cdot \boldsymbol{Y})\right]^{\frac{1}{2}}. \tag{3.49}$$

Combining the previous two expressions, we obtain

$$d(\boldsymbol{X}, \boldsymbol{Y}) \leq \left[3 \max_i \log^2 \frac{\sigma_i(\boldsymbol{Y})}{\sigma_3(\boldsymbol{X})}\right]^{\frac{1}{2}}, \quad d(\boldsymbol{X}, \boldsymbol{Y}) \leq \left[3 \max_i \log^2 \frac{\sigma_1(\boldsymbol{Y})}{\sigma_i(\boldsymbol{X})}\right]^{\frac{1}{2}}. \tag{3.50}$$

Choosing the stronger of the two inequalities, the distance between $\boldsymbol{X}$ and $\boldsymbol{Y}$ can then be bounded as

$$0 \leq d(\boldsymbol{X}, \boldsymbol{Y}) \leq \sqrt{3} \min \left\{ \max_i \left| \log \left(\frac{\sigma_i(\boldsymbol{Y})}{\sigma_3(\boldsymbol{X})} \right) \right|, \max_i \left| \log \left(\frac{\sigma_1(\boldsymbol{Y})}{\sigma_i(\boldsymbol{X})} \right) \right| \right\}. \tag{3.51}$$

where the lower bound is achieved for $\boldsymbol{R} = \boldsymbol{I}$. The upper bound in (3.51) is true for any $\boldsymbol{X}$ and $\boldsymbol{Y}$ but it is especially instructive when the two tensors only differ by a rotation, since then $\sigma_i(\boldsymbol{X}) = \sigma_i(\boldsymbol{Y})$. The upper bound suggests that a differential rotation of a second–order tensor, $\boldsymbol{X}$, leads to an excursion along $\mathbf{Pos}_3$ with a path length that depends on the anisotropy of $\boldsymbol{X}$. For isotropic $\boldsymbol{X}$, the path length is zero and it otherwise increases with increasing anisotropy.

The geometry of $\mathbf{Pos}_3$ and the properties discussed above are next used to define scalar measures that characterize the turbulent fluctuations in $\boldsymbol{G}$.

3.3.2 Scalar measures of the fluctuating conformation tensor

In this subsection we introduce scalar measures that can be used to quantify the fluctuating polymer deformation represented by $\boldsymbol{G}$. In what follows, we will denote the matrix logarithm of $\boldsymbol{G}$ as $\boldsymbol{\mathcal{G}}$, i.e.

$$\boldsymbol{G} = \sum_{k=0}^{\infty} \frac{\boldsymbol{\mathcal{G}}^k}{k!} \equiv \mathrm{e}^{\boldsymbol{\mathcal{G}}}. \tag{3.52}$$

The matrix logarithm is guaranteed to exist and is unique since $\boldsymbol{G}$ is positive-definite. A key point to note is that the eigenvalues of $\boldsymbol{\mathcal{G}}$ are the logarithms of the eigenvalues of $\boldsymbol{G}$.

3.3.2.1 Logarithmic volume ratio, ζ

Let $\Gamma_i = \sigma_i(\boldsymbol{G})$, for $i = 1, 2, 3$, be the eigenvalues of $\boldsymbol{G}$. Then $\log(\det \boldsymbol{G}) = \log(\prod_{i=1}^{3} \Gamma_i) = \sum_{i=1}^{3} \log \Gamma_i$. We thus define the logarithmic volume ratio of the fluctuation, ζ, as

$$\zeta \equiv \mathrm{tr}\ \boldsymbol{\mathcal{G}} = \log(\det \boldsymbol{G}) = \log\left(\frac{\det \boldsymbol{C}}{\det \overline{\boldsymbol{C}}}\right) = \sum_{i=1}^{3} \log \Gamma_i. \tag{3.53}$$

When $\zeta = 0$, the mean and the instantaneous conformation tensors have the same volume; when ζ is negative (positive), the instantaneous conformation tensor has a

smaller (larger) volume than the volume of the mean. The logarithm ensures that there is no asymmetry between compressions and expansions with respect to the mean.

3.3.2.2 Squared distance from the mean, κ

When $\boldsymbol{C} = \overline{\boldsymbol{C}}$, we have $\boldsymbol{G} = \boldsymbol{I}$. When $\boldsymbol{C} \neq \overline{\boldsymbol{C}}$, we wish to consider the (appropriately defined) shortest distance between $\boldsymbol{I}$ and $\boldsymbol{G}$ as a measure of the magnitude of the fluctuation. The shortest path between $\boldsymbol{I}$ and $\boldsymbol{G}$ along the manifold $\mathbf{Pos}_3$ is given by the geodesic along $\mathbf{Pos}_3$ connecting $\boldsymbol{I}$ and $\boldsymbol{G}$,

$$\boldsymbol{I} \#_r \boldsymbol{G} = \boldsymbol{G}^r = \mathrm{e}^{\boldsymbol{\mathcal{G}} r}. \tag{3.54}$$

The squared geodesic distance associated with this path is then

$$\kappa \equiv \mathrm{tr}\ \boldsymbol{\mathcal{G}}^2 = d^2(\boldsymbol{I}, \boldsymbol{G}) = \sum_{i=1}^{3} (\log\ \Gamma_i)^2, \tag{3.55}$$

where (3.55) follows from (3.43). Using (3.43), one can verify that $d^2(\boldsymbol{I}, \boldsymbol{G}) = d^2(\boldsymbol{I}, \boldsymbol{G}^{-1})$ and thus the squared distance measure treats both expansions and compressions with respect to the mean similarly. The affine-invariance property, furthermore, ensures that

$$d^2(\boldsymbol{I}, \boldsymbol{G}) = d^2([\boldsymbol{I}]_{\boldsymbol{A}}, [\boldsymbol{G}]_{\boldsymbol{A}}) \tag{3.56}$$

for all $\boldsymbol{A} \in \mathbf{GL}_3$. In particular, with $\boldsymbol{A} = \overline{\boldsymbol{F}}$, we obtain

$$d^2(\boldsymbol{I}, \boldsymbol{G}) = d^2(\overline{\boldsymbol{C}}, [\boldsymbol{G}]_{\overline{\boldsymbol{F}}}) = d^2(\overline{\boldsymbol{C}}, \boldsymbol{C}) = d^2(\overline{\boldsymbol{C}}^{-1}, \boldsymbol{C}^{-1}) \tag{3.57}$$

which exhibits the highly desirable property that the squared distance between $\boldsymbol{C}$ and $\overline{\boldsymbol{C}}$ is equal to the squared distance between $\boldsymbol{I}$ and $\boldsymbol{G}$. A further consequence of the affine-invariance property is that $d^2(\boldsymbol{I}, \boldsymbol{G})$ is independent of the choice of the rotation $\boldsymbol{R} \in \mathbf{SO}_3$ in (3.9).

The path between $\overline{\boldsymbol{C}}$ and $\boldsymbol{C}$ along $\mathbf{Pos}_3$ is given by

$$\overline{\boldsymbol{C}} \#_r \boldsymbol{C} = \left[\left([\boldsymbol{C}]_{\overline{\boldsymbol{C}}^{-\frac{1}{2}}} \right)^r \right]_{\overline{\boldsymbol{C}}^{\frac{1}{2}}}, \tag{3.58}$$

which reduces to

$$\overline{\boldsymbol{C}} \#_r \boldsymbol{C} = [\boldsymbol{G}^r]_{\overline{\boldsymbol{F}}} \tag{3.59}$$

when $\boldsymbol{R} = \boldsymbol{I}$ in (3.9). The choice $\boldsymbol{R} = \boldsymbol{I}$ is then natural in the sense that it allows the path along the manifold between $\overline{\boldsymbol{C}}$ and $\boldsymbol{C}$, whose distance is a measure of the fluctuation, to be described using only $\overline{\boldsymbol{F}}$ and $\boldsymbol{G}$.

We next consider realizability in the (ζ, κ) plane. Since $\boldsymbol{\mathcal{G}}$ is symmetric, its eigenvalues must be real, i.e. the eigenvalues must together belong in $\mathbb{R}^3$. In the $\mathbb{R}^3$ space of eigenvalues of $\boldsymbol{\mathcal{G}}$, surfaces of constant ζ are planes, and surfaces of constant κ are

spheres. A particular choice of ζ and κ is realizable only if the plane and sphere intersect.

In a spherical coordinate representation of $\mathbb{R}^3$ we have

$$\begin{aligned} \Gamma_1 &= R\cos\theta\sin\phi \\ \Gamma_2 &= R\sin\theta\sin\phi \\ \Gamma_3 &= R\cos\phi \end{aligned} \tag{3.60}$$

where $R \in [0, \infty)$ is the radial coordinate, $\phi \in [0, \pi]$ is the polar angle and $\theta \in [0, 2\pi)$ is the azimuthal angle. The scalar measures ζ and κ then satisfy the following equations

$$\Gamma_1 + \Gamma_2 + \Gamma_3 = \zeta \tag{3.61}$$

$$\Gamma_1^2 + \Gamma_2^2 + \Gamma_3^2 = \kappa \tag{3.62}$$

Substituting (3.60) into (3.62), we immediately obtain $R = \sqrt{\kappa}$. Substituting this result and (3.60) into (3.61) yields an equation defining the coordinates along the intersecting circle of the sphere as satisfying

$$\cos\theta\sin\phi + \sin\theta\sin\phi + \cos\phi = \frac{\zeta}{\sqrt{\kappa}}, \qquad \theta \in [0, 2\pi),\ \phi \in [0, \pi]. \tag{3.63}$$

In order to find the feasible angles in (ζ, κ) space, we strictly bound the left-hand side of (3.63). By the so-called harmonic addition theorem, $a\sin\gamma + b\cos\gamma =$

$\sqrt{a^2+b^2}\sin(\gamma+\arctan(b/a))$, we have

$$\cos\theta+\sin\theta=\sqrt{2}\sin\left(\theta+\frac{\pi}{4}\right) \tag{3.64}$$

and thus (3.63) can be written as

$$\sqrt{2}\sin\left(\theta+\frac{\pi}{4}\right)\sin\phi+\cos\phi=\frac{\zeta}{\sqrt{\kappa}}. \tag{3.65}$$

Since θ and ϕ are independent, we then have the sharp bounds

$$-\sqrt{2}\sin\phi+\cos\phi\leq\frac{\zeta}{\sqrt{\kappa}}\leq\sqrt{2}\sin\phi+\cos\phi. \tag{3.66}$$

Invoking the harmonic addition theorem again, we obtain

$$\pm\sqrt{2}\sin\phi+\cos\phi=\sqrt{3}\sin\left(\phi\pm\arctan\frac{1}{\sqrt{2}}\right), \tag{3.67}$$

which yields the following sharp bounds

$$-\sqrt{3}\leq\frac{\zeta}{\sqrt{\kappa}}\leq\sqrt{3}. \tag{3.68}$$

Thus, the physically realizable region in the (ζ,κ) plane is given by

$$-\sqrt{3\kappa}\leq\zeta\leq\sqrt{3\kappa}. \tag{3.69}$$

When $\kappa = \frac{1}{3}\zeta^2$, the circle of intersection reduces to a point and $\boldsymbol{\mathcal{G}}$ consequently has only two independent tensor invariants, ζ and κ.

The bounds derived above indicate that at a particular set of angles, $(\theta, \phi) = (\theta_{\max}, \phi_{\max})$ the left-hand side of (3.63) is maximized and is equal to $\sqrt{3}$. Similarly, at $(\theta, \phi) = (\theta_{\min}, \phi_{\min})$ it is minimized and is equal to $-\sqrt{3}$. Using (3.64) and (3.67), we find these angles to be

$$(\theta_{\max}, \phi_{\max}) = (\pi/4, \arctan\sqrt{2}), \qquad (\theta_{\min}, \phi_{\min}) = (5\pi/4, \pi - \arctan\sqrt{2}), \quad (3.70)$$

where we used the identity $\operatorname{arccot}\gamma = \pi/2 - \arctan\,\gamma$.

At $(\theta, \phi) = (\theta_{\max}, \phi_{\max})$ and $(\theta, \phi) = (\theta_{\min}, \phi_{\min})$, it is readily verified that $\kappa = \frac{1}{3}\zeta^2$ and also that the eigenvalues of $\boldsymbol{\mathcal{G}}$ are all equal. Thus $\boldsymbol{\mathcal{G}}$, and hence $\boldsymbol{G}$, is isotropic at the realizability bounds.

3.3.2.3 Anisotropy index, ξ

Following the approach taken by Moakher and co-authors,[170] we define the anisotropy index, ξ, of $\boldsymbol{G}$ as the squared geodesic distance between $\boldsymbol{G}$ and the closest isotropic tensor,

$$\xi \equiv \inf_a d^2(a\boldsymbol{I}, \boldsymbol{G}) = \inf_a \operatorname{tr}\,(\boldsymbol{\mathcal{G}} - (\log\,a)\boldsymbol{I})^2. \quad (3.71)$$

Setting the derivative of (3.71) with respect to a equal to 0, we obtain

$$\frac{\mathrm{d}\xi}{\mathrm{d}a} = \frac{\mathrm{d}}{\mathrm{d}a}\sum_{i=1}^{3}(\log\Gamma_i - \log a)^2 = \frac{2}{a}\sum_{i=1}^{3}(\log\Gamma_i - \log a) = 0 \tag{3.72}$$

and thus we find that $a = \left(\prod_{i=1}^{3}\Gamma_i\right)^{\frac{1}{3}} = (\det \boldsymbol{G})^{\frac{1}{3}}$ is a minimizing stationary point of (3.71) and hence the closest isotropic tensor to $\boldsymbol{G}$ along $\mathbf{Pos}_3$ is $(\sqrt[3]{\det \boldsymbol{G}})\boldsymbol{I}$. We then have

$$\xi = d^2((\sqrt[3]{\det \boldsymbol{G}})\boldsymbol{I}, \boldsymbol{G}) = \kappa - \frac{1}{3}\zeta^2. \tag{3.73}$$

Notice that $\chi = 0$ if and only if $\zeta^2 = 3\kappa$. But since we already showed that $\boldsymbol{\mathcal{G}}$, and hence $\boldsymbol{G}$, are isotropic at the bound $\zeta^2 = 3\kappa$, it follows that $\xi = 0$ only for isotropic tensors. The anisotropy index ξ can also be viewed as the squared Frobenius norm of the deviatoric part of $\boldsymbol{\mathcal{G}}$

$$\begin{aligned}\|\operatorname{dev}\boldsymbol{\mathcal{G}}\|_F^2 = \left\|\boldsymbol{\mathcal{G}} - \frac{\operatorname{tr}\boldsymbol{\mathcal{G}}}{3}\boldsymbol{I}\right\|_F^2 &= \operatorname{tr}\left[\left(\boldsymbol{\mathcal{G}} - \frac{\operatorname{tr}\boldsymbol{\mathcal{G}}}{3}\boldsymbol{I}\right)^2\right] \\ &= \operatorname{tr}\left(\boldsymbol{\mathcal{G}}^2 - \frac{2\operatorname{tr}\boldsymbol{\mathcal{G}}}{3}\boldsymbol{\mathcal{G}} + \frac{(\operatorname{tr}\boldsymbol{\mathcal{G}})^2}{9}\boldsymbol{I}\right) \\ &= \operatorname{tr}\boldsymbol{\mathcal{G}}^2 - \frac{(\operatorname{tr}\boldsymbol{\mathcal{G}})^2}{3} = \xi\end{aligned} \tag{3.74}$$

The index $\sqrt{\xi}$ was first introduced for characterizing positive-definite diffusion tensors measured in magnetic resonance imaging.[186] The index is analogous to the 'fractional anisotropy index' that is commonly used in turbulence and which provides

the Euclidean distance to the closest isotropic tensor,

$$\frac{\|\boldsymbol{G} - (\text{tr } \boldsymbol{G}/3)\boldsymbol{I}\|_F}{\|\boldsymbol{G}\|_F}, \tag{3.75}$$

where $\|\boldsymbol{A}\|_F = \text{tr } (\boldsymbol{A}^{\mathsf{T}} \cdot \boldsymbol{A})$ indicates the Frobenius norm of matrix $\boldsymbol{A}$.

The three scalar measures presented above can be used together to obtain a better understanding of the fluctuations in the conformation tensor. The logarithmic volume ratio, ζ, is positive (negative) for volumetric expansions (contractions) with respect to the mean. However, $\zeta = 0$ does not necessarily imply no deformation, since $\det(\det(\boldsymbol{G})\,\boldsymbol{A}) = \det(\boldsymbol{G})$ for all $\boldsymbol{A}$ with unit determinant. The squared geodesic distance to the identity, κ, helps distinguish such cases since $\kappa = 0$ only when $\boldsymbol{G} = \boldsymbol{I}$ ($\boldsymbol{C} = \overline{\boldsymbol{C}}$). Finally, the anisotropy index, ξ, provides a quantification of the deviation of the shape of the polymer from the shape of the mean conformation tensor because it is a measure of the distance from $\boldsymbol{G}$ to the closest isotropic tensor, or equivalently, the minimizing distance between $\boldsymbol{C}$ and $a\overline{\boldsymbol{C}}$ over all $a > 0$.

We next derive evolution equations for the scalar measures presented above and for the particular case when $\overline{\boldsymbol{C}} = \langle \boldsymbol{C} \rangle$.

3.3.3 Evolution equations for scalar measures

Since ζ, κ and ξ are scalar characterizations of $\boldsymbol{G}$, one need only evolve $\boldsymbol{G}$ (or equivalently, $\boldsymbol{C}$) to obtain the field-valued ζ, κ and ξ. Nevertheless, it is of interest to

mathematically evaluate the evolution equations of these scalar measures separately in order to find the quantities that contribute to their dynamics.

It is most straightforward to derive the equations for the scalar measures in terms of the eigenvalues of $\boldsymbol{G}$ and then to revert back to the full forms of the tensors. Diagonalizing the tensors $\boldsymbol{G}$ and $\boldsymbol{\mathcal{G}}$ yields

$$\boldsymbol{G} = \mathcal{G} \cdot \boldsymbol{\Gamma} \cdot \mathcal{G}^{\mathsf{T}}, \qquad \boldsymbol{\mathcal{G}} = \log \boldsymbol{G} = \mathcal{G} \cdot \log \boldsymbol{\Gamma} \cdot \mathcal{G}^{\mathsf{T}} \tag{3.76}$$

where $\boldsymbol{\Gamma}$ is a diagonal matrix with eigenvalues Γ_i on the diagonal (for $i = 1, 2, 3$), and $\mathcal{G} \in \mathbf{SO}_3$ is a rotation matrix.

Using the definition of ζ in terms of the eigenvalues of $\boldsymbol{G}$ given in (3.53) we obtain

$$\begin{aligned} \frac{\mathrm{D}\zeta}{\mathrm{D}t} = \sum_{i=1}^{3} \frac{\mathrm{D}\log\,\Gamma_i}{\mathrm{D}t} &= \sum_{i=1}^{3} \frac{1}{\Gamma_i} \frac{\mathrm{D}\Gamma_i}{\mathrm{D}t} \\ &= \mathrm{tr}\left(\boldsymbol{\Gamma}^{-1} \cdot \frac{\mathrm{D}\boldsymbol{\Gamma}}{\mathrm{D}t}\right). \end{aligned} \tag{3.77}$$

Similarly, using the definition of κ given in (3.55) we obtain

$$\begin{aligned} \frac{\mathrm{D}\kappa}{\mathrm{D}t} = \sum_{i=1}^{3} \frac{\mathrm{D}(\log\,\Gamma_i)^2}{\mathrm{D}t} = \sum_{i=1}^{3} 2\,\log\,\Gamma_i \frac{\mathrm{D}\log\,\Gamma_i}{\mathrm{D}t} &= \sum_{i=1}^{3} \frac{2\,\log\,\Gamma_i}{\Gamma_i} \frac{\mathrm{D}\Gamma_i}{\mathrm{D}t} \\ &= 2\,\mathrm{tr}\left(\log \boldsymbol{\Gamma} \cdot \boldsymbol{\Gamma}^{-1} \cdot \frac{\mathrm{D}\boldsymbol{\Gamma}}{\mathrm{D}t}\right). \end{aligned} \tag{3.78}$$

Differentiating the $\boldsymbol{G}$ expressed in terms of its spectral decomposition in (3.76)

yields

$$\frac{\mathrm{D}\boldsymbol{G}}{\mathrm{D}t} = \frac{\mathrm{D}\mathcal{G}}{\mathrm{D}t} \cdot \boldsymbol{\Gamma} \cdot \mathcal{G}^{\mathsf{T}} + \mathcal{G} \cdot \frac{\mathrm{D}\boldsymbol{\Gamma}}{\mathrm{D}t} \cdot \mathcal{G}^{\mathsf{T}} + \mathcal{G} \cdot \boldsymbol{\Gamma} \cdot \frac{\mathrm{D}\mathcal{G}^{\mathsf{T}}}{\mathrm{D}t}. \tag{3.79}$$

Multiplying on the left by $\mathcal{G}^{\mathsf{T}}$ and on the right by $\mathcal{G}$ gives

$$\mathcal{G}^{\mathsf{T}} \cdot \frac{\mathrm{D}\boldsymbol{G}}{\mathrm{D}t} \cdot \mathcal{G} = \mathcal{G}^{\mathsf{T}} \cdot \frac{\mathrm{D}\mathcal{G}}{\mathrm{D}t} \cdot \boldsymbol{\Gamma} + \frac{\mathrm{D}\boldsymbol{\Gamma}}{\mathrm{D}t} + \boldsymbol{\Gamma} \cdot \frac{\mathrm{D}\mathcal{G}^{\mathsf{T}}}{\mathrm{D}t} \cdot \mathcal{G}. \tag{3.80}$$

Substituting this expression in the evolution equation for (3.24) multiplied on the left by $\mathcal{G}^{\mathsf{T}}$ and on the right by $\mathcal{G}$ gives

$$\mathcal{G}^{\mathsf{T}} \cdot \frac{\mathrm{D}\mathcal{G}}{\mathrm{D}t} \cdot \boldsymbol{\Gamma} + \frac{\mathrm{D}\boldsymbol{\Gamma}}{\mathrm{D}t} + \boldsymbol{\Gamma} \cdot \frac{\mathrm{D}\mathcal{G}^{\mathsf{T}}}{\mathrm{D}t} \cdot \mathcal{G} = 2\,\mathrm{sym}\left(\mathcal{G}^{\mathsf{T}} \cdot \boldsymbol{G} \cdot \mathcal{G} \cdot \mathcal{G}^{\mathsf{T}} \cdot \boldsymbol{K} \cdot \mathcal{G}\right) - \mathcal{G}^{\mathsf{T}} \cdot \boldsymbol{M} \cdot \mathcal{G} \tag{3.81}$$

where we used the identity $\mathcal{G} \cdot \mathcal{G}^{\mathsf{T}} = \boldsymbol{I}$. Now since

$$\boldsymbol{0} = \frac{\mathrm{D}\boldsymbol{I}}{\mathrm{D}t} = \frac{\mathrm{D}(\mathcal{G}^{\mathsf{T}} \cdot \mathcal{G})}{\mathrm{D}t} = \frac{\mathrm{D}\mathcal{G}^{\mathsf{T}}}{\mathrm{D}t} \cdot \mathcal{G} + \mathcal{G}^{\mathsf{T}} \cdot \frac{\mathrm{D}\mathcal{G}}{\mathrm{D}t} \tag{3.82}$$

we have

$$\frac{\mathrm{D}\mathcal{G}^{\mathsf{T}}}{\mathrm{D}t} \cdot \mathcal{G} = -\left(\frac{\mathrm{D}\mathcal{G}^{\mathsf{T}}}{\mathrm{D}t} \cdot \mathcal{G}\right)^{\mathsf{T}} \tag{3.83}$$

which shows that the quantity on the left-hand side of the above expression is skew-

symmetric. Skew-symmetric tensors have zero diagonal, and therefore the diagonal components of (3.81) are

$$\begin{aligned} \frac{\mathrm{D}\Gamma_i}{\mathrm{D}t} &= [2\,\mathrm{sym}\,(\boldsymbol{\Gamma}\cdot\mathscr{K}) - \mathscr{M}]_{ii}, \qquad i = 1,2,3 \\ &= \Gamma_i\,\mathscr{D}_{ii}, \qquad i = 1,2,3 \end{aligned} \tag{3.84}$$

where we have not used the Einstein summation notation and

$$\mathscr{M} \equiv \mathcal{G}^{\mathsf{T}}\cdot\boldsymbol{M}\cdot\mathcal{G}, \qquad \mathscr{K} \equiv \mathcal{G}^{\mathsf{T}}\cdot\boldsymbol{K}\cdot\mathcal{G}, \qquad \mathscr{D} \equiv 2\,\mathrm{sym}\,\mathscr{K} - \boldsymbol{\Gamma}^{-1}\cdot\mathscr{M}. \tag{3.85}$$

To derive (3.84), we used the spectral decomposition in (3.76) and the fact that $\boldsymbol{\Gamma}$ is diagonal.

Using the expression (3.84) and the cyclical property of the trace in (3.77) then yields

$$\frac{\mathrm{D}\zeta}{\mathrm{D}t} = \mathrm{tr}\left(\boldsymbol{\Gamma}^{-1}\cdot\frac{\mathrm{D}\boldsymbol{\Gamma}}{\mathrm{D}t}\right) = \sum_{i=1}^{3}\Gamma_i^{-1}\frac{\mathrm{D}\Gamma_i}{\mathrm{D}t} = \mathrm{tr}\,\mathscr{D}. \tag{3.86}$$

Doing the same in (3.78) yields

$$\frac{\mathrm{D}\kappa}{\mathrm{D}t} = 2\,\mathrm{tr}\left(\log\boldsymbol{\Gamma}\cdot\boldsymbol{\Gamma}^{-1}\cdot\frac{\mathrm{D}\boldsymbol{\Gamma}}{\mathrm{D}t}\right) = \sum_{i=1}^{3}2\,\mathrm{tr}\left(\frac{\log\Gamma_i}{\Gamma_i}\frac{\mathrm{D}\Gamma_i}{\mathrm{D}t}\right) = 2\,\mathrm{tr}\,(\log\boldsymbol{\Gamma}\cdot\mathscr{D})\,. \tag{3.87}$$

An evolution equation for the anisotropy index ξ can be found by directly differenti-

ating (3.73), so that

$$\begin{aligned}\frac{\mathrm{D}\xi}{\mathrm{D}t} &= \frac{\mathrm{D}\kappa}{\mathrm{D}t} - \frac{2\,\zeta}{3}\frac{\mathrm{D}\zeta}{\mathrm{D}t} \\ &= 2\,\mathrm{tr}\ (\log\,\boldsymbol{\Gamma}\cdot\mathscr{D}) - \frac{2\,\zeta}{3}\mathrm{tr}\,\mathscr{D} \\ &= 2\,\mathrm{tr}\ \left[\left(\log\,\boldsymbol{\Gamma} - \frac{\mathrm{tr}\ \log\,\boldsymbol{\Gamma}}{3}\boldsymbol{I}\right)\cdot\mathscr{D}\right] \end{aligned} \tag{3.88}$$

Substituting the spectral decomposition (3.76) back into the evolution equations allows us to express them only in terms of the tensor $\boldsymbol{G}$ and $\boldsymbol{\mathcal{G}}$, as follows

$$\frac{\mathrm{D}\zeta}{\mathrm{D}t} = \mathrm{tr}\ \boldsymbol{\mathcal{D}}, \qquad \frac{1}{2}\frac{\mathrm{D}\kappa}{\mathrm{D}t} = \mathrm{tr}\ (\boldsymbol{\mathcal{D}}\cdot\boldsymbol{\mathcal{G}}), \qquad \frac{1}{2}\frac{\mathrm{D}\xi}{\mathrm{D}t} = \mathrm{tr}\ (\boldsymbol{\mathcal{D}}\cdot\mathrm{dev}\,\boldsymbol{\mathcal{G}}) \tag{3.89}$$

where $\mathrm{dev}\,\boldsymbol{\mathcal{G}} = \boldsymbol{\mathcal{G}} - (\mathrm{tr}\ \boldsymbol{\mathcal{G}}/3)\boldsymbol{I}$ is the deviatoric part of $\boldsymbol{\mathcal{G}}$, and $\boldsymbol{\mathcal{D}}$ is defined as

$$\boldsymbol{\mathcal{D}} \equiv 2\,\mathrm{sym}\,\boldsymbol{K} - \boldsymbol{M}\cdot\mathrm{e}^{-\boldsymbol{\mathcal{G}}}. \tag{3.90}$$

By the Cauchy-Schwarz inequality, we have

$$\mathrm{tr}^{\,2}\,(\boldsymbol{\mathcal{D}}\cdot\boldsymbol{\mathcal{G}}) \leq \|\boldsymbol{\mathcal{D}}\|_F^2\|\boldsymbol{\mathcal{G}}\|_F^2 = \kappa\,\|\boldsymbol{\mathcal{D}}\|_F^2 \tag{3.91}$$

$$\mathrm{tr}^{\,2}\,(\boldsymbol{\mathcal{D}}\cdot\mathrm{dev}\,\boldsymbol{\mathcal{G}}) \leq \|\boldsymbol{\mathcal{D}}\|_F^2\|\mathrm{dev}\,\boldsymbol{\mathcal{G}}\|_F^2 = \xi\,\|\boldsymbol{\mathcal{D}}\|_F^2 \tag{3.92}$$

Using the above in (3.89) and invoking the definition of κ in (3.55) and the equivalence of ξ with the squared norm of the deviatoric part of $\boldsymbol{\mathcal{G}}$ proved in (3.74), we can show

that

$$\begin{aligned} \left| \frac{\mathrm{D}\sqrt{\kappa}}{\mathrm{D}t} \right| &\leq \|\boldsymbol{\mathcal{D}}\|_F \\ \left| \frac{\mathrm{D}\sqrt{\xi}}{\mathrm{D}t} \right| &\leq \|\boldsymbol{\mathcal{D}}\|_F. \end{aligned} \tag{3.93}$$

The bounds in (3.93) illustrate the role of the stretching and relaxation balance, $\boldsymbol{\mathcal{D}}$, in bounding the growth of κ and ξ. It is interesting to note that (3.93) shows that the growth rate of a quantity with dimensions of length along $\mathbf{Pos}_3$, rather than squared length, is bounded by the norm of $\boldsymbol{\mathcal{D}}$.

In the Reynolds-filtered case, $\boldsymbol{\mathcal{D}}$ can be simplified using (3.30). In particular, rearranging (3.30) and using $\overline{\boldsymbol{u}} = \boldsymbol{u} - \boldsymbol{u}'$ yields

$$\begin{aligned} -2\,\mathrm{sym}\left(\overline{\boldsymbol{F}}^{-1} \cdot \frac{\mathrm{D}\overline{\boldsymbol{F}}}{\mathrm{D}t}\right)^{\mathsf{T}} &= \overline{\boldsymbol{M}} + \langle \boldsymbol{u}' \cdot \boldsymbol{\nabla} \boldsymbol{G} \rangle \\ &\quad + 2\,\mathrm{sym}\left[-\overline{\boldsymbol{E}} - \langle \boldsymbol{G} \cdot \boldsymbol{E}' \rangle - (\boldsymbol{u}' - \langle \boldsymbol{G} \cdot \boldsymbol{u}' \rangle) \cdot \boldsymbol{\nabla} \overline{\boldsymbol{F}}^{\mathsf{T}} \cdot \overline{\boldsymbol{F}}^{-\mathsf{T}} \right] \end{aligned} \tag{3.94}$$

Substituting the above expression in that for the symmetric part of $\boldsymbol{K}$ obtained from (3.27), we have

$$\begin{aligned} 2\,\mathrm{sym}\,\boldsymbol{K} &= \overline{\boldsymbol{M}} + \langle \boldsymbol{u}' \cdot \boldsymbol{\nabla} \boldsymbol{G} \rangle \\ &\quad + 2\,\mathrm{sym}\left[\boldsymbol{E}' - \langle \boldsymbol{G} \cdot \boldsymbol{E}' \rangle + (\langle \boldsymbol{G} \cdot \boldsymbol{u}' \rangle - \boldsymbol{u}') \cdot \boldsymbol{\nabla} \overline{\boldsymbol{F}}^{\mathsf{T}} \cdot \overline{\boldsymbol{F}}^{-\mathsf{T}} \right] \end{aligned} \tag{3.95}$$

Thus, (3.90) is given by

$$\boldsymbol{\mathcal{D}} = 2\,\mathrm{sym}\left[\boldsymbol{E}' - \langle \boldsymbol{G}\cdot\boldsymbol{E}'\rangle + (\langle \boldsymbol{G}\cdot\boldsymbol{u}'\rangle - \boldsymbol{u}')\cdot\boldsymbol{\nabla}\overline{\boldsymbol{F}}^{\mathsf{T}}\cdot\overline{\boldsymbol{F}}^{-\mathsf{T}}\right] + \langle \boldsymbol{u}'\cdot\boldsymbol{\nabla}\boldsymbol{G}\rangle - (\boldsymbol{M}\cdot\boldsymbol{G}^{-1} - \overline{\boldsymbol{M}}) \quad (3.96)$$

which shows that the turbulence intensity of the fluctuating conformation tensor, as measured by κ, is not directly affected by the mean velocity gradient tensor $\boldsymbol{\nabla}\overline{\boldsymbol{u}}$. The contribution of $\boldsymbol{\nabla}\overline{\boldsymbol{u}}$ to κ is captured indirectly through $\overline{\boldsymbol{F}}$, which is determined based on the mean balance.

According to (3.96), the tensor $\boldsymbol{\mathcal{D}}$ consists of a stretching component: the symmetric part of $\boldsymbol{E}' - \langle \boldsymbol{G}\cdot\boldsymbol{E}'\rangle$, a component that arises due to gradients in $\overline{\boldsymbol{F}}$ and represents modified advection of $\overline{\boldsymbol{F}}$: the symmetric part of $(\langle \boldsymbol{G}\cdot\boldsymbol{u}'\rangle - \boldsymbol{u}')\cdot\boldsymbol{\nabla}\overline{\boldsymbol{F}}^{\mathsf{T}}\cdot\overline{\boldsymbol{F}}^{-\mathsf{T}}$, a component that comprises mean advection of $\boldsymbol{G}$ by the fluctuating velocity field: $\langle \boldsymbol{u}'\cdot\boldsymbol{\nabla}\boldsymbol{G}\rangle$, and finally a component that resembles a fluctuating relaxation contribution: $-\left(\boldsymbol{M}\cdot\boldsymbol{G}^{-1} - \overline{\boldsymbol{M}}\right)$.

3.3.3.1 Reynolds-filtering the evolution equations

As a first–order statistical characterization of the fluctuating quantities, ζ, κ and ξ, we will consider their filtered or averaged values,

$$\overline{\zeta} \equiv \langle\zeta\rangle, \qquad \overline{\kappa} \equiv \langle\kappa\rangle, \qquad \overline{\xi} \equiv \langle\xi\rangle. \quad (3.97)$$

Reynolds-filtering (3.89) and using the expression (3.96), we obtain the filtered evolution equations for ζ, κ and ξ. The filtered equation for ζ is given by

$$\left\langle \frac{\mathrm{D}\zeta}{\mathrm{D}t} \right\rangle = -2\,\mathrm{tr}\,\mathrm{sym}\,\left(\langle \boldsymbol{G}\cdot\boldsymbol{E}'\rangle - \langle \boldsymbol{G}\cdot\boldsymbol{u}'\rangle\cdot\boldsymbol{\nabla}\overline{\boldsymbol{F}}^{\mathsf{T}}\cdot\overline{\boldsymbol{F}}^{-\mathsf{T}} \right) - \mathrm{tr}\,\left(-\langle \boldsymbol{u}'\cdot\boldsymbol{\nabla}\boldsymbol{G}\rangle + \langle \boldsymbol{M}\cdot\boldsymbol{G}^{-1}\rangle - \overline{\boldsymbol{M}} \right) \quad (3.98)$$

where each term can be compared to those in (3.96) that were described in the previous subsection. Similarly, the filtered equation for κ is given by

$$\frac{1}{2}\left\langle \frac{\mathrm{D}\kappa}{\mathrm{D}t} \right\rangle = 2\,\mathrm{tr}\,\left\langle \mathrm{sym}\,\left(\boldsymbol{E}' - \boldsymbol{u}'\cdot\boldsymbol{\nabla}\overline{\boldsymbol{F}}^{\mathsf{T}}\cdot\overline{\boldsymbol{F}}^{-\mathsf{T}} \right)\cdot\boldsymbol{\mathcal{G}} \right\rangle - \mathrm{tr}\,\left\langle \boldsymbol{M}\cdot\boldsymbol{G}^{-1}\cdot\boldsymbol{\mathcal{G}} \right\rangle$$
$$- \mathrm{tr}\,\left\{ \left[2\,\mathrm{sym}\,\left(\langle \boldsymbol{G}\cdot\boldsymbol{E}'\rangle - \langle \boldsymbol{G}\cdot\boldsymbol{u}'\rangle\cdot\boldsymbol{\nabla}\overline{\boldsymbol{F}}^{\mathsf{T}}\cdot\overline{\boldsymbol{F}}^{-\mathsf{T}} \right) - \langle \boldsymbol{u}'\cdot\boldsymbol{\nabla}\boldsymbol{G}\rangle - \overline{\boldsymbol{M}} \right]\cdot\langle\boldsymbol{\mathcal{G}}\rangle \right\}. \quad (3.99)$$

3.4 Case study: viscoelastic turbulent channel flow

The general framework we have developed can be applied to a variety of flows. We focus on the classical problem of viscoelastic turbulent channel flow as a case study and use direct numerical simulations (DNS) to investigate the turbulent dynamics. The algorithmic details of the simulation are documented in appendix B. The code employed was validated against linear growth rates of Tollmien–Schlichting waves (see

chapter 4) and also against the results for the evolution of a localized disturbance in shear flow.[187]

The simulation setup and flow geometry is the same as that described in §1.3.1. The parameters for the calculation are listed in Table 3.1 and 3.2. The friction Reynolds number Re_τ is defined based on the friction velocity and channel half-height. The friction velocity in the present work is calculated using the slope of the mean velocity at the wall and thus ignores the direct contribution of the polymer stress to the shear stress at the wall ($\sim \mathrm{d}\mathcal{T}_{xy}/\mathrm{d}y$). This assumption is reasonable in the limit $(1-\beta)/(Re\,Wi) \to 0$. In the present simulations $(1-\beta)/(Re\,Wi) \sim \mathcal{O}(10^{-6})$. The symbol $\langle\cdot\rangle$ denotes averaging over x, z and t. Therefore, all of the averaged quantities are functions of only y.

The computational grid is uniform in the (x, z) directions and employs hyperbolic tangent stretching in the y-direction with a Planck taper[188] applied such that grid spacing very close to the wall is constant. The maximum change of the grid spacing in the y-direction is less than 3% throughout in the domain. The details of the spatiotemporal discretization is listed in Table 3.2. The initial turbulent state was generated from a separate simulation that followed the evolution of a Tollmien–Schlichting wave to the fully turbulent state.[91] A snapshot from the fully turbulent state from previous work[91] was used as an initial condition and first run for at least 150 convective time units before any statistics were collected. The evolution of the friction Reynolds number, Re_τ, was used to check whether the simulation had reached

Re	Re_τ	Wi	$L_{\max}$	β	Domain size $L_x \times L_y \times L_z$
4667	180	6.67	100	0.9	$4\pi \times 2 \times 4\pi$

Table 3.1: Physical parameters used in the simulation of viscoelastic (FENE-P) turbulent channel flow. The size of the domain in the p-th direction is L_p.

Grid size $N_x \times N_y \times N_z$	Time step Δt	Spatial resolution $\Delta_x^+ \times \Delta_y^+ \times \Delta_z^+$
$512 \times 400 \times 512$	2.5×10^{-3}	$4.42 \times [0.13, 1.90] \times 4.42$

Table 3.2: Details of the spatiotemporal discretization for the viscoelastic (FENE-P) turbulent channel flow simulation. In the p-th directon, the number of grid points is N_p, and the spatial resolution, in friction units, is Δ_p^+. See also Table 3.1.

a statistically stationary state.

3.4.1 Mean profiles and comparisons with the laminar profiles

The statistics presented in this section were obtained by averaging in space and over 750 time units, and by exploiting the symmetry of the flow about the centreline. Halving the number of samples maintained the trends and caused only minor deviations in the statistics, with no impact on the conclusions.

The mean streamwise velocity profile is shown in figure 3.2 as a function of $y^+ = Re_\tau(y+1)$, where Re_τ is always taken to be the turbulent frictional Reynolds number

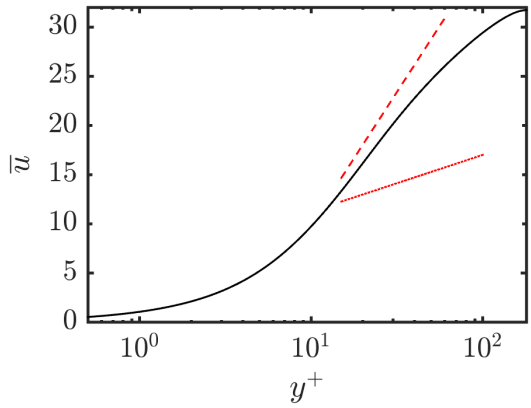

Figure 3.2: Mean velocity profile from a FENE-P drag-reduced channel flow simulation. The solid line (——) is the mean streamwise velocity, the red dotted (lower) line (·····) is the von Kármán log-law, $\overline{u}^+_{\text{von Kármán}} = 2.5y^+ + 5.5$, and the red dashed (upper) line (– – –) is Virk's asymptote, $\overline{u}^+_{\text{Virk}} = 11.7y^+ - 17.0$.

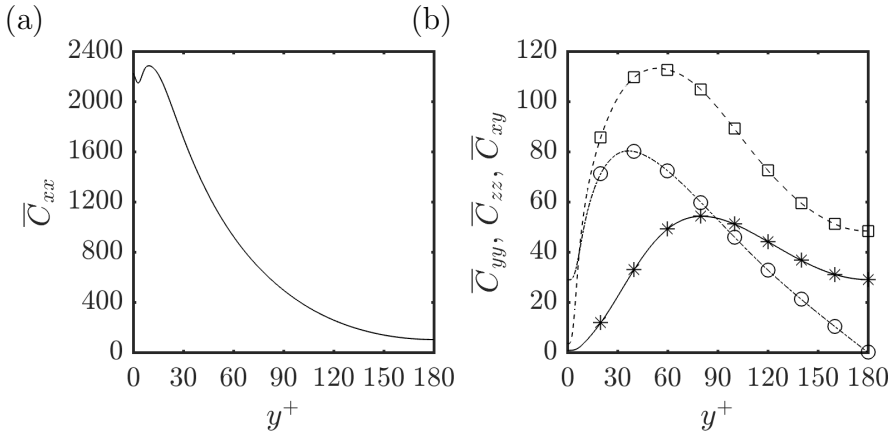

Figure 3.3: Mean conformation tensor profiles from a FENE-P drag-reduced channel flow simulation. (a) $\overline{C}_{xx}$ (b) the solid line with star symbols (—∗—) is $\overline{C}_{yy}$, the dashed line with square symbols (– –□– –) is $\overline{C}_{zz}$, and the dashed-dot line with circle symbols (–·○–·) is $\overline{C}_{xy}$. The remaining components of the mean conformation tensor are 0. Note that the symbols in (b) are identifiers and are thus only a small subset of all the data points used in the line plots.

given in Table 3.1. Also shown are the von Kármán log-law and Virk's maximum drag reduction asymptote. The mean velocity lies in between these two lines, indicating a drag-reduced state. Using Dean's correlation for the skin-friction,[189] we obtain a friction Reynolds number of approximately 284 for a Newtonian flow with $Re = 4667$ and thus the drag reduction percentage is

$$\mathrm{DR}\% \equiv \left[1 - \left(\frac{Re_\tau}{Re_\tau|_{\mathrm{Newtonian}}}\right)^2\right] \times 100 = 59.8\%. \tag{3.100}$$

The non-zero components of $\langle \boldsymbol{C} \rangle$ calculated for the same parameter values, are shown in figure 3.3. All the components of $\langle \boldsymbol{C} \rangle$ are even functions of y except $\langle C_{xy} \rangle$, which is an odd function of y. The streamwise stretch $\langle C_{xx} \rangle$ is four times larger than the laminar case (not shown) near the wall. It is also an order of magnitude larger than $\langle C_{yy} \rangle$ and $\langle C_{zz} \rangle$. The remaining normal components of the conformation tensor are also larger in the turbulent case than the laminar: figure 3.3 shows that $\max_y \langle C_{yy} \rangle \approx 45$ and $\max_y \langle C_{zz} \rangle \approx 120$, while $C_{yy} = C_{zz} \approx 1$ throughout the channel when the flow is laminar. The peak values of each of the components $\langle C_{xx} \rangle$, $\langle C_{yy} \rangle$ and $\langle C_{zz} \rangle$ occur at different locations in the channel. Figure 3.3 also shows that $\langle C_{zz} \rangle \geq \langle C_{yy} \rangle$ throughout the channel. The trends above are consistent with those reported in the literature.[190]

Figure 3.4(a) shows the logarithmic volume of the mean and laminar conformation tensors along with the distance from the origin on the manifold of positive-definite

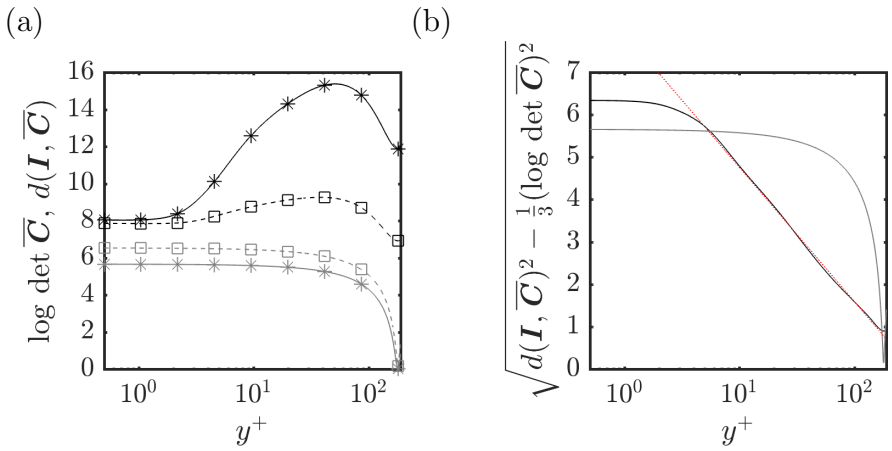

Figure 3.4: Scalar measures applied to nominal conformation tensors, in equivalent dimensions, plotted as functions of y^+. (a) The solid line with star symbols (—∗—) is log det $\overline{\boldsymbol{C}}$, the logarithmic volume; the dashed line with square symbols (– – □– –) is $d(\boldsymbol{I}, \overline{\boldsymbol{C}})$, the geodesic distance between $\overline{\boldsymbol{C}}$ and $\boldsymbol{I}$ on $\mathbf{Pos}_3$, (b) anisotropy index, $\sqrt{(d(\boldsymbol{I}, \overline{\boldsymbol{C}}))^2 - \frac{1}{3}(\log \det \overline{\boldsymbol{C}})^2}$, which is the geodesic distance from the closest isotropic tensor. For both (a) and (b), black lines are for $\overline{\boldsymbol{C}} = \langle \boldsymbol{C} \rangle$ and grey lines are when $\overline{\boldsymbol{C}}$ is equal to the FENE-P laminar conformation tensor. The red dotted line (------) in (b) is $-1.375 \log y^+ + 7.925$. Note that the symbols in (a) are identifiers and are thus only a small subset of all the data points used in the line plots.

tensors. The figure shows that both the logarithmic volume, log det $\overline{\boldsymbol{C}}$, and the distance from the origin, $d(\boldsymbol{I}, \overline{\boldsymbol{C}})$ are larger in the turbulent case compared to the laminar. Furthermore, these two quantities are monotonically decreasing in the laminar case but have peaks around $y^+ \approx 60$ in the turbulent case. Both quantities in the two cases asymptote to a constant at locations very close to the wall, $y^+ \leq 2$. The weak growth in $d(\boldsymbol{I}, \overline{\boldsymbol{C}})$ in the turbulent case despite a rapid increase in log det $\overline{\boldsymbol{C}}$ is due to the increase in isotropy (sphericity) as we move away from the wall, since for a given volume the tensor closest to $\boldsymbol{I}$ is an isotropic tensor. In figure 3.3 we see that the mean normal stretches in the y and z directions in the turbulent case peak between $y^+ \approx 40$ and $y^+ \approx 70$ and are at least an order of magnitude larger than the stretches in the laminar case, where $\overline{C}_{yy} = \overline{C}_{zz} \approx 1$. The term $\overline{C}_{xx}$ is decreasing towards the channel centre in both the turbulent and laminar case but is accompanied by an increase in $\overline{C}_{yy}$, $\overline{C}_{zz}$ in the turbulent flow which leads to increased isotropy for locations sufficiently removed from the wall.

Figure 3.4(b) shows the anisotropy, the geodesic distance to the closest isotropic tensor, of the mean and laminar conformation tensors. The anisotropy index is approximately constant in the vicinity of the wall for both the laminar and turbulent cases, and decays away from the wall. In the turbulent flow, the decay starts very close to the wall — approximately three friction units away from the wall, and then shows a remarkable logarithmic decay that proceeds all the way to very close to the centreline where it sharply turns and forms a stationary point. The increased isotropy

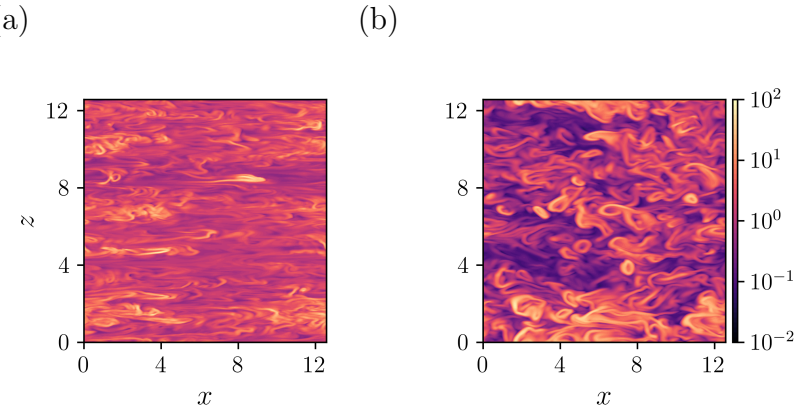

Figure 3.5: Wall-parallel (x, z) planes of isocontours of instantaneous $\mathrm{I}_{\boldsymbol{G}} = \mathrm{tr}\,\boldsymbol{G}$. (a) at $y^+ = 15$ and (b) $y^+ = 180$ (centreline).

in the turbulent case may be explained by the fact that, although more stretching occurs in this case, the stretching in the cross-stream directions is much larger than in the laminar case. Overall, this leads to a more isotropic mean conformation tensor.

3.4.2 Invariants of the fluctuating conformation tensor

In order to motivate the scalar measures proposed in the present work, we consider the invariants of $\boldsymbol{G}$ as alternatives in this subsection. Figure 3.5 shows isocontours of instantaneous $\mathrm{I}_{\boldsymbol{G}}$ at a given time at two wall-parallel planes, $y^+ = 15$ and $y^+ = 180$ (centreline). The isocontours of instantaneous $\mathrm{II}_{\boldsymbol{G}}$ and $\mathrm{III}_{\boldsymbol{G}}$ are qualitatively similar to those of $\mathrm{I}_{\boldsymbol{G}}$ and are thus not shown here. The instantaneous $\mathrm{I}_{\boldsymbol{G}}$ can vary over several orders of magnitude. As a result, obtaining reliable statistics for the invariants

is challenging. We found that the peak root-mean-square (RMS) of the invariants (not shown) are at least an order of magnitude larger than the corresponding mean values. This large spread in the instantaneous invariants of $\boldsymbol{G}$ suggests that log $\boldsymbol{G}$ is a more appropriate quantity to consider, and reinforces the need for the geometrically consistent scalar measures introduced in §3.3.

3.4.3 The scalar measures: ζ, κ and ξ

Figure 3.6 shows isocontours of instantaneous values of ζ, κ and ξ for two wall-parallel planes, $y^+ = 15$ and $y^+ = 180$. As a comparison, the fluctuating tensor $\boldsymbol{C}'_{xx}$ obtained by the Reynolds decomposition (3.2) and normalized by the local $\overline{\boldsymbol{C}}_{xx}$ is shown in figure 3.7. We normalized $\boldsymbol{C}'_{xx}$ so that the fluctuations near the wall could be compared to those at the centreline, since $\overline{\boldsymbol{C}}_{xx}$ differs by an order of magnitude between the two locations. The isocontours of $C'_{xx}/\overline{\boldsymbol{C}}_{xx}$, and in particular the negative values, are difficult to interpret since the correspondence to a physical deformation or a mathematical metric is unclear.

Figures 3.6(a)–(b) show the logarithmic volume ratio, ζ. This quantity is the logarithm of $\mathrm{III}_{\boldsymbol{G}}$, which itself is qualitatively similar to $\mathrm{I}_{\boldsymbol{G}}$ and hence we observe a strong visual resemblance between figures 3.5 and 3.6(a)–(b). The colour scale in the former is logarithmic and is thus consistent with the linear scale in figure 3.6. Both figure 3.6(a) and (b) have predominantly negative values, indicating that the instantaneous volume is smaller than the volume of the mean conformation. We also

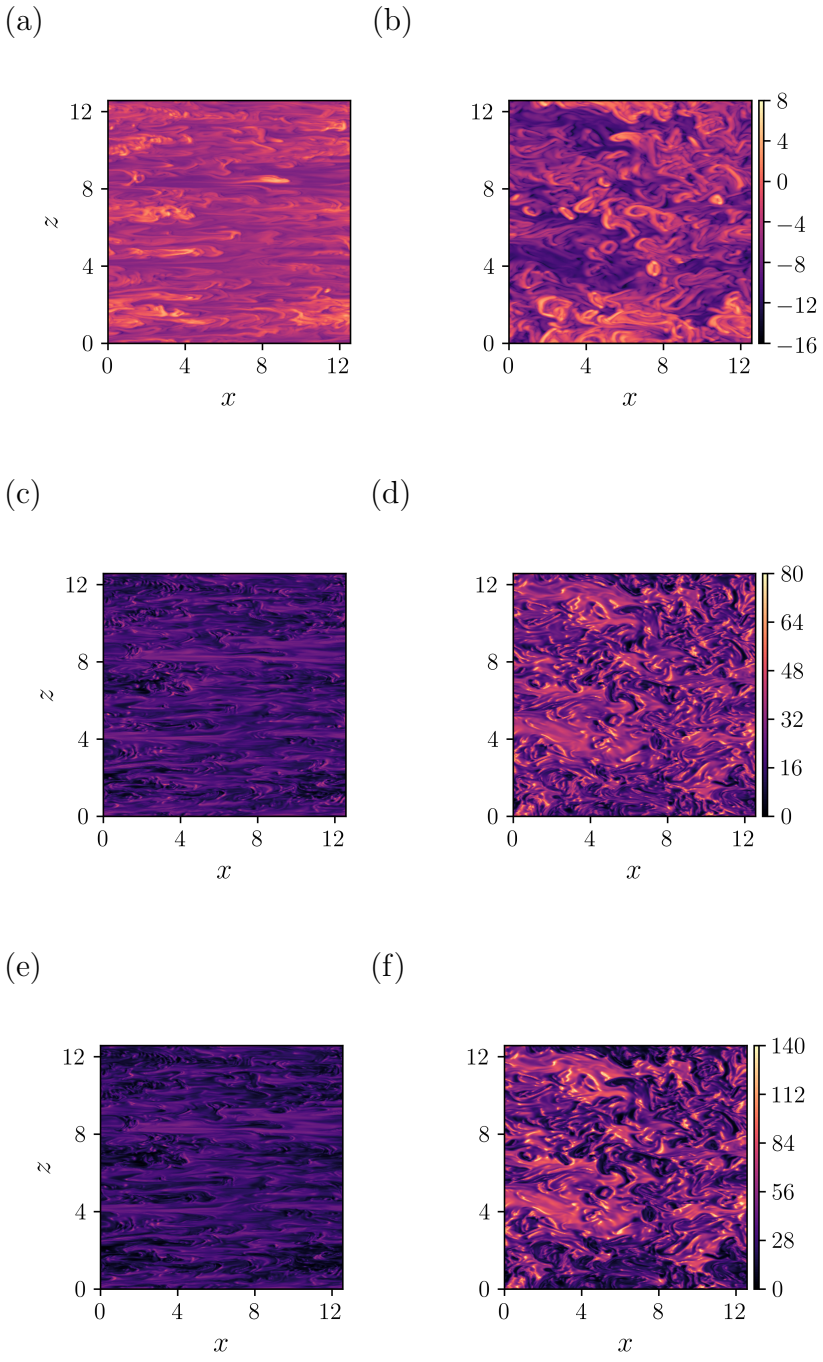

Figure 3.6: Wall-parallel (x, z) planes of isocontours of instantaneous (a)–(b): logarithmic volume ratio, ζ, (c)–(d): geodesic distance from the identity, κ, and (e)–(f): anisotropy index, ξ. (a),(c), and (e): $y^+ = 15$. (b), (d), and (f): $y^+ = 180$ (centreline).

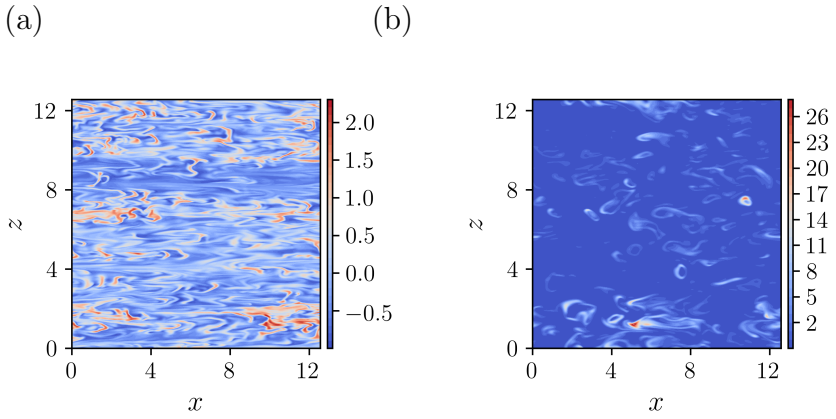

Figure 3.7: Wall-parallel (x, z) planes of isocontours of instantaneous $C'_{xx}/\overline{C}_{xx}$ at (a) $y^+ = 15$ (b) $y^+ = 180$ (centreline), where $\overline{C}_{xx}(y^+ = 15) = 2.22 \times 10^3$ and $\overline{C}_{xx}(y^+ = 180) = 1.02 \times 10^2$. The limits of the divergent colour map are set at the planar maxima and minima of $C'_{xx}/\overline{C}_{xx}$.

find regions of very high ζ adjacent to regions of very low values, especially at the centreline. This is partially a result of the lack of diffusion in the polymers since there is no direct mechanism for smoothing out shocks in the conformation tensor field.

Another important effect is that of memory: polymers are stretched near the wall where the shear is significant, and are then transported out to the centreline. If the the half-channel transit time, the ratio of the channel half-height to the RMS wall-normal velocity, is smaller than the polymer relaxation time, we expect to observe a footprint of the near-wall stretching all the way out to the centreline. In the present case, the relaxation time is two to three times the half-channel transit time. Since material points that are initially close are exponentially diverging in a turbulent flow,[191] it is unsurprising to find adjacent regions of strongly and weakly stretched polymers.

The reductionist explanation given above is useful for a basic understanding but is

insufficient to account for other observed features of the flow. For example, the present considerations would suggest that the streamwise elongated shape of the isocontours of ζ near the wall would lead to a similar shape at the centreline. However, this is manifestly not the case. Instead, the ζ field appears to generate, on the whole, highly curved isocontours at the centre of the channel.

The measure ζ does not distinguish between volume-preserving deformations. For example, ζ does not distinguish between $\boldsymbol{C}$ and (det $\boldsymbol{C}$)$\boldsymbol{A}$ for *any* $\boldsymbol{A}$ with determinant $= 1$. In particular, $\zeta = 0$, does not imply $\boldsymbol{C} = \overline{\boldsymbol{C}}$. In order to identify regions where $\boldsymbol{C} = \overline{\boldsymbol{C}}$ is true, and quantify the deviation when it is not, we use the squared distance away from the origin ($\boldsymbol{I}$) along the manifold, κ. Figure 3.6(c)–(d) shows isocontours of instantaneous κ. Most of the conformation tensor field is significantly far away, in the sense of distance along the manifold, from $\overline{\boldsymbol{C}}$. However, regions where $\overline{\boldsymbol{C}}$ is a good representation of $\boldsymbol{C}$ are interspersed between regions where κ is large. This behaviour is true both in the near-wall region as well as the channel centre but more so in the latter. In contrast, it is well-known that kinetic energy fluctuations are weakest at the centreline in a Newtonian channel flow. A different behaviour for the polymers is unsurprising since, due to the strong memory effect, $\boldsymbol{C}$ at each point is strongly dependent on the Lagrangian path that is obtained by a pull-back of the particular Eulerian point of interest.

Figures 3.6(e)–(f) show isocontours of instantaneous ξ, the anisotropy index. This index shows how close the shape of instantaneous conformation tensor is to the shape

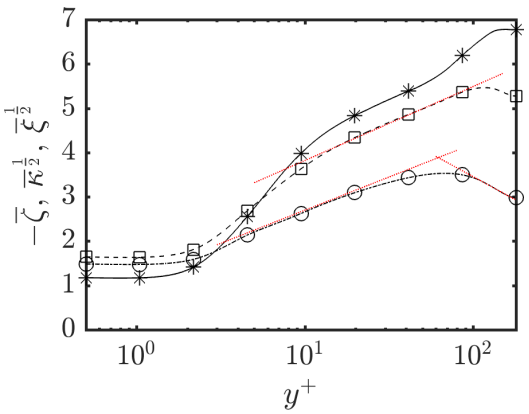

Figure 3.8: Mean scalar measures, plotted in equivalent dimensions, as functions of y^+. The solid line with star symbols (—∗—) is minus the mean volume ratio: $-\overline{\zeta} = -\langle\zeta\rangle$, the dashed line with square symbols (– –□– –) is the square–root of the mean geodesic distance from the identity: $\overline{\kappa}^{\frac{1}{2}} = \sqrt{\langle\kappa\rangle}$, the dashed-dot line with circle symbols (–·○–·) is the square–root of the mean anisotropy index: $\overline{\xi}^{\frac{1}{2}} = \sqrt{\langle\xi\rangle}$. Red dotted lines (·····) are logarithmic fits to the profiles: the fit to the $\overline{\kappa}^{\frac{1}{2}}$ profile (– –□ – –) is given by $0.725 \log y^+ + 2.15$, the fits to the $\overline{\xi}^{\frac{1}{2}}$ profile (–·○–·) are given by $0.65 \log y^+ + 1.20$ and $-0.9 \log y^+ + 7.6$. Note that the symbols are identifiers and are thus only a small subset of all the data points used in the line plots.

of the mean conformation tensor, irrespective of volumetric changes. The visual resemblance of κ and ξ suggests that deformations to the mean conformation are largely anisotropic, or in other words, lead to shape change.

Figure 3.8 shows the mean values of ζ , κ and ξ in dimensions of distance along the manifold. These statistics were generated using 225 convective time units. We checked for convergence by halving the number of samples. This process led to only minor deviations in the results, with no material significance to the discussion that follows. As was inferred earlier, the average logarithmic volume ratio is negative throughout the channel and is monotonically decreasing towards the centreline where it becomes roughly constant, similar to the behaviour very near the wall $y^+ \lesssim 2$.

This behaviour of the mean logarithmic volume being smaller than the volume of the mean is consistent with the 'swelling' problem associated with the arithmetic mean of positive-definite tensors that has been previously reported in the literature.[192] It also suggests that, although an arithmetic mean of the conformation tensor may be unavoidable for modelling in the averaged equations, it may not be the most representative conformation tensor for deducing the most likely physical deformation of the polymers. A more extensive study, beyond the scope of the present work, is required to determine better alternatives to the arithmetic mean.

The square–root mean squared distance from the origin along the manifold, $\overline{\kappa}^{\frac{1}{2}}$, is logarithmically increasing up to close to the centreline but peaks at $y^+ \approx 100$. The anisotropy, $\overline{\xi}^{\frac{1}{2}}$, shows logarithmic increase over a small range $3 \lesssim y^+ \lesssim 20$, peaking at $y^+ \approx 60$, but then shows a logarithmic decrease towards the centreline. The logarithmic behaviour in these quantities, especially in $\overline{\kappa}^{\frac{1}{2}}$ where the behaviour extends over a significant range, resembles the behaviour that appears in the mean velocity as well as in the statistical moments and two-point correlations of the velocity fluctuations in wall-bounded shear flows.[193,194]

If we momentarily accept the simplified picture of polymers being deformed closer to the wall in an 'active' region and then passively transported out to the centreline of the channel, then these results indicate that the active region of the channel exists all the way up to $y^+ \approx 100$. Beyond this region, the stretching of polymers weakens and thus $\overline{\kappa}^{\frac{1}{2}}$ decreases monotonically. The active region involves a region of logarithmic

increase, and so we can write $\overline{\kappa}^{\frac{1}{2}} = a_1 \int y^{-1}\,\mathrm{d}y + a_0$ for constants a_1 and a_0. If the stretching at each wall-normal station is actually additive, the polymers are undergo deformation that on average leads to a diminishing increment in the deformation. This behaviour is consistent with the velocity gradients weakening with wall-normal distance. At $y^+ \approx 100$, the velocity gradients then either weaken or act on such long time scales that polymers relax quickly enough not to retain any additional deformation.

In order to quantify the fluctuations observed in figure 3.6 in more detail, we calculated the joint probability density function (JPDF) for ζ and κ using 12 snapshots evenly spaced over 120 convective time units. The JPDF, at four different wall-normal locations, are shown in figure 3.9 along with isocontours of ξ, which is purely a function of ζ and κ.

The JPDF are non-zero primarily on the lower half of the realizability region, which is consistent with the isocontours in figure 3.6(a)–(b) and $\overline{\zeta} < 0$ throughout the channel in figure 3.8. In addition, the isocontours tend to concentrate along the isotropy line (thick red dashed line) that was derived in (3.69) as a realizability bound. However, with the exception of the centreline, the most probable (ζ, κ) are located away from the isotropy line. This implies that the most likely conformation tensor away from the centreline does not have the same shape as the local mean conformation tensor. Although the most likely conformation tensor at the centreline assumes the shape of the mean conformation tensor, the JPDF at the centreline occupies a greater

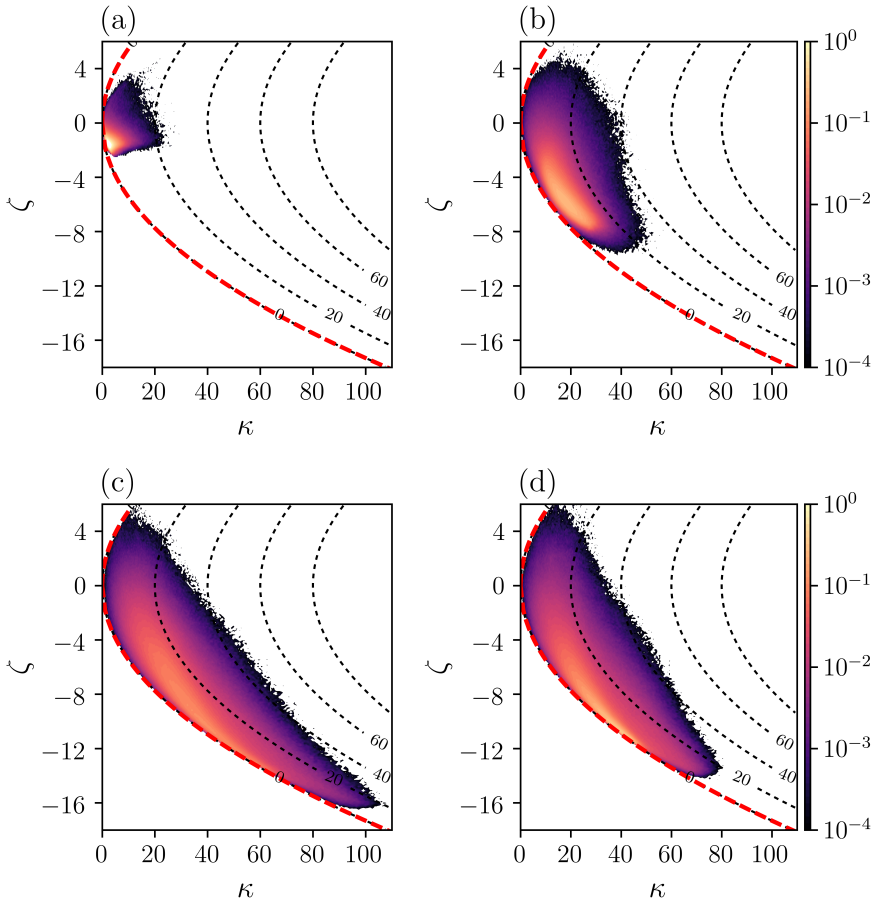

Figure 3.9: Joint probability density functions (JPDF) of the logarithmic volume ratio, ζ, and the geodesic distance from the identity, κ, at four different wall-normal locations: (a) $y^+ = 2$, (b) $y^+ = 15$, (c) $y^+ = 100$ and (d) $y^+ = 180$ (centreline). Dotted lines (------) are isocontours of the anisotropy index, ξ. The thick red dashed line (- - -) denotes the realizability bound, $\kappa = \frac{1}{3}\zeta^2$, derived in (3.69), which coincides with the zero anisotropy index isocontour ($\xi = 0$).

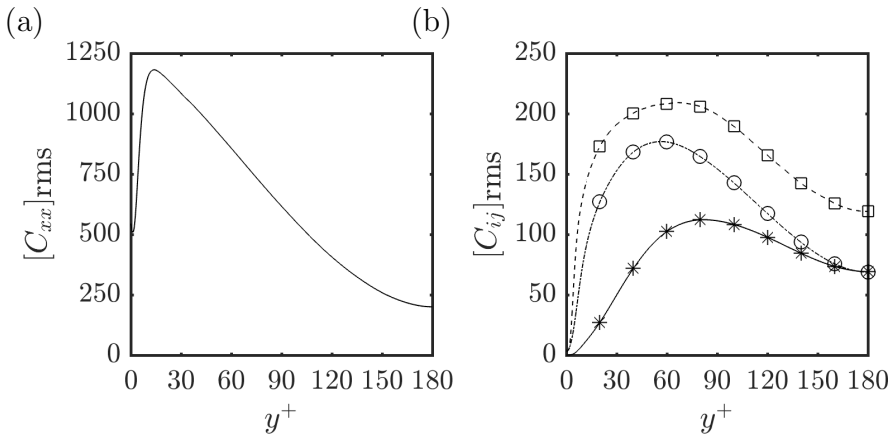

Figure 3.10: Root-mean-square profiles of $\boldsymbol{C}'$, $[C_{ij}]_{\text{rms}} = \sqrt{\langle C_{ij}^2 \rangle - \langle C_{ij} \rangle^2}$ based on the Reynolds decomposition (3.2). (a) $[C_{xx}]_{\text{rms}}$ (b) the solid line with star symbols (—∗—) is $[C_{yy}]_{\text{rms}}$, the dashed line with square symbols (−−□−−) is $[C_{zz}]_{\text{rms}}$, and the dashed-dot line with circle symbols (−·○−·) is $[C_{xy}]_{\text{rms}}$. Note that the symbols in (b) are identifiers and are thus only a small subset of all the data points used in the line plots.

area in the (ζ, κ) plane than at $y^+ = 2$ or $y^+ = 15$ which implies a greater degree of uncertainty. In addition, the most likely conformation tensor, as determined by the peak of the JPDF, is further away from the mean than at any other wall-normal location.

The JPDF indicate that the most intermittent region of the flow, determined by the most extreme excursions away from the identity on $\mathbf{Pos}_3$, do not occur near the wall or at the centreline. This can be seen in figure 3.9, where the JPDF at $y^+ = 100$ shows events with up to $\kappa = 100$. This behaviour is consistent with the peak $\overline{\kappa}$ occurring away from the centreline in figure 3.8.

Finally the RMS of $\boldsymbol{C}'$, defined according to the Reynolds decomposition (3.2), is shown in figure 3.10 for comparison to the present approach. The protocol used to

obtain these quantities was the same as that used to obtain the mean conformation tensor in figure 3.3. The RMS of $\boldsymbol{C}'$ are of similar magnitude to the components of $\langle \boldsymbol{C} \rangle$. In fact, the peak RMS of C_{yy}, C_{zz} and C_{xy} are larger than their respective mean values. Interestingly, the peak fluctuating deformation found at $y^+ \approx 100$ using our present framework is not discernible from the RMS fluctuations. Different components of the RMS tensor peak at different locations in the channel with $[C_{yy}]_{\mathrm{rms}}$ showing a peak that is closest to $y^+ = 100$. The RMS quantities only show the component-wise behaviour of the conformation tensor, and hence are not indicative of the total polymer deformation. A more appropriate quantity to evaluate in the context of $\boldsymbol{C}'$ would then be the JPDF of all six independent components of $\boldsymbol{C}'$. Owing to high-dimensionality, this characterization is more difficult to both calculate and analyse. The scalar measures suggested in the present work provide a good alternative to such a characterization.

3.5 Conclusion

We have developed a geometric decomposition, given in (3.12), that overcomes the difficulties associated with the traditional Reynolds decomposition of $\boldsymbol{C}$. The geometric decomposition yields a conformation tensor, $\boldsymbol{G}$, that describes the deformation of the polymer with respect to the mean deformation. We characterized the fluctuations in $\boldsymbol{G}$ by using a geometry specifically constructed for $\mathbf{Pos}_3$ and obtained

three scalar measures: the logarithmic volume ratio, ζ, given in (3.53), the squared geodesic distance of the perturbation conformation tensor away from the origin, κ, given in (3.55), and the anisotropy index, ξ given in (3.73), defined as the squared geodesic distance to the closest isotropic tensor. The average values and JPDF of these scalar measures provided interesting insights about the fluctuating polymer deformation that are not readily available from a Reynolds decomposition of $\boldsymbol{C}$. These insights include the following:

1. The anisotropy in $\overline{\boldsymbol{C}}$, measured as geodesic distance away from $\boldsymbol{I}$ on $\mathbf{Pos}_3$, decreases logarithmically from $y^+ = 5$ to close to the centreline.

2. The mean conformation tensor tends to be significantly different than the most likely conformation tensor observed in the flow.

3. The mean polymer deformation, measured in terms of $\overline{\kappa}$, increases logarithmically from $y^+ = 10$ and peaks at $y^+ \approx 100$.

4. As evidenced by the JPDF of κ, the peak turbulence intensity in the polymers occurs in between the wall and centreline, at approximately $y^+ \approx 100$.

The universality of the trends mentioned above, and others documented in the present work, and their connection to larger issues in viscoelastic turbulence are open questions. The framework we have developed can be used to probe the dynamics in viscoelastic turbulence beyond channel flow and can also be exploited for developing and benchmarking reduced-order models for viscoelastic turbulence. The approach

can also be adapted to other similar problems, for example in the analysis of deforming droplets in turbulence using a model based on the droplet conformation tensor.[151,195]

An important, open question that needs to be resolved in future work is the relationship between the fluctuating conformation tensor $\boldsymbol{G}$ and elastic energy of the polymers. In contrast to the clear meaning of the kinetic energy associated with fluctuating velocity field, a deeper understanding of the elastic energy and its relation to $\boldsymbol{G}$, and the scalar measures introduced in the present work, is unavailable. The attainment of such an understanding is partially hindered by the myriad of constitutive models prevalent in the literature.[102] Instead of using the details of a particular constitutive model, the aim of the present work was to maintain as much generality as possible by exploiting the mathematical structure of $\boldsymbol{G}$ to characterize the fluctuating polymer deformation.

Chapter 4

Perturbations to the conformation tensor

4.1 Introduction

When analysing viscoelastic flows, we are frequently interested in generating small perturbations to a given base-flow conformation tensor, e.g. for linear stability analysis or for deriving solutions for a flow that can be cast as a small perturbation of a known flow solution. The standard approach is a generalization of the weakly nonlinear expansions, as in (1.2), used for the velocity field: the perturbed conformation tensor is a sum of the base-flow tensor and a perturbation tensor, a symmetric tensor expressed as a series expansion in a small parameter. This approach has been used in a myriad of different ways in the literature and has proven useful for extracting

important mechanisms from the governing equations. However, unlike for the velocity field, the standard method has several important limitations when applied to the conformation tensor, including: (a) the perturbation tensor has no physical interpretation like the conformation tensor (b) finite-amplitude perturbations are not possible in general and (c) the norm of the perturbation tensor is not an appropriate metric to quantify the size of the perturbation. In this chapter, we address these limitations by developing a framework to generate perturbations that are consistent with the physical interpretation of the conformation tensor. The framework helps to reconcile classical linear stability analysis and weakly nonlinear expansions with the physical interpretation of the conformation tensor and the geometry of the set of positive–definite tensors.

Studies utilizing conformation tensor perturbations have yielded important predictions regarding viscoelastic flows that have then been confirmed in experiments. We review some of these studies below. An infinitesimally small linear perturbation is the simplest form of the perturbation tensor and has been widely used for linear stability analysis and also for energy amplification. Linear stability analysis was early on found to predict purely elastic two-dimensional instabilities in flows with curved streamlines,[78,79] a result that was later confirmed by Groisman and Steinberg[13,14] in low Reynolds number experiments. This remarkable discovery increased interest in possible curvature-independent elastic instabilities, particularly in viscoelastic channel flow where increasing elasticity beyond a certain minimum threshold increases the

critical Reynolds number.[91] In this flow, Jovanović and Kumar[196] found that linearly stable perturbations to the conformation tensor can nevertheless show significant amplification and transient growth due to purely elastic mechanisms. These authors suggested that the amplification, which exists even in the complete absence of inertia,[197] may be sufficient to trigger nonlinear instabilities. A purely elastic nonmodal route to instability was also anticipated by Doering *et al.*[198] Although elasticity leads to unique amplification mechanisms in two-dimensions, e.g. the reverse Orr mechanism,[105] the most amplified perturbations are generally three-dimensional.[199,200] Meulenbroek *et al.*[201] used weakly nonlinear expansions to show that sufficiently large transient growth in a viscoelastic channel flow acting over a slow time scale appears as a streamline curvature-inducing modification to the base-state, thereby producing the necessary conditions for a fast time scale curved streamline instability. These theoretical results predicting an elastic instability in channel flow were experimentally confirmed by Pan *et al.*[15] as well as by Qin and Arratia,[16] who found a turbulent-like in a channel flow at low Reynolds number. Another way in which perturbation expansions have been used is to derive exact solutions, and associated asymptotic dynamics. Page and Zaki[202] considered laminar viscoelastic channel flow with a wavy wall and found exact solutions in terms of Hankel functions. The authors then used perturbation expansions to derive reduced dynamics in various asymptotic limits, which revealed the underlying physical mechanisms in these limits, e.g. the existence of an elastic critical layer that mediates the dynamics. The results of Page and Zaki

were partially reproduced in experiment by Haward and Shen.[203]

Despite the success described above, the standard approach to perturbing the conformation tensor is not satisfactory because the conformation tensor is a positive–definite tensor and $\mathbf{Pos}_3$ does not form vector space; the non-Euclidean geometry of $\mathbf{Pos}_3$ was described in detail in §3.3. As a result, several issues arise with the standard approach to perturbations that do not arise when we perturb a vector space quantity like the velocity field. These issues are similar to those that arise with the Reynolds decomposition of the conformation tensor and which were discussed in chapter 3. We examine some of these issues below. The perturbation tensor used in the standard approach is not a conformation tensor, but rather a symmetric tensor that can only be interpreted component-wise. Thus, quantities that depend on the tensorial nature of the perturbation are meaningless, e.g. the eigenvalues, which are not necessarily positive, are no longer representative of the principal stretches of the polymer. The perturbation magnitude can also only be infinitesimal in general because a finite-amplitude perturbation may violate the positive–definiteness requirement on the conformation tensor. An example of such an issue arises when generalizing the Stuart's projection[204] to viscoelastic flows. Here we use a base-state augmented with the associated linear modes at finite-amplitude to describe a nonlinear flow state. The relevant amplitudes can be explicitly calculated in viscoelastic Taylor-Couette flow, but the resulting polymer stress turns out to be physically unrealizable due to a violation of the positive–definiteness constraint on the associated conformation tensor (T.

A. Zaki, private communication, January 10, 2018). Another issue that arises is that there is no appropriate functional norm that can be used to quantify the magnitude of the conformation tensor and the perturbation. The lack of a functional norm was noted by Doering *et al.*[198] as an obstacle to performing energy stability analysis in viscoelastic flows. The authors found that using the elastic energy was problematic because it was not strictly a metric and, in particular, did not satisfy the triangle inequality. In prior work, the issues outlined above, and others that arise because the conformation tensor is not a vector space quantity, are frequently concealed because the polymer stress is used instead of the conformation tensor. While the former does not strictly need to be positive–definite, it is positive–definite up to an additive constant for most models of interest. Furthermore, the dynamics are usually expressed in terms of the conformation tensor rather than the polymer stress.

In this chapter, we formulate a geometrically and physically consistent approach to generate small perturbations to the conformation tensor, analogous to the weakly nonlinear expansion of the velocity field in (1.2). The approach relies on exploiting the interpretation of the conformation tensor as the left Cauchy-Green tensor that was shown in chapter 2 and the geometry of the manifold of positive–definite tensors that was introduced in chapter 3. The perturbation is cast as a sequence of successively smaller deformations to the base-state. When specialized to a single deformation, the approach reduces to the standard method used for linear perturbations but now with an explicit underlying physical interpretation and also an inherent geometric

structure derived from the manifold geometry. The framework provides new physical insights into polymer dynamics, and has implications for studies utilizing small perturbations to the conformation tensor since it resolves the outstanding issues with the standard approach that were highlighted in this introduction. Namely, the framework generates perturbation tensors that are physically meaningful as left Cauchy-Green tensors representing the perturbation polymer deformation. It provides a way to generate finite-amplitude perturbations whose size can be quantified using the geometric structure of the set of positive–definite tensors. In addition, explicit relationships can be found between the present and standard approaches used for generating small perturbations, both linear and weakly nonlinear. These relationships enrich our understanding of the approaches used so far in the literature.

We briefly comment on the standard approach to generate perturbations in §4.1.1.

4.1.1 The standard approach

The celebrated success of linear stability theory, which is founded on infinitesimal additive perturbations to the conformation tensor, owes itself to the tangent space structure of $\mathbf{Pos}_3$. An application of Weyl's theorem can be used to show that $\mathbf{Sym}_3$ is the local tangent space everywhere on $\mathbf{Pos}_3$. Thus, a sufficiently small additive perturbation by a symmetric tensor keeps the base-state conformation tensor, $\overline{\boldsymbol{C}}$, on $\mathbf{Pos}_3$. By assuming that perturbations are arbitrarily small, linear stability theory usually ignores the precise sense in which the perturbation, or distance be-

tween $\overline{\boldsymbol{C}}$ and the perturbed tensor, must be sufficiently small. This distance, which may be important in comparing the effect of different linear modes or for generating finite-amplitude perturbations in numerical calculations, cannot be evaluated using Euclidean distances because $\mathbf{Pos}_3$ is non-Euclidean. For example, let $\overline{\boldsymbol{C}} = \boldsymbol{I}$ and the conformation tensor, $\boldsymbol{C}$, be given by

$$\boldsymbol{C} = \overline{\boldsymbol{C}} + \epsilon \boldsymbol{I} = (1+\epsilon)\boldsymbol{I} \tag{4.1}$$

where $\epsilon \in \mathbb{R}$ is a perturbation parameter. The positive–definiteness constraint is satisfied for all positive ϵ, but we require $|\epsilon| < 1$ if ϵ is negative. However, the Euclidean distance from $\overline{\boldsymbol{C}}$ is the same for both positive and negative ϵ.

The asymmetry between positive and negative perturbations arises because the eigenvalues of the conformation tensor represent the principal stretches of the polymer normalized by the thermodynamic equilibrium stretch. Thus eigenvalues greater than 1 represent stretches, and those less than 1 represent compressions. Thus, the compression converse to the stretch $(1+|\epsilon|)\boldsymbol{I}$ is given by

$$\left(\frac{1}{1+|\epsilon|}\right)\boldsymbol{I} = \left(1 - |\epsilon| + |\epsilon|^2 - |\epsilon|^3 + \ldots\right)\boldsymbol{I} \tag{4.2}$$

which means that a negative ϵ in (4.1) is equivalent to a physical contraction up to $\mathcal{O}(\epsilon^2)$, an approximation that may be inadequate. It is not clear how to generalize the approach used for the simplified example presented here to more general cases. This

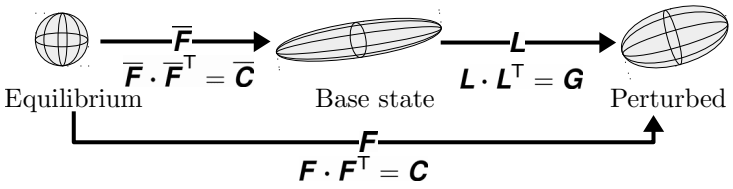

Figure 4.1: Schematic of the geometric decomposition, adapted from chapter 3.

discussion highlights the importance of defining a consistent geometry on $\mathbf{Pos}_3$ that allows us to measure distances and define shortest paths, and formulate perturbations with respect to that geometry.

The main theoretical results, which consistent of physically and geometrically meaningful perturbative expansions, are presented next in §4.2. The evolution equations relevant to the perturbation expansions are developed in §4.3. In §4.4, we illustrate our approach using direct numerical simulations of the nonlinear evolution of viscoelastic Tollmien-Schlichiting waves.[91] The chapter is concluded in §4.5.

4.2 Perturbative expansions

In order to generate perturbative expansions of the conformation tensor $\boldsymbol{C}$ about the base state $\overline{\boldsymbol{C}}$, we first define an appropriate fluctuating conformation. For this, we follow the approach adopted in chapter 3, which we outline below. Later, we will also exploit this approach to generate the perturbative expansion we are seeking.

As discussed in chapter 2 and 3, the conformation tensor is a left Cauchy-Green

tensor

$$\boldsymbol{C} = \boldsymbol{F} \cdot \boldsymbol{F}^{\mathsf{T}} = [\boldsymbol{I}]_{\boldsymbol{F}}\,, \tag{3.7}$$

where $\boldsymbol{F}$ is the total deformation gradient that describes deformation with respect to the thermodynamic equilibrium. We decompose this deformation into two deformations: a deformation about the thermodynamics equilibrium that yields the base state, and a deformation about the base state that yields the total deformation. Accordingly, we decompose the deformation gradient as follows

$$\boldsymbol{F} = \overline{\boldsymbol{F}} \cdot \boldsymbol{L} \tag{3.11}$$

where $\boldsymbol{L}$ is the fluctuating deformation gradient, and $\overline{\boldsymbol{F}}$ is the deformation gradient associated with $\overline{\boldsymbol{C}}$,

$$\overline{\boldsymbol{F}} = \overline{\boldsymbol{C}}^{\frac{1}{2}} \cdot \boldsymbol{R}. \tag{3.9}$$

Here $\boldsymbol{R} \in \mathbf{SO}_3$ is an arbitrary rotation tensor. It is readily verified that $\overline{\boldsymbol{C}} = \overline{\boldsymbol{F}} \cdot \overline{\boldsymbol{F}}^{\mathsf{T}}$. We set $\boldsymbol{R} = \boldsymbol{I}$ in the present work. The fluctuating deformation gradient has the associated tensor $\boldsymbol{G} = \boldsymbol{L} \cdot \boldsymbol{L}^{\boldsymbol{T}}$, which satisfies the relationship

$$\boldsymbol{C} = [\boldsymbol{G}]_{\overline{\boldsymbol{F}}} = \overline{\boldsymbol{F}} \cdot \boldsymbol{G} \cdot \overline{\boldsymbol{F}}^{\mathsf{T}} \tag{3.12}$$

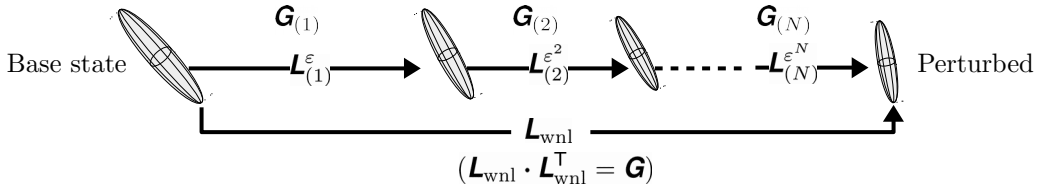

Figure 4.2: Schematic of a weakly nonlinear deformation, consisting of a sequence of successively smaller deformations.

The tensor $\boldsymbol{G}$ is positive–definite and is equivalent to $\boldsymbol{C}$ but is transformed so that $\boldsymbol{C} = \overline{\boldsymbol{C}}$ if and only if $\boldsymbol{G} = \boldsymbol{I}$. Thus $\boldsymbol{G}$ acts as a conformation tensor representing the fluctuation of $\boldsymbol{C}$ around $\overline{\boldsymbol{C}}$.

The geometry of $\mathbf{Pos}_3$ can be used to quantify the fluctuating polymer deformation. Using (3.43), the geodesic distance between $\boldsymbol{C}$ and $\overline{\boldsymbol{C}}$ can be written as

$$d(\overline{\boldsymbol{C}}, \boldsymbol{C}) = d(\boldsymbol{I}, \boldsymbol{G}) = \operatorname{tr} \boldsymbol{\mathcal{G}}^2 \tag{4.3}$$

where $\boldsymbol{\mathcal{G}} \equiv \log \boldsymbol{G}$, and is a measure of the mangnitude of the fluctuation. Similarly, we can evaluate whether a deformation is compressive or expansive with respect to the base state by examining the logarithmic volume ratio, $\operatorname{tr} \boldsymbol{\mathcal{G}}$.

4.2.1 Weakly nonlinear deformations

A weakly nonlinear expansion up to the N-th power of the velocity field is given by

$$\boldsymbol{u} = \overline{\boldsymbol{u}} + \boldsymbol{u}' = \overline{\boldsymbol{u}} + \sum_{k=1}^{N} \epsilon^k \boldsymbol{u}_{(k)}. \tag{1.2}$$

where $\boldsymbol{u}_{(k)}(\boldsymbol{x}, t)$ for $k \in [1, N]$ are velocities. A similar expansion for $\boldsymbol{C}$ is inappropriate because it is positive–definite and there is no *a priori* guarantee on this property. In order to obtain an analogous expansion for the conformation tensor, we generalize the geometric decomposition of chapter 3 by multiplicatively decomposing the fluctuating deformation gradient into N separate components. The construction of this fluctuating deformation gradient, denoted $\boldsymbol{L}_{\text{wnl}}$, through a series of successively smaller deformations is illustrated in figure 4.2. Mathematically, we write

$$\boldsymbol{L}_{\text{wnl}} = \boldsymbol{L}_{(1)}^{\epsilon} \cdot \boldsymbol{L}_{(2)}^{\epsilon^2} \cdot \ldots \cdot \boldsymbol{L}_{(N)}^{\epsilon^N}. \tag{4.4}$$

We further assume that each $\boldsymbol{L}_{(k)}^{\epsilon^k}$ in (4.4) is rotation-free. By the polar decomposition and the requirement that $\det \boldsymbol{L}_{(k)} > 0$, this assumption implies that each $\boldsymbol{L}_{(k)}$ is positive–definite. Although each $\boldsymbol{L}_{(k)}$ is rotation-free, the overall fluctuating deformation gradient $\boldsymbol{L}_{\text{wnl}}$ given by (4.4) is not because the product of positive–definite tensors is not necessarily positive–definite. The rotation appears if the principal axes of $\boldsymbol{L}_{(k)}$

and $\boldsymbol{L}_{(k')}$, when $k \neq k'$, are misaligned. The deformation gradient $\boldsymbol{L}_{\text{wnl}}$ is also not necessarily the same as $\boldsymbol{L}$ defined previously. However, since $\boldsymbol{L}_{\text{wnl}} \cdot \boldsymbol{L}_{\text{wnl}}^{\mathsf{T}} = \boldsymbol{L} \cdot \boldsymbol{L}^{\mathsf{T}} = \boldsymbol{G}$, the polar decomposition can be used to show that $\boldsymbol{L}_{\text{wnl}} = \boldsymbol{V} \cdot \boldsymbol{L}$ for some rotation tensor $\boldsymbol{V}$.

Each deformation gradient $\boldsymbol{L}_{(k)}^{\epsilon^k}$ in (4.4) has an associated left Cauchy-Green tensor, $\boldsymbol{G}_{(k)}^{\epsilon^k} = \boldsymbol{L}_{(k)}^{\epsilon^k} \cdot (\boldsymbol{L}_{(k)}^{\epsilon^k})^{\mathsf{T}}$, which can be viewed as a geodesic of length $|\epsilon|^k \|\boldsymbol{\mathcal{G}}_{(k)}\| \sim |\epsilon|^k$ on $\mathbf{Pos}_3$ emanating from $\boldsymbol{I}$ and can be expressed conveniently as

$$\boldsymbol{G}_{(k)}^{\epsilon^k} = \mathrm{e}^{\epsilon^k \boldsymbol{\mathcal{G}}_{(k)}} \tag{4.5}$$

where $\mathrm{e}^{\boldsymbol{\mathcal{A}}}$ is the matrix exponential of $\boldsymbol{\mathcal{A}}$, $\boldsymbol{\mathcal{G}}_{(k)} \in \mathbf{Sym}_3$ are tangents on $\mathbf{Pos}_3$, and $\boldsymbol{\mathcal{G}}_{(0)} = \mathbf{0}$. With (4.5), it is easy to show that $\det \boldsymbol{L}_{\text{wnl}} > 0$, which means that $\boldsymbol{L}_{\text{wnl}}$ is a physically admissible deformation gradient.

The tangents on $\mathbf{Pos}_3$, $\boldsymbol{\mathcal{G}}_{(k)}$, can be used to physically characterize the perturbation deformation. The associated deformation gradient is given by $\boldsymbol{L}_{(k)}^{\epsilon^k} = \mathrm{e}^{\epsilon \boldsymbol{\mathcal{G}}_{(k)}/2}$. When $\boldsymbol{\mathcal{G}}_{(k)}$ is diagonal, $\boldsymbol{L}_{(k)}^{\epsilon^k}$ is diagonal and thus the deformation is a shear free, or purely volumetric, distortion. On the other hand, when $\operatorname{tr} \boldsymbol{\mathcal{G}}_{(k)} = 0$, then $\det \boldsymbol{L}_{(k)}^{\epsilon^k} = 1$, and the deformation is purely shearing, or volume preserving.

Substituting (4.5) into the definition of the left Cauchy-Green tensor $\boldsymbol{G} = \boldsymbol{L} \cdot \boldsymbol{L}^{\mathsf{T}}$,

we have

$$\boldsymbol{G} = \mathrm{e}^{\epsilon\boldsymbol{\mathcal{G}}_{(1)}/2} \cdot \ldots \cdot \mathrm{e}^{\epsilon^{N-1}\boldsymbol{\mathcal{G}}_{(N-1)}/2} \cdot \mathrm{e}^{\epsilon^{N}\boldsymbol{\mathcal{G}}_{(N)}} \cdot \mathrm{e}^{\epsilon^{N-1}\boldsymbol{\mathcal{G}}_{(N-1)}/2} \cdot \ldots \cdot \mathrm{e}^{\epsilon\boldsymbol{\mathcal{G}}_{(1)}/2}. \tag{4.6}$$

Using the expansion $\mathrm{e}^{\epsilon^k\boldsymbol{\mathcal{G}}_{(k)}} = \sum_{p=0}^{\infty} \epsilon^{kp}\boldsymbol{\mathcal{G}}_{(k)}^p/p!$ in (4.6) and collecting terms in like powers of ϵ, we obtain

$$\begin{aligned}
\boldsymbol{G} = \boldsymbol{I} &+ \epsilon\boldsymbol{\mathcal{G}}_{(1)} + \epsilon^2\left(\frac{\boldsymbol{\mathcal{G}}_{(1)}^2}{2} + \boldsymbol{\mathcal{G}}_{(2)}\right) + \epsilon^3\left[\frac{\boldsymbol{\mathcal{G}}_{(1)}^3}{6} + \mathrm{sym}\,\left(\boldsymbol{\mathcal{G}}_{(1)}\cdot\boldsymbol{\mathcal{G}}_{(2)}\right) + \boldsymbol{\mathcal{G}}_{(3)}\right] \\
&+ \epsilon^4\left[\mathrm{sym}\,\left(\boldsymbol{\mathcal{G}}_{(1)}\cdot\boldsymbol{\mathcal{G}}_{(3)} + \frac{\boldsymbol{\mathcal{G}}_{(1)}^2\cdot\boldsymbol{\mathcal{G}}_{(2)}}{4}\right) + \frac{\boldsymbol{\mathcal{G}}_{(2)}^2}{2} + \frac{\boldsymbol{\mathcal{G}}_{(1)}\cdot\boldsymbol{\mathcal{G}}_{(2)}\cdot\boldsymbol{\mathcal{G}}_{(1)}}{4} + \frac{\boldsymbol{\mathcal{G}}_{(1)}^4}{24} + \boldsymbol{\mathcal{G}}_{(4)}\right] \\
&+ \epsilon^5\left[\frac{1}{2}\mathrm{sym}\,\left(\boldsymbol{\mathcal{G}}_{(2)}^2\cdot\boldsymbol{\mathcal{G}}_{(1)} + \frac{\boldsymbol{\mathcal{G}}_{(1)}^2\cdot\boldsymbol{\mathcal{G}}_{(3)}}{2} + \frac{\boldsymbol{\mathcal{G}}_{(1)}^3\cdot\boldsymbol{\mathcal{G}}_{(2)}}{12} + \frac{\boldsymbol{\mathcal{G}}_{(1)}^2\cdot\boldsymbol{\mathcal{G}}_{(2)}\cdot\boldsymbol{\mathcal{G}}_{(1)}}{4}\right)\right. \\
&\left.+ \mathrm{sym}\,\left(\boldsymbol{\mathcal{G}}_{(4)}\cdot\boldsymbol{\mathcal{G}}_{(1)} + \boldsymbol{\mathcal{G}}_{(3)}\cdot\boldsymbol{\mathcal{G}}_{(2)}\right) + \frac{\boldsymbol{\mathcal{G}}_{(1)}\cdot\boldsymbol{\mathcal{G}}_{(3)}\cdot\boldsymbol{\mathcal{G}}_{(1)}}{2} + \frac{\boldsymbol{\mathcal{G}}_{(1)}^5}{120} + \boldsymbol{\mathcal{G}}_{(5)}\right] + \ldots
\end{aligned} \tag{4.7}$$

The expression (4.7) is a series expansion of the conformation tensor that serves as an analogue to the weakly nonlinear expansion of the velocity in (1.2). In fact, the terms in (4.7) can be related to the standard weakly nonlinear expansion of the conformation tensor, $\boldsymbol{C} = \overline{\boldsymbol{C}} + \sum_{k=1}^{\infty}\epsilon^k\boldsymbol{C}_{(k)}$. The difference between $\boldsymbol{C}_{(k)}$ and $\boldsymbol{\mathcal{G}}_{(k)}$ is that the latter can be related to a polymer perturbation deformation by means of the framework introduced above. Furthermore, (4.7) shows that the $\boldsymbol{C}_{(k)}$ are not independent of one another, even before the expansion is applied in the governing equations to examine the dynamics. This behaviour is consistent with the curved geometry of $\mathbf{Pos}_3$

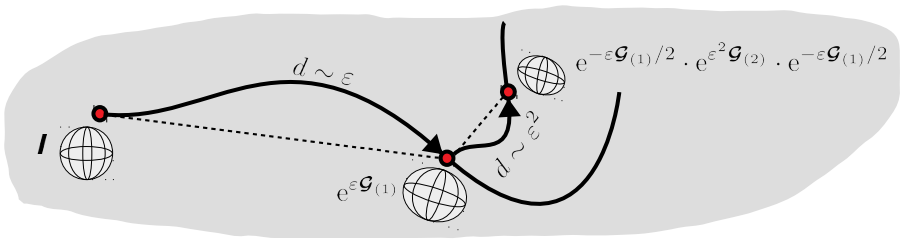

Figure 4.3: Illustration of weakly nonlinear deformation when $N = 2$. In this case, the deformation corresponds to a piece-wise geodesic on $\mathbf{Pos}_3$. The thick black lines represent geodesics and dashed lines are Euclidean paths on $\mathbf{Pos}_3$.

because, unlike in Euclidean space, the characteristics of a particular perturbation depends on the location on the manifold where the perturbation is applied. In this view of the geometry, the deformation associated with $\boldsymbol{L}^{\epsilon^n}_{(n)}$ is a perturbation to the deformation associated with $\boldsymbol{L}^{\epsilon}_{(1)} \cdot \boldsymbol{L}^{\epsilon^2}_{(2)} \cdot \ldots \cdot \boldsymbol{L}^{\epsilon^{n-1}}_{(n-1)}$ and thus the n-th order term in the series expansion must depend on all $\boldsymbol{\mathcal{G}}_{(k)}$ with $k = 1, \ldots n$. The behaviour is also consistent with a physical understanding of successive deformations of the polymer; a deformation is only sensible with respect to an existing configuration and is thus dependent on it from the point of view of an independent observer.

One aspect of the relationship between the present approach of decomposing the total deformation into a series of successive deformations (cf. figure 4.2) and the geometry of $\mathbf{Pos}_3$ is that the left Cauchy-Green tensor associated with each deformation is chosen to be a geodesic emanating from $\boldsymbol{I}$. Another direct connection between geodesics on $\mathbf{Pos}_3$ and the overall deformation represented by $\boldsymbol{G}$ can be made when $N \leq 2$. When $N = 1$, $\boldsymbol{G} = \mathrm{e}^{\epsilon \boldsymbol{\mathcal{G}}_{(1)}}$ is simply a geodesic of length $\sim \epsilon$ emanating from $\boldsymbol{I}$

in the direction $\boldsymbol{\mathcal{G}}_{(1)}$. When $N = 2$, we have

$$\boldsymbol{G} = \mathrm{e}^{\epsilon\boldsymbol{\mathcal{G}}_{(1)}/2} \cdot \mathrm{e}^{\epsilon^2\boldsymbol{\mathcal{G}}_{(2)}} \cdot \mathrm{e}^{\epsilon\boldsymbol{\mathcal{G}}_{(1)}/2}, \tag{4.8}$$

which implies that $\boldsymbol{G}$ is 'piece-wise geodesic': it consists of a geodesic of length $\sim \epsilon$ emanating from $\boldsymbol{I}$ in the direction $\boldsymbol{\mathcal{G}}_{(1)}$, followed by a geodesic of length $\sim \epsilon^2$ in the direction $\boldsymbol{\mathcal{G}}_{(2)}$, as illustrated in figure 4.3. Such an interpretation is reminiscent of the one associated with the weakly nonlinear expansion of the velocity as in figure 1.2.

The piece-wise geodesic interpretation is not generally possible for $N > 2$ because then $\mathrm{e}^{\epsilon\boldsymbol{\mathcal{G}}_{(1)}/2} \cdot \ldots \cdot \mathrm{e}^{\epsilon^{N-1}\boldsymbol{\mathcal{G}}_{(N-1)}/2}$ need not be in $\mathbf{Pos}_3$. If we assume that $\boldsymbol{\mathcal{G}}_{(1)}, \ldots, \boldsymbol{\mathcal{G}}_{(N-1)}$ are commutative with respect to multiplication, then

$$\mathrm{e}^{\epsilon\boldsymbol{\mathcal{G}}_{(1)}/2} \cdot \ldots \cdot \mathrm{e}^{\epsilon^{N-1}\boldsymbol{\mathcal{G}}_{(N-1)}/2} = \mathrm{e}^{\frac{1}{2}\sum_{k=1}^{N-1}\epsilon^k\boldsymbol{\mathcal{G}}_{(k)}} \in \mathbf{Pos}_3. \tag{4.9}$$

Thus, in this case, the interpretation of the successive deformations as a piece-wise geodesic on $\mathbf{Pos}_3$ holds for arbitrary N. The inability to extend the piece-wise geodesic intepretation to arbitrary N arises because successive deformations are, in general, physically misaligned and thus, by the polar decomposition, a rotation is imparted to the deformation gradient that depends on the order in which successive intermediate deformations were performed. This order of the intermediate deformations is only relevant when $N \geq 2$. When the deformations are physically aligned, the overall deformation gradient is positive–definite: it has no associated rotation and

the order of the intermediate deformations can be arbitrarily changed.

An alternative to the present approach for generating a series expansion of $\boldsymbol{G}$ is to expand the tangent vector on $\mathbf{Pos}_3$,

$$\boldsymbol{G} = \exp\left(\sum_{k=1}^{N} \epsilon^k \boldsymbol{\mathcal{G}}_{(k)}\right) = \boldsymbol{I} + \sum_{k=1}^{N} \epsilon^k \boldsymbol{\mathcal{G}}_{(k)} + \frac{1}{2}\left(\sum_{k=1}^{N} \epsilon^k \boldsymbol{\mathcal{G}}_{(k)}\right)^2 + \dots \tag{4.10}$$

It is easy to show that our proposed approach (4.7) and the alternative (4.10) are equivalent if $\boldsymbol{\mathcal{G}}_{(1)}, \dots, \boldsymbol{\mathcal{G}}_{(N)}$ are commutative with respect to multiplication. When the latter condition is not satisfied, by expanding (4.10) and collecting terms in like powers of ϵ, we obtain

$$\begin{aligned}
\boldsymbol{G} = \boldsymbol{I} &+ \epsilon \boldsymbol{\mathcal{G}}_{(1)} + \epsilon^2 \left(\frac{\boldsymbol{\mathcal{G}}_{(1)}^2}{2} + \boldsymbol{\mathcal{G}}_{(2)}\right) + \epsilon^3 \left[\frac{\boldsymbol{\mathcal{G}}_{(1)}^3}{6} + \text{sym}\left(\boldsymbol{\mathcal{G}}_{(1)} \cdot \boldsymbol{\mathcal{G}}_{(2)}\right) + \boldsymbol{\mathcal{G}}_{(3)}\right] \\
&+ \epsilon^4 \left[\text{sym}\left(\boldsymbol{\mathcal{G}}_{(1)} \cdot \boldsymbol{\mathcal{G}}_{(3)} + \frac{\boldsymbol{\mathcal{G}}_{(1)}^2 \cdot \boldsymbol{\mathcal{G}}_{(2)}}{3}\right) + \frac{\boldsymbol{\mathcal{G}}_{(2)}^2}{2} + \frac{\boldsymbol{\mathcal{G}}_{(1)} \cdot \boldsymbol{\mathcal{G}}_{(2)} \cdot \boldsymbol{\mathcal{G}}_{(1)}}{6} + \frac{\boldsymbol{\mathcal{G}}_{(1)}^4}{24} + \boldsymbol{\mathcal{G}}_{(4)}\right] \\
&+ \epsilon^5 \left[\frac{1}{3}\text{sym}\left(\boldsymbol{\mathcal{G}}_{(2)}^2 \cdot \boldsymbol{\mathcal{G}}_{(1)} + \boldsymbol{\mathcal{G}}_{(1)}^2 \cdot \boldsymbol{\mathcal{G}}_{(3)} + \frac{\boldsymbol{\mathcal{G}}_{(1)}^3 \cdot \boldsymbol{\mathcal{G}}_{(2)} + \boldsymbol{\mathcal{G}}_{(1)}^2 \cdot \boldsymbol{\mathcal{G}}_{(2)} \cdot \boldsymbol{\mathcal{G}}_{(1)}}{4}\right)\right. \\
&\left. + \text{sym}\left(\boldsymbol{\mathcal{G}}_{(4)} \cdot \boldsymbol{\mathcal{G}}_{(1)} + \boldsymbol{\mathcal{G}}_{(3)} \cdot \boldsymbol{\mathcal{G}}_{(2)}\right) + \frac{\boldsymbol{\mathcal{G}}_{(1)} \cdot \boldsymbol{\mathcal{G}}_{(3)} \cdot \boldsymbol{\mathcal{G}}_{(1)}}{6} + \frac{\boldsymbol{\mathcal{G}}_{(1)}^5}{120} + \boldsymbol{\mathcal{G}}_{(5)}\right] + \dots
\end{aligned} \tag{4.11}$$

and thus the two approaches are still equivalent up to $\mathcal{O}(\epsilon^4)$.

The drawback with using (4.10) is that the individual terms of the expansion cannot be associated with a polymer deformation because $\mathrm{e}^{\boldsymbol{A}+\boldsymbol{B}} \neq \mathrm{e}^{\boldsymbol{A}} \cdot \mathrm{e}^{\boldsymbol{B}}$. The expansion (4.10) also cannot be related to the geometry of $\mathbf{Pos}_3$ in the same way as

(4.7).

We developed an approach to generate a perturbation deformation of the polymers with arbitrarily many deformations. The magnitudes of the deformations are of successively higher order with respect to the distance metric on the manifold. We next consider the case of linear perturbations, where a single deformation is involved.

4.2.2 Linear perturbations

We can generate a small perturbation about $\overline{\boldsymbol{C}}$ by translating the conformation tensor along a geodesic emanating from $\overline{\boldsymbol{C}}$. This can be accomplished by setting

$$\boldsymbol{G} = \boldsymbol{I} \#_{\epsilon} \mathrm{e}^{\boldsymbol{\mathcal{G}}_{(1)}} = \mathrm{e}^{\epsilon \boldsymbol{\mathcal{G}}_{(1)}} \tag{4.12}$$

where $\boldsymbol{\mathcal{G}}_{(1)}$ is a prescribed tangent on $\mathbf{Pos}_3$, $\epsilon \in \mathbb{R}$ and $d(\boldsymbol{I}, \mathrm{e}^{\epsilon \boldsymbol{\mathcal{G}}_{(1)}}) = |\epsilon| \|\boldsymbol{\mathcal{G}}_{(1)}\| \sim \epsilon$. The parameter ϵ here represents the amount of volumetric deformation encoded in the perturbation because the volume of $\boldsymbol{G}$ is given by $\det \boldsymbol{G} = \mathrm{e}^{\epsilon \mathrm{tr}\, \boldsymbol{\mathcal{G}}_{(1)}}$, or equivalently $\det \boldsymbol{C} = c^{\epsilon} \det \overline{\boldsymbol{C}}$ for constant $c = \mathrm{e}^{\mathrm{tr}\, \boldsymbol{\mathcal{G}}_{(1)}}$. The expression (4.12) is valid, in a kinematic sense, for all $\epsilon \in \mathbb{R}$. In the case when $\epsilon \to 0$, we may approximate the matrix exponential, $\mathrm{e}^{\epsilon \boldsymbol{\mathcal{G}}_{(1)}} = \sum_{k=0}^{\infty} \epsilon^k \boldsymbol{\mathcal{G}}_{(1)}^k / k!$, as

$$\boldsymbol{G} = \mathrm{e}^{\epsilon \boldsymbol{\mathcal{G}}_{(1)}} = \boldsymbol{I} + \epsilon \boldsymbol{\mathcal{G}}_{(1)} + \mathcal{O}(\epsilon^2 \mathrm{e}^{\epsilon}) \tag{4.13}$$

where the truncation error is based on the bounds derived by Suzuki.[205] The result (4.13) is similar to the weakly nonlinear expansion (4.7) with

$$\boldsymbol{\mathcal{G}}_{(2)} = \boldsymbol{\mathcal{G}}_{(3)} = \ldots = \boldsymbol{\mathcal{G}}_{(N)} = \mathbf{0}. \tag{4.14}$$

Multiplying (4.13) by $\overline{\boldsymbol{F}}$ on both sides, we obtain

$$\boldsymbol{C} = \overline{\boldsymbol{C}} + \epsilon \boldsymbol{C}_{(1)} + \mathcal{O}(\epsilon^2 \mathrm{e}^{\epsilon}) \tag{4.15}$$

where $\boldsymbol{C}_{(1)} = \overline{\boldsymbol{F}} \cdot \boldsymbol{\mathcal{G}}_{(1)} \cdot \overline{\boldsymbol{F}}^{\mathsf{T}}$, which is similar to the standard approach involving an additive perturbation to $\overline{\boldsymbol{C}}$. However, now the fluctuation, $\boldsymbol{C}' = \epsilon \boldsymbol{C}_{(1)}$, has a clear interpretation as a tangent to the manifold at the base-point $\overline{\boldsymbol{C}}$. Furthermore, the normalization of $\boldsymbol{C}'$ is proportional to the geodesic distance away from $\overline{\boldsymbol{C}}$ on $\mathbf{Pos}_3$.

The geometric structure on $\mathbf{Pos}_3$ supplies us with the natural scalar product to be used in the analysis of linear perturbations. This scalar product, which depends on $\overline{\boldsymbol{C}}$, is induced by the global distance metric on $\mathbf{Pos}_3$ and is given in (3.41). If we use the form of the additive perturbation given in (4.13), the natural scalar product reduces to the standard Frobenius norm. By taking the base-point into account, (3.41) also allows us to compare the norm of tangent vectors at *different* base-points.

In the next section, we derive evolution equations for $\boldsymbol{\mathcal{G}}_{(k)}$.

4.3 Evolution of perturbative deformations

In this section we derive the evolution equations for the first two fluctuating terms in the weakly nonlinear expansion/deformation of the velocity field/conformation tensor (coefficients of ϵ and ϵ^2). The governing equations for the dimensionless velocity, $\boldsymbol{u}$, and conformation tensor, $\boldsymbol{C}$, in a viscoelastic flow are

$$\boldsymbol{\nabla \cdot u} = 0 \tag{2.28}$$

$$\frac{\mathrm{D}\boldsymbol{u}}{\mathrm{D}t} = -\boldsymbol{\nabla} p + \frac{\beta}{Re}\boldsymbol{\Delta u} + \frac{1-\beta}{Re}\boldsymbol{\nabla \cdot T} + \boldsymbol{d} \tag{2.29}$$

$$\overset{\nabla}{\boldsymbol{C}} = -\boldsymbol{T} \tag{2.30}$$

where we let $\boldsymbol{d} = \boldsymbol{0}$. Rather than use the general constitutive relation in (2.25) we restrict ourselves to the FENE-P and Oldroyd-B models, where

$$\boldsymbol{T}(\boldsymbol{C}) = \frac{1}{Wi}\left[f(\mathrm{tr}\,\boldsymbol{C})\boldsymbol{C} - f(3)\boldsymbol{I}\right], \tag{4.16}$$

where $f(s) = [1 - (s/L_{\max}^2)]^{-1}$ and $L_{\max}$ is the maximum extensibility (cf. table 2.1). By setting $L_{\max} \to \infty$ we retrieve the Oldroyd-B model, where $f = 1$.

The velocity field and pressure are expressed as weakly nonlinear expansions

$$\boldsymbol{u} = \overline{\boldsymbol{u}} + \boldsymbol{u}' = \overline{\boldsymbol{u}} + \sum_{k=1}^{N} \epsilon^k \boldsymbol{u}_{(k)}. \tag{1.2}$$

$$p = \overline{p} + \sum_{k=1}^{N} \epsilon^k p_{(k)}. \tag{4.17}$$

and the weakly nonlinear deformation of the conformation tensor yields the expansion

$$\boldsymbol{G} = \boldsymbol{I} + \epsilon \boldsymbol{\mathcal{G}}_{(1)} + \epsilon^2 \left(\frac{\boldsymbol{\mathcal{G}}_{(1)}^2}{2} + \boldsymbol{\mathcal{G}}_{(2)} \right) + \dots \tag{4.7}$$

where we note, by (3.12), we can re-write (4.7) as

$$\boldsymbol{C} = \overline{\boldsymbol{C}} + \epsilon \overline{\boldsymbol{F}} \cdot \boldsymbol{\mathcal{G}}_{(1)} \cdot \overline{\boldsymbol{F}}^{\mathsf{T}} + \epsilon^2 \overline{\boldsymbol{F}} \cdot \left(\frac{\boldsymbol{\mathcal{G}}_{(1)}^2}{2} + \boldsymbol{\mathcal{G}}_{(2)} \right) \cdot \overline{\boldsymbol{F}}^{\mathsf{T}} + \dots . \tag{4.18}$$

The base-state is assumed to be time-invariant.

Before finding the evolution equations for $\boldsymbol{u}_{(k)}$ and $\boldsymbol{\mathcal{G}}_{(1)}$, we first need to find an expansion for the polymer stress. This quantity, given in (4.16), is a function of the conformation tensor and therefore the weakly nonlinear deformation in (4.7) needs to be used to find the relevant expansion. The scalar function $f(s)$ in (4.7) makes the stress, in general, nonlinear in the conformation tensor. Expanding $f(s)$ in a Taylor

series about some $\overline{s}$ yields

$$\begin{aligned} f(s) &= \sum_{k=0}^{\infty} \frac{(s-\overline{s})^k}{k!} \left.\frac{\mathrm{d}^k f}{\mathrm{d}s^k}\right|_{s=\overline{s}} \\ &= f(\overline{s}) \left[1 + \left(\frac{s-\overline{s}}{L_{\max}^2 - \overline{s}}\right) + \left(\frac{s-\overline{s}}{L_{\max}^2 - \overline{s}}\right)^2 + \ldots\right] \end{aligned} \tag{4.19}$$

where we used the fact that

$$\frac{\mathrm{d}^k f}{\mathrm{d}s^k} = f(s) \left(\frac{f(s)}{L_{\max}^2}\right)^k k! \qquad k > 0. \tag{4.20}$$

Next, from (4.18) we have

$$\begin{aligned} \mathrm{tr}\left(\boldsymbol{C} - \overline{\boldsymbol{C}}\right) &= \epsilon \mathrm{tr}\left(\overline{\boldsymbol{F}}^{\mathsf{T}} \cdot \overline{\boldsymbol{F}} \cdot \boldsymbol{\mathcal{G}}_{(1)}\right) + \epsilon^2 \mathrm{tr}\left[\overline{\boldsymbol{F}}^{\mathsf{T}} \cdot \overline{\boldsymbol{F}} \cdot \left(\frac{\boldsymbol{\mathcal{G}}_{(1)}^2}{2} + \boldsymbol{\mathcal{G}}_{(2)}\right)\right] + \ldots \\ \mathrm{tr}^2\left(\boldsymbol{C} - \overline{\boldsymbol{C}}\right) &= \epsilon^2 \mathrm{tr}^2\left(\overline{\boldsymbol{F}}^{\mathsf{T}} \cdot \overline{\boldsymbol{F}} \cdot \boldsymbol{\mathcal{G}}_{(1)}\right) + \ldots \end{aligned} \tag{4.21}$$

Combining (4.19) and (4.21), and using the fact that $f(s)/L_{\max}^2 = 1/(L_{\max}^2 - s)$, we obtain

$$\begin{aligned} f(\mathrm{tr}\,\boldsymbol{C}) &= f(\mathrm{tr}\,\overline{\boldsymbol{C}}) \left[1 + \left(\frac{\mathrm{tr}\,\boldsymbol{C} - \mathrm{tr}\,\overline{\boldsymbol{C}}}{L_{\max}^2 - \mathrm{tr}\,\overline{\boldsymbol{C}}}\right) + \left(\frac{\mathrm{tr}\,\boldsymbol{C} - \mathrm{tr}\,\overline{\boldsymbol{C}}}{L_{\max}^2 - \mathrm{tr}\,\overline{\boldsymbol{C}}}\right)^2 + \ldots\right] \\ &= f(\mathrm{tr}\,\overline{\boldsymbol{C}}) + \epsilon \mathrm{tr}\left(\overline{\boldsymbol{F}}^{\mathsf{T}} \cdot \overline{\boldsymbol{F}} \cdot \boldsymbol{\mathcal{G}}_{(1)}\right) \frac{f^2(\mathrm{tr}\,\overline{\boldsymbol{C}})}{L_{\max}^2} \\ &+ \epsilon^2 \left[\mathrm{tr}\left(\overline{\boldsymbol{F}}^{\mathsf{T}} \cdot \overline{\boldsymbol{F}} \cdot \left(\frac{\boldsymbol{\mathcal{G}}_{(1)}^2}{2} + \boldsymbol{\mathcal{G}}_{(2)}\right)\right) + \frac{f(\mathrm{tr}\,\overline{\boldsymbol{C}})}{L_{\max}^2} \mathrm{tr}^2\left(\overline{\boldsymbol{F}}^{\mathsf{T}} \cdot \overline{\boldsymbol{F}} \cdot \boldsymbol{\mathcal{G}}_{(1)}\right)\right] \frac{f^2(\mathrm{tr}\,\overline{\boldsymbol{C}})}{L_{\max}^2} + \ldots \end{aligned} \tag{4.22}$$

Using the expansions (4.18) and (4.22) in the polymer stress relation in (4.16) finally yields an appropriate expansion for $\boldsymbol{T}$

$$
\begin{aligned}
Wi\,\boldsymbol{T} = -f(3)\boldsymbol{I} + \Bigg\{ & f(\operatorname{tr}\overline{\boldsymbol{C}}) + \epsilon \operatorname{tr}\left(\overline{\boldsymbol{F}}^{\mathsf{T}}\cdot\overline{\boldsymbol{F}}\cdot\boldsymbol{\mathcal{G}}_{(1)}\right)\frac{f^2(\operatorname{tr}\overline{\boldsymbol{C}})}{L_{\max}^2} \\
& + \epsilon^2\left[\operatorname{tr}\left(\overline{\boldsymbol{F}}^{\mathsf{T}}\cdot\overline{\boldsymbol{F}}\cdot\left(\frac{\boldsymbol{\mathcal{G}}_{(1)}^2}{2}+\boldsymbol{\mathcal{G}}_{(2)}\right)\right) + \frac{f(\operatorname{tr}\overline{\boldsymbol{C}})}{L_{\max}^2}\operatorname{tr}^2\left(\overline{\boldsymbol{F}}^{\mathsf{T}}\cdot\overline{\boldsymbol{F}}\cdot\boldsymbol{\mathcal{G}}_{(1)}\right)\right]\frac{f^2(\operatorname{tr}\overline{\boldsymbol{C}})}{L_{\max}^2}\Bigg\}\times \\
& \left[\overline{\boldsymbol{C}} + \epsilon\overline{\boldsymbol{F}}\cdot\boldsymbol{\mathcal{G}}_{(1)}\cdot\overline{\boldsymbol{F}}^{\mathsf{T}} + \epsilon^2\overline{\boldsymbol{F}}\cdot\left(\frac{\boldsymbol{\mathcal{G}}_{(1)}^2}{2}+\boldsymbol{\mathcal{G}}_{(2)}\right)\cdot\overline{\boldsymbol{F}}^{\mathsf{T}}\right] + \ldots \\
= {} & f(\operatorname{tr}\overline{\boldsymbol{C}})\overline{\boldsymbol{C}} - f(3)\boldsymbol{I} + \epsilon\left[\operatorname{tr}\left(\overline{\boldsymbol{F}}^{\mathsf{T}}\cdot\overline{\boldsymbol{F}}\cdot\boldsymbol{\mathcal{G}}_{(1)}\right)\frac{f^2(\operatorname{tr}\overline{\boldsymbol{C}})}{L_{\max}^2}\overline{\boldsymbol{C}} + f(\operatorname{tr}\overline{\boldsymbol{C}})\overline{\boldsymbol{F}}\cdot\boldsymbol{\mathcal{G}}_{(1)}\cdot\overline{\boldsymbol{F}}^{\mathsf{T}}\right] \\
& + \epsilon^2\frac{f^2(\operatorname{tr}\overline{\boldsymbol{C}})}{L_{\max}^2}\Bigg[\operatorname{tr}\left(\overline{\boldsymbol{F}}^{\mathsf{T}}\cdot\overline{\boldsymbol{F}}\cdot\left(\frac{\boldsymbol{\mathcal{G}}_{(1)}^2}{2}+\boldsymbol{\mathcal{G}}_{(2)}\right)\right)\overline{\boldsymbol{C}} + \frac{f(\operatorname{tr}\overline{\boldsymbol{C}})}{L_{\max}^2}\operatorname{tr}^2\left(\overline{\boldsymbol{F}}^{\mathsf{T}}\cdot\overline{\boldsymbol{F}}\cdot\boldsymbol{\mathcal{G}}_{(1)}\right)\overline{\boldsymbol{C}} \\
& + \operatorname{tr}\left(\overline{\boldsymbol{F}}^{\mathsf{T}}\cdot\overline{\boldsymbol{F}}\cdot\boldsymbol{\mathcal{G}}_{(1)}\right)\overline{\boldsymbol{F}}\cdot\boldsymbol{\mathcal{G}}_{(1)}\cdot\overline{\boldsymbol{F}}^{\mathsf{T}} + \overline{\boldsymbol{F}}\cdot\left(\frac{\boldsymbol{\mathcal{G}}_{(1)}^2}{2}+\boldsymbol{\mathcal{G}}_{(2)}\right)\cdot\overline{\boldsymbol{F}}^{\mathsf{T}}\frac{L_{\max}^2}{f(\operatorname{tr}\overline{\boldsymbol{C}})}\Bigg] + \ldots \qquad (4.23)
\end{aligned}
$$

We first consider the momentum equation (2.29). Using the weakly nonlinear expansion (1.2), the convective term expands to

$$
\begin{aligned}
\boldsymbol{u}\cdot\boldsymbol{\nabla}\boldsymbol{u} = \overline{\boldsymbol{u}}\cdot\boldsymbol{\nabla}\overline{\boldsymbol{u}} + \epsilon\left(\overline{\boldsymbol{u}}\cdot\boldsymbol{\nabla}\boldsymbol{u}_{(1)} + \boldsymbol{u}_{(1)}\cdot\boldsymbol{\nabla}\overline{\boldsymbol{u}}\right) \\
+ \epsilon^2\left(\overline{\boldsymbol{u}}\cdot\boldsymbol{\nabla}\boldsymbol{u}_{(2)} + \boldsymbol{u}_{(2)}\cdot\boldsymbol{\nabla}\overline{\boldsymbol{u}} + \boldsymbol{u}_{(1)}\cdot\boldsymbol{\nabla}\boldsymbol{u}_{(1)}\right) + \ldots \qquad (4.24)
\end{aligned}
$$

Substituting (1.2), (4.24) and (4.23) into (2.29), and equating coefficients of ϵ yields

the evolution equation for $\boldsymbol{u}_{(1)}$,

$$\partial_t \boldsymbol{u}_{(1)} + \overline{\boldsymbol{u}} \cdot \boldsymbol{\nabla} \boldsymbol{u}_{(1)} + \boldsymbol{u}_{(1)} \cdot \boldsymbol{\nabla} \overline{\boldsymbol{u}} = -\boldsymbol{\nabla} p_{(1)} + \frac{\beta}{Re} \boldsymbol{\Delta} \boldsymbol{u}_{(1)} + \frac{1-\beta}{WiRe} \boldsymbol{\nabla} \cdot \left[f(\operatorname{tr} \overline{\boldsymbol{C}}) \overline{\boldsymbol{F}} \cdot \boldsymbol{\mathcal{G}}_{(1)} \cdot \overline{\boldsymbol{F}}^{\mathsf{T}} \right] + \frac{1-\beta}{WiRe} \boldsymbol{\nabla} \cdot \left[\frac{f^2(\operatorname{tr} \overline{\boldsymbol{C}})}{L_{\max}^2} \operatorname{tr} \left(\overline{\boldsymbol{F}}^{\mathsf{T}} \cdot \overline{\boldsymbol{F}} \cdot \boldsymbol{\mathcal{G}}_{(1)} \right) \overline{\boldsymbol{C}} \right]. \quad (4.25)$$

Similarly, equating coefficients of ϵ^2 yields the evolution equation for $\boldsymbol{u}_{(2)}$,

$$\begin{aligned} \partial_t \boldsymbol{u}_{(2)} + \overline{\boldsymbol{u}} \cdot \boldsymbol{\nabla} \boldsymbol{u}_{(2)} + \boldsymbol{u}_{(2)} \cdot \boldsymbol{\nabla} \overline{\boldsymbol{u}} + \boldsymbol{u}_{(1)} \cdot \boldsymbol{\nabla} \boldsymbol{u}_{(1)} &= -\boldsymbol{\nabla} p_{(2)} + \frac{\beta}{Re} \boldsymbol{\Delta} \boldsymbol{u}_{(2)} \\ &+ \frac{1-\beta}{WiRe} \boldsymbol{\nabla} \cdot \left[\overline{\boldsymbol{F}} \cdot \left(\frac{\boldsymbol{\mathcal{G}}_{(1)}^2}{2} + \boldsymbol{\mathcal{G}}_{(2)} \right) \cdot \overline{\boldsymbol{F}}^{\mathsf{T}} f(\operatorname{tr} \overline{\boldsymbol{C}}) \right] \\ &+ \frac{1-\beta}{WiRe} \boldsymbol{\nabla} \cdot \left\{ \frac{f^2(\operatorname{tr} \overline{\boldsymbol{C}})}{L_{\max}^2} \left[\operatorname{tr} \left(\overline{\boldsymbol{F}}^{\mathsf{T}} \cdot \overline{\boldsymbol{F}} \cdot \left(\frac{\boldsymbol{\mathcal{G}}_{(1)}^2}{2} + \boldsymbol{\mathcal{G}}_{(2)} \right) \right) \overline{\boldsymbol{C}} \right. \right. \\ &\left. \left. + \frac{f(\operatorname{tr} \overline{\boldsymbol{C}})}{L_{\max}^2} \operatorname{tr}^2 \left(\overline{\boldsymbol{F}}^{\mathsf{T}} \cdot \overline{\boldsymbol{F}} \cdot \boldsymbol{\mathcal{G}}_{(1)} \right) \overline{\boldsymbol{C}} + \operatorname{tr} \left(\overline{\boldsymbol{F}}^{\mathsf{T}} \cdot \overline{\boldsymbol{F}} \cdot \boldsymbol{\mathcal{G}}_{(1)} \right) \overline{\boldsymbol{F}} \cdot \boldsymbol{\mathcal{G}}_{(1)} \cdot \overline{\boldsymbol{F}}^{\mathsf{T}} \right] \right\}. \end{aligned} \quad (4.26)$$

We next consider the conformation tensor equation (2.30). Rather than proceed directly with the conformation tensor, we start from the equation for the fluctuating conformation tensor given in chapter 3 for an arbitrary base-state,

$$\partial_t \boldsymbol{G} + \boldsymbol{u} \cdot \boldsymbol{\nabla} \boldsymbol{G} = 2 \operatorname{sym} (\boldsymbol{G} \cdot \boldsymbol{K}) - \boldsymbol{M} \quad (3.24)$$

where recall

$$\boldsymbol{E}(\boldsymbol{u}) \equiv \overline{\boldsymbol{F}}^{\mathsf{T}} \cdot \boldsymbol{\nabla u} \cdot \overline{\boldsymbol{F}}^{-\mathsf{T}} \tag{3.25}$$

$$\boldsymbol{M} \equiv \overline{\boldsymbol{F}}^{-1} \cdot \boldsymbol{T} \cdot \overline{\boldsymbol{F}}^{-\mathsf{T}}. \tag{3.26}$$

$$\boldsymbol{K} \equiv \boldsymbol{E}(\boldsymbol{u}) - \left(\overline{\boldsymbol{F}}^{-1} \cdot \frac{\mathrm{D}\overline{\boldsymbol{F}}}{\mathrm{D}t} \right)^{\mathsf{T}}. \tag{3.27}$$

We now consider three groups of terms that make up (3.24): the material time derivative of $\boldsymbol{G}$ that appears on the left-hand side, the stretching term $2\,\mathrm{sym}\,(\boldsymbol{G}\cdot\boldsymbol{K})$, and the relaxation $\boldsymbol{M}$. Substituting (1.2) and (4.7) into the left-hand side of (3.24) yields the following expansion for the material time derivative of $\boldsymbol{G}$

$$\begin{aligned} \partial_t \boldsymbol{G} + \boldsymbol{u}\cdot\boldsymbol{\nabla}\boldsymbol{G} &= \epsilon(\partial_t \boldsymbol{\mathcal{G}}_{(1)} + \overline{\boldsymbol{u}}\cdot\boldsymbol{\nabla}\boldsymbol{\mathcal{G}}_{(1)}) \\ &+ \epsilon^2 \left(\mathrm{sym}\,(\boldsymbol{\mathcal{G}}_{(1)}\cdot(\partial_t + \overline{\boldsymbol{u}}\cdot\boldsymbol{\nabla})\boldsymbol{\mathcal{G}}_{(1)}) + (\partial_t + \overline{\boldsymbol{u}}\cdot\boldsymbol{\nabla})\boldsymbol{\mathcal{G}}_{(2)} + \boldsymbol{u}_{(1)}\cdot\boldsymbol{\nabla}\boldsymbol{\mathcal{G}}_{(1)} \right) + \dots \end{aligned} \tag{4.27}$$

For the stretching term, we first expand $\boldsymbol{K}$ defined in (3.27). Substituting (1.2) in (3.27) we obtain

$$\begin{aligned} \boldsymbol{K} &= \overline{\boldsymbol{F}}^{\mathsf{T}} \cdot \boldsymbol{\nabla u} \cdot \overline{\boldsymbol{F}}^{-\mathsf{T}} - \left(\overline{\boldsymbol{F}}^{-1} \cdot (\boldsymbol{u}\cdot\boldsymbol{\nabla})\,\overline{\boldsymbol{F}} \right)^{\mathsf{T}} \\ &= \mathscr{F}(\overline{\boldsymbol{u}}) + \epsilon\mathscr{F}(\boldsymbol{u}_{(1)}) + \epsilon^2\mathscr{F}(\boldsymbol{u}_{(2)}) + \dots \end{aligned} \tag{4.28}$$

where we defined the following tensor valued function for notational convenience

$$\mathscr{F}(\boldsymbol{a}) = \overline{\boldsymbol{F}}^{\mathsf{T}} \cdot \boldsymbol{\nabla a} \cdot \overline{\boldsymbol{F}}^{-\mathsf{T}} - \left(\overline{\boldsymbol{F}}^{-1} \cdot (\boldsymbol{a} \cdot \boldsymbol{\nabla})\, \overline{\boldsymbol{F}}\right)^{\mathsf{T}} \tag{4.29}$$

for any vector $\boldsymbol{a}$. Using (4.7) and (4.28), we then obtain

$$\begin{aligned}\boldsymbol{G} \cdot \boldsymbol{K} = {} & \mathscr{F}(\overline{\boldsymbol{u}}) + \epsilon \left[\mathscr{F}(\boldsymbol{u}_{(1)}) + \boldsymbol{\mathcal{G}}_{(1)} \cdot \mathscr{F}(\overline{\boldsymbol{u}})\right] \\ & + \epsilon^2 \left[\mathscr{F}(\boldsymbol{u}_{(2)}) + \boldsymbol{\mathcal{G}}_{(1)} \cdot \mathscr{F}(\boldsymbol{u}_{(1)}) + \left(\frac{\boldsymbol{\mathcal{G}}_{(1)}^2}{2} + \boldsymbol{\mathcal{G}}_{(2)}\right) \cdot \mathscr{F}(\overline{\boldsymbol{u}})\right] + \dots \end{aligned} \tag{4.30}$$

Finally, an expansion of the relaxation term $\boldsymbol{M}$ can be easily obtained using the definition of $\boldsymbol{M}$ in (3.26) and the expansion of the stress $\boldsymbol{T}$ in (4.23),

$$\begin{aligned}\boldsymbol{M} = {} & \frac{1}{Wi}\left[f(\operatorname{tr}\overline{\boldsymbol{C}})\boldsymbol{I} - f(3)\overline{\boldsymbol{F}}^{-1} \cdot \overline{\boldsymbol{F}}^{-\mathsf{T}}\right] \\ & + \epsilon \frac{1}{Wi}\left[\operatorname{tr}\left(\overline{\boldsymbol{F}}^{\mathsf{T}} \cdot \overline{\boldsymbol{F}} \cdot \boldsymbol{\mathcal{G}}_{(1)}\right) \frac{f^2(\operatorname{tr}\overline{\boldsymbol{C}})}{L_{\max}^2}\boldsymbol{I} + f(\operatorname{tr}\overline{\boldsymbol{C}})\boldsymbol{\mathcal{G}}_{(1)}\right] \\ & + \epsilon^2 \frac{f^2(\operatorname{tr}\overline{\boldsymbol{C}})}{L_{\max}^2 Wi}\left[\operatorname{tr}\left(\overline{\boldsymbol{F}}^{\mathsf{T}} \cdot \overline{\boldsymbol{F}} \cdot \left(\frac{\boldsymbol{\mathcal{G}}_{(1)}^2}{2} + \boldsymbol{\mathcal{G}}_{(2)}\right)\right)\boldsymbol{I} + \frac{f(\operatorname{tr}\overline{\boldsymbol{C}})}{L_{\max}^2}\operatorname{tr}^2\left(\overline{\boldsymbol{F}}^{\mathsf{T}} \cdot \overline{\boldsymbol{F}} \cdot \boldsymbol{\mathcal{G}}_{(1)}\right)\boldsymbol{I}\right. \\ & \left. + \operatorname{tr}\left(\overline{\boldsymbol{F}}^{\mathsf{T}} \cdot \overline{\boldsymbol{F}} \cdot \boldsymbol{\mathcal{G}}_{(1)}\right)\boldsymbol{\mathcal{G}}_{(1)} + \left(\frac{\boldsymbol{\mathcal{G}}_{(1)}^2}{2} + \boldsymbol{\mathcal{G}}_{(2)}\right)\frac{L_{\max}^2}{f(\operatorname{tr}\overline{\boldsymbol{C}})}\right] + \dots \end{aligned} \tag{4.31}$$

Substituting the expansions (4.27), (4.30), and (4.31) into the evolution equation for $\boldsymbol{G}$ given in (3.27), and equating coefficients of ϵ yields an equation for the evolution

of $\boldsymbol{\mathcal{G}}_{(1)}$ as

$$\partial_t \boldsymbol{\mathcal{G}}_{(1)} + \overline{\boldsymbol{u}} \cdot \boldsymbol{\nabla} \boldsymbol{\mathcal{G}}_{(1)} = 2\,\mathrm{sym}\,\left[\mathscr{F}(\boldsymbol{u}_{(1)}) + \boldsymbol{\mathcal{G}}_{(1)} \cdot \mathscr{F}(\overline{\boldsymbol{u}})\right] - \frac{1}{Wi} f(\mathrm{tr}\,\overline{\boldsymbol{C}}) \boldsymbol{\mathcal{G}}_{(1)} - \frac{f^2(\mathrm{tr}\,\overline{\boldsymbol{C}})}{L_{\max}^2 Wi} \mathrm{tr}\,\left(\overline{\boldsymbol{F}}^{\mathsf{T}} \cdot \overline{\boldsymbol{F}} \cdot \boldsymbol{\mathcal{G}}_{(1)}\right) \boldsymbol{I}. \quad (4.32)$$

Similarly, equating the coefficients of ϵ^2 yields an equation for the evolution of $\boldsymbol{\mathcal{G}}_{(2)}$ as

$$\begin{aligned} \partial_t \boldsymbol{\mathcal{G}}_{(2)} + \overline{\boldsymbol{u}} \cdot \boldsymbol{\nabla} \boldsymbol{\mathcal{G}}_{(2)} = &-\mathrm{sym}\left[\boldsymbol{\mathcal{G}}_{(1)} \cdot \left(\partial_t \boldsymbol{\mathcal{G}}_{(1)} + (\overline{\boldsymbol{u}} \cdot \boldsymbol{\nabla}) \boldsymbol{\mathcal{G}}_{(1)}\right)\right] - \boldsymbol{u}_{(1)} \cdot \boldsymbol{\nabla} \boldsymbol{\mathcal{G}}_{(1)} + \\ &2\,\mathrm{sym}\left[\mathscr{F}(\boldsymbol{u}_{(2)}) + \boldsymbol{\mathcal{G}}_{(1)} \cdot \mathscr{F}(\boldsymbol{u}_{(1)}) + \left(\frac{\boldsymbol{\mathcal{G}}_{(1)}^2}{2} + \boldsymbol{\mathcal{G}}_{(2)}\right) \cdot \mathscr{F}(\overline{\boldsymbol{u}})\right] \\ &- \frac{f^2(\mathrm{tr}\,\overline{\boldsymbol{C}})}{L_{\max}^2 Wi}\left[\mathrm{tr}\,\left(\overline{\boldsymbol{F}}^{\mathsf{T}} \cdot \overline{\boldsymbol{F}} \cdot \left(\frac{\boldsymbol{\mathcal{G}}_{(1)}^2}{2} + \boldsymbol{\mathcal{G}}_{(2)}\right)\right) \boldsymbol{I} + \frac{f(\mathrm{tr}\,\overline{\boldsymbol{C}})}{L_{\max}^2} \mathrm{tr}^{\,2}\left(\overline{\boldsymbol{F}}^{\mathsf{T}} \cdot \overline{\boldsymbol{F}} \cdot \boldsymbol{\mathcal{G}}_{(1)}\right) \boldsymbol{I}\right. \\ &\left. + \mathrm{tr}\,\left(\overline{\boldsymbol{F}}^{\mathsf{T}} \cdot \overline{\boldsymbol{F}} \cdot \boldsymbol{\mathcal{G}}_{(1)}\right) \boldsymbol{\mathcal{G}}_{(1)} + \left(\frac{\boldsymbol{\mathcal{G}}_{(1)}^2}{2} + \boldsymbol{\mathcal{G}}_{(2)}\right) \frac{L_{\max}^2}{f(\mathrm{tr}\,\overline{\boldsymbol{C}})}\right]. \quad (4.33) \end{aligned}$$

The expansion in (4.33) depends on the time rate of change of $\boldsymbol{\mathcal{G}}_{(1)}$ for which an equation is provided in (4.32). From (4.32), we have

$$\begin{aligned} \mathrm{sym}\,\left[\boldsymbol{\mathcal{G}}_{(1)} \cdot (\partial_t \boldsymbol{\mathcal{G}}_{(1)} + \overline{\boldsymbol{u}} \cdot \boldsymbol{\nabla} \boldsymbol{\mathcal{G}}_{(1)})\right] = &\boldsymbol{\mathcal{G}}_{(1)} \cdot \mathrm{sym}\,[\mathscr{F}(\boldsymbol{u}_{(1)})] + \mathrm{sym}\,[\mathscr{F}(\boldsymbol{u}_{(1)})] \cdot \boldsymbol{\mathcal{G}}_{(1)} \\ &+ \mathrm{sym}\,[\boldsymbol{\mathcal{G}}_{(1)}^2 \cdot \mathscr{F}(\overline{\boldsymbol{u}})] + \boldsymbol{\mathcal{G}}_{(1)} \cdot \mathrm{sym}\,[\mathscr{F}(\overline{\boldsymbol{u}})] \cdot \boldsymbol{\mathcal{G}}_{(1)} \\ &- \frac{1}{Wi}\left[\frac{f^2(\mathrm{tr}\,\overline{\boldsymbol{C}})}{L_{\max}^2} \mathrm{tr}\,\left(\overline{\boldsymbol{F}}^{\mathsf{T}} \cdot \overline{\boldsymbol{F}} \cdot \boldsymbol{\mathcal{G}}_{(1)}\right) \boldsymbol{\mathcal{G}}_{(1)} + f(\mathrm{tr}\,\overline{\boldsymbol{C}}) \boldsymbol{\mathcal{G}}_{(1)}^2\right] \quad (4.34) \end{aligned}$$

Substituting the above expression into (4.33) and simplifying yields an expression for the evolution of $\boldsymbol{\mathcal{G}}_{(2)}$ as

$$\begin{aligned}\partial_t \boldsymbol{\mathcal{G}}_{(2)} + \overline{\boldsymbol{u}} \cdot \boldsymbol{\nabla} \boldsymbol{\mathcal{G}}_{(2)} &= 2\,\mathrm{sym}\left[\mathscr{F}(\boldsymbol{u}_{(2)}) + \boldsymbol{\mathcal{G}}_{(2)} \cdot \mathscr{F}(\overline{\boldsymbol{u}})\right] - \frac{f(\mathrm{tr}\,\overline{\boldsymbol{C}})}{Wi}\boldsymbol{\mathcal{G}}_{(2)} \\ &\quad - \boldsymbol{u}_{(1)} \cdot \boldsymbol{\nabla}\boldsymbol{\mathcal{G}}_{(1)} - \boldsymbol{\mathcal{G}}_{(1)} \cdot \mathrm{sym}\left[\mathscr{F}(\overline{\boldsymbol{u}})\right] \cdot \boldsymbol{\mathcal{G}}_{(1)} \\ &\quad + \boldsymbol{\mathcal{G}}_{(1)} \cdot \mathrm{asym}\left[\mathscr{F}(\boldsymbol{u}_{(1)})\right] - \mathrm{asym}\left[\mathscr{F}(\boldsymbol{u}_{(1)})\right] \cdot \boldsymbol{\mathcal{G}}_{(1)} + \frac{f(\mathrm{tr}\,\overline{\boldsymbol{C}})}{2\,Wi}\boldsymbol{\mathcal{G}}_{(1)}^2 \\ &\quad - \frac{f^2(\mathrm{tr}\,\overline{\boldsymbol{C}})}{L_{\max}^2 Wi}\left[\mathrm{tr}\left(\overline{\boldsymbol{F}}^{\mathsf{T}} \cdot \overline{\boldsymbol{F}} \cdot \left(\frac{\boldsymbol{\mathcal{G}}_{(1)}^2}{2} + \boldsymbol{\mathcal{G}}_{(2)}\right)\right) + \frac{f(\mathrm{tr}\,\overline{\boldsymbol{C}})}{L_{\max}^2}\mathrm{tr}^{\,2}\left(\overline{\boldsymbol{F}}^{\mathsf{T}} \cdot \overline{\boldsymbol{F}} \cdot \boldsymbol{\mathcal{G}}_{(1)}\right)\right]\boldsymbol{I} \quad (4.35)\end{aligned}$$

where $\mathrm{asym}\,(\boldsymbol{A}) = \frac{1}{2}(\boldsymbol{A} - \boldsymbol{A}^{\mathsf{T}})$ is the asymmetric part of the tensor $\boldsymbol{A}$.

The above equations are valid for the FENE-P model. By setting $L_{\max} \to \infty$, we can retrieve the relevant Oldroyd-B equations. Thus. for the Oldroyd-B model, the equation for $\boldsymbol{u}_{(1)}$ in (4.25) reduces to

$$\begin{aligned}\partial_t \boldsymbol{u}_{(1)} + \overline{\boldsymbol{u}} \cdot \boldsymbol{\nabla}\boldsymbol{u}_{(1)} + \boldsymbol{u}_{(1)} \cdot \boldsymbol{\nabla}\overline{\boldsymbol{u}} &= -\boldsymbol{\nabla} p_{(1)} + \frac{\beta}{Re}\boldsymbol{\Delta}\boldsymbol{u}_{(1)} \\ &\quad + \frac{1-\beta}{WiRe}\boldsymbol{\nabla} \cdot \left[f(\mathrm{tr}\,\overline{\boldsymbol{C}})\overline{\boldsymbol{F}} \cdot \boldsymbol{\mathcal{G}}_{(1)} \cdot \overline{\boldsymbol{F}}^{\mathsf{T}}\right], \quad (4.36)\end{aligned}$$

the equation for $\boldsymbol{u}_{(2)}$ in (4.26) reduces to

$$\begin{aligned}\partial_t \boldsymbol{u}_{(2)} + \overline{\boldsymbol{u}} \cdot \boldsymbol{\nabla}\boldsymbol{u}_{(2)} + \boldsymbol{u}_{(2)} \cdot \boldsymbol{\nabla}\overline{\boldsymbol{u}} + \boldsymbol{u}_{(1)} \cdot \boldsymbol{\nabla}\boldsymbol{u}_{(1)} &= -\boldsymbol{\nabla} p_{(2)} + \frac{\beta}{Re}\boldsymbol{\Delta}\boldsymbol{u}_{(2)} \\ &\quad + \frac{1-\beta}{WiRe}\boldsymbol{\nabla} \cdot \left[\overline{\boldsymbol{F}} \cdot \left(\frac{\boldsymbol{\mathcal{G}}_{(1)}^2}{2} + \boldsymbol{\mathcal{G}}_{(2)}\right) \cdot \overline{\boldsymbol{F}}^{\mathsf{T}} f(\mathrm{tr}\,\overline{\boldsymbol{C}})\right], \quad (4.37)\end{aligned}$$

the equation for $\boldsymbol{\mathcal{G}}_{(1)}$ in (4.32) reduces to

$$\partial_t \boldsymbol{\mathcal{G}}_{(1)} + \overline{\boldsymbol{u}} \cdot \boldsymbol{\nabla} \boldsymbol{\mathcal{G}}_{(1)} = 2\,\mathrm{sym}\,\left[\mathscr{F}(\boldsymbol{u}_{(1)}) + \boldsymbol{\mathcal{G}}_{(1)} \cdot \mathscr{F}(\overline{\boldsymbol{u}})\right] - \frac{1}{Wi}\boldsymbol{\mathcal{G}}_{(1)}, \tag{4.38}$$

and finally, the equation for $\boldsymbol{\mathcal{G}}_{(2)}$ in (4.35) reduces to

$$\begin{aligned}\partial_t \boldsymbol{\mathcal{G}}_{(2)} + \overline{\boldsymbol{u}} \cdot \boldsymbol{\nabla} \boldsymbol{\mathcal{G}}_{(2)} = {} & 2\,\mathrm{sym}\,[\mathscr{F}(\boldsymbol{u}_{(2)}) + \boldsymbol{\mathcal{G}}_{(2)} \cdot \mathscr{F}(\overline{\boldsymbol{u}})] - \frac{1}{Wi}\boldsymbol{\mathcal{G}}_{(2)} \\ & - \boldsymbol{u}_{(1)} \cdot \boldsymbol{\nabla} \boldsymbol{\mathcal{G}}_{(1)} - \boldsymbol{\mathcal{G}}_{(1)} \cdot \mathrm{sym}\,[\mathscr{F}(\overline{\boldsymbol{u}})] \cdot \boldsymbol{\mathcal{G}}_{(1)} \\ & + \boldsymbol{\mathcal{G}}_{(1)} \cdot \mathrm{asym}\,[\mathscr{F}(\boldsymbol{u}_{(1)})] - \mathrm{asym}\,[\mathscr{F}(\boldsymbol{u}_{(1)})] \cdot \boldsymbol{\mathcal{G}}_{(1)} + \frac{1}{2\,Wi}\boldsymbol{\mathcal{G}}_{(1)}^2. \end{aligned} \tag{4.39}$$

The following skew-symmetric term appears in the equations for $\boldsymbol{\mathcal{G}}_{(2)}$, (4.35) and (4.39),

$$\boldsymbol{\mathcal{G}}_{(1)} \cdot \mathrm{asym}\,[\mathscr{F}(\boldsymbol{u}_{(1)})] - \mathrm{asym}\,[\mathscr{F}(\boldsymbol{u}_{(1)})] \cdot \boldsymbol{\mathcal{G}}_{(1)}. \tag{4.40}$$

Since the term is skew-symmetric, it has zero trace and therefore does not contribute towards the evolution of $\mathrm{tr}\,\boldsymbol{\mathcal{G}}_{(2)}$ and thus represents a volume-preserving deformation. The latter fact can be shown by taking the logarithm of the weakly nonlinear

deformation (4.6)

$$\log\det \boldsymbol{G} = \det(\mathrm{e}^{\epsilon\boldsymbol{\mathcal{G}}_{(1)}/2} \cdot \mathrm{e}^{\epsilon^2\boldsymbol{\mathcal{G}}_{(2)}} \cdot \mathrm{e}^{\epsilon\boldsymbol{\mathcal{G}}_{(1)}/2}) \tag{4.41}$$

$$= \log\det \mathrm{e}^{\epsilon\boldsymbol{\mathcal{G}}_{(1)}/2} + \log\det \mathrm{e}^{\epsilon^2\boldsymbol{\mathcal{G}}_{(2)}} + \log\det \mathrm{e}^{\epsilon\boldsymbol{\mathcal{G}}_{(1)}/2} \tag{4.42}$$

$$= \epsilon \mathrm{tr}\, \boldsymbol{\mathcal{G}}_{(1)} + \epsilon^2 \mathrm{tr}\, \boldsymbol{\mathcal{G}}_{(2)} \tag{4.43}$$

where, without loss of generality, we assumed $N = 2$. If $\mathrm{tr}\, \boldsymbol{\mathcal{G}}_{(2)} = 0$, the deformation associated with $\boldsymbol{\mathcal{G}}_{(2)}$ does not contribute to $\log\det \boldsymbol{G}$ and is volume-preserving. The interesting part about the volume-preserving component of the evolution (4.40) of $\boldsymbol{\mathcal{G}}_{(2)}$ is that it only depends on $\boldsymbol{u}_{(1)}$ and $\boldsymbol{\mathcal{G}}_{(1)}$.

We will be particularly interested in the case of linear perturbations. Here we set

$$\boldsymbol{\mathcal{G}}_{(k)} = \boldsymbol{0}, \qquad k > 1 \tag{4.44}$$

and thus

$$\boldsymbol{G} = \mathrm{e}^{\boldsymbol{\mathcal{G}}} = \mathrm{e}^{\epsilon\boldsymbol{\mathcal{G}}_{(1)}} = \boldsymbol{I} + \epsilon\boldsymbol{\mathcal{G}}_{(1)} + \dots \tag{4.45}$$

The state variables in the linearized equations, (4.25) and (4.32), are then a velocity field and a tangent to $\mathbf{Pos}_3$, unlike in the full governing equations, (2.28)–(2.30), where the state variables are a velocity field and conformation tensor field. This is important to note, since tangents to $\mathbf{Pos}_3$ have a distinct interpretation from $\boldsymbol{C}$ and are in $\mathbf{Sym}_3$,

they are not required to be positive–definite. The tangent to $\mathbf{Pos}_3$ in the equations has been expressed using $\boldsymbol{\mathcal{G}}$ but, by (4.13), it can equivalently expressed using $\boldsymbol{C}'$. Such linearized equations in terms of $\boldsymbol{C}'$ have been derived previously by directly applying an additive decomposition to the governing equations.[91,206] The present work expresses the perturbation equations in terms of $\boldsymbol{\mathcal{G}}$ because then the scalar product on the local tangent space on $\mathbf{Pos}_3$ coincides with the standard Frobenius scalar product. Such a formulation is important when the scalar product is needed. As an example, consider the eigenmodes associated with linearized equations, (4.25) and (4.32). These modes are equivalent in both approaches, because the eigenvalue problem (see e.g. Zhang *et al.*[206]) does not depend on the scalar product. However, projection of a flow state on one of the modes depends on the scalar product. It follows that projections using the function space generalization of the Frobenius scalar product are most appropriate when we use $\boldsymbol{\mathcal{G}}$, and not $\boldsymbol{C}'$, since then the scalar product is consistent with the global metric on $\mathbf{Pos}_3$. We will be considering the evolution of such modes in the present work. We first derive a simple kinematic constraint on the linear evolution of the modes, which arises due to the positive–definiteness condition on $\boldsymbol{G}$.

4.3.1 Constraint on linear evolution

Suppose we set the flow initial condition as a perturbed base-flow, $\boldsymbol{u}|_{t=0} = \overline{\boldsymbol{u}} + \epsilon \boldsymbol{q}$, $\boldsymbol{G}|_{t=0} = \boldsymbol{I} + \epsilon \boldsymbol{\mathcal{Q}}$, with $\epsilon \ll 1$, and $(\boldsymbol{q}, \boldsymbol{\mathcal{Q}})$ is an unstable mode of the equations (4.25)

and (4.32), with associated growth rate, $\omega_{\mathrm{i}} > 0$. If we assume that the mode grows according to linear theory for some time and $\boldsymbol{G}$ evolves along Euclidean lines, then $\boldsymbol{G}(t) = \boldsymbol{I} + \epsilon \boldsymbol{\mathcal{Q}} \mathrm{e}^{\omega_{\mathrm{i}} t}$. Suppose $\boldsymbol{\mathcal{Q}}$ is not zero and is harmonic in a spatial direction, then $\boldsymbol{\mathcal{Q}}$ has a strictly negative eigenvalue somewhere in the domain. For positive–definiteness of $\boldsymbol{G}$, we require $1 + \epsilon \sigma_i(\boldsymbol{\mathcal{Q}}) \mathrm{e}^{\omega_{\mathrm{i}} t} > 0$ for each $i = 1, 2, 3$, where $\sigma_i(\boldsymbol{A})$ denotes the i-th largest eigenvalue of the tensor $\boldsymbol{A}$. Wherever $\sigma_i(\boldsymbol{\mathcal{Q}}) < 0$, the dynamics must induce a curvature on the evolution along $\mathbf{Pos}_3$ before a time $t_{\max}$ when the eigenvalue crosses zero. This $t_{\max}$ is given by

$$\omega_{\mathrm{i}} t_{\max} = -\left(\log \epsilon + \log \max_i |\sigma_i(\boldsymbol{\mathcal{Q}})| \right), \tag{4.46}$$

and determines an upper bound on the time for which evolution of $\boldsymbol{G}$ along Euclidean lines does not violate the positive definiteness constraint on the conformation tensor. The condition (4.46) also serves as a guide for selecting initial perturbation amplitudes based on the growth rate and the spectrum of the tensor $\boldsymbol{\mathcal{Q}}$. Instead of evolving along Euclidean lines, one may assume that $\boldsymbol{G}$ evolves along geodesics. We would then formally have the superexponential evolution $\boldsymbol{G} = \mathrm{e}^{\epsilon \boldsymbol{\mathcal{Q}} \mathrm{e}^{\omega_{\mathrm{i}} t}}$, but by expanding the exponentials it can be easily shown that such an evolution is equivalent to evolution along Euclidean lines for sufficiently small ϵ.

Physically, a perturbation that is harmonic in space leads to regions of the flow where the polymers are compressed much more, in the sense of a volumetric change,

than the maximum expansion. This is because positive and negative additive perturbations to $\overline{\boldsymbol{C}}$ with equal magnitudes are not of equal magnitude with respect to the natural distance on $\mathbf{Pos}_3$. Where highly compressed, the polymers rapidly release stored elastic energy, leading to nonlinear evolution.

4.4 Tollmien–Schlichting waves

In this section, we use direct numerical simulations to examine the nonlinear evolution of a Tollmien–Schlichting wave in channel flow of a FENE-P fluid. The initial disturbance to the steady base flow is a two-dimensional unstable eigenmode of the linearized equations, (4.25) and (4.32), with a stress relation of the form (4.16). Results from the DNS will be used to illustrate the theoretical developments described in the previous sections.

The simulation setup is identical to the one described in Reference 91, including initial conditions and the base-flow and instability-wave parameters. The simulation physical parameters are reported in table 4.1 and the details of the spatiotemporal discretization is listed in table 4.2. The flow setup and geometry is the same as described in §1.3.1. As in Reference 91, we consider the evolution of the most unstable eigenmode for fixed Re, β, $L_{\max}$, and two different Wi. These modes have streamwise wavenumber of $k_x = 1$, with the associated growth rate ω_{i} and phase velocity ω_{r}/k_x listed in table 4.1. The only difference between the present simulation and that by

Reference 91 is the numerical algorithm used to march the conformation tensor, which is designed to ensure positive–definiteness. Details of the DNS algorithm is provided in appendix B.

We use the standard laminar base-state, which can be derived from the governing equations by assuming that the flow is fully developed so that the state variables are only functions of y. The authors in Reference 91 also used the standard laminar base-state. The velocity components are given by

$$\overline{u}(y) = \frac{1}{2}\frac{Re}{\beta}\frac{\mathrm{d}\overline{p}}{\mathrm{d}x}(y^2-1) - \frac{1-\beta}{\beta}\int_{-1}^{y}\overline{T}_{xy}(s)\,\mathrm{d}s, \quad \overline{v}=0, \quad \overline{w}=0 \tag{4.47}$$

and the laminar pressure gradient $\mathrm{d}\overline{p}/\mathrm{d}x$ is a fixed constant chosen so that the bulk velocity is one, $\frac{1}{2}\int_{-1}^{1}\overline{u}(y)\,\mathrm{d}y = 1$. The polymer stress component $\overline{T}_{xy}$ is a solution to the following depressed cubic equation

$$\frac{1}{L_{\max}^2}\overline{T}_{xy}^3 + \frac{f(3)}{2\,Wi^2}\left(1 + \frac{2f(3)+1}{L_{\max}^2} + \frac{1-\beta}{\beta}f(3)\right)\overline{T}_{xy} - \frac{Ref^2(3)}{2\beta\,Wi^2}\frac{\mathrm{d}\overline{p}}{\mathrm{d}x}y = 0. \tag{4.48}$$

The discriminant of (4.48) is negative and thus there is only one real root, which can be obtained using standard methods such as the analytical approach due to Cardano.[207] The remaining components of the stress are

$$\overline{T}_{xx} = \frac{2\,Wi}{f(3)}\overline{T}_{xy}^2, \quad \overline{T}_{yy} = \overline{T}_{zz} = \overline{T}_{xz} = \overline{T}_{yz} = 0 \tag{4.49}$$

and the associated conformation tensor can be calculated using the stress relation (4.16).

The simulation initial condition consists of of a small-amplitude perturbation eigenmode superimposed onto the laminar base state $(\overline{\boldsymbol{u}}, \overline{\boldsymbol{C}})$,

$$\boldsymbol{u}|_{t=0} = \overline{\boldsymbol{u}} + \mathrm{Re}\{\hat{\boldsymbol{u}}'|_{t=0} \mathrm{e}^{\mathrm{i}k_x x}\}, \qquad \boldsymbol{C}|_{t=0} = \overline{\boldsymbol{C}} + \mathrm{Re}\{\hat{\boldsymbol{C}}'|_{t=0} \mathrm{e}^{\mathrm{i}k_x x}\} \tag{4.50}$$

where the initial perturbation is fixed at 0.01% of the bulk velocity. The non-zero components of $\hat{\boldsymbol{C}}'|_{t=0}$ are shown in figures 4.4 and 4.5, along with the non-zero components of $\hat{\boldsymbol{\mathcal{G}}}|_{t=0}$, which is the perturbation tangent along $\mathbf{Pos}_3$ obtained by pre and post multiplying (4.50) by $\overline{\boldsymbol{F}}^{-1}$,

$$\boldsymbol{G}|_{t=0} = \boldsymbol{I} + \mathrm{Re}\{\hat{\boldsymbol{\mathcal{G}}}|_{t=0} \mathrm{e}^{\mathrm{i}k_x x}\}. \tag{4.51}$$

The correct form of the tangent on $\mathbf{Pos}_3$, $\hat{\boldsymbol{\mathcal{G}}}|_{t=0}$, reveals details about the perturbation that are not apparent from $\hat{\boldsymbol{C}}'|_{t=0}$. We describe the most salient of these points below.

We first consider the low Weissenberg number case, $Wi = 1.83$. The perturbation streamwise normal stretch, $\hat{C}'_{xx}|_{t=0}$, shown in 4.4(a) suggests that the polymer perturbation deformation rapidly tapers off above the critical layer, the location where the perturbation phase speed equals to the local mean velocity. However, the magnitude of $|(\hat{\mathcal{G}}_{xx}|_{t=0})|$ in 4.4(e) remains similar to that at the critical layer up to 0.84 channel half-heights away from the wall. Since $\mathrm{tr}\,\hat{\boldsymbol{\mathcal{G}}}|_{t=0} \approx \hat{\mathcal{G}}_{xx}|_{t=0}$, the large values

of $\hat{\mathcal{G}}_{xx}|_{t=0}$ imply that the volumetric deformation with respect to the mean induced by the perturbation is similar deep in the channel and at the critical layer. This is a reflection of the fact that the mean volume is smaller closer to the centreline and therefore deformations with respect to it appear, in general, larger than those with respect to the near wall configuration. While the maximum of $|(\hat{\mathcal{C}}'_{yy}|_{t=0})|$ is located at the critical layer, the maximum of $|(\hat{\mathcal{G}}_{yy}|_{t=0})|$ occurs at the wall. A sub critical-layer peak also appears in $|(\hat{\mathcal{G}}_{xy}|_{t=0})|$ that is missing from $|(\hat{\mathcal{C}}'_{xy}|_{t=0})|$. Since the component $\hat{\mathcal{G}}_{xy}|_{t=0}$ captures the shearing deformation induced by perturbation on the mean configuration, the perturbation induces the most shearing of the mean configuration below the critical layer. The region of weakest shearing is not at the channel centreline, but approximately 0.84 channel half-heights away from the wall. For the high Weissenberg number case, $Wi = 6.67$, figures 4.5(a)–(e) show that both $\hat{\mathcal{C}}'_{xx}|_{t=0}$ and $|(\hat{\mathcal{G}}_{xx}|_{t=0})|$, tapers off above the critical layer unlike for the low Weissenberg number case. The peak $|(\hat{\mathcal{G}}_{xx}|_{t=0})|$ is no longer at the wall, but at the critical layer. On the other hand, while the maximum of $|(\hat{\mathcal{C}}'_{yy}|_{t=0})|$ is located at the critical layer, the maximum of $|(\hat{\mathcal{G}}_{yy}|_{t=0})|$ below the critical layer. Similar to the low Weissenberg number case, we find a smaller peak in $|(\hat{\mathcal{G}}_{xx}|_{t=0})|$ and $|(\hat{\mathcal{G}}_{yy}|_{t=0})|$ near the centreline. However, the peak occurs at ≈ 0.95 channel half-heights away from the wall, which is closer to the centreline than in the low Weissenberg number case. The same location also shows minimum shearing with respect to the mean configuration.

The upper bound for which $\boldsymbol{G}$ can evolve along a Euclidean path on $\mathbf{Pos}_3$ was

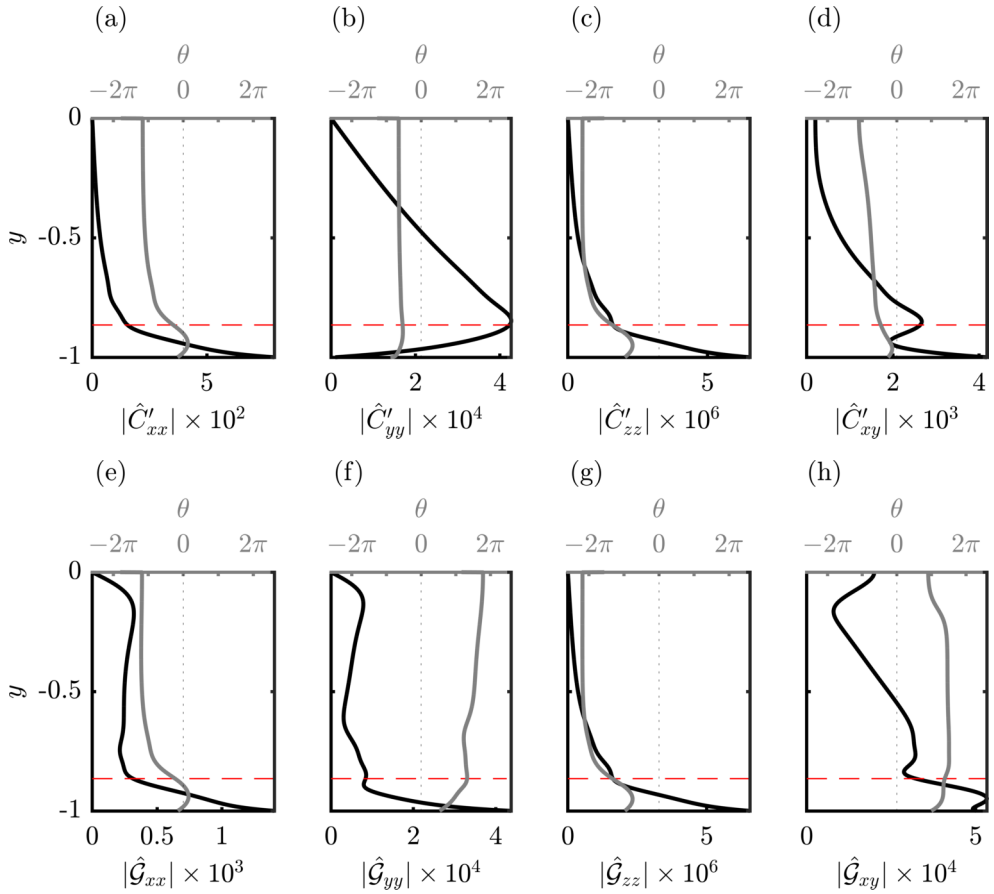

Figure 4.4: $Wi = 1.83$. Components of the initial perturbation tensor Fourier mode: (a)–(d) in the native form, $\hat{\boldsymbol{C}}'|_{t=0}$, and (e)–(h) in the form of a tangent on $\mathbf{Pos}_3$, $\hat{\boldsymbol{\mathcal{G}}}|_{t=0}$. In all panels: solid black lines are the absolute magnitudes of the modes, solid gray lines are the phase angles θ. The horizontal red dashed line is the location of the critical layer, and the vertical thin black dotted line marks zero phase angle.

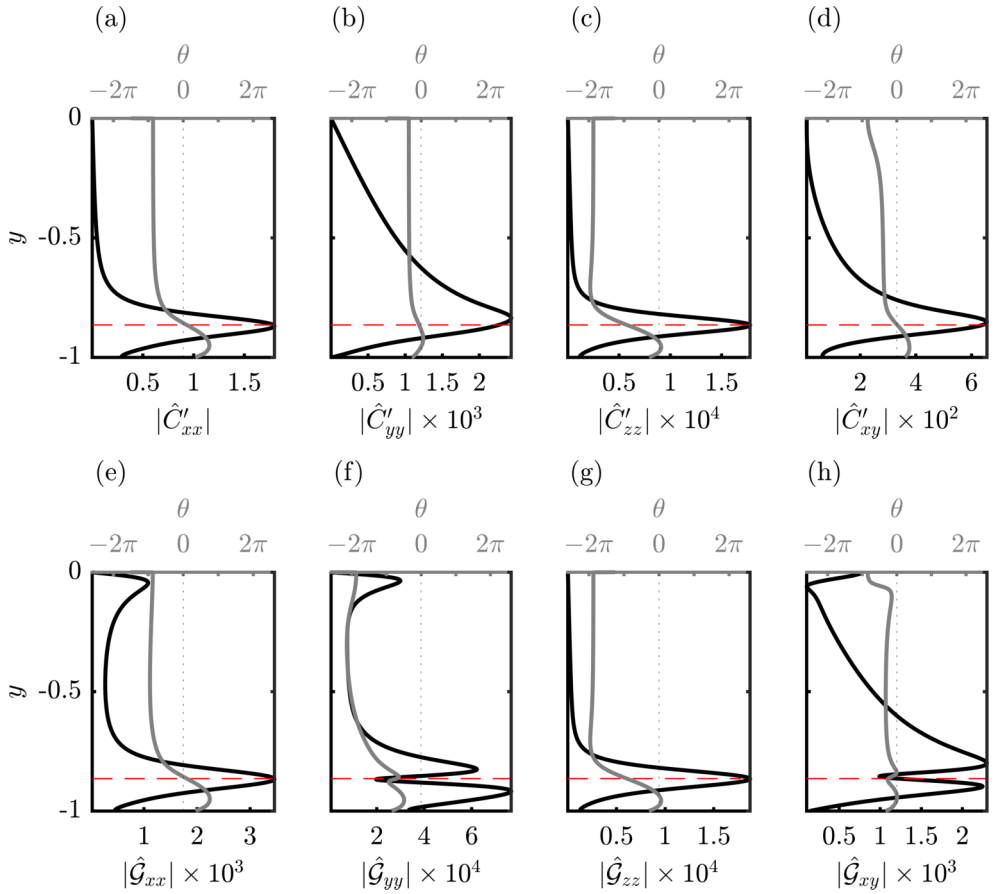

Figure 4.5: $Wi = 6.67$. Components of the initial perturbation tensor Fourier mode: (a)–(d) in the native form, $\hat{\boldsymbol{C}}'|_{t=0}$, and (e)–(h) in the form of a tangent on $\mathbf{Pos}_3$, $\hat{\boldsymbol{\mathcal{G}}}|_{t=0}$. In all panels: solid black lines are the absolute magnitudes of the modes, solid gray lines are the phase angles θ. The horizontal red dashed line is the location of the critical layer, and the vertical thin black dotted line marks zero phase angle.

				Domain size		Eigenvalue, $\omega_r + i\omega_i$	
Re	β	L_{max}	k_x	$L_x \times L_y \times L_z$	Wi	ω_r	ω_i
4667	0.90	100	1.00	$2\pi \times 2 \times 0.1$	1.83	0.3792	3.489×10^{-3}
					6.67	0.3799	1.571×10^{-3}

Table 4.1: Physical parameters of the viscoelastic (FENE-P) Tollmien–Schlichting wave simulation.

Grid size	Time step	Spatial resolution
$N_x \times N_y \times N_z$	Δt	$\Delta_x \times \Delta_y \times \Delta_z$
$160 \times 2048 \times 16$	2.5×10^{-3}	$0.0393 \times 0.000976562 \times 0.0063$

Table 4.2: Details of the spatiotemporal discretization for the viscoelastic (FENE-P) Tollmien–Schlichting wave simulation.

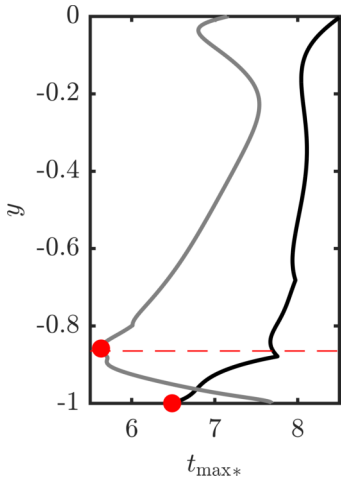

Figure 4.6: Upper bound, for each wall-normal plane, on the time for which evolution of $\boldsymbol{G}$ along Euclidean lines remains positive–definite, as defined in (4.46). The time is normalized by the growth rate, $t_{max*} = \omega_i t_{max}$. Black line is for $Wi = 1.83$ and grey line is for $Wi = 6.67$. The red markers indicate the lowest t_{max*} for each curve: $t_{max*} = 6.48$ for $Wi = 1.83$, and $t_{max*} = 5.63$ for $Wi = 6.67$. The location of the critical layer for $Wi = 6.67$, which is approximately equal to that for the $Wi = 1.83$ case, is shown as a red dashed line.

derived in (4.46). This upper bounded, calculated independently for each wall-normal plane, is shown in figure 4.6. The minimum upper bound determines the upper bound in the entire domain. For the low Weissenberg number case, $Wi = 1.83$, the minimum upper bounded is located at the wall, while for the $Wi = 6.67$, it is located at the critical layer suggesting that the critical layer plays an important role in the latter case.

In order to track the time evolution of the unstable modes, we consider the following scalar quantities

$$E \equiv \frac{1}{L_x L_y L_z} \int |\boldsymbol{u}'|^2 \,\mathrm{d}x \,\mathrm{d}y \,\mathrm{d}z, \quad J \equiv \frac{1}{L_x L_y L_z} \int d^2(\overline{\boldsymbol{C}}, \boldsymbol{C}) \,\mathrm{d}x \,\mathrm{d}y \,\mathrm{d}z \tag{4.52}$$

where $d^2(\overline{\boldsymbol{C}}, \boldsymbol{C}) = d^2(\boldsymbol{I}, \boldsymbol{G}) = \operatorname{tr} \boldsymbol{\mathcal{G}}^2$, and $\boldsymbol{\mathcal{G}} = \log \boldsymbol{G}$. The quantity E is the volume-averaged kinetic energy associated with $\boldsymbol{u}'$ and was used by the authors in Reference 91 to characterize viscoelastic Tollmien–Schlichting waves. The quantity E is also the volume-averaged Euclidean norm of $\boldsymbol{u}'$. The quantity J is the volume-averaged squared geodesic distance of $\boldsymbol{C}$ away from $\overline{\boldsymbol{C}}$.[208] The geodesic distance is the natural way to measure the size of the fluctuating deformation in $\boldsymbol{C}$ because we cannot define a norm on $\mathbf{Pos}_3$, since it is not a vector space.

The time evolutions of normalized E and J for both Wi are shown in figure 4.7(a) as a function of the normalized time $t_* = \omega_\mathrm{i} t$. For $Wi = 1.83$, the evolution of E matches the prediction by linear theory for $t_* \lesssim 5$, then shows superexponential

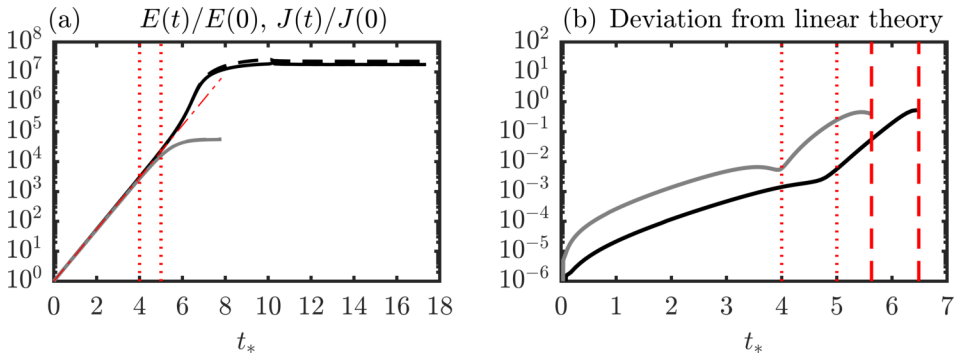

Figure 4.7: (a) Evolution of E and J, as defined in (4.52), normalized by the initial values: $E(0) = 2.05 \times 10^{-9}$, $J(0) = 1.53 \times 10^{-7}$ for $Wi = 1.83$ and $E(0) = 1.97 \times 10^{-9}$, $J(0) = 2.03 \times 10^{-6}$ for $Wi = 6.67$. Solid lines are $J(t)/J(0)$ while dashed lines are $E(t)/E(0)$. Black lines are $Wi = 1.83$ and gray lines are $Wi = 6.67$. The red dashed line in is the prediction by linear theory. (b) deviation from linear theory as defined by (4.54): volume-averaged geodesic distance between $\boldsymbol{G}$ and the conformation tensor predicted by linear theory, $\boldsymbol{I} + \mathrm{Re}\{\hat{\boldsymbol{\mathcal{G}}}|_{t=0} \mathrm{e}^{\mathrm{i}(k_x x + \omega t)}\}$. Black line is $Wi = 1.83$ and gray line is $Wi = 6.67$. The red dashed lines indicate the minimum $t_{\max *} = t_{\max} \omega_{\mathrm{i}}$ as defined in (4.46) and shown by red markers in figure 4.6. The red dotted lines mark $t_* = 4$ and $t_* = 5$ in both (a) and (b).

growth and finally saturates at $t_* \approx 10$. For $Wi = 6.67$, the evolution agrees with linear theory for $t_* \lesssim 4$, shows no superexponential growth and saturates at $t_* \approx 8$. The results for E agree with those in Reference 91 and suggest that different physical mechanisms are at play at the different Weissenberg numbers. The evolution of normalized J closely matches that of normalized E, and is consistent with an assumption that $\boldsymbol{G}$ initially evolves along a linear approximation of the geodesic on $\mathbf{Pos}_3$ emanating from $\boldsymbol{I}$ because for $t_* \lesssim 5$,

$$d^2(\overline{\boldsymbol{C}}, \boldsymbol{C}) = \mathrm{tr}\, \log^2 \boldsymbol{G} \approx \mathrm{tr}\, \log^2 (\boldsymbol{I} + \boldsymbol{\mathcal{G}}) \approx \mathrm{tr}\, \boldsymbol{\mathcal{G}}^2 \sim \epsilon^2 \mathrm{e}^{2\omega_{\mathrm{i}} t} \tag{4.53}$$

where we used the matrix Mercator series,[209] and assumed $\|\boldsymbol{\mathcal{G}}\| \sim \epsilon \ll 1$.

The deviation of the conformation tensor from the prediction by linear theory is considered in more detail in figure 4.7(b), which shows the volume-averaged geodesic distance between the conformation tensor obtained from the linear prediction and one obtained from the full nonlinear evolution,

$$\frac{1}{L_x L_y L_z} \int d(\boldsymbol{G}, \boldsymbol{I} + \mathrm{Re}\{\hat{\boldsymbol{G}}|_{t=0} \mathrm{e}^{\mathrm{i}(k_x x + \omega t)}\}) \, \mathrm{d}x \, \mathrm{d}y \, \mathrm{d}z. \tag{4.54}$$

The deviation is a measure of the importance of nonlinear effects. For the $Wi = 1.83$ case, it grows slowly until $t_* \approx 5$, when it abruptly begins to grow exponentially until $t_* \approx 6.5$. For larger times, the linear approximation does not remain positive–definite everywhere in the domain and thus the deviation cannot be calculated further. The upper bound for this linear evolution is shown in figure 4.6 and is calculated using (4.46). The initial growth in the deviation is associated with part of the region matching linear theory in the evolution of J, $0 \lesssim t_* \lesssim 5$, while the later growth may be associated with superexponential growth in E and J that appears before saturation. For the $Wi = 6.67$ case, we see a similar slow initial growth in the deviation until $t_* \approx 4$ where the growth abruptly becomes faster. However, the deviation eventually grows more slowly than the deviation does for the $Wi = 1.83$ case above $t_* \approx 5$.

Figures 4.8 and 4.9 show isocontours of two geometric measures, for the initial condition ($t_* = 0$) and for the saturated states ($t_* \approx 17$ for $Wi = 1.83$ and $t_* \approx 8$ for $Wi = 6.67$). Figures 4.8(a) and 4.9(a) show the logarithmic volume ratio (3.53)

with respect to the base-state: the ratio of the volume of $\boldsymbol{C}$ to the volume of $\overline{\boldsymbol{C}}$. Figures 4.8(b) and 4.9(b) show the geodesic distance (3.43) from the base-state. The isocontours of the logarithmic volume ratio at $Wi = 1.83$ differ significantly between the initial condition and the saturated state. For the initial condition, the most significant variations occur near the wall below the critical layer. On the other hand, the main activity in the saturated state is focused at approximately $y = -0.5$ where we find thin, elongated region of large volumetric expansion, with a secondary region of volumetric expansion centred at 0.9 channel half-heights away from the wall. The geodesic distance shown in figure 4.8(b) is consistent with these volumetric changes. In addition, the geodesic distance peaks at $x \approx 0.3\pi$ in the critical layer, even though this region only shows weak compression in figure 4.8(a). These observations are not incongruent, since the polymer can undergo a purely shearing deformation. The isocontours of the logarithmic volume ratio at $Wi = 6.67$, as shown in figure 4.9(a), are similar at both times. The geodesic distance in 4.9(b) is also similar at both times. Unlike in the low Wi case, the largest deviations in both the volume and the geodesic distance are located near the critical layer.

In order to examine the initial deviation away from the linear theory, we adopt the approach used by Benny and Lin[61] and assume that $\boldsymbol{G}$ can be expressed as a weakly nonlinear deformation, as in (4.7), at $t_* = 4$. The total deformation can be analysed using the tangents on $\mathbf{Pos}_3$, $\boldsymbol{\mathcal{G}}_{(k)}$. Figures 4.10(a)–(c) and 4.11(a)–(c) show, at $Wi = 1.83$ and $Wi = 6.67$, respectively, the xx, yy and zz components of $\epsilon\boldsymbol{\mathcal{G}}_{(1)}$

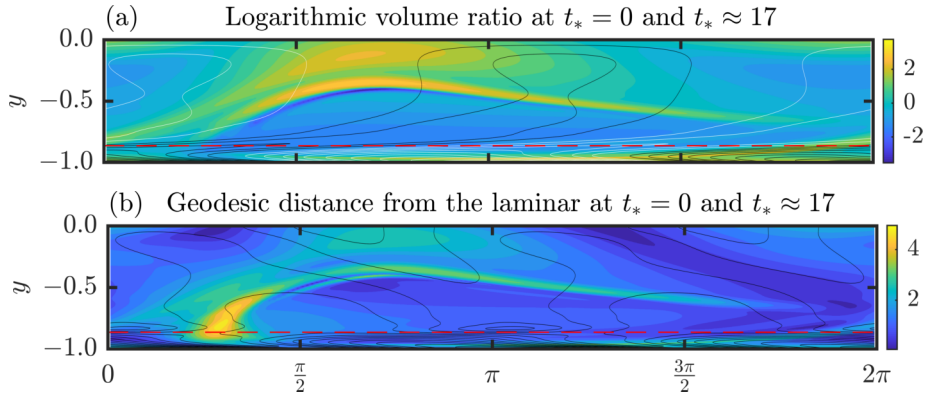

Figure 4.8: $Wi = 1.83$. Isocontours of (a) logarithmic volume ratio, $\operatorname{tr} \boldsymbol{\mathcal{G}} = \log(\det \boldsymbol{C} / \det \overline{\boldsymbol{C}})$, (b) geodesic distance from the laminar, $\sqrt{\operatorname{tr} \boldsymbol{\mathcal{G}}^2} = d(\boldsymbol{I}, \boldsymbol{G}) = d(\overline{\boldsymbol{C}}, \boldsymbol{C})$, at $t_* \in \{0, 17\}$. In both panels: flooded isocontours are at $t_* \approx 17$, thin white lines are negative isocontours at $t_* = 0$, and thin black lines are positive isocontours at $t_* = 0$. The isocontours in (a) lie in the range $[-1.1, 1.1] \times 10^{-3}$, with increment 1.1×10^{-4}, and in (b) lie in the range $[0.10, 1.50] \times 10^{-3}$, with increment 9.73×10^{-5}. The horizontal red dashed line is the location of the critical layer.

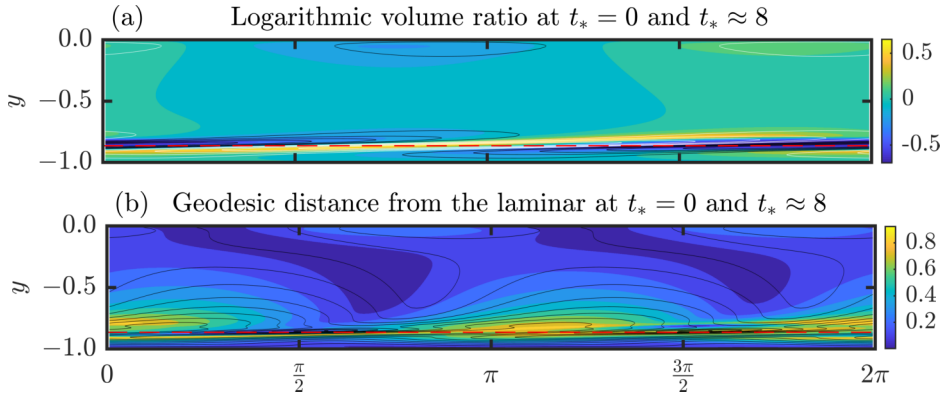

Figure 4.9: $Wi = 6.67$. Isocontours of (a) logarithmic volume ratio, $\operatorname{tr} \boldsymbol{\mathcal{G}} = \log(\det \boldsymbol{C} / \det \overline{\boldsymbol{C}})$, (b) geodesic distance from the laminar, $\sqrt{\operatorname{tr} \boldsymbol{\mathcal{G}}^2} = d(\boldsymbol{I}, \boldsymbol{G}) = d(\overline{\boldsymbol{C}}, \boldsymbol{C})$, at $t_* \in \{0, 8\}$. In both panels: flooded isocontours are at $t_* \approx 8$, thin white lines are negative isocontours at $t_* = 0$, and thin black lines are positive isocontours at $t_* = 0$. The isocontours in (a) lie in the range $[-2.6, 2.6] \times 10^{-3}$, with increment 5.2×10^{-4}, and in (b) lie in the range $[4.13, 32] \times 10^{-4}$, with increment 4.6×10^{-4}. The horizontal red dashed line is the location of the critical layer.

and $\epsilon^2\boldsymbol{\mathcal{G}}_{(2)}$. We use the growth rate and phase speed predicted by linear theory to calculate $\epsilon\boldsymbol{\mathcal{G}}_{(1)}$,

$$\epsilon\boldsymbol{\mathcal{G}}_{(1)} = \mathrm{Re}\{\hat{\boldsymbol{\mathcal{G}}}|_{t=0}\mathrm{e}^{\mathrm{i}(k_x x-\omega t)}\}. \tag{4.55}$$

where ω is the eigenvalue listed in Table 4.1. The nonlinear correction to the linear evolution is equal to $\epsilon^2\boldsymbol{\mathcal{G}}_{(2)} + \mathcal{O}(\epsilon^3)$. Using (4.7) we obtain

$$\epsilon^2\boldsymbol{\mathcal{G}}_{(2)} = \boldsymbol{G} - \left(\boldsymbol{I} + \epsilon\boldsymbol{\mathcal{G}}_{(1)} + \frac{1}{2}\epsilon^2\boldsymbol{\mathcal{G}}_{(1)}^2\right) + \mathcal{O}(\epsilon^3). \tag{4.56}$$

For the $Wi = 1.83$ case, the xx components of both $\epsilon\boldsymbol{\mathcal{G}}_{(1)}$ and $\epsilon^2\boldsymbol{\mathcal{G}}_{(2)}$ in figure 4.10(a) show similar isocontours above the critical layer but are out of phase with each other. Since $\mathrm{tr}\,\boldsymbol{\mathcal{G}}_{(1)} \approx (\mathcal{G}_{(1)})_{xx}$, the xx component determines the volumetric deformation due to the initial perturbation, $\epsilon\boldsymbol{\mathcal{G}}_{(1)}$. Such a simplification does not occur with $\epsilon^2\boldsymbol{\mathcal{G}}_{(2)}$ because the yy contribution to the trace is of the same order of magnitude as the xx contribution. The yy component of $\epsilon\boldsymbol{\mathcal{G}}_{(1)}$ and $\epsilon^2\boldsymbol{\mathcal{G}}_{(2)}$ have similar, but out-of-phase, isocontours below the critical layer but are dissimilar above. The isocontours of $\epsilon^2\boldsymbol{\mathcal{G}}_{(2)}$ are tilted away from the wall compared to $\epsilon\boldsymbol{\mathcal{G}}_{(1)}$. The isocontours of the xy component of $\epsilon\boldsymbol{\mathcal{G}}_{(1)}$ and $\epsilon^2\boldsymbol{\mathcal{G}}_{(2)}$ are shown in figure 4.10(c). This component represents the shearing deformation. For the prediction by linear theory, $\epsilon\boldsymbol{\mathcal{G}}_{(1)}$, the perturbations are most strongly shearing above the critical layer at $y \approx -0.75$, whereas for the nonlinear correction, $\epsilon^2\boldsymbol{\mathcal{G}}_{(2)}$, the shearing is focused closer to the critical and localized

in x. This nonlinear correction with significant localized shear is consistent with figure 4.8, where there is a region, localized in x and close to the critical layer, that shows the most significant geodesic deviation but locally only weakly compresses the polymer. These two factors indicate a shearing deformation. Figure 4.11 shows $\epsilon\boldsymbol{\mathcal{G}}_{(1)}$ and $\epsilon^2\boldsymbol{\mathcal{G}}_{(2)}$ at $Wi = 6.67$. The isocontours of $\epsilon\boldsymbol{\mathcal{G}}_{(1)}$ and $\epsilon^2\boldsymbol{\mathcal{G}}_{(2)}$ are similar but out-of-phase, especially near the critical layer. The main differences between the isocontours arise closer to the centreline, where the contours of $\epsilon^2\boldsymbol{\mathcal{G}}_{(2)}$ are more tilted towards the wall than $\epsilon\boldsymbol{\mathcal{G}}_{(1)}$.

4.5 Conclusion

Perturbing the conformation tensor, while maintaining physical and geometric consistency, is a more complicated proposition than perturbing a Euclidean object like the velocity field. In this chapter, we developed methods to perturb the conformation tensor in a linear (4.13) as well as weakly nonlinear manner (4.7) that maintain this consistency. Our approach provided us with a way to relate a perturbation to geometric behaviour on the manifold $\mathbf{Pos}_3$, as well as to the polymer deformation. The latter allowed us to study the deformation of the polymer during the nonlinear evolution of viscoelastic Tollmien–Schlichting waves. At low Wi, the insights we uncovered include the fact that the initial perturbation deformation shows significant volumetric deformation far from the wall, and the nonlinear effects provide an intense

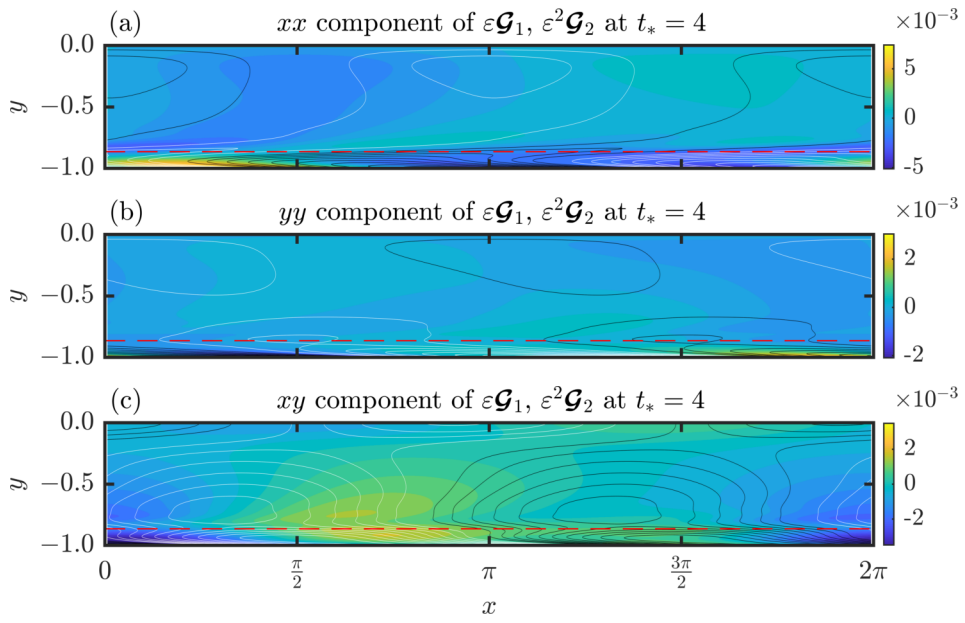

Figure 4.10: $Wi = 1.83$. Components of $\epsilon^k \boldsymbol{\mathcal{G}}_k$ for $k \in \{1, 2\}$, the tangents on $\mathbf{Pos}_3$ that appear in the weakly nonlinear expansion (4.7) at $t_* = 4$: (a) $\epsilon^k(\boldsymbol{\mathcal{G}}_k)_{xx}$, (b) $\epsilon^k(\boldsymbol{\mathcal{G}}_k)_{yy}$, and (c) $\epsilon^k(\boldsymbol{\mathcal{G}}_k)_{xy}$. In all panels: flooded isocontours are $\epsilon^2\boldsymbol{\mathcal{G}}_2$, thin white lines are negative isocontours of $\epsilon\boldsymbol{\mathcal{G}}_1$, and thin black lines are positive isocontours of $\epsilon\boldsymbol{\mathcal{G}}_1$. The positive isocontours in (a) lie in the range $[7.1, 71] \times 10^{-3}$, with increment 7.1×10^{-3}, in (b) lie in the range $[2.2, 22] \times 10^{-3}$, with increment 2.2×10^{-3}, and in (c) lie in the range $[2.7, 27] \times 10^{-3}$, with increment 2.7×10^{-3}. The negative isocontours are the minus the positive isocontours. The horizontal red dashed line is the location of the critical layer.

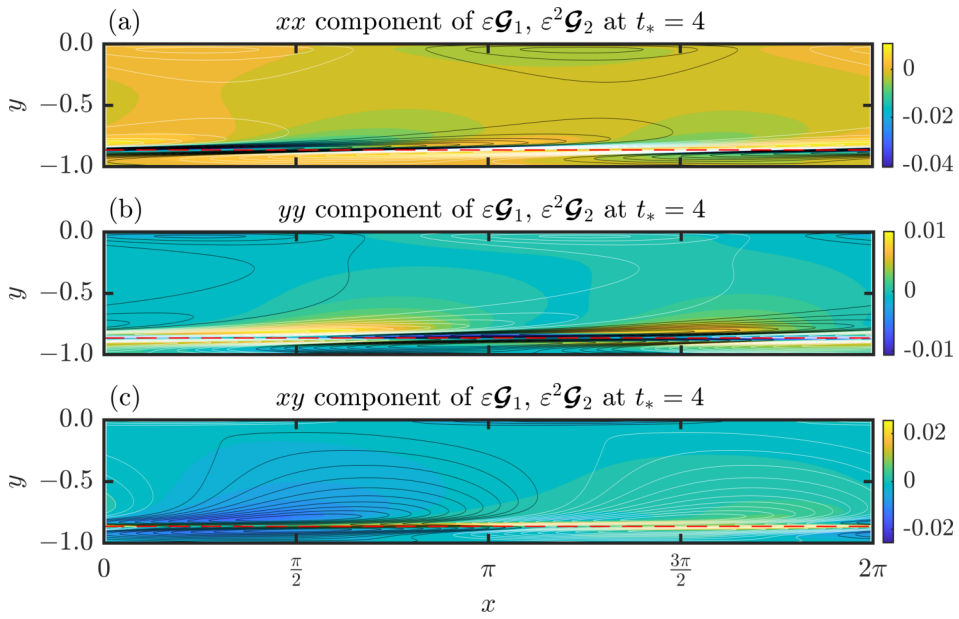

Figure 4.11: $Wi = 6.67$. Components of $\epsilon^k \boldsymbol{\mathcal{G}}_k$ for $k \in \{1, 2\}$, the tangents on $\mathbf{Pos}_3$ that appear in the weakly nonlinear expansion (4.7) at $t_* = 4$: (a) $\epsilon^k(\boldsymbol{\mathcal{G}}_k)_{xx}$, (b) $\epsilon^k(\boldsymbol{\mathcal{G}}_k)_{yy}$, and (c) $\epsilon^k(\boldsymbol{\mathcal{G}}_k)_{xy}$. In all panels: flooded isocontours are $\epsilon^2\boldsymbol{\mathcal{G}}_2$, thin white lines are negative isocontours of $\epsilon\boldsymbol{\mathcal{G}}_1$, and thin black lines are positive isocontours of $\epsilon\boldsymbol{\mathcal{G}}_1$. The positive isocontours in (a) lie in the range $[1.7, 17] \times 10^{-2}$, with increment 1.7×10^{-2}, in (b) lie in the range $[3.8, 38] \times 10^{-3}$, with increment 3.8×10^{-3}, and in (c) lie in the range $[1.1, 11] \times 10^{-2}$, with increment 1.1×10^{-2}. The negative isocontours are the minus the positive isocontours. The horizontal red dashed line is the location of the critical layer.

shearing deformation in a region localized in the streamwise direction and in the critical layer. The signature of this shearing appears in the saturated state.

Chapter 5

Conclusions

5.1 Overview

We started this dissertation by discussing the approach to turbulence adopted in Newtonian flows and presented why a similar path has not yet been embarked upon in viscoelastic flows. The problem is that the analysis of viscoelastic turbulence requires an evaluation of the fluctuations in the velocity field as well as in the elastic deformation of the polymers. The relevant deformation history can be captured using a positive–definite tensor, here called the conformation tensor, which is a new variable that does not appear in Newtonian flows. The problem of viscoelastic turbulence is then of quantifying the fluctuations in the velocity field and the conformation tensor. This is challenging because the standard approaches developed for the velocity field in Newtonian flows cannot be extended to the conformation tensor as the latter is not

a vector space quantity but rather belongs to a non-Euclidean Riemannian manifold. Hence, despite advances in direct numerical simulations, detailed quantitative analyses of the conformation tensor fluctuations have been lacking in the literature. This lack of analysis presents a fundamental barrier in developing theories of viscoelastic turbulence. The goal of this dissertation was to develop a theoretical framework that can be used to study viscoelastic turbulence and overcome the inherent problems outlined above. In broad strokes, the goal was achieved by the following accomplishments:

1. As an alternative to the Reynolds decomposition, we developed a decomposition of the conformation tensor that separates a base-state such as a statistically persistent mean from the fluctuations in a way that preserves the physical character of the variables. The resulting fluctuating conformation tensor also preserves a geometric interpretation associated with the Reynolds decomposition of the velocity field: the Reynolds decomposition is an affine transformation of the velocity field in Euclidean space, while the geometric decomposition is an affine transformation of the conformation tensor on the Riemannian manifold of positive–definite tensors.

2. We proposed scalar measures that can be used to quantify the fluctuations in the conformation tensor. Unlike any measures used before in the literature, the scalar measures here are based on the geometry of the set of positive–definite tensors and thus are not only analogous to the measures used to quantify

fluctuations in the velocity field, but are also mathematically sensible.

3. As an alternative to the standard weakly nonlinear expansion of the velocity field, we developed an approach to perturb the conformation tensor by successively smaller deformations applied to the fluctuating conformation tensor. We term this a weakly nonlinear deformation.

The accomplishments were, wherever possible, vivified by direct numerical simulations of viscoelastic (FENE-P) channel flow. The results of these simulations revealed new features of the concerned flows that were not previously obvious, and thereby buttressed the approach argued for in the present work.

The above achievements were executed over three chapters, each that provided distinct contributions towards the end goal. We summarize each of these chapters in the subsections below.

5.1.1 Interpretation of the conformation tensor

The first step to be taken was to determine the admissible physical interpretations of the conformation tensor. This exercise was undertaken in chapter 2, where we considered two different derivations of the constitutive equations available in the literature. One approach was based on a continuum thermodynamics framework that required the specification of energy storage and rate of dissipation functions.[116] In this approach, the conformation tensor was found to be a left Cauchy–Green ten-

sor associated with the polymer deformation from a natural configuration. Natural configurations are distinct from reference configurations in that the fluid elastically relaxes to a natural configuration, and not necessarily to a fixed reference configuration, when instantaneously stopped. The other approach was based on kinetic theory: the continuum-scale equations were sought by coarse-graining the microscopic dynamics.[75] In the microscopic dynamics, a polymer molecule was conceptualized as two beads connected with a spring, submersed in a solvent bath and experiencing random fluctuations. In this approach, the conformation tensor was the coarse-grained dyad formed using the end-to-end vector associated with the polymer molecule. We found that the two approaches yield the same equations only in the small deformation limit which implies that it was not necessarily thermodynamically consistent to use both interpretations of the conformation tensor.

In order to resolve the difficulty, we invoked the Beris–Edwards thermodynamic formalism.[102] The formalism provides a way to derive constitutive equations in a thermodynamically consistent manner. Crucially, it does not rely on a particular interpretation of the conformation tensor since it is treated as a generic 'structure' tensor representing the microscopic dynamics. All the present models of interest may be derived using the Beris–Edwards formalism and therefore we may freely interpret the conformation tensor as desired. The interpretation of the conformation tensor as a left Cauchy–Green tensor is one interpretation that we later find particularly useful since it provides an interpretation of the conformation tensor in terms of continuum-

scale kinematics.

5.1.2 Decomposition of the deformation

The additive decomposition that is obtained by extending the Reynolds decompositions to the conformation tensor leads to physically unrealizable fluctuating tensors. Scalar characterizations of this fluctuating tensor are different in magnitude based on whether a fluctuation is compressive or expansive. In chapter 3, we addressed the challenges described above by developing a geometric decomposition of the conformation tensor as an alternative to the Reynolds decomposition, and then proposed scalar measures to quantify the conformation tensor fluctuations.

Instead of the additive decomposition, it is more appropriate to decompose the polymer deformation instead. We took this path by multiplicatively decomposing the deformation gradient, obtained from the interpretation of the conformation tensor as a left Cauchy–Green tensor, into a deformation from the thermodynamic equilibrium to the mean configuration, and then another deformation from the mean to the instantaneous configuration. Such a process, which we called the geometric decomposition of the conformation tensor, was found to yield a fluctuating conformation tensor that has a clear physical interpretation as a deformation with respect to the mean configuration.

Once an appropriate fluctuating conformation tensor has been defined, scalar measures are required to quantify the turbulent fluctuations in this tensor. In Euclidean

space, the standard approach to formulate scalar measures relies on the 2–norm. For the velocity field, this choice leads to the kinetic energy as the relevant scalar measure. For symmetric tensors, this choice results in the squared Frobenius norm (here, the second moment invariant). The Frobenius norm is not meaningful for positive–definite tensors because the latter do not form a Euclidean space. For example, an undesirable consequence of the curved non-Euclidean nature of the set of positive–definite tensors is that the Frobenius norm associated with a compression has a finite upper bound, while the Frobenius norm associated with an expansion has no upper bound. In order to address such problems, we instead used a non-Euclidean geometry specifically constructed for the manifold of positive–definite tensors to develop three scalar measures.

Firstly, we obtained the geodesic distance of the fluctuating conformation tensor from the identity as a scalar measure of the magnitude of the fluctuating polymer deformation. The manifold of positive–definite tensors forms a metric space under the geodesic distance and thus, similar to the fluctuating kinetic energy, the (square–root) of our proposed scalar measure satisfies all the desirable properties of a metric such as the triangle inequality.

Secondly, in order to distinguish between compressions and expansions, we used the logarithmic volume ratio: the logarithm of the volume of the fluctuating conformation tensor to the instantaneous volume.

Thirdly, we proposed an anisotropy index to compare the shape of the deformation

ellipsoid associated with the fluctuating conformation tensor to that associated with the mean conformation tensor. This anisotropy index is the geodesic distance to the closest isotropic tensor on the manifold of positive–definite tensors.

We illustrated the approach we developed using drag-reduced turbulent channel flow and found several interesting features that enhance the present understanding of this flow. Of particular note is the geodesic distance of the mean conformation tensor from the closest isotropic tensor. This quantity shows a dramatic logarithmic decrease from very close to the wall, all the way to the near the centreline. We also found the fluctuations in the polymer peaked close to $y^+ = 100$ – a result that is not found when using the classical Reynolds decomposition. The isocontours of the three scalar measures were plotted and shown to have rich spatial structure. Finally, a found that the volume of mean conformation tensor is, on average, much larger than the mean volume. This finding suggests that the mean conformation tensor is not a good representative of the typical conformation tensor.

5.1.3 Weakly nonlinear deformations

In chapter 4, we considered the particular limit of small perturbations to a base-state conformation tensor. In order to obtain a weakly nonlinear expansion of the conformation tensor, similar to what is used for the velocity field, we again began our analysis by focusing on polymer deformation and not on the resulting conformation tensor. As with the geometric decomposition, instead of algebraically decomposing

the conformation tensor, we decomposed the polymer deformation. However, in this case we consider a series of successively smaller polymer deformations. Each deformation is analogous to a term in the weakly nonlinear expansion of the velocity field. The size of each small deformation is not based on the Euclidean norm but rather on the geodesic distance from the manifold. We thus call this a weakly nonlinear deformation.

By approximating the geodesics with their series expansions, we then obtained a weakly nonlinear type of expansion of the conformation tensor that is based on a physical decomposition of the polymer deformation. In general, the terms of the series are interdependent, prior to any consideration of the dynamics, reflecting the underlying curved geometry of the set of positive–definite tensors. From the vantage point of this general framework, we consider the limit of a single deformation and found that this yields equations similar to those obtained by a standard linearization. However, there is an added benefit with the present approach in that it supplies the correct scalar product is to be used in the analysis of the linear system. This scalar product is the one induced by the global metric on the set of positive–definite tensors. By using an appropriately transformed perturbation conformation tensor, one can revert to using the standard Frobenius inner product. To illustrate the ideas, we used simulations of viscoelastic Tollmien–Schlichting waves at two different Weissenberg numbers.

5.2 Future work and open questions

The present dissertation was concerned with developing a general framework to study viscoelastic turbulence. By definition, therefore, a considerable range of studies exploring viscoelastic turbulence can be undertaken using the framework developed herein. We explore some of these possibilities below, with a keen focus on particular questions directly raised by the results in this dissertation.

5.2.1 Turbulent channel flow

The most immediate questions of interest arise from the results of the direct numerical simulation of drag-reduced channel flow presented in chapter 3. Drag reduction is a technologically important aspect of viscoelastic flows that is still not fully understood. The results in chapter 3 suggest two routes for future work: one related to the fluctuations, and another related to the mean conformation tensor.

5.2.1.1 Spatial structure of fluctuations

The rich spatial structure seen in the contours of the scalar measures of the fluctuating conformation tensor, especially in the geodesic distance from the identity, is reminiscent of the spatial structure seen in the dissipation rate in Newtonian flows (see figure 5.1). The dissipation rate in Newtonian flows is highly intermittent, showing singularities or highly spiked regions, and evidence suggests the dissipation rate

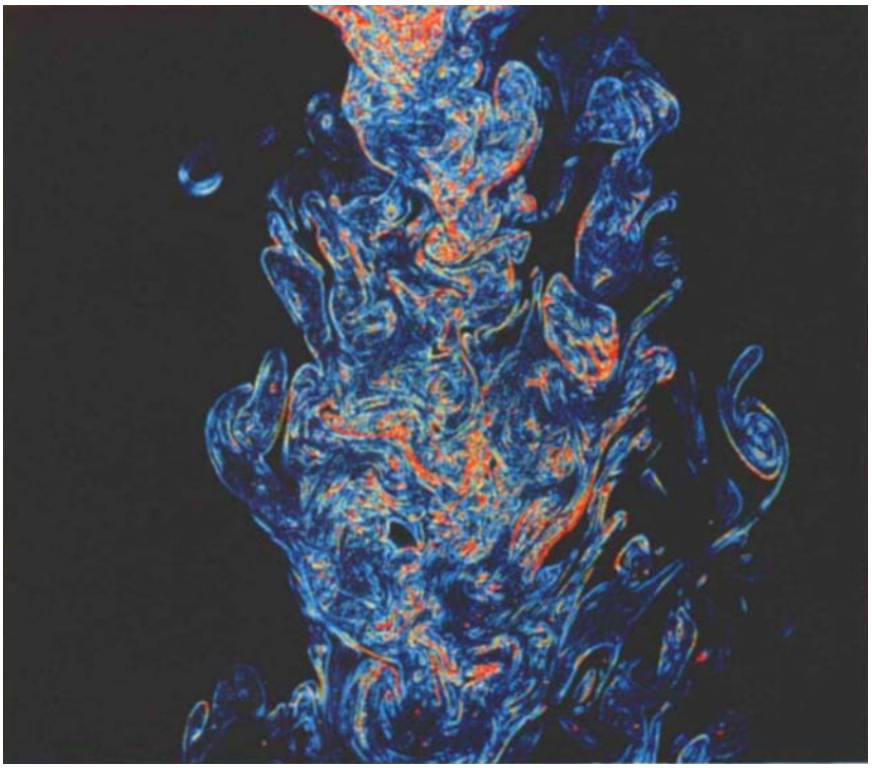

Figure 5.1: Concentration 'dissipation' rate, calculated from LIF map of a turbulent jet. Colours represent varying magnitudes of the dissipation rate; deep blue is small and red is large. Reproduced from figure 14a of Reference 212.

also shows 'universal' scale–similarity, ostensibly inherited from the scale invariance properties of the Navier–Stokes equations.[210–213] A natural question that arises then is whether the spatial structure of the conformation tensor fluctuations, as quantified by the scalar measures, also shows such behaviour. Tools used to analyze the spatial structure of the dissipation rate, most notably the multifractal approach,[212,214–219] may then be extended to viscoelastic turbulence to shed light on the turbulent polymer deformation. A related line of inquiry, but in Fourier space rather than physical space, can be pursued via the spectra of the scalar measures.

5.2.1.2 The mean conformation tensor

The results in chapter 3 also raise questions regarding the mean conformation tensor. The geodesic distance of the mean conformation tensor from the closest isotropic tensor, which is a measure of anisotropy, shows a dramatic logarithmic decrease from very close to the wall, to near the centreline. As a result, the anisotropy through much of the channel may be written in a simple closed functional form. This is an interesting result because it raises several questions. Namely, how does this behaviour depend on the parameters? Is it related to the attached-eddy hypodissertation that purports to explain the mean profile in turbulent channel flow, and leads to logarithmic behaviour in the mean velocity profile? Answering these questions may hold the key to developing theoretical models for the mean conformation tensor, and hence drag reduction, in turbulent viscoelastic channel flow.

The probability density, mean value and isocontours of the instantaneous logarithmic volume ratio in chapter 3 show that the mean conformation tensor is most certainly not the most representative conformation tensor in the flow. The volume of the mean conformation tensor is much greater than the volume of a typical conformation tensor in the flow and its shape, as measured by the anisotropy index of the fluctuating conformation tensor, is also different. At the same time, the mean conformation tensor is directly relevant to the mean momentum balance, which determines the drag. This perplexing finding, that a quantity that appears to be not physically representative is critical in determining a physically meaningful quantity, can be re-

solved by interpreting the mean conformation tensor not as the statistically persistent mean state of the polymer deformation but rather as a derived quantity that depends, in some yet undetermined way, on more physically representative conformation tensors. The problem is then of finding a physically representative replacement of the mean conformation tensor, evaluating the fluctuations around this new tensor, and then finally relating the mean conformation tensor to the new tensor and fluctuations about it. Such an approach has not been adopted in the literature before but is similar in spirit to studying the Reynolds stress not by directly modelling it, but by modelling the underlying velocity field and then constructing the associated Reynolds stress. The first step, the problem of finding the most representative conformation tensor, has also not been directly studied in the literature before. However, several viable alternatives may be pursued, e.g. geometric means, or using the squared mean of the square–root of the conformation tensor. The question of the most appropriate of these, and others, is open.

5.2.2 Generalizing weakly nonlinear deformations

The tools developed in chapter 4 allow for physically consistent weakly nonlinear expansions, or deformations, of the conformation tensor about a given base-state. Such expansions are relevant in a variety of circumstances, such as for deriving solutions for flows that can be cast as perturbations of a known flow. In the latter case, our results will likely need to be generalized to deformations where the powers of the

perturbation parameter are ordered rational numbers and not simply integers. When using standard expansions, such a need typically arises due to singularities in the underlying differential equation whose solution is sought. This interplay, between the form of expansion and an underlying differential equation, was not considered in the present work but is an aspect that needs to be fully explored for further progress. The question here then is related to the perturbative deformations that are asymptotically admissible under a constraint in the form of a differential equation.

5.2.3 Non-modal stability analysis

In chapter 4, we showed that the mathematically sensible inner product to use for analysis of the linearized dynamics in viscoelastic flows is the one induced locally by the global metric on the manifold of positive–definite tensors. This scalar product is different from the Frobenius inner product, although the latter can be used if the perturbation tensor is suitably transformed. We showed, through an analysis of the perturbation tensor, that the transformed tensor can be significantly different than one obtained via a naive additive perturbation of the conformation tensor.

The above findings have a significant impact on non-modal stability analyses of viscoelastic flows. Such analyses are performed using a variety of tools, e.g. one approach evaluates the impulse response of the linearized system,[197,199,200] while another obtains initial conditions that yield the optimal energy growth associated with the linearized dynamics at a prescribed future time.[206] These type of studies all rely

on inner products and associated induced norms and thus the lack of an inner product appropriate to the conformation tensor has hindered progress. For example, since the elastic energy is not a norm, Zhang *et al.*[206] only considered optimal kinetic energy growth and only allowed initial conditions that did not perturb the conformation tensor. In other studies, the difficulty has been unwittingly concealed by examining individual components of the polymer stress in conjunction with the standard Euclidean inner product.[196,197] By providing mathematically sensible inner products on the tangent spaces on the set of positive–definite tensors, the theoretical framework introduced in chapter 4 removes the difficulties cited above, thereby paving the way for more complete non-modal stability analyses.

In recent years, variational approaches have been used to develop nonlinear non-modal stability analysis approaches.[220] These approaches can be extended to viscoelastic flows by evaluating fluctuations in the conformation tensor via the global metric on the manifold of positive–definite tensors, i.e. the geodesic distance of the fluctuating conformation tensor from the identity.

A question that arises when using geometrically consistent measures is how to relate them to the elastic energy and relaxational dissipation. This is an important avenue for future investigation and is discussed in the next section.

5.2.4 Elastic energy and relaxational dissipation

Elastic energy and the scalar relaxational dissipation were not considered in a great amount of detail in the present work. The reasons were clarified in detail in the preceding chapters but may be classified in two categories: (a) the lack of clarity with respect to the definition of these quantities and their particular relevance to the continuum-scale dynamics, and (b) these scalar measures are usually not well-defined distance functions, either on the manifold of positive–definite tensors or even on the larger space of symmetric tensors. Nevertheless, both quantities have been used previously in the literature and occupy a central position in some approaches to deriving the governing equations, e.g. the Rajagopal–Srivinasa formalism.[116]

Although some bounds were derived in §3.2.2 to illuminate the approach developed in the present work, more precise relationships between fluctuating conformation tensor and the elastic energy and also the relaxational dissipation are needed. An arguably more vital need is for relationships between the latter quantities and the scalar measures developed in the present dissertation. The present dissertation argues, based on physical and mathematical considerations of the kinematics which are encapsulated in the conformation tensor, that the scalar measures developed are the most appropriate or 'rational'. However, if we assume the base-state to be the thermodynamic equilibrium, these scalar measures are distinct from the purportedly physically relevant scalar measures: the elastic energy and scalar relaxational dissipation. Why is this the case?

The answer to the question above is not trivial and has implications in different fields. For example, in the simple case of the Oldroyd-B model, the elastic energy is related to the trace of the conformation tensor. In the kinetic theory approach, the latter elastic energy is obtained from the Hookean spring assumption which is itself justified on the basis of the entropic elasticity of an ideal Gaussian polymer chain. The assumption of ideal Gaussian polymer chains is known to not be satisfactory[221–228] and the development of other models of nonlinear viscoelasticity has been spurred on by its known deficiencies.[102] The reason then for the discrepancy we find between mathematically consistent scalar measures at the continuum-scale with those obtained by coarse-graining the microscopic dynamics can conceivably be due to the necessarily simplified models used at the microscopic scale. On the other hand, in the continuum-scale approach of Rajagopal–Srinivasa, one explicitly assumes a form for the elastic energy. To derive the Oldroyd-B equation, the assumption is that the elastic energy is again related to the trace of the conformation tensor. The discrepancy is thus simpler to address in continuum-scale modelling: one has to only use a mathematically sensible definition of the elastic energy, i.e. one based on the geometry of the set of positive–definite tensors. The latter approach has implications beyond viscoelastic flows, for the larger field of solid mechanics. In a recent work, Neff *et al.*[229] used geodesic distances to define a strain measure analogous to the Hencky strain. Such strain measures can then be used to propose expressions for the elastic energy.

Appendix A

Riemannian structure of the set of positive-definite matrices

The theoretical results presented in this section on the geometric structure of $\mathbf{Pos}_n$ are standard with detailed accounts available in pp. 322–339 of Reference 181 and also pp. 201–235 of Reference 182.

A.1 Riemannian metric

We can define an inner product $(\cdot, \cdot) : \mathbb{R}^{n\times n} \times \mathbb{R}^{n\times n} \to \mathbb{R}$

$$(\boldsymbol{A}, \boldsymbol{B})_{\boldsymbol{X}} = \text{tr } \left(\boldsymbol{X}^{-1} \cdot \boldsymbol{A}^{\mathsf{T}} \cdot \boldsymbol{X}^{-1} \cdot \boldsymbol{B}\right) \tag{A.1}$$

for $\boldsymbol{A}, \boldsymbol{B} \in \mathbb{R}^{n\times n}$ where $\boldsymbol{X} \in \mathbf{Pos}_n$ is fixed. When $\boldsymbol{X} = \boldsymbol{I}$, (A.1) reduces to the definition of the standard Frobenius inner product. The guaranteed factorization $\boldsymbol{X} = \boldsymbol{X}^{\frac{1}{2}} \cdot \boldsymbol{X}^{\frac{1}{2}}$ and the cyclical property of the trace ensures the positivity of $\|\boldsymbol{A}\|_{\boldsymbol{X}}$, while the remaining properties of the inner product and the norm follow-on from the standard Frobenius theory. The space $\mathbb{R}^{n\times n}$ is a Hilbert space when equipped with such an inner product and the norm induced by it: $\|\boldsymbol{A}\|_{\boldsymbol{X}} = \sqrt{(\boldsymbol{A}, \boldsymbol{A})_{\boldsymbol{X}}}$. The subset of $\mathbb{R}^{n\times n}$ consisting of symmetric matrices forms a vector space, $\mathbf{Sym}_n$, and can also be Hilbertized under the inner product (A.1). $\mathbf{Pos}_n$ is an open subset of $\mathbb{R}^{n\times n}$ (and also $\mathbf{Sym}_n$) in the $\|\cdot\|_{\boldsymbol{X}}$ metric and is thus a (smooth) manifold.

The tangent bundle of $\mathbf{Pos}_n$, which consists of the manifold $\mathbf{Pos}_n$ equipped with a tangent space $T_{\boldsymbol{X}}\mathbf{Pos}_n$ at each point $\boldsymbol{X}$ of $\mathbf{Pos}_n$, provides a natural projection that can be used to study the geometry of $\mathbf{Pos}_n$. A simple argument[1] shows that the tangent space at each point of $\mathbf{Pos}_n$ coincides with $\mathbf{Sym}_n$. The latter result is the geometric underpinning of numerical algorithms that time march the conformation tensor by translations of $\boldsymbol{C}$ by symmetric matrices (the right-hand side of the evolution equation for $\boldsymbol{C}$).

A manifold $\mathbf{M}$ equipped with a scalar product over $T_{\boldsymbol{X}}\mathbf{M}$ for each $\boldsymbol{X} \in \mathbf{M}$ is a Riemannian manifold. The set of such scalar products is called the Riemannian metric of the manifold. $\mathbf{Pos}_n$ is a Riemannian manifold with Riemannian metric

[1]Let $\boldsymbol{Y}$ be defined by $\boldsymbol{Y} = \boldsymbol{X} + \varepsilon\boldsymbol{S}$, for some $\boldsymbol{X} \in \mathbf{Pos}_n$, $\varepsilon \in \mathbb{R}$, $\boldsymbol{S} \in \mathbf{Sym}_n$. By Weyl's inequality, there exists some $\varepsilon > 0$ sufficiently small such that $\boldsymbol{Y} \in \mathbf{Pos}_n$. This implies that $\mathbf{Sym}_n \subseteq T_{\boldsymbol{X}}\mathbf{Pos}_n$. Since $\boldsymbol{Y} \notin \mathbf{Pos}_n$ for any $\varepsilon \neq 0$ and $\boldsymbol{S} \notin \mathbf{Sym}_n$, we have $\mathbf{Sym}_n = T_{\boldsymbol{X}}\mathbf{Pos}_n$.

given by[181,182]

$$g = \{(\cdot,\cdot)_{\boldsymbol{X}} | \boldsymbol{X} \in \mathbf{Pos}_n\} \tag{A.2}$$

with the understanding that the scalar product on $T_{\boldsymbol{X}}\mathbf{Pos}_n$ is $(\cdot,\cdot)_{\boldsymbol{X}} \in g$ and the domain of $(\cdot,\cdot)_{\boldsymbol{X}}$ is restricted to $\mathbf{Sym}_n = T_{\boldsymbol{X}}\mathbf{Pos}_n$. An infinitesimal distance around the point $\boldsymbol{X}$ on the manifold is given by

$$ds^2 = \|\mathrm{d}\boldsymbol{X}\|^2_{\boldsymbol{X}} = \mathrm{tr}\ \left[(\boldsymbol{X}^{-1} \cdot \mathrm{d}\boldsymbol{X})^2\right] \tag{A.3}$$

The metric given by (A.2) ensures that distances between points $\boldsymbol{X}, \boldsymbol{Y} \in \mathbf{Pos}_n$ along the manifold calculated using (A.3) are invariant under the action $[\cdot]_{\boldsymbol{A}}$ of any $\boldsymbol{A} \in \mathbf{GL}_n$.

A.2 Geodesic curves and distances

Consider a parameterized curve on $\mathbf{Pos}_n$ connecting points $\boldsymbol{X}, \boldsymbol{Y} \in \mathbf{Pos}_n$, i.e. $\boldsymbol{P} : [0,1] \to \mathbf{Pos}_n$ with $\boldsymbol{P}(0) = \boldsymbol{X}$ and $\boldsymbol{P}(1) = \boldsymbol{Y}$. The distance, in the sense of the metric g, traversed on the manifold along the curve $\boldsymbol{P} = \boldsymbol{P}(r)$ is given by

$$\ell_{\boldsymbol{P}}(r) \equiv \int_0^r \left\| \frac{\mathrm{d}\boldsymbol{P}(r')}{\mathrm{d}t} \right\|_{\boldsymbol{P}(r')} \mathrm{d}r'. \tag{A.4}$$

$\ell_{\boldsymbol{P}}$ has an attractive property in that it is invariant under affine transformations.

APPENDIX A. RIEMANNIAN STRUCTURE OF THE SET OF POSITIVE-DEFINITE MATRICES

Lemma 1 (Affine invariance)**.** *For each positive-definite* $\boldsymbol{A}$ *and differentiable path* $\boldsymbol{P}$ *on the Riemannian manifold of positive-definite matrices, we have*

$$\ell_{\boldsymbol{P}} = \ell_{[\boldsymbol{P}]_{\boldsymbol{A}}}. \tag{A.5}$$

Proof. §6.1.1 in Reference 182. □

We call a curve $\boldsymbol{P}(r)$ on $\mathbf{Pos}_n$ that minimizes $\ell_{\boldsymbol{P}}(1)$ a *geodesic curve* connecting $\boldsymbol{X}$ and $\boldsymbol{Y}$. In general, the existence and/or uniqueness of a geodesic curve is not guaranteed. We also define $d(\boldsymbol{X}, \boldsymbol{Y})$, the *geodesic distance* between $\boldsymbol{X}$ and $\boldsymbol{Y}$ as the infimum of $\ell_{\boldsymbol{P}}(1)$ over all possible curves $\boldsymbol{P}$ connecting $\boldsymbol{X}$ and $\boldsymbol{Y}$

$$d(\boldsymbol{X}, \boldsymbol{Y}) \equiv \inf_{\boldsymbol{P}} \left\{ \ell_{\boldsymbol{P}}(1) | \boldsymbol{P}(r) \in \mathbf{Pos}_n, \boldsymbol{P}(0) = \boldsymbol{X}, \boldsymbol{P}(1) = \boldsymbol{Y} \right\}. \tag{A.6}$$

A corollary of affine invariance is that $d(\boldsymbol{X}, \boldsymbol{Y}) = d([\boldsymbol{X}]_{\boldsymbol{A}}, [\boldsymbol{Y}]_{\boldsymbol{A}})$.

It turns out that the existence and uniqueness of geodesics is guaranteed on $\mathbf{Pos}_n$. Furthermore, we can obtain analytical expressions for these geodesics. Following Reference 182, we present three key theorems that allow this construction.

Theorem 1 (Exponential metric increasing property)**.** *For any two real symmetric* $\boldsymbol{\mathcal{X}}$ *and* $\boldsymbol{\mathcal{Y}}$

$$d(e^{\boldsymbol{\mathcal{X}}}, e^{\boldsymbol{\mathcal{Y}}}) \leq \|\boldsymbol{\mathcal{X}} - \boldsymbol{\mathcal{Y}}\|_{\boldsymbol{I}} \tag{A.7}$$

where we note that $e^{\boldsymbol{\mathcal{X}}}$, $e^{\boldsymbol{\mathcal{Y}}}$ *are positive-definite matrices.*

Proof. §XII.2 in Reference 181 and §6.1.4 in Reference 182. □

Equality is achieved in (A.7) when $\boldsymbol{X}$ and $\boldsymbol{Y}$ commute and we can also parameterize the geodesic in this case, as expressed in the proposition below.

Proposition 1. *Let* $\boldsymbol{X} = e^{\boldsymbol{\mathcal{X}}}$ *and* $\boldsymbol{Y} = e^{\boldsymbol{\mathcal{Y}}}$ *be positive-definite matrices such that* $\boldsymbol{X} \cdot \boldsymbol{Y} = \boldsymbol{Y} \cdot \boldsymbol{X}$. *Then, the exponential function maps the line segment*

$$(1 - r)\boldsymbol{\mathcal{X}} + r\boldsymbol{\mathcal{Y}}, \qquad 0 \leq r \leq 1 \tag{A.8}$$

in the Euclidean space of symmetric matrices to the geodesic between $\boldsymbol{X}$ *and* $\boldsymbol{Y}$ *on the Riemannian manifold of positive-definite matrices and*

$$d(\boldsymbol{X}, \boldsymbol{Y}) = \|\boldsymbol{\mathcal{X}} - \boldsymbol{\mathcal{Y}}\|_{\boldsymbol{I}} \tag{A.9}$$

Proof. Chapter 6 in Reference 182. □

Finally, using the affine invariance property of the Riemannian metric and noting that $\boldsymbol{I}$ commutes with every element of $\mathbf{Pos}_n$, one can prove the following theorem.

Theorem 2. *Let* $\boldsymbol{X}$ *and* $\boldsymbol{Y}$ *be positive-definite matrices. There exists a unique geodesic* $\boldsymbol{X} \#_r \boldsymbol{Y}$ *on the Riemannian manifold of positive-definite matrices that joins* $\boldsymbol{X}$ *and* $\boldsymbol{Y}$

with the following parametrisation

$$\boldsymbol{X} \#_r \boldsymbol{Y} = \boldsymbol{X}^{\frac{1}{2}} \cdot \left(\boldsymbol{X}^{-\frac{1}{2}} \cdot \boldsymbol{Y} \cdot \boldsymbol{X}^{-\frac{1}{2}} \right)^r \cdot \boldsymbol{X}^{\frac{1}{2}} \tag{A.10}$$

which is natural in the sense that

$$d(\boldsymbol{X}, \boldsymbol{X} \#_r \boldsymbol{Y}) = r d(\boldsymbol{X}, \boldsymbol{Y}) \tag{A.11}$$

for each $r \in \mathbb{R}$. *Furthermore, we have*

$$d(\boldsymbol{X}, \boldsymbol{Y}) = \left\| \log \left(\boldsymbol{X}^{-\frac{1}{2}} \cdot \boldsymbol{Y} \cdot \boldsymbol{X}^{-\frac{1}{2}} \right) \right\|_{\boldsymbol{I}} = \left[\sum_{i=1}^{3} \left(\log \, \sigma_i \left(\boldsymbol{X}^{-1} \cdot \boldsymbol{Y} \right) \right)^2 \right]^{\frac{1}{2}} \tag{A.12}$$

Proof. Chapter 6 in Reference 182. □

Appendix B

Numerical approach

In this section, we provide details of the numerical approach used for direct numerical simulations of the FENE-P fluid. The code implementing the numerical approach is based on the FlowDNS code developed by the Zaki group at Johns Hopkins University (see e.g. Reference 91). A new Runge-Kutta time-marching scheme and associated code were developed for the conformation tensor. To ensure positive-definiteness, a new spatial discretization scheme for the advection term in the conformation tensor equation was also developed.

The spatial discretization is based on the control-volume formulation of Rosenfeld *et al.*,[230] and a fractional step approach (operator splitting) is used for time-marching. Integrating the governing equations over a spatial volume Ω, depicted in figure B.1

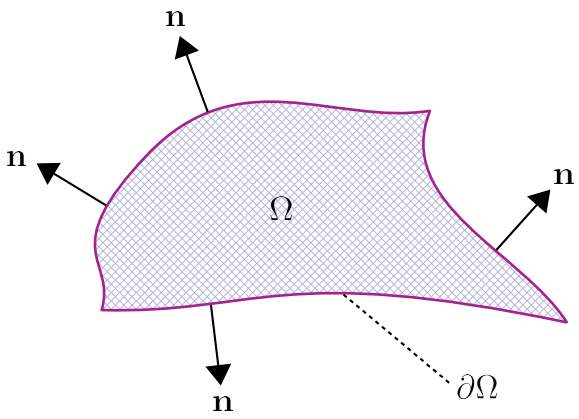

Figure B.1: An arbitrary volume in two-dimensional space. The volume is indicated by Ω, its boundary by $\partial\Omega$, and the outward normals to its surface are denoted $\mathbf{n}$.

for the two-dimensional case, yields the following exact equations

$$0 = \oint_{\partial\Omega} \boldsymbol{u} \cdot \mathbf{n} \, \mathrm{d}\mu(\partial\Omega) \tag{B.1}$$

$$\partial_t [\boldsymbol{u}]_\Omega = \frac{1}{\mu(\Omega)} \oint_{\partial\Omega} \left(-\boldsymbol{u}\boldsymbol{u} - p\boldsymbol{I} + \frac{\beta}{Re}(\boldsymbol{\nabla u} + \boldsymbol{\nabla}^{\mathsf{T}}\boldsymbol{u}) + \frac{1-\beta}{Re}\boldsymbol{T} \right) \cdot \mathbf{n} \, \mathrm{d}\mu(\partial\Omega) \tag{B.2}$$

$$\partial_t [\boldsymbol{C}]_\Omega = \frac{1}{\mu(\Omega)} \oint_{\partial\Omega} -\boldsymbol{C}(\boldsymbol{u} \cdot \mathbf{n}) \, \mathrm{d}\mu(\partial\Omega) + \mathrm{sym}\, ([\boldsymbol{C} \cdot \boldsymbol{\nabla u}]_\Omega) - [\boldsymbol{T}]_\Omega \tag{B.3}$$

where $\partial\Omega$ denotes the boundary of Ω, $\mu(\cdot)$ is the measure, $\mathbf{n}$ is the outward normal to the volume and

$$[\phi]_\Omega \equiv \frac{1}{\mu(\Omega)} \int_\Omega \phi \, \mathrm{d}\mu(\Omega). \tag{B.4}$$

for a function ϕ. Note that $\lim_{\mu(\Omega)\to 0} [\phi]_\Omega = \phi(\boldsymbol{x})$ for a volume Ω centred at $\boldsymbol{x}$.

To discretize the governing equations in integral form, we assume $\mu(\Omega) \ll 1$ so that

$[\phi]_\Omega \approx \phi(\boldsymbol{x})$ and generate a three-dimensional computational grid. The grid forms closed cells with well-defined cell-centres. The pressure and conformation tensor are solved on the cell centres while the velocities are solved on staggered grids: the velocity in the i-th direction is solved on a grid that is staggered in the i-th direction with respect to the cell centre grid. Each staggered grid has its own associated cells (closed volumes with surfaces). The staggering of grids prevents the well-known checker board problem associated with the pressure field. We use ghost cells to enforce boundary conditions where necessary.

In the present work, the numerical algorithm is developed for a computational grid that is curvilinear in the (x, y) but is uniform in the z direction, as illustrated in figure B.2. As a result, discretizing the integrals in (B.1)–(B.3) requires evaluating the metric tensor associated with the curvilinear grid. This process is algebraically involved but is standard, e.g. Rosenfeld *et al.*[230] provide the necessary details. The discretized integrals require the velocities and conformation tensor on the cell faces. If these quantities are not solved for directly, they are linearly interpolated using neighbouring grid values that are available. To make the notation in the following concise, we denote the surface integral discretization operator which involves the grid metric tensor and linear interpolation onto cell surfaces by $\Psi\{\cdot\}$. We assume that the operator $\Psi\{\cdot\}$ discretizes the surface integrals with respect cells defined using the grid that is appropriate for the equation being solved, e.g. the x momentum equation is discretized with respect to cells that are staggered in the x direction. Further details

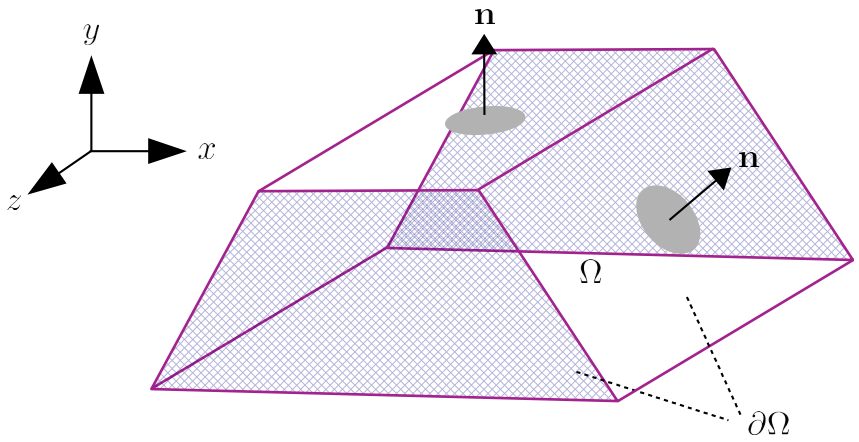

Figure B.2: A representative computational cell: curvilinear in (x, y) and uniform in z.

on the discretization may be found in Reference 231.

The equations (B.1)–(B.3) also require an appropriately discretized velocity gradient tensor. The velocity gradient tensor can be defined as follows

$$\boldsymbol{\nabla u} \equiv \lim_{\mu(\Omega)\to 0} \frac{1}{\mu(\Omega)} \oint_{\partial\Omega} \mathbf{n}\, \boldsymbol{u}\, \mathrm{d}\mu(\partial\Omega). \tag{B.5}$$

This can be discretized as follows

$$\boldsymbol{\nabla u} \approx \boldsymbol{\mathcal{D}u} \equiv \Psi \left\{ \frac{1}{\mu(\Omega)} \oint_{\partial\Omega} \mathbf{n}\, \boldsymbol{u}\, \mathrm{d}\mu(\partial\Omega) \right\} \tag{B.6}$$

With these definitions, the spatially discretized operators appearing in the mo-

mentum equation are

$$\mathbf{H}(\boldsymbol{u}) = \Psi\left\{-\frac{1}{\mu(\Omega)}\oint_{\partial\Omega}\boldsymbol{u}\boldsymbol{u}\cdot\mathbf{n}\,\mathrm{d}\mu(\partial\Omega)\right\} \tag{B.7}$$

$$\mathbf{R}(p\boldsymbol{I}) = \Psi\left\{-\frac{1}{\mu(\Omega)}\oint_{\partial\Omega}p(\boldsymbol{I}\cdot\mathbf{n})\,\mathrm{d}\mu(\partial\Omega)\right\} \tag{B.8}$$

$$\mathbf{D}_{\mathrm{exp}}(\boldsymbol{u}) + \mathbf{D}_{\mathrm{mix}}(\boldsymbol{u}) = \Psi\left\{\frac{1}{\mu(\Omega)}\oint_{\partial\Omega}\frac{\beta}{Re}\left(\mathfrak{D}\boldsymbol{u} + (\mathfrak{D}\boldsymbol{u})^{\mathsf{T}}\right)\cdot\mathbf{n}\,\mathrm{d}\mu(\partial\Omega)\right\} \tag{B.9}$$

$$\mathbf{P}(\boldsymbol{T}) = \Psi\left\{\frac{1}{\mu(\Omega)}\oint_{\partial\Omega}\frac{1-\beta}{Re}\boldsymbol{T}\cdot\mathbf{n}\,\mathrm{d}\mu(\partial\Omega)\right\} \tag{B.10}$$

The diffusion term is split into two parts. As discussed later, $\mathbf{D}_{\mathrm{exp}}$ represents the part that is treated purely explicitly in time and $\mathbf{D}_{\mathrm{mix}}$ represents the part that is not purely explicit. The choice of what terms to include in either part is relatively large. In the present algorithm, all the terms associated with cross-derivatives are in $\mathbf{D}_{\mathrm{exp}}$. Diffusion in the z direction is also fully put in $\mathbf{D}_{\mathrm{exp}}$. The remaining terms are in $\mathbf{D}_{\mathrm{mix}}$. Further details on the discretization of the terms in the momentum equation may be found in Reference 231.

The discretized operators appearing in the conformation tensor equation are

$$\mathbf{S}(\boldsymbol{u}, \boldsymbol{C}) = \mathrm{sym}\ ([\boldsymbol{C}]_{\Omega}\cdot\mathfrak{D}\boldsymbol{u}) \tag{B.11}$$

$$\mathbf{Q}(\boldsymbol{C}) = -\boldsymbol{T}([\boldsymbol{C}]_{\Omega}] \tag{B.12}$$

where we have not yet discussed the term associated with advection of $\boldsymbol{C}$. This term must be treated with care; using the same treatment as with the momentum

equation leads to numerical instabilities with the conformation tensor losing positive-definiteness. In the present work, we adapt the 'slope-limiting' approach proposed in Reference 232 (see also Reference 190 for an implementation). This approach guarantees positive-definiteness of the conformation tensor and avoids the need for artificial diffusion. We describe this discretization below but first note that we will denote it by the symbol Φ, so that

$$\mathbf{A}(\boldsymbol{u}, \boldsymbol{C}) = \Phi \left\{ -\frac{1}{\mu(\Omega)} \oint_{\partial\Omega} \boldsymbol{C}(\boldsymbol{u} \cdot \mathbf{n}) \, \mathrm{d}\mu(\partial\Omega) \right\} \tag{B.13}$$

The discretization operator Φ discretizes the surface integral, which is the net flux of $\boldsymbol{C}$ into the cell,

$$\oint_{\partial\Omega} \boldsymbol{C}(\boldsymbol{u} \cdot \mathbf{n}) \, \mathrm{d}\mu(\partial\Omega) = \sum_{\text{cell faces}} \text{flux of } \boldsymbol{C}. \tag{B.14}$$

In order to understand the slope-limiting approach, it is best to consider the uniform grid case and only one direction, as depicted in figure B.3. The surface integral above evaluates the total flux into the cell. In the x direction, we thus require the x velocity (u) and the conformation tensor components at the faces at $x = x_{i\pm\frac{1}{2}}$. The velocity can be obtained by linear interpolation and is single-valued because the velocity field is assumed to be smooth everywhere. However linear interpolation, or indeed any arbitrary interpolation scheme, of the conformation tensor does not guarantee that it remains positive-definite in the resulting time evolution. The conformation tensor

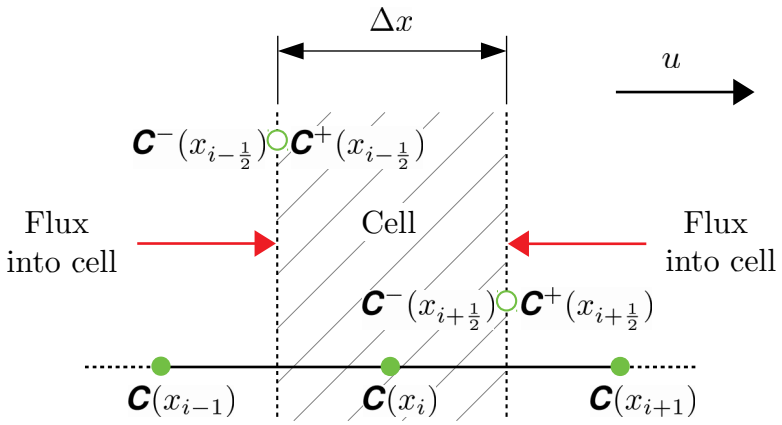

Figure B.3: Schematic of the flux of $\boldsymbol{C}$ into a computational cell.

can develop sharp gradients and thus upwinding is necessary to avoid unphysical interpolations. Assuming there is a shock at the cell face, then the value of the conformation tensor component that is fluxed into the cell depends on the direction of the velocity. In figure B.3, if $u > 0$, then the relevant conformation tensor that is transported across the left-side of the cell is denoted $\boldsymbol{C}^-(x_{i-\frac{1}{2}})$. Similarly, when $u < 0$, the relevant conformation tensor that is transported across the left-side of the cell is denoted $\boldsymbol{C}^+(x_{i-\frac{1}{2}})$. Presumably, $\boldsymbol{C}^+(x_{i-\frac{1}{2}})$ should only depend on values of the conformation tensor for $x \geq x_{i-\frac{1}{2}}$ and vice-versa for $\boldsymbol{C}^-(x_{i-\frac{1}{2}})$.

What remains is to define the interpolation approach needed to determine the conformation tensors at the cell faces. To simplify what follows, we consider interpolations that depend on the conformation tensor at x_i, i.e. $\boldsymbol{C}^{\pm}(x_{i\mp\frac{1}{2}})$. These conformation tensors are each only one of a pair at the relevant cell face, but the second of each pair may found using a similar approach applied to the appropriate

adjacent cell. The interpolated value for $\boldsymbol{C}^{\pm}(x_{i\mp\frac{1}{2}})$ may be written in general as

$$\boldsymbol{C}^{\pm}(x_{i\mp\frac{1}{2}}) = \boldsymbol{C}(x_i) \mp \frac{\Delta x}{2} \left.\frac{\partial \boldsymbol{C}}{\partial x}\right|_{x_i} \tag{B.15}$$

where Δx is the width of the cell, and the problem then reduces to one of determining the approximation to the slope, $\partial \boldsymbol{C}/\partial x$, at $x = x_i$ that ensures positive-definiteness of the conformation tensor during the subsequent time evolution. Clearly, the interpolation must guarantee that the resulting conformation tensor at the cell face is positive-definite. Using the incompressibility condition and the fact that convex sums of the positive-definite tensors are also positive-definite, Vaithianathan *et al.*[232] showed that, provided that positivity of the conformation tensor at the cell face is perserved, any of the following approximations of the slope ensure that the conformation tensor always remains positive

$$\left.\frac{\partial \boldsymbol{C}}{\partial x}\right|_{x_i} \approx \begin{cases} \frac{\boldsymbol{C}(x_{i+1}) - \boldsymbol{C}(x_{i-1})}{2\Delta x} & \text{central} \\ \frac{\boldsymbol{C}(x_i) - \boldsymbol{C}(x_{i-1})}{\Delta x} & \text{backward} \\ \frac{\boldsymbol{C}(x_{i+1}) - \boldsymbol{C}(x_i)}{\Delta x} & \text{forward} \\ 0 & \text{zero-th order.} \end{cases} \tag{B.16}$$

Here we note that the last choice, $\partial \boldsymbol{C}/\partial x = 0$, degrades the accuracy of the scheme from second-order to locally first-order and must only be chosen if no other approxi-

mation yields a positive-definite conformation tensor at the cell face.

In order to push the conformation tensor as far away from the outer boundary of admissible tensors, Vaithianathan *et al.*[232] prescribed that if more than one scheme from the above yields a positive-definite tensor at the cell face, then the interpolation must be chosen to maximize the eigenvalues of the resulting interpolated conformation tensor. In the present work, we found that above prescription by Vaithianathan *et al.*[232] was computationally expensive. In addition, there is no a priori reason why the choice of approximation that yields the largest eigenvalues is necessarily the physically relevant one. Thus, instead of this prescription, we ranked the schemes and selected the first one that satisfied positivity. The central scheme is ranked first since it is unbiased, the second scheme is upwind (which may be backward or forward depending on the local velocity field) because it is consistent with advection of the conformation tensor, the third scheme is downwind and finally if none of these work, we choose the zero-th order approximation. In practice, we find that case the central scheme is sufficient for the vast majority of the points in the domain ($> 90\%$) in turbulent channel flow. The local degradation of accuracy occurs at a small number of points: $\sim 0.1 - 0.3\%$ in the x and y directions and $\sim 3 - 5\%$ in the z-direction. The latter percentage is higher than the others because of the relatively coarser grid in the z direction.

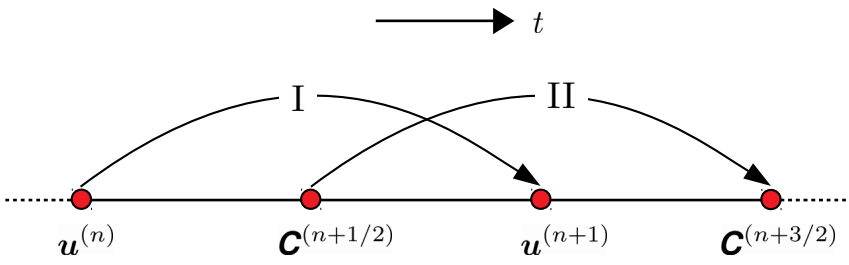

Figure B.4: Schematic of the time–advancement approach. Roman numerals indicate the order of advancement.

The spatially discretized equations read as follows

$$\partial_t \boldsymbol{u} \approx \mathbf{H}(\boldsymbol{u}) + \mathbf{R}(p) + \mathbf{D}_{\text{exp}}(\boldsymbol{u}) + \mathbf{D}_{\text{mix}}(\boldsymbol{u}) + \mathbf{P}(\boldsymbol{T}) \tag{B.17}$$

$$\partial_t \boldsymbol{C} \approx \mathbf{A}(\boldsymbol{u}, \boldsymbol{C}) + \mathbf{S}(\boldsymbol{u}, \boldsymbol{C}) + \mathbf{Q}(\boldsymbol{C}) \tag{B.18}$$

where, for clarity, we suppressed the dependence on the grid locations.

In the temporal discretization, the velocity field and conformation tensor are staggered in time, as shown in figure B.4. In this sense, the time-stepping is similar to the leapfrogging scheme used in classical mechanics. The velocity is advanced in time using the fractional step approach with a mixed explicit-implicit discretization in space. The conformation tensor is advanced in time using second-order explicit Runge–Kutta. Linear interpolation in time is used to transfer between the two temporal grids. For example, the polymer stress is a function of the conformation tensor but is required on the velocity temporal grid (since it appears in the momentum

equation). The value of polymer stress at the n-th time step is thus given by

$$\boldsymbol{T}^{(n)} = \boldsymbol{T}\left(\frac{\boldsymbol{C}^{(n-1/2)} + \boldsymbol{C}^{(n+1/2)}}{2}\right). \tag{B.19}$$

Similarly, we interpolate the velocity on to the conformation tensor temporal grid as follows

$$\boldsymbol{u}^{(n+1/2)} = \frac{\boldsymbol{u}^{(n)} + \boldsymbol{u}^{(n+1)}}{2} \tag{B.20}$$

As the time-discretization described in more detail will bear out, the order of the time advancement of the two variables, indicated in figure B.4 using roman numerals, ensures that fields necessary for interpolation are available when needed.

The polymer stress, convection, and explicit diffusion are discretized in time using second-order Adams–Bashforth, and the implicit diffusion is discretized using Crank–Nicholson. The first step of the fractional step method then reads

$$\begin{aligned}
&\frac{[\boldsymbol{u}^*]_\Omega - [\boldsymbol{u}^{(n)}]_\Omega}{\Delta t} \\
&= \underbrace{\frac{3}{2}\left[\mathbf{H}(\boldsymbol{u}^{(n)}) + \mathbf{D}_{\exp}(\boldsymbol{u}^{(n)}) + \mathbf{P}(\boldsymbol{T}^{(n)})\right] - \frac{1}{2}\left[\mathbf{H}(\boldsymbol{u}^{(n-1)}) + \mathbf{D}_{\exp}(\boldsymbol{u}^{(n-1)}) + \mathbf{P}(\boldsymbol{T}^{(n-1)})\right]}_{\text{Adams–Bashforth}} \\
&\qquad + \underbrace{\frac{1}{2}\left[\mathbf{D}_{\text{mix}}(\boldsymbol{u}^*) + \mathbf{D}_{\text{mix}}(\boldsymbol{u}^{(n)})\right]}_{\text{Crank–Nicholson}}
\end{aligned} \tag{B.21}$$

where $[\boldsymbol{u}^*]_\Omega$ is the intermediate velocity. The second (projection) step of the fractional

step method is

$$\frac{[\boldsymbol{u}^{(n+1)}]_\Omega - [\boldsymbol{u}^*]_\Omega}{\Delta t} = \mathbf{R}(p^{(n+1)}). \tag{B.22}$$

Here the pressure is treated implicitly and is obtained by solving the discretized pressure Poisson equation

$$\mathbf{R}([\boldsymbol{u}^*]_\Omega) = \mathbf{R}_{\text{poisson}}(p^{(n+1)}) \tag{B.23}$$

where

$$\mathbf{R}_{\text{poisson}}(p) = \Psi \left\{ -\frac{1}{\mu(\Omega)} \oint_{\partial\Omega} (\boldsymbol{\nabla} p) \cdot \mathbf{n} \, \mathrm{d}\mu(\partial\Omega) \right\}. \tag{B.24}$$

In all the simulations considered in the present thesis, the flow is homogenous in x and z. Therefore, we use a uniform grid in these directions. The pressure Poisson equation is then most efficiently solved in Fourier space and not by directly discretizing the full surface integrals as indicated in (B.24). This is the approach we adopt, and use modified wavenumbers instead of the true wavenumbers to maintain consistent behaviour in all directions. This approach was also adopted by Lee and Zaki in their simulations as well.[91]

The conformation tensor is discretized using a second-order explicit Runge–Kutta.

The first-step of the Runge-Kutta is given by

$$\frac{[\boldsymbol{C}^{(n+1)}]_\Omega - [\boldsymbol{C}^{(n+1/2)}]_\Omega}{\Delta t/2} = \mathbf{A}(\boldsymbol{u}^{(n+1/2)}, \boldsymbol{C}^{(n+1/2)}) + \mathbf{S}(\boldsymbol{u}^{(n+1/2)}, \boldsymbol{C}^{(n+1/2)}) + \frac{\mathbf{Q}(\boldsymbol{C}^{(n+1)}) + \mathbf{Q}(\boldsymbol{C}^{(n+1/2)})}{2} \quad \text{(B.25)}$$

and the second-step is given by

$$\frac{[\boldsymbol{C}^{(n+3/2)}]_\Omega - [\boldsymbol{C}^{(n+1/2)}]_\Omega}{\Delta t} = \mathbf{A}(\boldsymbol{u}^{(n+1)}, \boldsymbol{C}^{(n+1)}) + \mathbf{S}(\boldsymbol{u}^{(n+1)}, \boldsymbol{C}^{(n+1)}) + \frac{\mathbf{Q}(\boldsymbol{C}^{(n+3/2)}) + \mathbf{Q}(\boldsymbol{C}^{(n+1)})}{2}. \quad \text{(B.26)}$$

This two-step algorithm is slightly modified from the standard second-order explicit Runge–Kutta method because the relaxational term $\mathbf{Q}$ is treated semi-implicitly using Crank–Nicholson in both steps. Such a treatment is necessary because the FENE-P equation has finite extensibility and therefore it is critical that the time-stepping process not overshoot the upper bound on the extensibility. The extensibility constraint is enforced via the relaxation term $\mathbf{Q}$ that diverges at the maximum extension and thus as found by Dubief *et al.*,[149] this term needs to be treated implicitly to ensure that the conformation tensor at the subsequent step does not violate the constraint. Since the relaxational term is defined locally in space, treating it implicitly does not involve any large matrix inversions because it only contributes to diagonal of larger matrix representing the discretized operators. However, because the relaxation term

is a nonlinear function of the conformation tensor, treating it implicitly would normally involve a nonlinear inversion. In the present algorithm, we adopt the approach of Dubief *et al.*,[149] who showed that the nonlinear part of the implicit term can be found using the solution of a scalar quadratic equation. The nonlinear inversion then becomes trivial, and one can treat the relaxation term implicitly without significant additional computational cost.

The evolution equation for the conformation tensor has no associated boundary conditions since it is hyperbolic. The conformation tensor at the walls, where no derivatives of the conformation tensor are needed, is then explicitly marched in time.

Bibliography

[1] M. Chilcott and J. Rallison, "Creeping flow of dilute polymer solutions past cylinders and spheres," *J. Non-Newtonian Fluid Mech.*, vol. 29, pp. 381–432, 1988.

[2] F. H. Garner and A. H. Nissan, "Rheological Properties of High-Viscosity Solutions of Long Molecules," *Nature*, vol. 158, no. 4018, pp. 634–635, 1946.

[3] K. Weissenberg, "A continuum theory of rhelogical phenomena," *Nature*, vol. 159, no. 4035, pp. 310–311, 1947.

[4] G. Astarita and L. Nicodemo, "Extensional flow behaviour of polymer solutions," *Chem. Eng. J.*, vol. 1, no. 1, pp. 57–65, 1970.

[5] B. Toms, "Some observations on the flow of linear polymer solutions through straight tubes at large Reynolds numbers," in *Proc. 1st Int. Congr. Rheol.* North-Holland Amsterdam, 1948, pp. 135–141.

[6] K. J. Mysels, "Flow of thickened fluids," U.S. Patent 2 492 173, December 27, 1949.

[7] J. Lumley, "Drag Reduction by Additives," *Annu. Rev. Fluid Mech.*, vol. 1, no. 1, pp. 367–384, 1969.

[8] C. M. White and M. G. Mungal, "Mechanics and prediction of turbulent drag reduction with polymer additives," *Annu. Rev. Fluid Mech.*, vol. 40, no. 1, pp. 235–256, 2008.

[9] E. Burger, W. Munk, and H. Wahl, "Flow Increase in the Trans Alaska Pipeline Through Use of a Polymeric Drag-Reducing Additive," *J. Pet. Technol.*, vol. 34, no. 02, pp. 377–386, 1982.

[10] J. Woo Yang, H. Park, H. Hwan Chun, S. L. Ceccio, M. Perlin, and I. Lee, "Development and performance at high Reynolds number of a skin-friction reducing marine paint using polymer additives," *Ocean Eng.*, vol. 84, pp. 183–193, 2014.

[11] N. Berman, "Drag Reduction by Polymers," *Annu. Rev. Fluid Mech.*, vol. 10, no. 1, pp. 47–64, 1978.

[12] R. G. Larson, "Fluid dynamics: Turbulence without inertia," *Nature*, vol. 405, no. 6782, pp. 27–28, 2000.

[13] A. Groisman and V. Steinberg, "Elastic turbulence in a polymer solution flow," *Nature*, vol. 405, no. 6782, pp. 53–55, 2000.

[14] A. Groisman and V. Steinberg, "Elastic turbulence in curvilinear flows of polymer solutions," *New J. Phys.*, vol. 6, no. 1, p. 29, 2004.

[15] L. Pan, A. Morozov, C. Wagner, and P. E. Arratia, "Nonlinear elastic instability in channel flows at low Reynolds numbers," *Phys. Rev. Lett.*, vol. 110, no. 17, p. 174502, 2013.

[16] B. Qin and P. E. Arratia, "Characterizing elastic turbulence in channel flows at low Reynolds number," *Phys. Rev. Fluids*, vol. 2, no. 8, p. 083302, 2017.

[17] X. Li, F. Li, W. Cai, H. Zhang, and J. Yang, "Very-low-*Re* chaotic motions of viscoelastic fluid and its unique applications in microfluidic devices: A review," *Exp. Therm. Fluid Sci.*, vol. 39, pp. 1–16, 2012.

[18] E. S. Shaqfeh, "Purely Elastic Instabilities in Viscometric Flows," *Annu. Rev. Fluid Mech.*, vol. 28, no. 1, pp. 129–185, 1996.

[19] R. G. Larson, "Instabilities in viscoelastic flows," *Rheol. Acta*, vol. 31, no. 3, pp. 213–263, 1992.

[20] T. M. Squires and S. R. Quake, "Microfluidics: Fluid physics at the nanoliter scale," *Rev. Mod. Phys.*, vol. 77, no. 3, pp. 977–1026, 2005.

[21] D. Samanta, Y. Dubief, M. Holzner, C. Schäfer, A. N. Morozov, C. Wagner, and B. Hof, "Elasto-inertial turbulence," *Proc. Natl. Acad. Sci.*, vol. 110, no. 26, pp. 10 557–62, 2013.

[22] Y. Dubief, V. E. Terrapon, and J. Soria, "On the mechanism of elasto-inertial turbulence," *Phys. Fluids*, vol. 25, no. 11, p. 110817, 2013.

[23] V. E. Terrapon, Y. Dubief, and J. Soria, "On the role of pressure in elasto-inertial turbulence," *J. Turbul.*, vol. 16, no. 1, pp. 26–43, 2015.

[24] P. C. Valente, C. B. da Silva, and F. T. Pinho, "Energy spectra in elasto-inertial turbulence," *Phys. Fluids*, vol. 28, no. 7, p. 075108, 2016.

[25] G. Choueiri and B. Hof, "Elasto-inertial turbulence in straight pipes at low Reynolds numbers," in *Bull. Am. Phys. Soc. 70th Annu. Meet. APS Div. Fluid Dyn.* American Physical Society, 2017.

[26] J. W. Hoyt and A. Fabula, "The effect of additives on fluid friction (AD0612056)," Naval Ordnance Test Station, China Lake, Tech. Rep., 1964.

[27] J. W. Hoyt, "A Freeman Scholar Lecture: The Effect of Additives on Fluid Friction," *J. Basic Eng.*, vol. 94, no. 2, p. 258, 1972.

[28] J. Hoyt, "Recent Progress in Polymer Drag Reduction (ADA003941)," Naval Undersea Center, San Diego, Tech. Rep., 1974.

[29] P. S. Virk, "Drag reduction fundamentals," *AIChE*, vol. 21, no. 4, pp. 625–656, 1975.

[30] J. R. Pearson, "Instability in Non-Newtonian Flow," *Annu. Rev. Fluid Mech.*, vol. 8, no. 1, pp. 163–181, 1976.

BIBLIOGRAPHY

[31] A. Gyr and H. Bewersdorff, *Drag Reduction of Turbulent Flows by Additives*, ser. Fluid Mechanics and Its Applications. Dordrecht: Springer Netherlands, 1995, vol. 32.

[32] A. N. Morozov and W. van Saarloos, "An introductory essay on subcritical instabilities and the transition to turbulence in visco-elastic parallel shear flows," *Phys. Rep.*, vol. 447, no. 3-6, pp. 112–143, 2007.

[33] R. Benzi and E. S. Ching, "Polymers in Fluid Flows," *Annu. Rev. Fluid Mech.*, vol. 9, no. 1, pp. annurev–conmatphys–033 117–053 913, 2018.

[34] O. Reynolds, "An Experimental Investigation of the Circumstances Which Determine Whether the Motion of Water Shall Be Direct or Sinuous, and of the Law of Resistance in Parallel Channels," *Philos. Trans. R. Soc. London*, vol. 174, no. 0, pp. 935–982, 1883.

[35] O. Reynolds, "On the Dynamical Theory of Incompressible Viscous Fluids and the Determination of the Criterion," *Philos. Trans. R. Soc. London A*, vol. 186, pp. 123–164, 1895.

[36] P. A. Davidson, *A voyage through turbulence*. Cambridge University Press, 2011.

[37] S. B. Pope, *Turbulent flows*. Cambridge University Press, 2000.

BIBLIOGRAPHY

[38] A. A. Townsend, *The structure of turbulent shear flow*, 2nd ed. Cambridge: Cambridge University Press, 1976.

[39] W. D. McComb, *The physics of fluid turbulence*. Clarendon Press, 1990.

[40] P. A. Davidson, *Turbulence : an introduction for scientists and engineers*, 2nd ed. Cambridge University Press, 2015.

[41] M. Landahl and E. Mollo-Christensen, *Turbulence and random processes in fluid mechanics*. Cambridge University Press, 1992.

[42] R. J. Adrian, K. T. Christensen, and Z. Liu, "Analysis and interpretation of instantaneous turbulent velocity fields," *Exp. Fluids*, vol. 29, no. 3, pp. 275–290, 2000.

[43] Y. S. Kwon, N. Hutchins, and J. P. Monty, "On the use of the Reynolds decomposition in the intermittent region of turbulent boundary layers," *J. Fluid Mech.*, vol. 794, pp. 5–16, 2016.

[44] P. Sagaut, *Large eddy simulation for incompressible flows: an introduction*. Springer-Verlag, 2006.

[45] G. L. Eyink and H. Aluie, "Localness of energy cascade in hydrodynamic turbulence. I. Smooth coarse graining," *Phys. Fluids*, vol. 21, no. 11, p. 115107, 2009.

[46] A. K. M. F. Hussain and W. C. Reynolds, "The mechanics of an organized wave in turbulent shear flow," *J. Fluid Mech.*, vol. 41, no. 2, p. 241, 1970.

[47] W. M. Orr, "The Stability or Instability of the Steady Motions of a Perfect Liquid and of a Viscous Liquid. Part II: A Viscous Liquid," pp. 69–138, 1907.

[48] A. Sommerfeld, "Ein beitrag zur hydrodynamischen erklaerung der turbulenten fluessigkeitsbewegungen," in *Atti del IV. Cong. intern. dei Mat.*, G. Castelnuovo, Ed., vol. 3. Rome: Tip. della R. Accademia dei Lincei, 1908, pp. 116–124.

[49] W. Tollmien, "Über die Entstehung der Turbulenz," *Nachrichten von der Gesellschaft der Wissenschaften zu Göttingen, Math. Klasse*, pp. 21–44, 1929.

[50] H. Schlichting, "Zur Enstehung der Turbulenz bei der Plattenströmung," *Nachrichten von der Gesellschaft der Wissenschaften zu Göttingen, Math. Klasse*, pp. 181–208, 1933.

[51] H. Schlichting, "Hauptaufsätze. Turbulenz bei Wärmeschichtung," *ZAMM - Zeitschrift für Angew. Math. und Mech.*, vol. 15, no. 6, pp. 313–338, 1935.

[52] G. B. Schubauer and H. Skramstad, "Laminar-Boundary-Layer Oscillations and Transition on a Flat Plate (NACA Technical Report 909)," NACA, Washington, DC, Tech. Rep., 1948.

[53] M. T. Landahl, "A note on an algebraic instability of inviscid parallel shear flows," *J. Fluid Mech.*, vol. 98, no. 2, p. 243, 1980.

[54] L. N. Trefethen, A. E. Trefethen, S. C. Reddy, and T. A. Driscoll, "Hydrodynamic stability without eigenvalues." *Science (80-.).*, vol. 261, no. 5121, pp. 578–84, 1993.

[55] B. Farrell, "Developing disturbances in shear," *J. Atmos. Sci.*, vol. 44, no. 16, pp. 2191–2199, 1987.

[56] K. M. Butler and B. F. Farrell, "Three-dimensional optimal perturbations in viscous shear flow," *Phys. Fluids A-Fluid*, vol. 4, no. 8, pp. 1637–1650, 1992.

[57] P. J. Schmid and D. S. Henningson, *Stability and transition in shear flows*. Springer New York, 2001.

[58] M. R. Jovanović and B. Bamieh, "Componentwise energy amplification in channel flows," *J. Fluid Mech.*, vol. 534, pp. 145–183, 2005.

[59] A. Lundbladh, D. S. Henningson, and S. C. Reddy, "Threshold Amplitudes for Transition in Channel Flows," in *Transition, Turbul. Combust.* Springer, Dordrecht, 1994, pp. 309–318.

[60] S. J. Chapman, "Subcritical transition in channel flows," *J. Fluid Mech.*, vol. 451, pp. 35–97, 2002.

[61] D. J. Benney and C. C. Lin, "On the Secondary Motion Induced by Oscillations in a Shear Flow," *Phys. Fluids*, vol. 3, no. 4, p. 656, 1960.

[62] J. T. Stuart, "On the non-linear mechanics of wave disturbances in stable and unstable parallel flows. Part 1. The basic behaviour in plane Poiseuille flow," *J. Fluid Mech.*, vol. 9, no. 3, p. 353, 1960.

[63] J. Watson, "On the non-linear mechanics of wave disturbances in stable and unstable parallel flows. Part 2. The development of a solution for plane Poiseuille flow and for plane Couette flow," *J. Fluid Mech.*, vol. 9, no. 3, p. 371, 1960.

[64] W. C. Reynolds and M. C. Potter, "Finite-amplitude instability of parallel shear flows," *J. Fluid Mech.*, vol. 27, no. 03, p. 465, 1967.

[65] K. Stewartson and J. T. Stuart, "A non-linear instability theory for a wave system in plane Poiseuille flow," *J. Fluid Mech.*, vol. 48, no. 03, p. 529, 1971.

[66] K. Fujimura, "The Equivalence Between Two Perturbation Methods in Weakly Nonlinear Stability Theory for Parallel Shear Flows," *Proc. R. Soc. A Math. Phys. Eng. Sci.*, vol. 424, no. 1867, pp. 373–392, 1989.

[67] F. Charru and E. J. Hinch, "'Phase diagram' of interfacial instabilities in a two-layer Couette flow and mechanism of the long-wave instability," *J. Fluid Mech.*, vol. 414, pp. 195–223, 2000.

[68] M. T. Landahl, "A wave-guide model for turbulent shear flow," *J. Fluid Mech.*, vol. 29, no. 3, pp. 441–459, 1967.

[69] M. T. Landahl, "On sublayer streaks," *J. Fluid Mech.*, vol. 212, pp. 593–614, 1990.

[70] J. C. del Álamo and J. Jiménez, "Linear energy amplification in turbulent channels," *J. Fluid Mech.*, vol. 559, pp. 205–213, 2006.

[71] Y. Hwang and C. Cossu, "Linear non-normal energy amplification of harmonic and stochastic forcing in the turbulent channel flow," *J. Fluid Mech.*, vol. 664, pp. 51–73, 2010.

[72] B. J. McKeon and A. S. Sharma, "A critical-layer framework for turbulent pipe flow," *J. Fluid Mech.*, vol. 658, pp. 336–382, 2010.

[73] G. K. Patterson, J. L. Zakin, and J. M. Rodriguez, "Drag reduction – Polymer Solutions, Soap Solutions, and Solid Particle Suspensions in Pipe Flow," *Ind. Eng. Chem.*, vol. 61, no. 1, pp. 22–30, 1969.

[74] J. G. Oldroyd, "On the Formulation of Rheological Equations of State," *Proc. R. Soc. A Math. Phys. Eng. Sci.*, vol. 200, no. 1063, pp. 523–541, 1950.

[75] R. B. Bird, R. C. Armstrong, and O. Hassager, *Dynamics of polymeric liquids*. Wiley, 1987.

[76] J. Azaiez and G. M. Homsy, "Linear stability of free shear flow of viscoelastic liquids," *J. Fluid Mech.*, vol. 268, p. 37, 1994.

[77] J. M. Rallison and E. J. Hinch, "Instability of a high-speed submerged elastic jet," *J. Fluid Mech.*, vol. 288, p. 311, 1995.

[78] R. G. Larson, E. S. G. Shaqfeh, and S. J. Muller, "A purely elastic instability in Taylor–Couette flow," *J. Fluid Mech.*, vol. 218, p. 573, 1990.

[79] Y. L. Joo and E. S. G. Shaqfeh, "A purely elastic instability in Dean and Taylor–Dean flow," *Phys. Fluids A-Fluid*, vol. 4, no. 3, pp. 524–543, 1992.

[80] D. D. Joseph, *Fluid Dynamics of Viscoelastic Liquids*, ser. Applied Mathematical Sciences. New York, NY: Springer New York, 1990, vol. 84.

[81] R. Sureshkumar, A. N. Beris, and R. Handler, "Direct numerical simulation of the turbulent channel flow of a polymer solution," *Phys. Fluids*, vol. 9, no. 3, pp. 743–755, 1997.

[82] Y. Dubief, C. M. White, V. E. Terrapon, E. S. G. Shaqfeh, P. Moin, and S. K. Lele, "On the coherent drag-reducing and turbulence-enhancing behaviour of polymers in wall flows," *J. Fluid Mech.*, vol. 514, pp. 271–280, 2004.

[83] J. M. J. Den Toonder, M. A. Hulsen, G. D. C. Kuiken, and F. T. M. Nieuwstadt, "Drag reduction by polymer additives in a turbulent pipe flow: numerical and laboratory experiments," *J. Fluid Mech.*, vol. 337, pp. 193–231, 1997.

[84] C. D. Dimitropoulos, R. Sureshkumar, and A. N. Beris, "Direct numerical simulation of viscoelastic turbulent channel flow exhibiting drag reduction: effect

of the variation of rheological parameters," *J. Non-Newtonian Fluid Mech.*, vol. 79, no. 2-3, pp. 433–468, 1998.

[85] T. Min, J. Y. Yoo, and H. Choi, "Effect of spatial discretization schemes on numerical solutions of viscoelastic fluid flows," *J. Non-Newtonian Fluid Mech.*, vol. 100, no. 1-3, pp. 27–47, 2001.

[86] T. Min, H. Choi, and J. Y. Yoo, "Maximum drag reduction in a turbulent channel flow by polymer additives," *J. Fluid Mech.*, vol. 492, pp. 91–100, 2003.

[87] T. Min, J. Y. Yoo, H. Choi, and D. D. Joseph, "Drag reduction by polymer additives in a turbulent channel flow," *J. Fluid Mech.*, vol. 486, pp. 213–238, 2003.

[88] P. Pakdel and G. H. McKinley, "Elastic Instability and Curved Streamlines," *Phys. Rev. Lett.*, vol. 77, no. 12, pp. 2459–2462, 1996.

[89] D. Boger and Y. Yeow, "The impact of ideal elastic liquids in the development of non-Newtonian fluid mechanics," *Exp. Therm. Fluid Sci.*, vol. 5, no. 5, pp. 633–640, 1992.

[90] A. N. Beris and B. J. Edwards, "Poisson bracket formulation of incompressible flow equations in continuum mechanics," *J. Rheol.*, vol. 34, no. 1, pp. 55–78, 1990.

[91] S. J. Lee and T. A. Zaki, "Simulations of natural transition in viscoelastic channel flow," *J. Fluid Mech.*, vol. 820, pp. 232–262, 2017.

[92] M. Masoudian, K. Kim, F. T. Pinho, and R. Sureshkumar, "A viscoelastic k–ε–v^2–f turbulent flow model valid up to the maximum drag reduction limit," *J. Non-Newtonian Fluid Mech.*, vol. 202, pp. 99–111, 2013.

[93] G. Iaccarino, E. S. G. Shaqfeh, and Y. Dubief, "Reynolds-averaged modeling of polymer drag reduction in turbulent flows," *J. Non-Newtonian Fluid Mech.*, vol. 165, no. 7, pp. 376–384, 2010.

[94] C. F. Li, V. K. Gupta, R. Sureshkumar, and B. Khomami, "Turbulent channel flow of dilute polymeric solutions: drag reduction scaling and an eddy viscosity model," *J. Non-Newtonian Fluid Mech.*, vol. 139, no. 3, pp. 177–189, 2006.

[95] M. Masoudian, C. B. da Silva, and F. T. Pinho, "Grid and subgrid-scale interactions in viscoelastic turbulent flow and implications for modelling," *J. Turbul.*, vol. 17, no. 6, pp. 543–571, 2016.

[96] S. Wang, M. D. Graham, F. J. Hahn, and L. Xi, "Time-series and extended Karhunen–Loève analysis of turbulent drag reduction in polymer solutions," *AIChE*, vol. 60, no. 4, pp. 1460–1475, 2014.

[97] M. Lee and R. D. Moser, "Direct numerical simulation of turbulent channel flow up to $Re_\tau = 5200$," *J. Fluid Mech.*, vol. 774, pp. 395–415, 2015.

[98] J. C. Maxwell, "On the Dynamical Theory of Gases," pp. 49–88, 1867.

[99] G. Jeffery, "The two-dimensional steady motion of a viscous fluid," *London, Edinburgh, Dublin Philos. Mag. J. Sci.*, vol. 29, no. 172, pp. 455–465, 1915.

[100] J. E. Marsden and T. J. R. Hughes, *Mathematical foundations of elasticity*. Dover, 1994.

[101] C. Truesdell and W. Noll, *The non-linear field theories of mechanics*. Berlin, Heidelberg: Springer Berlin Heidelberg, 2004.

[102] A. N. Beris and B. J. Edwards, *Thermodynamics of flowing systems : with internal microstructure*. Oxford University Press, 1994.

[103] D. F. James, "Boger Fluids," *Annu. Rev. Fluid Mech.*, vol. 41, no. 1, pp. 129–142, 2009.

[104] A. Morozov and S. E. Spagnolie, "Introduction to Complex Fluids," in *Complex Fluids Biol. Syst.* Springer, New York, NY, 2015, pp. 3–52.

[105] J. Page and T. A. Zaki, "The dynamics of spanwise vorticity perturbations in homogeneous viscoelastic shear flow," *J. Fluid Mech.*, vol. 777, pp. 327–363, 2015.

[106] F. T. Trouton, "On the Coefficient of Viscous Traction and Its Relation to that of Viscosity," pp. 426–440, 1906.

[107] J. Wisniak, "Frederick Thomas Trouton: The Man, the Rule, and the Ratio," *Chem. Educ.*, vol. 6, no. 1, pp. 55–61, 2001.

[108] R. S. Rivlin and K. Sawyers, "Nonlinear Continuum Mechanics of Viscoelastic Fluids," *Annu. Rev. Fluid Mech.*, vol. 3, no. 1, pp. 117–146, 1971.

[109] D. Cioranescu, V. Girault, and K. Rajagopal, *Mechanics and mathematics of fluids of the differential type*, ser. Advances in Mechanics and Mathematics. Cham: Springer International Publishing, 2016, vol. 35.

[110] J. Dunn and K. Rajagopal, "Fluids of differential type: Critical review and thermodynamic analysis," *Int. J. Eng. Sci.*, vol. 33, no. 5, pp. 689–729, 1995.

[111] K. Rajagopal and A. Srinivasa, "On the development of fluid models of the differential type within a new thermodynamic framework," *Mech. Res. Commun.*, vol. 35, no. 7, pp. 483–489, 2008.

[112] G. G. Stokes, "On the theories of the internal friction of fluids in motion, and of the equilibrium and motion of elastic solids," *Trans. Cambridge Philos. Soc.*, vol. 8, pp. 287–305, 1845.

[113] M. Reiner, "A Mathematical Theory of Dilatancy," *Am. J. Math.*, vol. 67, no. 3, p. 350, 1945.

[114] J. L. Lumley, "Turbulence in Non-Newtonian Fluids," *Phys. Fluids*, vol. 7, no. 3, p. 335, 1964.

[115] Y. Kuo and R. I. Tanner, "A Burgers-Type Model of Turbulent Decay in a Non-Newtonian Fluid," *J. Appl. Mech.*, vol. 39, no. 3, p. 661, 1972.

[116] K. Rajagopal and A. Srinivasa, "A thermodynamic frame work for rate type fluid models," *J. Non-Newtonian Fluid Mech.*, vol. 88, no. 3, pp. 207–227, 2000.

[117] K. R. Rajagopal and A. R. Srinivasa, "On the thermodynamics of fluids defined by implicit constitutive relations," *Zeitschrift für Angew. Math. und Phys.*, vol. 59, no. 4, pp. 715–729, 2008.

[118] K. R. Rajagopal and A. R. Srinivasa, "A Gibbs-potential-based formulation for obtaining the response functions for a class of viscoelastic materials," *Proc. R. Soc. A Math. Phys. Eng. Sci.*, vol. 467, no. 2125, pp. 39–58, 2011.

[119] M. Grilli, A. Vázquez-Quesada, and M. Ellero, "Transition to Turbulence and Mixing in a Viscoelastic Fluid Flowing Inside a Channel with a Periodic Array of Cylindrical Obstacles," *Phys. Rev. Lett.*, vol. 110, no. 17, p. 174501, 2013.

[120] A. N. Beris, M. Avgousti, and A. Souvaliotis, "Spectral calculations of viscoelastic flows: evaluation of the Giesekus constitutive equation in model flow problems," *J. Non-Newtonian Fluid Mech.*, vol. 44, pp. 197–228, 1992.

[121] B. Yu, F. Li, and Y. Kawaguchi, "Numerical and experimental investigation of turbulent characteristics in a drag-reducing flow with surfactant additives," *Int. J. Heat Fluid Flow*, vol. 25, no. 6, pp. 961–974, 2004.

[122] K. Rajagopal and A. Srinivasa, "Mechanics of the inelastic behavior of materials. Part I: theoretical underpinnings," *Int. J. Plast.*, vol. 14, no. 10-11, pp. 945–967, 1998.

[123] K. Rajagopal and A. Srinivasa, "Mechanics of the inelastic behavior of materials. Part II: inelastic response," *Int. J. Plast.*, vol. 14, no. 10-11, pp. 969–995, 1998.

[124] M. Mooney, "A Theory of Large Elastic Deformation," *J. Appl. Phys.*, vol. 11, no. 9, pp. 582–592, 1940.

[125] R. S. Rivlin, "Large Elastic Deformations of Isotropic Materials. I. Fundamental Concepts," pp. 459–490, 1948.

[126] R. S. Rivlin, "Large Elastic Deformations of Isotropic Materials. IV. Further Developments of the General Theory," *Philos. Trans. R. Soc. A Math. Phys. Eng. Sci.*, vol. 241, no. 835, pp. 379–397, 1948.

[127] C. Eckart, "The Thermodynamics of Irreversible Processes. IV. The Theory of Elasticity and Anelasticity," *Phys. Rev.*, vol. 73, no. 4, pp. 373–382, 1948.

[128] A. Green and P. Naghdi, "Rate-type constitutive equations and elastic-plastic materials," *Int. J. Eng. Sci.*, vol. 11, no. 7, pp. 725–734, 1973.

[129] J. Casey and P. Naghdi, "A prescription for the identification of finite plastic strain," *Int. J. Eng. Sci.*, vol. 30, no. 10, pp. 1257–1278, 1992.

[130] H. Ziegler, *An introduction to thermomechanics.* North-Holland Pub. Co., 1983.

[131] H. Ziegler and C. Wehrli, "The Derivation of Constitutive Relations from the Free Energy and the Dissipation Function," *Adv. Appl. Mech.*, vol. 25, pp. 183–238, 1987.

[132] H. Ziegler and C. Wehrli, "On a Principle of Maximal Rate of Entropy Production," *J. Non-Equilibrium Thermodyn.*, vol. 12, no. 3, pp. 229–244, 1987.

[133] C. Lanczos, *The variational principles of mechanics.* Dover Publications, 1986.

[134] S. Harris, *An introduction to the theory of the Boltzmann equation.* Dover Publications, 2004.

[135] M. Kardar, *Statistical physics of particles.* Cambridge University Press, 2007.

[136] M. Doi and S. F. Edwards, *The theory of polymer dynamics.* Clarendon Press, 1986.

[137] A. Gyr and H. Bewersdorff, "Physico-Chemical Properties of Polymers in Solutions and Suspensions, Surfactants in Solutions; Characterization of Fibres," in *Drag Reduct. Turbul. Flows by Addit.*, 1995, pp. 17–32.

[138] L. G. Leal, "Dynamics of dilute polymer solutions," in *Struct. Turbul. Drag Reduct.* Berlin, Heidelberg: Springer Berlin Heidelberg, 1990, pp. 155–185.

[139] H. Kramers, "Het gedrag van macromoleculen in een stroomende vloeistof," *Physica*, vol. 11, no. 1, pp. 1–19, 1944.

[140] P. E. Rouse, "A Theory of the Linear Viscoelastic Properties of Dilute Solutions of Coiling Polymers," *J. Chem. Phys.*, vol. 21, no. 7, pp. 1272–1280, 1953.

[141] B. H. Zimm, "Dynamics of Polymer Molecules in Dilute Solution: Viscoelasticity, Flow Birefringence and Dielectric Loss," *J. Chem. Phys.*, vol. 24, no. 2, pp. 269–278, 1956.

[142] C. Curtiss and R. Bird, "A kinetic theory of polymeric fluids," *Phys. A Statistical Mech. its Appl.*, vol. 118, no. 1-3, pp. 191–204, 1983.

[143] H. R. Warner, "Kinetic Theory and Rheology of Dilute Suspensions of Finitely Extendible Dumbbells," *Ind. Eng. Chem. Fundam.*, vol. 11, no. 3, pp. 379–387, 1972.

[144] R. Bird, P. Dotson, and N. Johnson, "Polymer solution rheology based on a finitely extensible bead–spring chain model," *J. Non-Newtonian Fluid Mech.*, vol. 7, no. 2-3, pp. 213–235, 1980.

[145] A. Peterlin, "Hydrodynamics of macromolecules in a velocity field with longitudinal gradient," *J. Polym. Sci. Part C Polymer Lett.*, vol. 4, no. 4, pp. 287–291, 1966.

[146] R. Keunings, "On the Peterlin approximation for finitely extensible dumbbells," *J. Non-Newtonian Fluid Mech.*, vol. 68, no. 1, pp. 85–100, 1997.

[147] D. Vincenzi, P. Perlekar, L. Biferale, and F. Toschi, "Impact of the Peterlin approximation on polymer dynamics in turbulent flows," *Phys. Rev. E*, vol. 92, no. 5, p. 053004, 2015.

[148] M. D. Graham, "Drag reduction and the dynamics of turbulence in simple and complex fluids," *Phys. Fluids*, vol. 26, no. 10, p. 101301, 2014.

[149] Y. Dubief, V. E. Terrapon, C. M. White, E. S. G. Shaqfeh, P. Moin, and S. K. Lele, "New answers on the interaction between polymers and vortices in turbulent flows," *Flow, Turbul. Combust.*, vol. 74, no. 4, pp. 311–329, 2005.

[150] L. Woods, *The Thermodynamics Of Fluid Systems*, ser. Oxford Engineering Science. Oxford: Clarendon Press, 1975.

[151] P. L. Maffettone and M. Minale, "Equation of change for ellipsoidal drops in viscous flow," *J. Non-Newtonian Fluid Mech.*, vol. 78, no. 2, pp. 227–241, 1998.

[152] M. Grmela, M. Bousmina, and J. Palierne, "On the rheology of immiscible blends," *Rheol. Acta*, vol. 40, no. 6, pp. 560–569, 2001.

[153] M. Grmela, A. Ammar, F. Chinesta, and G. Maîtrejean, "A mesoscopic rheological model of moderately concentrated colloids," *J. Non-Newtonian Fluid Mech.*, vol. 212, pp. 1–12, 2014.

[154] P. M. Mwasame, N. J. Wagner, and A. N. Beris, "On the macroscopic modelling of dilute emulsions under flow," *J. Fluid Mech.*, vol. 831, pp. 433–473, 2017.

[155] W. W. Willmarth, T. Wei, and C. Lee, "Laser anemometer measurements of Reynolds stress in a turbulent channel flow with drag reducing polymer additives," *Phys. Fluids*, vol. 30, no. 4, pp. 933–935, 1987.

[156] M. D. Warholic, H. Massah, and T. Hanratty, "Influence of drag-reducing polymers on turbulence: effects of Reynolds number, concentration and mixing," *Exp. Fluids*, vol. 27, no. 5, pp. 461–472, 1999.

[157] E. de Angelis, C. Casciola, and R. Piva, "DNS of wall turbulence: dilute polymers and self-sustaining mechanisms," *Comput. Fluids*, vol. 31, no. 4, pp. 495–507, 2002.

[158] K. Kim, C. Li, R. Sureshkumar, S. Balachandar, and R. J. Adrian, "Effects of polymer stresses on eddy structures in drag-reduced turbulent channel flow," *J. Fluid Mech.*, vol. 584, pp. 281–299, 2007.

[159] K. Kim and R. Sureshkumar, "Spatiotemporal evolution of hairpin eddies, Reynolds stress, and polymer torque in polymer drag-reduced turbulent channel flows," *Phys. Rev. E*, vol. 87, no. 6, p. 063002, 2013.

[160] J. Page and T. A. Zaki, "Streak evolution in viscoelastic Couette flow," *J. Fluid Mech.*, vol. 742, pp. 520–551, 2014.

[161] K. D. Housiadas and A. Beris, "Polymer-induced drag reduction: Effects of the variations in elasticity and inertia in turbulent viscoelastic channel flow," *Phys. Fluids*, vol. 15, no. 8, pp. 2369–2384, 2003.

[162] L. Xi and M. D. Graham, "Turbulent drag reduction and multistage transitions in viscoelastic minimal flow units," *J. Fluid Mech.*, vol. 647, pp. 421–452, 2010.

[163] P. R. Resende, K. Kim, B. A. Younis, R. Sureshkumar, and F. T. Pinho, "A FENE-P k–ε turbulence model for low and intermediate regimes of polymer-induced drag reduction," *J. Non-Newtonian Fluid Mech.*, vol. 166, no. 12, pp. 639–660, 2011.

[164] J. L. Lumley, *Stochastic Tools in Turbulence*. Academic Press, 1970.

[165] G. K. Batchelor, "The effect of homogeneous turbulence on material lines and surfaces," *Proc. R. Soc. A Math. Phys. Eng. Sci.*, vol. 213, no. 1114, pp. 349–366, 1952.

[166] R. Fattal and R. Kupferman, "Constitutive laws for the matrix-logarithm of the conformation tensor," *J. Non-Newtonian Fluid Mech.*, vol. 123, no. 2, pp. 281–285, 2004.

[167] M. A. Hulsen, R. Fattal, and R. Kupferman, "Flow of viscoelastic fluids past a cylinder at high Weissenberg number: Stabilized simulations using matrix logarithms," *J. Non-Newtonian Fluid Mech.*, vol. 127, no. 1, pp. 27–39, 2005.

[168] P. Knechtges, M. Behr, and S. Elgeti, "Fully-implicit log-conformation formulation of constitutive laws," *J. Non-Newtonian Fluid Mech.*, vol. 214, pp. 78–87, 2014.

[169] P. Knechtges, "The fully-implicit log-conformation formulation and its application to three-dimensional flows," *J. Non-Newtonian Fluid Mech.*, vol. 223, pp. 209–220, 2015.

[170] M. Moakher and P. G. Batchelor, "Symmetric positive-definite matrices: from geometry to applications and visualization," *Vis. Process. Tensor Fields*, pp. 285–298, 2006.

[171] N. Balci, B. Thomases, M. Renardy, and C. R. Doering, "Symmetric factorization of the conformation tensor in viscoelastic fluid models," *J. Non-Newtonian Fluid Mech.*, vol. 166, no. 11, pp. 546–553, 2011.

[172] A. Hoger and D. Carlson, "Determination of the stretch and rotation in the polar decomposition of the deformation gradient," *Q. Appl. Math.*, vol. 42, no. 1, pp. 113–117, 1984.

[173] T. C. T. Ting, "Determination of $C^{1/2}$, $C^{-1/2}$ and more general isotropic tensor functions of C," *J. Elast.*, vol. 15, no. 3, pp. 319–323, 1985.

[174] J. Casey, "A convenient form of the multiplicative decomposition of the deformation gradient," *Math. Mech. Solids*, vol. 22, no. 3, pp. 1–10, 2015.

[175] S. Sadik and A. Yavari, "On the origins of the idea of the multiplicative decomposition of the deformation gradient," *Math. Mech. Solids*, vol. 22, no. 4, pp. 771–772, 2017.

[176] V. Lubarda, "Constitutive theories based on the multiplicative decomposition of deformation gradient: thermoelasticity, elastoplasticity, and biomechanics," *Appl. Mech. Rev.*, vol. 57, no. 2, pp. 95–108, 2004.

[177] L. Anand, "A theory for non-Newtonian viscoelastic polymeric liquids," *Int. J. Plast.*, vol. 83, pp. 273–301, 2016.

[178] S. Wang, T. Kuo, and C. Hsu, "Trace bounds on the solution of the algebraic matrix Riccati and Lyapunov equation," *IEEE Trans. Automat. Contr.*, vol. 31, no. 7, pp. 654–656, 1986.

[179] T. Mori, "Comments on 'A matrix inequality associated with bounds on solutions of algebraic Riccati and Lyapunov equation' by J.M. Saniuk and I.B. Rhodes," *IEEE Trans. Autom. Control*, vol. 33, no. 11, p. 1088, 1988.

[180] M. S. Klamkin, "Elementary approximations to the area of N-dimensional ellipsoids," *Am. Math. Mon.*, vol. 78, no. 3, pp. 280–283, 1971.

[181] S. Lang, *Fundamentals of Differential Geometry*, ser. Graduate Texts in Mathematics. New York, NY: Springer New York, 2001, vol. 191.

[182] R. Bhatia, *Positive definite matrices*. Princeton University Press, 2015.

[183] X. Pennec, P. Fillard, and N. Ayache, "A Riemannian framework for tensor computing," *Int. J. Comput. Vis.*, vol. 66, no. 1, pp. 41–66, 2006.

[184] P. T. Fletcher and S. Joshi, "Riemannian geometry for the statistical analysis of diffusion tensor data," *Signal Processing*, vol. 87, no. 2, pp. 250–262, 2007.

[185] D. S. Bernstein, *Matrix mathematics : theory, facts, and formulas*. Princeton University Press, 2009.

[186] P. G. Batchelor, M. Moakher, D. Atkinson, F. Calamante, and A. Connelly, "A rigorous framework for diffusion tensor calculus," *Magn. Reson. Med.*, vol. 53, no. 1, pp. 221–225, 2005.

[187] A. Agarwal, L. Brandt, and T. A. Zaki, "Linear and nonlinear evolution of a localized disturbance in polymeric channel flow," *J. Fluid Mech.*, vol. 760, pp. 278–303, 2014.

[188] D. J. A. McKechan, C. Robinson, and B. Sathyaprakash, "A tapering window for time-domain templates and simulated signals in the detection of gravitational waves from coalescing compact binaries," *Class. Quantum Gravity*, vol. 27, no. 8, p. 084020, 2010.

[189] R. B. Dean, "Reynolds number dependence of skin friction and other bulk flow variables in two-dimensional rectangular duct flow," *J. Fluids Engng.*, vol. 100, no. 2, pp. 215–223, 1978.

[190] V. Dallas, J. C. Vassilicos, and G. F. Hewitt, "Strong polymer-turbulence interactions in viscoelastic turbulent channel flow," *Phys. Rev. E*, vol. 82, no. 6, p. 066303, 2010.

[191] P. L. Johnson, S. S. Hamilton, R. Burns, and C. Meneveau, "Analysis of geometrical and statistical features of Lagrangian stretching in turbulent channel flow using a database task-parallel particle tracking algorithm," *Phys. Rev. Fluids*, vol. 2, no. 1, p. 014605, 2017.

[192] V. Arsigny, P. Fillard, X. Pennec, and N. Ayache, "Geometric means in a novel vector space structure on symmetric positive-definite matrices," *SIAM J. Matrix Anal. Appl.*, vol. 29, no. 1, pp. 328–347, 2007.

[193] C. Meneveau and I. Marusic, "Generalized logarithmic law for high-order moments in turbulent boundary layers," *J. Fluid Mech.*, vol. 719, p. R1, 2013.

[194] X. I. A. Yang, I. Marusic, and C. Meneveau, "Hierarchical random additive process and logarithmic scaling of generalized high order, two-point correlations in turbulent boundary layer flow," *Phys. Rev. Fluids*, vol. 1, no. 2, p. 024402, 2016.

[195] L. Biferale, C. Meneveau, and R. Verzicco, "Deformation statistics of sub-Kolmogorov-scale ellipsoidal neutrally buoyant drops in isotropic turbulence," *J. Fluid Mech.*, vol. 754, pp. 184–207, 2014.

[196] M. R. Jovanović and S. Kumar, "Nonmodal amplification of stochastic disturbances in strongly elastic channel flows," *J. Non-Newtonian Fluid Mech.*, vol. 166, no. 14-15, pp. 755–778, 2011.

[197] M. R. Jovanović and S. Kumar, "Transient growth without inertia," *Phys. Fluids*, vol. 22, no. 2, p. 023101, 2010.

[198] C. R. Doering, B. Eckhardt, and J. Schumacher, "Failure of energy stability in Oldroyd-B fluids at arbitrarily low Reynolds numbers," *J. Non-Newtonian Fluid Mech.*, vol. 135, no. 2-3, pp. 92–96, 2006.

[199] N. Hoda, M. R. Jovanović, and S. Kumar, "Energy amplification in channel flows of viscoelastic fluids," *J. Fluid Mech.*, vol. 601, pp. 407–424, 2008.

[200] N. Hoda, M. R. Jovanović, and S. Kumar, "Frequency responses of streamwise-constant perturbations in channel flows of Oldroyd-B fluids," *J. Fluid Mech.*, vol. 625, pp. 411–434, 2009.

[201] B. Meulenbroek, C. Storm, A. N. Morozov, and W. van Saarloos, "Weakly nonlinear subcritical instability of visco-elastic Poiseuille flow," *J. Non-Newtonian Fluid Mech.*, vol. 116, no. 2, pp. 235–268, 2004.

[202] J. Page and T. A. Zaki, "Viscoelastic shear flow over a wavy surface," *J. Fluid Mech.*, vol. 801, pp. 392–429, 2016.

[203] S. J. Haward and A. Q. Shen, "Viscoelastic shear flow through wavy-wall microchannels," in *Soc. Rheol. 89th Annu. Meet.*, Denver, 2017.

[204] J. T. Stuart, "On the non-linear mechanics of hydrodynamic stability," *J. Fluid Mech.*, vol. 4, no. 1, pp. 1–21, 1958.

[205] M. Suzuki, "Generalized Trotter's formula and systematic approximants of exponential operators and inner derivations with applications to many-body problems," *Commun. Math. Phys.*, vol. 51, no. 2, pp. 183–190, 1976.

[206] M. Zhang, I. Lashgari, T. A. Zaki, and L. Brandt, "Linear stability analysis of channel flow of viscoelastic Oldroyd-B and FENE-P fluids," *J. Fluid Mech.*, vol. 737, pp. 249–279, 2013.

[207] G. Cardano and T. R. Witmer, *Ars magna, or, The rules of algebra.* Dover, 1993.

[208] I. Hameduddin, C. Meneveau, T. A. Zaki, and D. F. Gayme, "Geometric decomposition of the conformation tensor in viscoelastic turbulence," *J. Fluid Mech.*, 2018 (accepted, to appear).

[209] N. J. Higham, *Functions of matrices.* Society for Industrial and Applied Mathematics, 2008.

[210] G. K. Batchelor and A. A. Townsend, "The Nature of Turbulent Motion at

Large Wave-Numbers," *Proc. R. Soc. A Math. Phys. Eng. Sci.*, vol. 199, no. 1057, pp. 238–255, 1949.

[211] C. C. Lin, "Aspects of the Problem of Turbulent Motion," *J. Aeronaut. Sci.*, vol. 23, no. 5, pp. 453–461, 1956.

[212] K. Sreenivasan, "Fractals and Multifractals in Fluid Turbulence," *Annu. Rev. Fluid Mech.*, vol. 23, no. 1, pp. 539–604, 1991.

[213] U. Frisch, *Turbulence : the legacy of A. N. Kolmogorov*. Cambridge University Press, 1995.

[214] U. Frisch and G. Parisi, "Fully developed turbulence and intermittency," *Turbul. Predict. Geophys. fluid Dyn. Clim. Dyn.*, vol. 88, pp. 71–88, 1985.

[215] B. B. Mandelbrot, "Possible refinement of the lognormal hypothesis concerning the distribution of energy dissipation in intermittent turbulence." Springer, Berlin, Heidelberg, 1972, pp. 333–351.

[216] B. B. Mandelbrot, "Intermittent turbulence in self-similar cascades: divergence of high moments and dimension of the carrier," *J. Fluid Mech.*, vol. 62, no. 02, p. 331, 1974.

[217] C. Meneveau and K. R. Sreenivasan, "Simple multifractal cascade model for fully developed turbulence," *Phys. Rev. Lett.*, vol. 59, no. 13, pp. 1424–1427, 1987.

[218] C. Meneveau, K. R. Sreenivasan, P. Kailasnath, and M. S. Fan, "Joint multifractal measures: Theory and applications to turbulence," *Phys. Rev. A*, vol. 41, no. 2, pp. 894–913, 1990.

[219] C. Meneveau and K. R. Sreenivasan, "The multifractal nature of turbulent energy dissipation," *J. Fluid Mech.*, vol. 224, p. 429, 1991.

[220] R. Kerswell, "Nonlinear Nonmodal Stability Theory," *Annu. Rev. Fluid Mech.*, vol. 50, no. 1, pp. 319–345, 2018.

[221] R. M. Neumann, "Nonequivalence of the stress and strain ensembles in describing polymer-chain elasticity," *Phys. Rev. A*, vol. 31, no. 5, pp. 3516–3517, 1985.

[222] R. M. Neumann, "Implications of using the entropy spring model for an ideal polymer chain," *Phys. Rev. A*, vol. 34, no. 4, pp. 3486–3488, 1986.

[223] R. M. Neumann, "Polymer stretching in an elongational flow," *J. Chem. Phys.*, vol. 110, no. 15, p. 7513, 1999.

[224] D. Keller, D. Swigon, and C. Bustamante, "Relating single-molecule measurements to thermodynamics." *Biophys. J.*, vol. 84, no. 2 Pt 1, pp. 733–8, 2003.

[225] R. Neumann, "On the precise meaning of extension in the interpretation of polymer-chain stretching experiments." *Biophys. J.*, vol. 85, no. 5, pp. 3418–20, 2003.

[226] M. Süzen, M. Sega, and C. Holm, "Ensemble inequivalence in single-molecule experiments," *Phys. Rev. E*, vol. 79, no. 5, p. 051118, 2009.

[227] J. T. Titantah, C. Pierleoni, and J. Ryckaert, "Single chain elasticity and thermoelasticity of polyethylene," *J. Chem. Phys.*, vol. 117, no. 19, pp. 9028–9036, 2002.

[228] V. A. Ivanov, L. I. Klushin, and A. M. Skvortsov, "How to understand the ensemble equivalence during stretching of a single macromolecule," *Polym. Sci. Ser. A*, vol. 54, no. 8, pp. 602–613, 2012.

[229] P. Neff, B. Eidel, and R. J. Martin, "Geometry of Logarithmic Strain Measures in Solid Mechanics," *Arch. Ration. Mech. Anal.*, vol. 222, no. 2, pp. 507–572, 2016.

[230] M. Rosenfeld, D. Kwak, and M. Vinokur, "A fractional step solution method for the unsteady incompressible Navier-Stokes equations in generalized coordinate systems," *J. Comput. Phys.*, vol. 94, no. 1, pp. 102–137, 1991.

[231] X. Wu, K. D. Squires, and Q. Wang, "Extension of the fractional step method to general curvilinear coordinate systems," *Numer. Heat Transf. Part B Fundam.*, vol. 27, no. 2, pp. 175–194, 1995.

[232] T. Vaithianathan, A. Robert, J. G. Brasseur, and L. R. Collins, "An improved

algorithm for simulating three-dimensional, viscoelastic turbulence," *J. Non-Newtonian Fluid Mech.*, vol. 140, no. 1, pp. 3–22, 2006.

Vita

Ismail Hameduddin was born on 14th July, 1988 in Jeddah, a coastal city in *al-Ḥijāz*. He completed the Cambridge A-level examinations and matriculated at the University of Missouri–Columbia, both in 2006. He received the Bachelor of Science degree in Mechanical Engineering with a minor in Mathematics from the University of Missouri–Columbia, graduating with honors in 2009. He enrolled in the Mechanical Engineering Ph.D. program at the Johns Hopkins University in August 2012 as a Jay D. Samstag Fellow. He received a Master of Science degree in Mechanical Engineering from the Johns Hopkins University in 2015.